MAX PLANCK INSTITUTE FOR CHEMISTRY
Max Planck Graduate Center mit der Johannes Gutenberg-Universität
JOHANNES GUTENBERG UNIVERSITÄT MAINZ

Multiphase chemistry and partitioning of organic aerosols: phase state, accretion chemistry, and emergent precursors

Hyun Gu Kang
Born on 09.09.1992 in Seoul, Republic of Korea

Dissertation

for the academic degree of

'Doctor rerum naturalium '(Dr. rer. nat.) of the faculties:

08 - Physics, Mathematics and Computer Science

09 - Chemistry, Pharmaceutical Sciences, Geography and Geosciences

10 - Biology

University Medicine

Mainz, April 2026

Supervisor:

Second supervisor:

Day of the oral examination: July 9th, 2026

© 2026 Hyun Gu Kang

All rights reserved.

This dissertation is a cumulative work and includes chapters that are based on or reproduce material from peer-reviewed journal publications. For these chapters, the copyright and license agreements of the respective original journals apply; all other content is subject to the copyright of the author.

For my family and those whose paths crossed mine.

恩重如山

I hereby declare that I wrote the dissertation submitted without any unauthorized external assistance and used only sources acknowledged in the work. All textual passages which are appropriated verbatim or paraphrased from published and unpublished texts as well as all information obtained from oral sources are duly indicated and listed in accordance with bibliographical rules. In carrying out this research, I complied with the rules of standard scientific practice as formulated in the statutes of Johannes Gutenberg-University Mainz to insure standard scientific practice.

Hyun Gu Kang
Mainz, April 23, 2026

A Multi-layered Problem
Hyun Gu Kang

To welcome gases, the bulk must flow,
but more oxygen makes tangles grow.
And how to make model aerosols shrink?
We achieve with many layers inter-linked.

While we seek what aerosols hide underneath,
we find intertwined fates go beyond skin-deep.

Abstract

Atmospheric aerosols drive air quality and act as nuclei onto which cloud droplets form. Thus, aerosols also impact climate by regulating the reflective and scattering properties of clouds, and a large fraction of atmospheric aerosol consist of secondary organic aerosol (SOA). SOA are formed by secondary processes in the atmosphere, primarily via the oxidation of volatile organic compounds (VOC) and the condensation of the resulting oxygenated organic molecules (OOM). This gas-particle partitioning describes the exchange of molecules between the gas and particle phases to reach equilibrium based on the vapor pressures of the molecules. A large variety of VOC are present in the atmosphere, and the chemical diversity of their oxidation products is high. Laboratory studies often categorize OOM by their vapor pressures and report the SOA mass yields (Y_{SOA}) for VOC common in the atmosphere, such as monoterpenes, which is a class of biogenic compounds. The Y_{SOA} are reported for individual VOC, and models that estimate atmospheric SOA formation often presume that the Y_{SOA} from different VOC are linearly additive and that gas-particle partitioning is rapid.

However, experiments have found that gas-particle partitioning can be kinetically-limited when the particles are viscous, which alters the particle composition and growth. Furthermore, OOM react with each other to form accretion products, and the OOM of different VOC cross-react such that Y_{SOA} is not linearly additive. There are also emerging organic pollutants, like decamethylcyclopentasiloxane (D_5), whose SOA formation are not as well-studied. In this thesis, I used the kinetic multilayer model of multiphase chemistry (KM3C) to study the effects that particle phase state has on the multiphase chemistry of SOA. I also addressed how the presence of multiple organic precursors affects SOA formation and the potential of D_5 to form SOA in the atmosphere. Key findings of this thesis include:

1. **The immediate oxidation products of D_5 are volatile and need to undergo further oxidation to form secondary organosiloxane aerosol (SOSiA).** D_5 is an emergent pollutant and is commonly emitted from household chemicals. However, the experimental SOSiA mass yields (Y_{SOSiA}) are inconsistent, with some studies reporting negligible SOSiA formation, while others find much higher values. To reconcile these Y_{SOSiA}, we oxidized D_5 with OH under different OH exposures (OH_{exp}) in a flow reactor. We also developed a chemical mechanism for a simple chemical kinetic box model that includes multigenerational chemical aging reactions, which progressively reduce volatility with increasing oxidation. We explained the divergent Y_{SOSiA} between different experiments as a result of the different OH_{exp} conditions, where higher OH_{exp} results in higher formation of low-volatile products and thus higher Y_{SOSiA}.

2. **SOA phase state and multiprecursor effects need to be accounted for to accurately describe SOA formation and evolution.** Monoterpene + NO_3 chamber

experiments have found that SOA would not quickly evaporate with increasing temperatures and that the Y_{SOA} were not linearly additive when two different monoterpenes are oxidized together. We introduced an empirical relationship between SOA volatility and particle-phase bulk diffusion, and KM3C explained the slow evaporation of SOA via slow diffusion and the formation of a viscous surface "crust." Furthermore, the model attributed the nonlinear Y_{SOA} to cross reactions between the different precursor-derived intermediates, resulting in accretion products. In addition, we modeled the thermal desorption of SOA collected in a filter inlet for gases and aerosols connected to a chemical ionization mass spectrometer (FIGAERO-CIMS). We modeled both the SOA evolution in the chamber and parallel thermal desorption measurements using a single kinetic multilayer model and a single kinetic parameter set, which helped to constrain the parameter optimization.

In a related study, we modeled the SOA growth and evaporation data from the chamber with an empirical viscosity parameterization that relates the SOA components' vapor pressures and glass transition temperatures (T_g). This parameterization resulted in a much stronger surface crust formation, highlighting the need for additional research to constrain relationships between volatility and T_g.

3. **Kinetically-limited condensation of OOM and changes in OOM volatility explains the nearly-uniform nanoparticle growth across different gas-phase OOM concentrations.** Previous measurements of new particle formation have found that the growth of sub-10 nm particles appear to be nearly independent of gas-phase OOM concentrations. This finding was unexpected as higher OOM concentrations should result in faster growth. Here, we used KM3C to model the growth rates of newly-formed nanoparticles reported in the literature. We found that the growth of viscous nanoparticles are kinetically limited and that lower-volatile OOM forms at higher temperatures and vice versa. This interplay results in an apparent near-constant growth rate of nanoparticles.

Zusammenfassung

Atmosphärische Aerosole beeinflussen die Luftqualität und dienen als Kristallisationskeime für Wolkentröpfchen. Sie wirken sich somit auch auf das Klima aus, indem sie die Reflexions- und Streueigenschaften von Wolken regulieren. Ein Großteil der atmosphärischen Aerosole besteht aus sekundären organischen Aerosolen (SOA). SOA entstehen durch sekundäre Prozesse in der Atmosphäre, vorwiegend durch die Oxidation flüchtiger organischer Verbindungen (VOC) und die Kondensation der dabei entstehenden sauerstoffhaltigen organischen Moleküle (OOM). Diese Gas-Partikel-Verteilung beschreibt den Austausch von Molekülen zwischen der Gas- und der Partikelphase, bis sich ein Gleichgewicht basierend auf den Dampfdrücken der Moleküle einstellt. In der Atmosphäre ist eine Vielzahl von VOCs vorhanden, und die chemische Diversität ihrer Oxidationsprodukte ist hoch. Laborstudien kategorisieren OOM häufig anhand ihrer Dampfdrücke und geben die SOA-Massenausbeuten (Y_{SOA}) für in der Atmosphäre häufig vorkommende VOCs an, wie beispielsweise Monoterpene, eine Klasse biogener Verbindungen. Die SOA-Massenausbeuten (Y_{SOA}) werden für einzelne VOCs angegeben, und Modelle zur Abschätzung der atmosphärischen SOA-Bildung gehen häufig davon aus, dass sich die Y_{SOA} verschiedener VOCs linear addieren und die Gas-Partikel-Verteilung schnell erfolgt.

Experimente haben jedoch gezeigt, dass die Gas-Partikel-Verteilung kinetisch limitiert sein kann, wenn die Partikel viskos sind, was die Partikelzusammensetzung und das Partikelwachstum beeinflusst. Darüber hinaus reagieren OOM miteinander und bilden Akkretionsprodukte. Die OOM verschiedener VOCs reagieren kreuzreagieren, sodass sich die Y_{SOA} nicht linear addieren. Es gibt auch neuartige organische Schadstoffe wie Decamethylcyclopentasiloxan (D_5), deren SOA-Bildung weniger gut untersucht ist. In dieser Arbeit habe ich das kinetische Multischicht-Modelle der Multiphasenchemie (KM3C) verwendet, um die Auswirkungen des Partikelphasenzustands auf die Multiphasenchemie von SOA zu untersuchen. Ich habe außerdem untersucht, wie das Vorhandensein mehrerer organischer Vorläufer die SOA-Bildung beeinflusst und welches Potenzial D_5 zur SOA-Bildung in der Atmosphäre besitzt. Zu den wichtigsten Ergebnissen dieser Arbeit gehören:

1. **Die unmittelbaren Oxidationsprodukte von D5 sind flüchtig und müssen weiter oxidiert werden, um sekundäres Organosiloxan-Aerosol (SOSiA) zu bilden.** D_5 ist ein neuartiger Schadstoff und wird häufig von Haushaltschemikalien freigesetzt. Die experimentell ermittelten SOSiA-Massenausbeuten (Y_{SOSiA}) sind jedoch inkonsistent: Einige Studien berichten von vernachlässigbarer SOSiA-Bildung, während andere deutlich höhere Werte finden. Um diese unterschiedlichen Y_{SOSiA}-Werte zu klären, oxidierten wir D_5 mit OH unter verschiedenen OH-Expositionen (OH_{exp}) in einem Strömungsreaktor. Wir entwickelten außerdem einen chemischen Mechanismus für ein einfaches chemisches kinetisches Boxmodell, das mehrstufige chemische Alterungsreaktionen berücksichtigt, welche die Flüchtigkeit

mit zunehmender Oxidation schrittweise reduzieren. Wir erklärten die unterschiedlichen Y_{SOSiA}-Werte zwischen verschiedenen Experimenten mit den unterschiedlichen OH_{exp}-Bedingungen, wobei höhere OH_{exp}-Werte zu einer stärkeren Bildung von schwerflüchtigen Produkten und damit zu höheren Y_{SOSiA}-Werten führen.

2. **Um die Bildung und Entwicklung von sekundären organischen Aerosolen (SOA) präzise zu beschreiben, müssen der Phasenzustand und die Effekte mehrerer Vorläufer berücksichtigt werden.** Experimente in Monoterpen- und NO_3-Kammern haben gezeigt, dass SOA mit steigenden Temperaturen nicht schnell verdunstet und dass die Y_{SOSiA} nicht linear additiv sind, wenn zwei verschiedene Monoterpene gemeinsam oxidiert werden. Wir haben eine empirische Beziehung zwischen der SOA-Flüchtigkeit und der Diffusion in der Partikelphase eingeführt. Das KM3C-Modell erklärt die langsame Verdunstung von SOA durch langsame Diffusion und die Bildung einer viskosen Oberflächenkruste. Darüber hinaus führt das Modell die nichtlinearen Y_{SOSiA} auf Kreuzreaktionen zwischen den verschiedenen Vorläufer-abgeleiteten Zwischenprodukten zurück, die zu Akkretionsprodukte führen. Zusätzlich haben wir die thermische Desorption von SOA modelliert, die in einem Filtereinlass für Gase und Aerosole gesammelt wurde, der an ein chemisches Ionisationsmassenspektrometer (FIGAERO-CIMS) angeschlossen ist. Wir modellierten sowohl die Entwicklung sekundärer organischer Aerosole (SOA) in der Kammer als auch parallele thermische Desorptionsmessungen mithilfe eines einzigen kinetischen Multischicht-Modelle und eines einzigen kinetischen Parametersatzes. Dies trug zur Einschränkung der Parameteroptimierung bei.

   In einer ähnlichen Studie modellierten wir das Wachstum und die Verdampfungsdaten der SOA aus der Kammer mit einer empirischen Viskositätsparametrisierung, die die Dampfdrücke der SOA-Komponenten und die Glasübergangstemperaturen (T_g) verknüpft. Diese Parametrisierung führte zu einer deutlich stärkeren Oberflächenkrustenbildung und unterstreicht damit den Bedarf an weiterer Forschung zur Bestimmung der Zusammenhänge zwischen Flüchtigkeit und T_g.

3. **Die kinetisch limitierte Kondensation von OOM und Änderungen ihrer Flüchtigkeit erklären das nahezu gleichmäßige Nanopartikelwachstum bei unterschiedlichen OOM-Konzentrationen in der Gasphase.** Frühere Messungen der Neubildung von Partikeln ergaben, dass das Wachstum von Partikeln unter 10 nm nahezu unabhängig von der OOM-Konzentration in der Gasphase zu sein scheint. Dieser Befund war unerwartet, da höhere OOM-Konzentrationen zu einem schnelleren Wachstum führen sollten. In dieser Studie modellierten wir mithilfe des KM3C-Modells die in der Literatur beschriebenen Wachstumsraten neu gebildeter Nanopartikel. Wir fanden heraus, dass das Wachstum viskoser Nanopartikel kinetisch limitiert ist und dass sich bei höheren Temperaturen weniger flüchtige OOM

bilden und umgekehrt. Dieses Zusammenspiel führt zu einer scheinbar nahezu konstanten Wachstumsrate der Nanopartikel.

Acknowledgements

This thesis is the culmination of work and support from many people, and I am grateful to have been a part. I extend my gratitude to those whose efforts formed in me a firm grounding for me to pursue my curiosity in atmospheric chemistry.

List of Abbreviations

AVOC	Anthropogenic volatile organic compounds
CIMS	Chemical ionization mass spectrometer
CMAQ	Community Multiscale Air Quality model
C^*	Effective saturation mass concentration
D_b	Bulk diffusion coefficient
EMAC	ECHAM/MESSy Atmospheric Chemistry general circulation model
FIGAERO	Filter inlet for gases and aerosols
GECKO-A	Generator for explicit chemistry and kinetics of organics in the atmosphere
KM-SUB	Kinetic multi-layer model of aerosol surface and bulk chemistry
KM-GAP	Kinetic multi-layer model of gas-particle interactions in aerosols and clouds
KM-MEMO	Kinetic multi-layer meta model
KM3C	Kinetic multi-layer model of multiphase chemistry
MCGA	Monte Carlo genetic algorithm
MCM	Master chemical mechanism
OA	Organic aerosol
OH_{exp}	OH exposure
OOM	Oxygenated organic molecules
PEG	Polyethylene glycol
PM	Particulate matter
POA	Primary organic aerosol
PRA	Pöschl, Rudich, and Ammann
SMPS	Scanning mobility particle sizer
SOA	Secondary organic aerosol
SOSiA	Secondary organosiloxane aerosol
T_g	Glass transition temperature
VBS	Volatility basis set

VCP	Volatile chemical products
VOC	Volatile organic compounds

Contents

1. Introduction **1**
1.1. Atmospheric aerosol 1
1.2. Secondary organic aerosol 1
1.3. Volatile chemical products 2
1.4. Partitioning theory 3
1.5. Phase state of organic aerosol 4
1.6. Kinetic multilayer models 5
1.7. Research objectives 6

2. Results **7**
2.1. Overview 7
2.2. Volatile oxidation products and secondary organosiloxane aerosol from D_5 + OH at varying OH exposures 9
2.3. Multiphase chemistry and phase state explain nonlinear effects in the formation and evaporation of SOA from mixed monoterpene precursors 27
2.4. Surface crust formation controls evaporation kinetics of secondary organic aerosols 39
2.5. Temperature-dependent multiphase chemical kinetics explain uniform atmospheric nanoparticle growth rates 52

3. Conclusions and outlook **64**

4. Bibliography **66**

A. Personal List of Publications **76**

B. Supplement **78**

1. Introduction

1.1. Atmospheric aerosol

Aerosols are solid or liquid droplets suspended in gas. The collection of aerosols present in ambient air is often referred to as particulate matter (PM), and PM can be categorized by aerodynamic diameter, where these size categorizations come from how likely the particles are to be inhaled into the lungs (Seinfeld, 2016; Schraufnagel, 2020). Particles with aerodynamic diameters of 10 μm or smaller are considered coarse (PM10), 2.5 μm or smaller are fine (PM2.5), and 100 nm or smaller are ultrafine (PM0.1). These ultrafine particles are small enough to diffuse through the lipid bilayer of cell walls (Oberdörster et al., 2002; Schraufnagel, 2020). Exposure to PM is known to increase mortality and the likelihood of cardiovascular (Zhao et al., 2025) and pulmonary diseases (Pope et al., 2019; Safiri et al., 2022).

Atmospheric aerosols have complex effects on climate (Calvin et al., 2023), where aerosols can serve as nucleating surfaces for cloud droplet formation (Berkemeier et al., 2014) or directly scatter solar radiation (Li et al., 2022), both of which increase Earth's albedo. On the other hand, darker particles absorb infrared radiation and have a net warming effect (Feng et al., 2013). The composition of atmospheric aerosol is complex, where organic compounds, ammonium, sulfate, nitrate, sea salt, mineral dust, and black or elemental carbon are the predominant components (Pöschl, 2005).

1.2. Secondary organic aerosol

A large fraction of atmospheric organic aerosol (OA) are secondary organic aerosol (SOA, Jimenez et al., 2009). Volatile organic compounds (VOC) in the atmosphere react with hydroxyl radicals (OH), ozone (O_3), nitrate radicals (NO_3), and chlorine radicals (Cl) to produce oxygenated organic molecules (OOM, Shrivastava et al., 2017; Stolzenburg et al., 2025). Low-vapor pressure OOM from those reactions condense to form SOA (Seinfeld, 2016; Berkemeier et al., 2020), and SOA is estimated to be > 20 % of PM2.5 in urban environments (Nault et al., 2021). In addition to gas-phase reactions, SOA is also formed in the particle-phase through multiphase chemistry, which is the chemical interaction of species present in different phases (George and Abbatt, 2010; Shiraiwa et al., 2013; George et al., 2015; Abbatt and Ravishankara, 2023). This chemistry takes place on the surface of particles and within the particles (Ravishankara, 1997; Abbatt and Ravishankara, 2023). OOM also react with each other to form larger accretion products, both through gas-phase dimer formation and particle-phase oligomerization

(Berkemeier et al., 2020). Large molecules, indicative of accretion products, have been found in laboratory (Srivastava et al., 2022) and ambient particle samples (Kourtchev et al., 2016), highlighting the need for these species to be accounted for in chemical mechanisms (Heitto et al., 2022).

In the laboratory, SOA can be synthesized in flow reactors or in chambers, which are chemical reactors where SOA precursors are injected and SOA formation observed (Stolzenburg et al., 2022; Kenagy et al., 2024; Zhang et al., 2024). As for the VOC precursors, experiments with biogenic precursors like isoprene (C_5H_8) and monoterpenes ($C_{10}H_{16}$), like α-pinene and limonene, are available in the literature (Jokinen et al., 2015; Berkemeier et al., 2020; Takeuchi et al., 2022), but there remain VOC that are not as well-studied. SOA can be chemically analyzed with mass spectrometry (Thoma et al., 2022), and the filter inlet for gases and aerosols chemical ionization mass spectrometer (FIGAERO-CIMS) is used to study the composition of SOA by thermally desorbing SOA collected on a Teflon filter (Lopez-Hilfiker et al., 2014; Schobesberger et al., 2018; Takeuchi et al., 2022). Furthermore, the desorption temperatures reveal information about the vapor pressures of the SOA components (Lopez-Hilfiker et al., 2014). However, accretion products are suspected to undergo thermal decomposition in the FIGAERO-CIMS (Hall and Johnston, 2012), and models need to include this decomposition to model thermograms.

The SOA mass yield (Y_{SOA}) is the ratio of the mass of SOA produced over the mass of VOC reacted, and air quality models use Y_{SOA} derived from laboratory experiments to estimate atmospheric SOA formation. These experiments often quantify Y_{SOA} for individual VOC, and models presume that the Y_{SOA} of different VOC are linearly additive and that the OOM from different precursors do not cross-react (Takeuchi et al., 2022). However, multiprecursor experiments (Ahlberg et al., 2017; McFiggans et al., 2019; Takeuchi et al., 2022) have found that the total Y_{SOA} from the different precursors are not necessarily a linear sum. Models that address multiprecursor effects on Y_{SOA} and experiments to quantify the SOA formation potential of less-studied VOC are needed to improve estimates of SOA formation.

1.3. Volatile chemical products

A large portion of VOC in urban environments come from anthropogenic sources (AVOC, Coggon et al., 2021), and common examples include benzene and toluene from vehicle emissions (Huang et al., 2015). However, volatile chemical products (VCP, McDonald et al., 2018), which are AVOC emitted from everyday consumer products, such as personal care products, cleaning agents, paint, pesticides, glue, etc., are emerging as a dominant source of AVOC (Seltzer et al., 2021). In addition to being precursors to PM (Nault et al., 2021), AVOC are precursors to tropospheric ozone production (Bufalini et al., 1976; Coggon et al., 2021), and the US Environmental Protection Agency sets emissions rules based on the species' ozone formation potential (Chen and Luo, 2012).

Coggon et al. (2021) found that VCP accounts for more than 50 % of AVOC emissions and are driving urban ozone production in New York City.

Siloxanes, which are entirely synthetic molecules composed of silicon, oxygen, and alkyl groups, are emitted from silicone production and commercial chemicals, such as cosmetics and lubricants (Rücker and Kümmerer, 2015; Brunet et al., 2024). Of the siloxanes, decamethylcyclopentasiloxane (D_5) is a common emerging pollutant that is used as a VCP tracer species (Coggon et al., 2021), since D_5 is emitted from personal care products and is a precursor to making silicone rubber (Coggon et al., 2021). D_5 reacts with OH in the atmosphere (Rücker and Kümmerer, 2015) and is predicted to produce formaldehyde (HCHO) during oxidation (Fu et al., 2020), and HCHO contributes to ozone formation (Bufalini et al., 1976). Despite the predicted HCHO production, D_5 is not suspected to contribute to surface ozone formation (Carter et al., 1993; McDonald et al., 2018), and the production of HCHO has not been experimentally verified. Furthermore, D_5 produces secondary organosiloxane aerosol (SOSiA) in laboratory experiments, but the SOSiA mass yields (Y_{SOSiA}) reported in the literature are inconsistent (Wu and Johnston, 2017; Janechek et al., 2019; Charan et al., 2022). The experiments were also performed at different OH exposures ($\mathrm{OH_{exp}}$), which is the multiple of the OH concentration and experiment time. Higher $\mathrm{OH_{exp}}$ may increase the oxidation state and reduce the volatility of the products (Donahue et al., 2006; Robinson et al., 2007), and chemical mechanisms need to address the effect of $\mathrm{OH_{exp}}$ on Y_{SOSiA}.

1.4. Partitioning theory

Molecular exchange between the gas and particle phases is called gas-particle partitioning. The fraction of an organic species condensed in the particle phase at equilibrium is found with absorptive partitioning theory (Pankow, 1994), which assumes a homogeneous and rapidly-mixed particle bulk and that condensing species are solvated into the bulk immediately (absorption). At equilibrium, the mass fraction of a species in the particle phase (F_{p}) can be calculated using the OA mass loading (C_{OA}), which is the mass concentration of OA, and the effective saturation mass concentration (C^*). C^* is a unit conversion of vapor pressure into mass concentrations (Donahue et al., 2006; Stolzenburg et al., 2022). In general, molecules with higher numbers of hydrogen-bond forming functional groups and larger molecules have lower vapor pressures (Pankow and Asher, 2008). As Eq. 1.1 shows, higher mass fractions of species with lower vapor pressures will be in the particle-phase and vice versa.

$$F_{\mathrm{p}} = \frac{1}{1 + \frac{C^*}{C_{\mathrm{OA}}}} \tag{1.1}$$

The chemistry behind atmospheric SOA formation is complex, in part due to the number of precursors involved and the chemical diversity of OOM, and identifying each partitioning species is challenging. For reference, the Generator for Explicit Chemistry and Kinetics of Organics in the Atmosphere (GECKO-A) mechanism for the OH

oxidation of dodecane (C_8H_{18}) contains >10^5 species (Aumont et al., 2012), and the Master Chemical Mechanism (MCM, Saunders et al., 2003) contains thousands of species and more than ten thousand reactions. This chemical complexity makes implementing SOA chemistry in large-scale air quality models challenging. As a result, a variety of approaches to simplify the chemical mechanisms behind SOA formation have been proposed, such as the volatility basis set (VBS, Donahue et al., 2006; Stolzenburg et al., 2022).

The VBS simplifies estimating SOA formation and is used in air established quality models, such as the Community Multiscale Air Quality model (CMAQ, Koo et al., 2014; Woody et al., 2016) and the ECHAM/MESSy Atmospheric Chemistry general circulation model (EMAC, Pozzer et al., 2022). The VBS parameterization works by distributing the mass yields of OOM (α_i) into pre-designated and logarithmically-spaced "volatility bins" (Donahue et al., 2006; Stolzenburg et al., 2022), where these bins are defined by their C^*. The condensed fraction at equilibrium (Eq. 1.2) can be calculated With absorptive partitioning theory (Pankow, 1994; Donahue et al., 2006), and the sum of these condensed product fractions equals Y_{SOA}.

$$Y_{SOA} = \sum \frac{\alpha_i}{1 + \frac{C_i^*}{C_{OA}}} \tag{1.2}$$

The α_i for each volatility bin needs to be determined, and experiments (Schobesberger et al., 2018; Stolzenburg et al., 2022) or modeling the products from chemical mechanisms are used to derive the α_i. Laboratory experiments collect Y_{SOA} for different VOC (Stolzenburg et al., 2022), and the α_i are optimized using that data. Explicit chemical mechanisms, such as GECKO-A (Lannuque et al., 2018), predict OOM structures and yields, and the vapor pressures of these predicted OOM can be estimated (Pankow and Asher, 2008; Compernolle et al., 2011; Krüger et al., 2025) to retrieve α_i. Furthermore, the VBS allows for chemical aging reactions to be easily applied in chemical mechanisms (Donahue et al., 2006). For example, the decrease in vapor pressure of a molecule by the addition of polar functional groups (Pankow and Asher, 2008) can be represented via "bin-hopping" reactions (Robinson et al., 2007; Sommers et al., 2022).

1.5. Phase state of organic aerosol

Atmospheric and synthetic SOA can be viscous (Shiraiwa et al., 2011, 2017; Li et al., 2020; Galeazzo et al., 2024), and the gas-particle partitioning timescales can exceed experiment or reaction timescales. Such non-equilibrium scenarios follow adsorptive partitioning (Pöschl et al., 2007), where a monolayer of adsorbing species covers the surface, but the adsorbed species do not immediately solvate into the bulk. These adsorbed species are uptaken into the bulk based on the local bulk diffusivity near the surface. Particles under dry or cold conditions are suspected to be semi-solid or "glassy," particularly above the tropospheric boundary layer (Shiraiwa et al., 2017; Schmedding et al., 2020), which lies about 1 km above the surface depending on regional meteorology (Zhang

et al., 2025). Under such conditions, mixing timescales for such nanoparticles may be on the order of months to years (Shiraiwa et al., 2011), and the assumption that SOA are absorptive does not hold. The phase state of atmospheric particles need to assessed to improve the predictions of air quality models.

D_b is the bulk diffusion coefficient, which is used to calculate the mass transfer rate at which molecules move through the interior of a material, in this case the SOA bulk. Parameterizations based on particle composition have been proposed to estimate the D_b of SOA. Studies have found that there is a log-log relationship between viscosity and vapor pressures (Mitra, 1954; Woodman et al., 1960; Frank, 1962; Johnston and Sargent, 1970), suggesting there is a similar relationship between D_b and C^*. Li et al. (2020) found an empirical second-order polynomial relationship between modeled glass transition temperatures (T_g) and C^* of chemical standards, where T_g refers to the temperature where the material bulk changes from a glass-like solid state to a viscous-fluid state. T_g can be converted into D_b using a modified version of the Vogel–Fulcher–Tammann equation (Eq. 1.3 and 1.4, Li et al., 2020) and the Stokes-Einstein equation (Eq. 1.5, Einstein, 1905). Here, k_b is the Boltzmann constant, r_m is the molecular radius, T is the temperature, T_0 is the Vogel temperature, η is the viscosity, and D is the unitless fragility parameter, which is often assumed to be 10 for organic mixtures typical for atmospheric aerosol (Shiraiwa et al., 2017).

$$T_0 = \frac{39.17 \times T_0}{D + 39.17} \tag{1.3}$$

$$log_{10}(\eta) = -5 + 0.434 \times \frac{T_0 \times D}{T - T_0} \tag{1.4}$$

$$D_b = \frac{k_b T}{6\pi r_m \eta} \tag{1.5}$$

1.6. Kinetic multilayer models

To address scenarios where diffusion in a material is slow, kinetic multilayer models have been developed, where the bulk phase is divided into multiple layers, and mass transfer between those layers is explicitly calculated (Shiraiwa et al., 2013, 2017). This multilayer approach is based on the Pöschl, Rudich, and Ammann (PRA, Pöschl et al., 2007) framework and simulates the effects that slow mass transport may have on chemical outcomes. The PRA framework provides general flux-based rate equations and parameters to address mass transport and chemical reactions, which enables a molecular process-level description of interfacial processes.

Examples of kinetic multilayer models used for aerosols include the kinetic multilayer model of aerosol surface and bulk chemistry (KM-SUB, Shiraiwa et al., 2010) and the kinetic multilayer model of gas-particle interactions in aerosols and clouds (KM-GAP, Shiraiwa et al., 2012). In addition to atmospheric aerosols, these kinetic multilayer models have been applied to other reaction-diffusion systems, such as films

(Mishra et al., 2025), epithelial lung fluid (Mishra et al., 2023), and oleic acid ozonolysis (Berkemeier et al., 2021). Heterogeneous reactions on the surfaces of soot particles can also be explicitly modeled, like in the case of KM-GAP-CARBON (Berkemeier and Pöschl, 2024).

However, numerical stiffness can arise when a model layer approaches depletion. To resolve this issue, the model needs a numerical method to adaptively resize the model layers as the particle grows and evaporates. Furthermore, kinetic models may invoke large sets of parameters which are difficult to constrain (Berkemeier et al., 2017, 2021), so global optimization algorithms are necessary to optimize for multiple parameters. The Monte Carlo genetic algorithm (MCGA) is an example of such an algorithm (Berkemeier et al., 2017). AG Berkemeier has developed the Kinetic multilayer meta model (KM-MEMO), which is a kinetic multilayer model file generator written in Matlab that simplifies the model development process and global optimization.

1.7. Research objectives

This interdisciplinary PhD project encompasses laboratory experiments, computational model construction, and numerical method development between physics and atmospheric chemistry. Understanding gas-phase oxidation, particle-phase reactions, and diffusion are important across these multiphase chemical systems. The primary research obejectives of this thesis are:

1. Develop a chemical mechanism with multigenerational chemical aging to explain the divergent SOSiA mass yields reported in the literature, and perform D_5 + OH experiments with an oxidation flow reactor under different OH_{exp} conditions. Quantify Y_{SOSiA} and the gas-phase formation of HCHO.

2. Investigate the effects of a viscous phase state on the growth and evaporation of SOA from α-pinene and limonene + NO_3 in chamber experiments and the thermal desorption of that SOA. Address the effect of cross reactions on Y_{SOA}. Resolve numerical stiffness that arises as a model layer approaches depletion, and implement parameterizations to relate the diffusivity of model layers to composition.

3. Explain the near-uniform nanoparticle growth rates found in experiments and ambient air measurements with a kinetic multilayer model. Address the effects of slow particle-phase diffusion on nanoparticle growth.

2. Results

2.1. Overview

The findings of this PhD project are described in the following four sections of this dissertation. Three sections are manuscripts published in internationally-renowned peer-reviewed academic journals, two of which are first-author publications and one where I am the second author. The last section is a manuscript under preparation, where I will be the second author. Each section of this thesis starts with a quick summary of the findings, and the below figure (Figure 2.1) is an overview of this thesis.

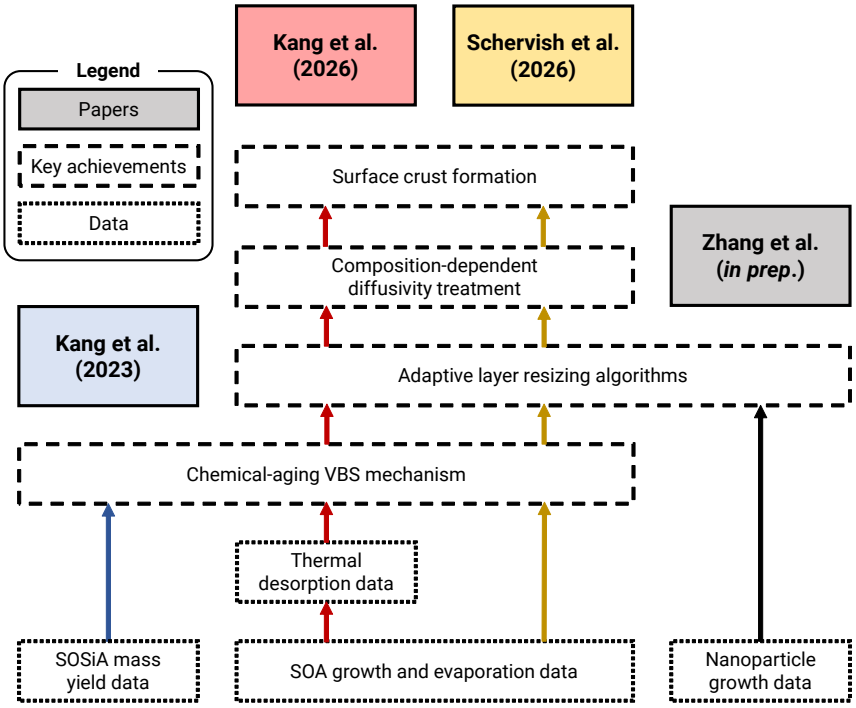


Figure 2.1.: *Overview of the PhD project, where each paper is a section in this thesis. The arrows indicate developments in the model and boxes indicate the data used, the key achievements, and papers in this thesis.*

The studies in this PhD project involve experiments and kinetic models of organic aerosol, which includes chemical mechanism development and the multiphase chemistry of SOA. An outline of the thesis is shown below:

Section 2.2 is an experimental study of SOSiA formation from D_5 + OH, where we also developed a chemical-aging model to explain the wide range of Y_{SOSiA} found at different OH_{exp}. We found that a chemical mechanism which accounts for reductions in volatility with increasing OH_{exp} reconciles the wide range of Y_{SOSiA}. The experiments in this study were performed in collaboration with Prof. Dr. Hwajin Kim at Seoul National University.

Section 2.3 describes the development and application of KM3C to model the growth and evaporation of monoterpene + NO_3 SOA in chambers and thermal desorption in the FIGAERO-CIMS. We concluded that SOA phase state and multiprecursor effects need to be addressed. This paper was the result of an international collaboration with Prof. Dr. Nga Lee Ng at the Georgia Institute of Technology.

Section 2.4 shows the kinetic modeling results of the limonene SOA chamber data in Berkemeier et al. (2020), where we used an empirical T_g–C^* relationship to estimate D_b. We found that surface crust formation explains the slow evaporation observed in the data. This study results from an international collaboration with Prof. Dr. Manabu Shiraiwa at the University of California, Irvine.

Section 2.5 is a not-yet-published modeling study on the near-uniform initial growth rates of newly-nucleated particles, regardless of OOM concentrations. We used KM3C conclude that kinetically-limited uptake and changing volatility distributions with temperature explain the observations.

2.2. Volatile oxidation products and secondary organosiloxane aerosol from D_5 + OH at varying OH exposures

This section has been published as a research article in the journal *Atmospheric Chemistry and Physics*, where I am the first author. I performed the experiments with assistance from Dr. Yanfang Chen and Yoojin Park. I analyzed the experiment data under the supervision of Prof. Dr. Hwajin Kim and developed and optimized the kinetic box model under the supervision of Dr. Thomas Berkemeier. I produced the figures and wrote the manuscript in collaboration with co-authors, and the supplement to this work is in Appendix B.1.

Kang, H. G., Chen, Y., Park, Y., Berkemeier, T., Kim, H.: Volatile oxidation products and secondary organosiloxane aerosol from D_5 + OH at varying OH exposures, *Atmos. Chem. Phys.* 23, 14307-14323 (2023).

In this experiment and modeling study, we reconciled the discrepant Y_{SOSiA} reported in the literature, where we noticed that the experiments were performed under varying OH_{exp}. We conducted our own D_5 + OH experiments in a flow reactor, developed an aging-VBS mechanism, and performed global optimizations of the model parameters. We found that the initial oxidation products are volatile and that multigenerational chemical aging of the D_5 products explains the higher Y_{SOSiA} found in high OH_{exp} experiments.

Atmos. Chem. Phys., 23, 14307–14323, 2023
https://doi.org/10.5194/acp-23-14307-2023
© Author(s) 2023. This work is distributed under
the Creative Commons Attribution 4.0 License.

Atmospheric Chemistry and Physics
Open Access
EGU

Volatile oxidation products and secondary organosiloxane aerosol from $D_5 + OH$ at varying OH exposures

Hyun Gu Kang[1], Yanfang Chen[2], Yoojin Park[3], Thomas Berkemeier[1], and Hwajin Kim[2,4]

[1]Multiphase Chemistry Department, Max Planck Institute for Chemistry, 55128 Mainz, Germany
[2]Department of Environmental Health Sciences, Graduate School of Public Health, Seoul National University, 08826 Seoul, South Korea
[3]Department of Environmental Science and Engineering, College of Engineering, Ewha Womans University, 03760 Seoul, South Korea
[4]Institute of Health and Environment, Graduate School of Public Health, Seoul National University, 08826 Seoul, South Korea

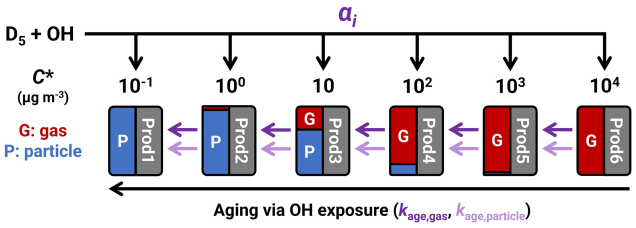
Correspondence: Thomas Berkemeier (t.berkemeier@mpic.de) and Hwajin Kim (khj0116@snu.ac.kr)

Received: 17 May 2023 – Discussion started: 12 June 2023
Revised: 15 September 2023 – Accepted: 21 September 2023 – Published: 20 November 2023

Abstract. Siloxanes are composed of silicon, oxygen, and alkyl groups and are emitted from consumer chemicals. Despite being entirely anthropogenic, siloxanes are being detected in remote regions and are ubiquitous in indoor and urban environments. Decamethylcyclopentasiloxane (D_5) is one of the most common cyclic congeners, and smog chamber and oxidation flow reactor (OFR) experiments have found $D_5 + OH$ to form secondary organosiloxane aerosol (SOSiA). However, there is uncertainty about the reaction products and the reported SOSiA mass yields (Y_{SOSiA}) appear inconsistent. To quantify small volatile oxidation products (VOPs) and to consolidate the Y_{SOSiA} in the literature, we performed experiments using a potential aerosol mass OFR while varying D_5 concentration, humidity, and OH exposure (OH_{exp}). We use a proton transfer reaction time-of-flight mass spectrometer to quantify D_5, HCHO, and HCOOH and to detect other VOPs, which we tentatively identify as siloxanols and siloxanyl formates. We determine molar yields of HCHO and HCOOH between 52 %–211 % and 45 %–127 %, respectively. With particle size distributions measured with a scanning mobility particle sizer, we find Y_{SOSiA} to be < 10 % at $OH_{exp} < 1.3 \times 10^{11}$ s cm^{-3} and ~ 20 % at OH_{exp}, corresponding to that of the lifetime of D_5 at atmospheric OH concentrations. We also find that Y_{SOSiA} is dependent on both organic aerosol mass loading and OH_{exp}. We use a kinetic box model of SOSiA formation and oxidative aging to explain the Y_{SOSiA} values found in this study and the literature. The model uses a volatility basis set (VBS) of the primary oxidation products as well as an aging rate coefficient in the gas phase, $k_{age,gas}$, of 2.2×10^{-12} cm^3 s^{-1} and an effective aging rate coefficient in the particle phase, $k_{age,particle}$, of 2.0×10^{-12} cm^3 s^{-1}. The combination of a primary VBS and OH-dependent oxidative aging predicts SOSiA formation much better than a standard-VBS parameterization that does not consider aging (root mean square error = 42.6 vs. 96.5). In the model, multi-generational aging of SOSiA products occurred predominantly in the particle phase. The need for an aging-dependent parameterization to accurately model SOSiA formation shows that concepts developed for secondary organic aerosol precursors, which can form low-volatile products at low OH_{exp}, do not necessarily apply to $D_5 + OH$. The resulting yields of HCHO and HCOOH and the parameterization of Y_{SOSiA} may be used in larger-scale models to assess the implications of siloxanes for air quality.

Published by Copernicus Publications on behalf of the European Geosciences Union.

Graphical abstract: schematic of the kinetic box model



1 Introduction

Organosiloxanes are molecules composed of silicon–oxygen bonds with alkyl groups on the silicons and encompass linear and cyclic species, some of which have vapor pressures on par with volatile organic compounds (VOCs). Siloxanes are entirely anthropogenic pollutants (Rücker and Kümmerer, 2015) commonly used in consumer and industrial chemical products (Seltzer et al., 2021a; Gkatzelis et al., 2021) and their emissions are projected to increase in the coming decades (Tansel and Surita, 2017). Decamethylcyclopentasiloxane (D_5, $C_{10}H_{30}O_5Si_5$), where "D" refers to silicon center atoms bonded to two oxygens, is a ubiquitous cyclosiloxane in the ambient environment.

Siloxanes have been detected in the indoor environment (Tang et al., 2015; Tran and Kannan, 2015; Arata et al., 2021; Katz et al., 2021; Kaikiti et al., 2022; Wang et al., 2022), near landfills (Schweigkofler and Niessner, 1999), and near sewage treatment sites (Lee et al., 2014; Horii et al., 2019). Siloxanes are also found in outdoor urban air (Xiang et al., 2021), and organosilicon compounds have been found in varying amounts in ambient particulates in China (Lu et al., 2019; Cheng et al., 2021; Meng et al., 2021; Song et al., 2022; Xu et al., 2022) and the United States (Milani et al., 2021).

Siloxanes are suspected to be environmentally persistent or emitted continuously to appear as such (Howard and Muir, 2010; Xiang et al., 2021), while other studies have found that methyl siloxanes would be removed on timescales of days to weeks (Graiver et al., 2003; Whelan and Kim, 2021). Reaction rate coefficients of D_5 with atmospheric oxidants have been reported, and Atkinson (1991) found D_5 to be effectively unreactive with atmospheric concentrations of O_3 ($k_{D_5+O3} < 3 \times 10^{-20}\,cm^3\,s^{-1}$) and NO_3 radicals ($k_{D_5+NO_3} < 3 \times 10^{-16}\,cm^3\,s^{-1}$) at ~ 298 K. While D_5 is reactive with OH and Cl, Alton and Browne (2020) calculated that the removal of D_5 by Cl radicals would only be a few percent of that by OH radicals at typical ambient oxidant concentrations.

Atkinson (1991), Safron et al. (2015), Xiao et al. (2015), Kim and Xu (2017), and Alton and Browne (2020) have measured k_{D_5+OH} at ~ 298 K to be 1.55×10^{-12}, 2.6×10^{-12}, 2.46×10^{-12}, 1.46×10^{-12}, and $2.1 \times 10^{-12}\,cm^3\,s^{-1}$, respectively. These measurements are summarized in Table S1 in the Supplement. Xiao et al. (2015) derived k_{D_5+OH} computationally as $2.90 \times 10^{-12}\,cm^3\,s^{-1}$. In this paper, we use $k_{D_5+OH} = 2.0 \times 10^{-12}\,cm^3\,s^{-1}$, which is a rounded average of the empirically determined rate coefficients. This k_{D_5+OH} corresponds to a D_5 atmospheric lifetime of about 4 d via removal by OH, assuming a daily average OH concentration ($[OH]_{avg}$) of $1.5 \times 10^6\,cm^{-3}$.

D_5 is expected to suppress O_3 formation in urban environments. Carter et al. (1993) performed a series of chamber experiments mimicking urban air conditions and found that D_5 siloxane would inhibit ozone formation by suppressing the OH radical. In contrast, formaldehyde (HCHO) is known to contribute to O_3 formation (Derwent et al., 1996). Fu et al. (2020) predicted the formation of HCHO as a product of $D_5 + OH$ in low-NO/HO_2 conditions using quantum chemical calculations and kinetics modeling, but an experimental yield of HCHO from $D_5 + OH$ has not been reported. Atkinson (1991) proposed HCHO as a product of the siloxane alkoxyl radical (RO) pathway, assuming an analogous mechanism to that of VOCs. Sommerlade et al. (1993) suggested that HCHO may arise from siloxane RO decomposition and from ROOH rearrangement in the presence of acids and H_2O. Alton and Browne (2022) predicted HCHO as a product of RO_2 rearrangement in the case of D_3 siloxane. Because HCHO is a secondary product, the O_3 formation potential of D_5 may differ between at a source and at downwind locations.

Formic acid (HCOOH) is a common acid catalyst in the atmosphere (Hazra et al., 2014) and a particle-nucleating species (Yu, 2000). Studies have identified some HCOOH sources in the atmosphere (Millet et al., 2015; Franco et al., 2021); however, HCOOH is suspected to have unidentified anthropogenic sources in the troposphere (Millet et al., 2015; Chen et al., 2021) as some urban sources remain unaccounted for (Le Breton et al., 2012; Yuan et al., 2015). Chandramouli and Kamens (2001) proposed that the RO_2 initially formed from $D_5 + OH$ makes a siloxanyl formate ($D_4T(OCHO)$, where "T" refers to a silicon center bonded to three oxygens) that reacts with H_2O to form a siloxanol ($D_4T(OH)$) and HCOOH. However, we are unaware of experimental HCOOH yields reported for $D_5 + OH$.

Whelan et al. (2004) used known siloxane chemistry in a partitioning model to assess the atmospheric fate of siloxanes and found that silanols are the predominant oxidation products. These silanols are generally water soluble and either removed from the atmosphere via wet deposition or undergo a pH-dependent process of hydrolysis, forming smaller and smaller silanols (Whelan et al., 2004). Eventually, the small silanols are converted to SiO_2, H_2O, and CO_2 through photolytic reactions in water or biological processes in soil (Spivack et al., 1997; Stevens, 1998; Graiver et al., 2003).

The intermediate products between D_5 and those small silanols are less studied, and the OH-oxidation rate coefficients of these intermediates have not been reported. Sommerlade et al. (1993) and Alton and Browne (2022) used

mass spectrometry to study the gaseous products of D_5 oxidation in chambers, while Fu et al. (2020) used quantum chemistry modeling. These studies found that gaseous intermediates are composed of a variety of alcohols, aldehydes, esters, and hydroperoxides. Given that such volatile oxidation products (VOPs) in experiments with higher OH_{exp} are likely to undergo multiple oxidation steps, there is a need to address their subsequent oxidation rate coefficients. Moreover, while the formation of HCHO and HCOOH has been predicted in mechanisms, it has not been quantified.

Secondary aerosol mass yield (Y, Eq. 1) is defined as the ratio of produced aerosol mass (Δm(SOSiA)) to reacted precursor mass ($\Delta m(D_5)$), which we adopt here for secondary organosiloxane aerosol (SOSiA). Reports about secondary aerosol formation from D_5 siloxane seem conflicting, with some experiments reporting much higher Y_{SOSiA} than others. For instance, Wu and Johnston (2017) and Janechek et al. (2019) saw maximum Y_{SOSiA} of 23 % and 50 %, respectively, in their photo-oxidation chamber and oxidation flow reactor (OFR) experiments, albeit at different OH exposures (OH_{exp}). Charan et al. (2022) found a Y_{SOSiA} of 158 % with their OFR at an OH_{exp} of 3.2×10^{12} s cm^{-3}. Avery et al. (2023) reported a wide range of Y_{SOSiA} values (2 %–146 %) from their OFR experiments.

$$Y_{SOSiA} = \frac{\Delta m(SOSiA)}{\Delta m(D_5)} \quad (1)$$

In contrast, Charan et al. (2022) reported almost negligible Y_{SOSiA} (< 5 %) from their chamber studies where [OH] was on the order of $\sim 10^6$ cm^{-3}, which is closer to [OH] found in ambient conditions (Peng and Jimenez, 2020). Han et al. (2022) conducted OFR experiments and found that Y_{SOSiA} would be 2 % at [OH] of 4.6×10^8 cm^{-3} or OH_{exp} of 5.5×10^{10} s cm^{-3}. The variation of Y_{SOSiA} reported in the literature suggests that oxidation conditions need to be considered to accurately parameterize Y_{SOSiA}, especially given that D_5 is being considered in air-quality models as a part of volatile chemical product inventories (Pennington et al., 2021; Seltzer et al., 2021a, b).

In this study, we aim to assess the OH oxidation of D_5 by determining the rate coefficients of secondary reactions of VOPs with OH (i.e., chemical aging) and providing a first quantification of HCHO and HCOOH yields. We also measure Y_{SOSiA} under diverse OH_{exp} and $[D_5]_0$ conditions. Lastly, we develop parameterizations of SOSiA yield using a kinetic model with a chemical aging reaction scheme to reconcile the reported Y_{SOSiA} from D_5+ OH in the literature and for use in air-quality models.

2 Method and materials

2.1 Experiments

The Aerodyne Research (Billerica, MA, USA) potential aerosol mass OFR (PAM-OFR) (Kang et al., 2007) has a volume of 13.3 L and is made of chromated aluminum (Xu and Collins, 2021). We operated the PAM-OFR in *OFR185* mode (Peng and Jimenez, 2020), where 185 nm lamps that also emit 254 nm light (GPH436T5VH, LightSources, Orange, CT, USA) generate OH and O_3 with injected H_2O vapor from a Nafion humidifier (FC-100-80-6MKK, Perma Pure, Lakewood, NJ, USA). There were two of these 185 nm lamps placed across from each other in clear fused quartz sleeves. The 185 nm lamps were wrapped with covers at even intervals to reduce the UV intensity so that 90 % of the lamp surface was covered. We operated the PAM-OFR at residence times (τ_{res}) of 120 and 180 s with flow rates of 6.65 and 4.43 L min^{-1}, respectively. Additional details about the experiment setup are summarized in Fig. S1 and Sect. S1.

We use the D_5 siloxane trace measured from the proton transfer reaction mass spectrometer (PTR-MS) to calculate OH_{exp} with Eq. (2), where $k_{D_5+OH} = 2.0 \times 10^{-12}$ cm^3 s^{-1}. $[D_5]_0$ and $[D_5]_{final}$ are the D_5 concentrations before and after the exposure to OH.

$$OH_{exp} = -\frac{1}{k_{D_5+OH}} \times \ln\left(\frac{[D_5]_{final}}{[D_5]_0}\right) \quad (2)$$

Prior to experiments, we checked the background particle and D_5 concentrations with the scanning mobility particle sizer (SMPS) and PTR-MS. In all experiments, the background particle number concentrations were < 10 cm^{-3}, and the background $[D_5]$ values were below the limit of detection ($3\sigma = 80$ ppt). Then, we injected D_5 with a syringe pump while monitoring the PTR-MS, with major ions at m/z 371 and m/z 355. We performed the experiments with a target $[D_5]_0$ of 50, 100, or 200 ppb. With these target $[D_5]_0$ values, we get external OH reactivities (OHR_{ext}) of 2.5–9.8 s^{-1} at 298.15 K and 1 atm, where OHR_{ext} is the reactivity caused by the injection of D_5 into the PAM-OFR (Peng and Jimenez, 2020). With these OHR_{ext} values, we reduce the risk of OH suppression and VOCs photolysis (Peng and Jimenez, 2020).

When the D_5 trace stabilized near the target $[D_5]_0$, we began the experiment by turning the UV lamps in the PAM-OFR on at either 2.4 or 8.0 V. We waited 30 min for the UV lamps to stabilize and for the PAM-OFR walls to equilibrate with gaseous species. The Y_{SOSiA} values (Eq. 1) were calculated using the average SOSiA mass concentration from four SMPS cycles following that 30 min. We obtained $\Delta m(D_5)$ as the difference between $[D_5]_0$ and $[D_5]_{final}$. At the end of an experiment, we turned off the UV lamps to check the D_5 trace return.

To clean the PAM-OFR between experiments, we stopped the syringe pump and removed the syringe from the glass bulb while keeping the humid airflow in the PAM-OFR. We

turned on the PAM-OFR UV lamps and connected the outlet directly to the exhaust, until D_5 and particle number concentrations were below the limit of detection. We used Igor Pro 9 (WaveMetrics, Portland, OR, USA) for data post-processing and visualization.

2.2 Instrumentation

2.2.1 PTR-MS

To measure D_5 and VOPs, we used a PTR-MS (PTR-TOF 1000, IONICON Analytik, Innsbruck, Austria) equipped with the extended volatility range (EVR) option (Piel et al., 2021), where the wetted inlet components and the drift tube are passivated with a silicon coating. The PTR-MS also had an ion transfer lens between the drift tube and time-of-flight mass spectrometer (Jordan et al., 2009). An internal permeation source (PerMaSCal) emitted a steady stream of 1,3-diiodobenzene into the mass spectrometer for mass calibration scale adjustments. Additional PTR-MS details are in Sect. S1.

To reduce H_2O clusters at high humidities, we operated the PTR-MS at 137 Td ($U_{drift} = 600$ V; Td is the Townsend unit where 1 Td $= 10^{-17}$ V cm^2) for quantification. The drift tube pressure and temperature were set to 2.30 mbar and 80 °C. For the reagent ion source, we set the U_s, U_{so}, and H_2O flow rate to 150 V, 80 V, and 6.00 sccm respectively. The ion source hollow-cathode discharge current was set to 5.0 mA. The PTR-MS drift tube was 9.6 cm long, and at 137 Td the $[H_2O]H^+$ reaction time (Δt) was 94 µs (de Gouw et al., 2003). We calculate the primary reagent ion signal, $[H_2O]H^+$, by multiplying the signal of its isotope, $[H_2^{18}O]H^+$, by 500.

We use the PTR-MS data for the quantification of D_5 (m/z 371), HCHO (m/z 31), and HCOOH (m/z 47), where the primary reagent ion counts were normalized to 10^6 counts per second (ncps). For D_5, we used a calibration gas cylinder (Apel-Riemer Environmental, Miami, FL, USA) containing D_5 to calibrate the PTR-MS. We also calculate the normalized measurement sensitivity (ncps ppb^{-1}) of D_5, HCHO, and HCOOH using Eq. (3) adapted from de Gouw and Warneke (2007). $I_{(VOC)H+}$ and $I_{(H_2O)H+}$ are the ion counts of the protonated VOCs and the reagent ion, respectively. Additional details on the mass spectra interpretation and quantification are in Sects. S1.5 and S3.

$$\text{Sensitivity} = \frac{\frac{I_{(VOC)H^+}}{I_{(H_2O)H^+}} \times 10^6}{[VOC]} \quad (3)$$

We tested the instrument sensitivity response with humidity by keeping the species concentrations constant while changing the sample air humidity. The sensitivity of D_5 at m/z 371 was not heavily affected by humidity at 137 Td, and we did not correct for humidity in the D_5 quantification (Fig. S5). On the other hand, HCHO and HCOOH sensitivities varied with humidity, and we corrected their sensitivities as detailed in Sect. S3. Prior to experiments, we tuned the micro-channel plate (MCP) to prevent signal bias against higher-mass ions (Müller et al., 2014). We adjusted the MCP voltage in steps to increase the signal strength at m/z 331, a diiodobenzene ion, until the relative signal increase was < 20 %.

2.2.2 Scanning mobility particle sizer

An SMPS 3938 (TSI, Shoreview, MN, USA) equipped with an impactor (0.0508 cm) measured the particle mobility diameter size distribution between diameters of 14.3 and 723.4 nm. The SMPS consisted of a model 3082 electrostatic classifier, a model 3081A differential mobility analyzer (DMA), a model 3088 soft X-ray neutralizer, and a model 3756 ultrafine condensation particle counter. We set the SMPS sheath flow at 3.0 L min^{-1} and the aerosol flow rate at 0.3 L min^{-1}, and the DMA voltage ranged from 10.6 to 9921.4 V. The SMPS scanned for 150 s, followed by a 5 s retrace and 10 s purge while recording on a 3 min cycle. We referred to the manufacturer's recommendations when deciding these SMPS settings (TSI Inc., 2012), and a sample particle size distribution from experiment 12 (Table 1) is shown in Fig. S4.

For the Y_{SOSiA} calculations, we convert the SMPS integrated particle volumes into mass using a SOSiA mass density (ρ_{SOSiA}) of 1.07 g cm^{-3} for all experiments. We obtained this ρ_{SOSiA} from PAM-OFR experiments separate from the ones described here, where we weighed the masses of SOSiA collected on filters and obtained particle volumes with the SMPS. Additional details on ρ_{SOSiA} are available in Sect. S2.

2.3 Volatility distribution parameterization

Janechek et al. (2019) and Charan et al. (2022) fitted their Y_{SOSiA} data to the Odum two-product model (Odum et al., 1996), and we follow the same methodology for comparison with the literature (Sect. S4). Similarly, we fit the standard volatility basis set (VBS) parameters α (Donahue et al., 2006) in Eq. (4) to the measured Δm(SOSiA) using the measured $\Delta m(D_5)$, where α_i is the product mass yield for volatility bin i.

$$\Delta m\,(\text{SOSiA}) = \Delta m\,(D_5) \times \sum_{i=1}^{n} \frac{\alpha_i}{1 + \frac{C_i^*}{C_{OA}}} \quad (4)$$

In the experiments, the organosiloxane aerosol mass loading (C_{OA}) was equivalent to the SOSiA mass concentrations. As the produced aerosol mass in the experiments ranged from 3.7 to 965.7 µg m^{-3}, we use six logarithmically spaced effective saturation mass concentration (C^*) bins ranging from 0.1 to 10 000 µg m^{-3} at 298.15 K to cover the low- and high-volatility products. For reference, D_5 liquid has a vapor pressure of 20.4 Pa at 298.15 K or $C^* = 3.05 \times 10^6$ µg m^{-3} (Lei et al., 2010). Since the experiments had slight variations in

Table 1. Summary of SOSiA mass yields (Y_{SOSiA}) with aerosol sampling line corrections assuming $\rho_{SOSiA} = 1.07\,g\,cm^{-3}$ for all experiments. [H_2O] is the molar mixing ratio of H_2O in air. For C_{OA} and [D_5] the errors are the standard deviation of the data points averaged, while for Y_{SOSiA} they are calculated with error propagation. For reference, at 25 °C and 1 atm, 1 ppb of D_5 is $\sim 15\,\mu g\,m^{-3}$ and 1 d equivalent of OH_{exp} is $\sim 1.3 \times 10^{11}\,s\,cm^{-3}$ at a daily $[OH]_{avg}$ of $1.5 \times 10^6\,cm^{-3}$.

Experiment	Y_{SOSiA} (%)	[H_2O] (%)	C_{OA} ($\mu g\,m^{-3}$)	OH_{exp} ($s\,cm^{-3}$)	[OH] (cm^{-3})	$[D_5]_0$ (ppb)	$1 - [D_5]_{final}/[D_5]_0$
1	5.4 ± 0.9	0.892	10.5 ± 0.7	1.73×10^{11}	9.59×10^8	43.4 ± 1.3	0.292
2	4.6 ± 0.6	0.828	19.0 ± 0.6	1.90×10^{11}	1.06×10^9	85.7 ± 2.5	0.316
3	3.1 ± 0.6	0.742	17.7 ± 0.5	1.26×10^{11}	6.99×10^8	165.8 ± 4.5	0.222
4	18.3 ± 1.5	1.95	75.2 ± 1.9	4.66×10^{11}	2.59×10^9	44.0 ± 1.7	0.606
5	28.0 ± 2.7	2.06	179.2 ± 3.1	3.80×10^{11}	2.11×10^9	78.3 ± 3.2	0.532
6	25.5 ± 1.8	2.09	286.2 ± 7.1	3.12×10^{11}	1.73×10^9	157.8 ± 3.6	0.464
7	8.0 ± 0.5	0.733	36.8 ± 1.3	5.76×10^{11}	3.20×10^9	43.8 ± 1.3	0.684
8	17.8 ± 1.7	0.736	118.6 ± 5.6	4.00×10^{11}	2.22×10^9	78.9 ± 3.2	0.550
9	21.1 ± 1.1	0.797	304.5 ± 2.8	4.19×10^{11}	2.33×10^9	166.8 ± 4.1	0.567
10	38.0 ± 2.2	1.93	212.9 ± 8.1	9.01×10^{11}	5.00×10^9	43.8 ± 1.4	0.835
11	45.6 ± 1.9	2.08	420.2 ± 3.0	7.78×10^{11}	4.32×10^9	76.5 ± 2.2	0.789
12	52.3 ± 2.4	2.15	965.7 ± 25	7.39×10^{11}	4.10×10^9	156.9 ± 3.9	0.772
13	4.2 ± 1.7	0.712	3.9 ± 0.3	8.70×10^{10}	7.25×10^8	37.9 ± 1.6	0.160
14	1.7 ± 0.4	0.718	4.1 ± 0.3	1.09×10^{11}	9.10×10^8	80.8 ± 2.3	0.196
15	1.0 ± 0.3	0.704	3.7 ± 0.7	8.29×10^{10}	6.91×10^8	162.8 ± 4.9	0.153

temperature, we correct for temperature impacts on C^* between experiments using the Clausius–Clapeyron equation and an enthalpy of vaporization of $60\,kJ\,mol^{-1}$, which is that of D_5 siloxane (Lei et al., 2010).

As the experiments were performed for a range of OH_{exp}, the products between experiments may have varied due to multi-generational aging (Zhao et al., 2015). To account for aging and parameterize Y_{SOSiA} as a function of OH_{exp}, we also analyze the yield data using a kinetic box model with four chemical reactions (Reactions R1–R3) written in MATLAB (MathWorks, Natick, MA, USA).

$$D_5 + OH \rightarrow \sum \alpha_i \times \text{prod}(i) \quad \left(k_{D_5+OH} = 2.0 \times 10^{-12}\,cm^3\,s^{-1}\right) \tag{R1}$$

$$(1 - f_i) \times \text{prod}(i) + OH \rightarrow (1 - f_i) \times \text{prod}(i-1) \left(k_{age,gas}, i = 2, \ldots, 6\right) \tag{R2}$$

$$f_i \times \text{prod}(i) + OH \rightarrow f_i \times \text{prod}(i-1) \left(k_{age,particle}, i = 2, \ldots, 6\right) \tag{R3}$$

Reaction (R1) describes the initial oxidation of D_5 and immediate formation of products of varying volatility. Here, prod(i) refers to the sum of products (gas + particle) in volatility bin i, which are formed with a molar branching ratio α_i. We assume that prod(i) values have the same molecular weights ($g\,mol^{-1}$) as D_5, and so the α_i values are equivalent to the product mass yields at $OH_{exp} \rightarrow 0$. In the model, a fraction f_i of each oxidation product partitions instantaneously from the gas phase to the particle phase according to absorptive partitioning theory (Donahue et al., 2006) (Eq. 5).

$$f_i = \left(\frac{1}{1 + \frac{C_i^*}{C_{OA}}}\right) \tag{5}$$

Reactions (R2) and (R3) describe how OH_{exp} causes volatility to decrease (Robinson et al., 2007). This decrease in volatility via "bin hopping" (Sommers et al., 2022) occurs at a rate proportional to the chemical aging rate coefficient for the gas-phase ($k_{age,gas}$, $cm^3\,s^{-1}$) and an effective aging rate coefficient for the particle-phase species ($k_{age,particle}$, $cm^3\,s^{-1}$). Here we assume that products in the lowest-volatility bin ($i = 1$) cannot be removed from that bin and that the highest-volatility bin ($i = 6$) does not receive product with aging. The [OH] values are set by dividing the experimental OH_{exp} from Eq. (2) by the PAM-OFR residence times.

We use $k_{age,gas}$ and $k_{age,particle}$ as aggregate chemical aging rate coefficients, not specific to any species or volatility bin. Studies on chamber experiments (Robinson et al., 2007) and ambient measurements (Sommers et al., 2022) have applied chemical aging only to the gas phase as heterogeneous aging is slower. However, studies have found that the high oxidant concentrations in OFRs would appreciably oxidize organic aerosol (OA) within experiment timescales (Kessler et al., 2012; Kroll et al., 2015). To accommodate OH uptake to the bulk phase, we include particle-phase aging that also decreases the volatility of particle-phase products. The timescales and atmospheric relevance of heterogeneous oxidation in OFRs are areas of ongoing research (Zhao et al., 2019; Peng and Jimenez, 2020), but for now we opt to fit

chemical aging rate coefficients for each phase. Note that surface and bulk accommodation processes are not explicitly resolved in the kinetic model and $k_{age,particle}$ acts on the concentrations of particle-phase products per unit gas volume (Sect. S1.6).

We fit $k_{age,gas}$, $k_{age,particle}$, and α_i in the aging-VBS model to the experimental SOSiA mass using the Monte Carlo genetic algorithm (MCGA) (Berkemeier et al., 2017). We obtain a best model fit and a fit ensemble consisting of 1059 parameter sets for which the model's root mean square error (RMSE) is below the threshold of 50. We find this ensemble to estimate the parametric uncertainty associated with the model fit (Berkemeier et al., 2021).

We use the OFR chemistry template with KinSim (Peng and Jimenez, 2020) to estimate the RO_2 fates and expect the fates to have been uniform across the experiments (Sect. S5). Although there are uncertainties in the RO_2 reaction rate coefficients for siloxanes, we expect that the variation in Y_{SOSiA} is not driven by RO_2 fate in these experiments. We also report the condensational sink and condensation lifetimes (Palm et al., 2016) calculated using the particle size distributions in Sect. S1.3.

3 Results and discussion

3.1 Volatile organic products (VOPs)

3.1.1 Siloxanol and formate ester trends

In Fig. 1, the PTR-MS signals before and after D_5 is oxidized are displayed relative to the protonated D_5 ion at m/z 371 on the y axis. We perform this scaling because the isotopologues of the product fragment ions overlap with the isotopologues of D_5. Thus, changes in signal intensity are caused by both product formation and D_5 oxidation. We choose to normalize the spectra at m/z 371 because we assume that no product ion peaks overlap with the $[D_5]H^+$ signal at m/z 371. While this scaling makes the product peaks appear larger, the changes in the mass spectrum are also qualitatively highlighted. For example, D_5 loses a methyl group during the PTR, which forms a large signal at m/z 355. The isotopologues of the -CH_4 fragment of $[D_5]H^+$ overlap with fragments of VOPs. By scaling the mass spectrum with the ratio of $[D_5]H^+$ signal before and after oxidation, the signal of the VOPs is separated from that of remaining D_5.

Using the mass spectra and species reported by Alton and Browne (2022), we attribute the indicated ions in Fig. 1 to siloxanol ($D_4T(OH)$), siloxanediol ($D_3T_2(OH)_2$), siloxanyl formate ($D_4T(OCHO)$), and siloxanolyl formate ($D_3T_2(OH)(OCHO)$). Here, D and T refer to silicon centers bonded to two and three oxygen atoms, respectively. The multifunctional VOPs are reported to arise from multiple steps of oxidation (Alton and Browne, 2022). The red and pink shaded areas in the inset of Fig. 1 refer to the enhancement in signal over that of the -CH_4 fragment of $[D_5]H^+$,

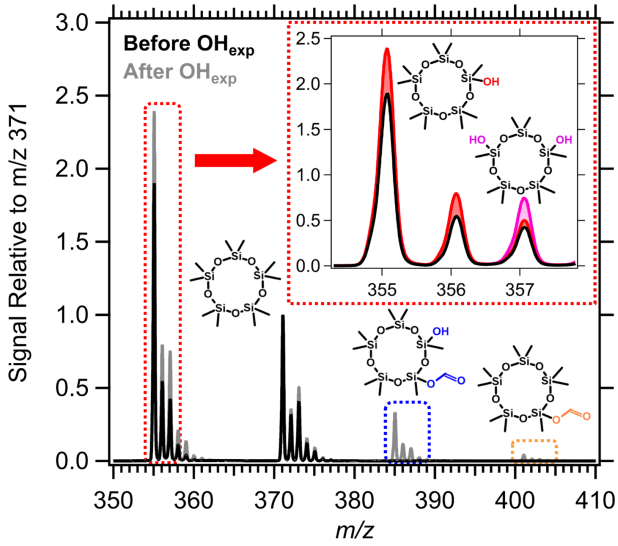


Figure 1. Example PTR-MS mass spectra from experiment 12 and proposed VOP ions. For visualization, the signal intensities before (black) and after (gray) oxidation are shown relative to the maximum signal intensity of the $[D_5]H^+$ ion at m/z 371, which is set to 1. The multifunctional species (blue, pink) are expected to be formed through multiple steps of OH oxidation. The red and pink areas in the inset each refer to the enhancement in signal attributed to $D_4T(OH)$ and $D_3T_2(OH)_2$ over that of the -CH_4 fragment of $[D_5]H^+$ and isotope signals, respectively.

which we attribute to the -H_2O fragments of $[D_4T(OH)]H^+$ and $[D_3T_2(OH)_2]H^+$, respectively. We use the masses of the -H_2O fragments of the protonated siloxanols as large alcohols dissociate during the PTR (Brown et al., 2010). We also attribute the ions in the blue- and yellow-dotted boxes to the -H_2O fragments of $[D_3T_2(OH)(OCHO)]H^+$ and $[D_4T(OCHO)]H^+$.

As we did not have calibration standards to quantify these VOPs, we calculate the molar yields of the VOPs relative to that of protonated D_5 siloxane at m/z 371 to study the trends of siloxane VOPs (Fig. 2). For each VOP, we choose a characteristic peak in the mass spectrum and calculate the change in signal due to VOP formation (Sect. S1.5). Then, we calculate the ratios of the changes in the VOP and D_5 signals to get the relative molar yields ($Y_{rel,VOPi}$). In the right-side panels for each VOP in Fig. 2, the $Y_{rel,VOPi}$ decreases with increasing OH_{exp} (x axes). This decrease in VOP signal is consistent with these gaseous products undergoing further oxidation or increased gas–particle partitioning due to higher C_{OA} at higher OH_{exp}. We use the colors to highlight the functional groups on the D_5 backbone.

In the left-side panels for each VOP in Fig. 2, the relative signals of the VOPs (y axes) decrease with increasing OH_{exp} (color scale). Then, assuming that [OH] is constant throughout the PAM-OFR, that $D_5 + OH$ is the rate-limiting step in VOP formation, and that removal via gas–particle partitioning is negligible (Alton and Browne, 2022), we can consider

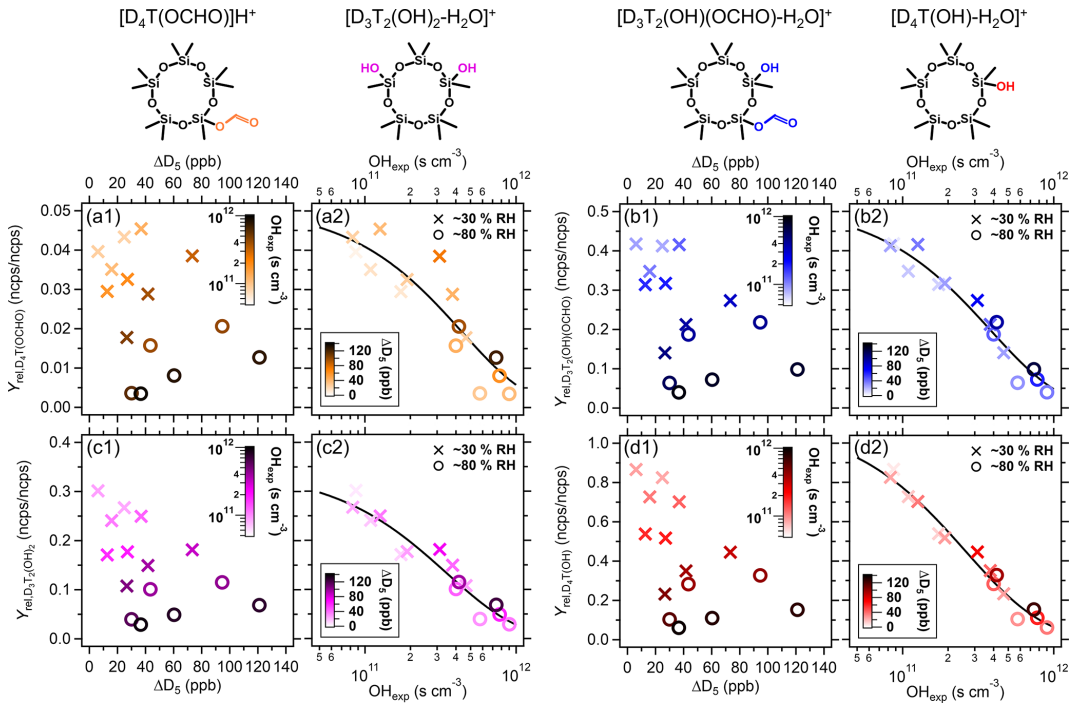


Figure 2. Relative molar yields of VOPs as a function of OH_{exp} and D_5 consumed: **(a1, a2)** $D_4T(OCHO)$, **(b1, b2)** $D_3T_2(OH)(OCHO)$, **(c1, c2)** $D_3T_2(OH)_2$, and **(d1, d2)** $D_4T(OH)$. The colors correspond to the attributed mass ions and molecular structures shown at the top. We did not have a calibration for the suspected VOPs, so the y axes are relative molar yields (ncps / ncps) calculated with the change in signal attributed to each VOP and that of D_5 at m/z 371. The relative molar yields decrease with OH_{exp}, which is used to fit their OH-oxidation rate coefficients and γ_i (black lines).

a simplified $D_5 + OH$ chemical mechanism, Reactions (R4) and (R5).

$$D_5 + OH \rightarrow \sum \gamma_i VOP_i \left(k_{D_5+OH} = 2.0 \times 10^{-12}\,cm^3\,s^{-1}\right) \quad (R4)$$

$$VOP_i + OH \rightarrow \qquad (k_{VOPi+OH}) \quad (R5)$$

In Reaction (R4), γ_i is the relative molar yield of a given VOP_i found by extrapolating Y_{rel,VOP_i} (y axes in Fig. 2) to $OH_{exp} \rightarrow 0$. With ordinary differential equations (Eqs. 6 and 7) from these reactions and experimental inputs, we fit γ_i and the $VOP_i + OH$ rate coefficient ($k_{VOPi+OH}$, $cm^3\,s^{-1}$). The fits are shown as black lines in the right-side panels of each VOP in Fig. 2.

$$\frac{d[D_5]}{dt} = -k_{D_5+OH}[D_5][OH] \quad (6)$$

$$\frac{d[VOP_i]}{dt} = \gamma_i k_{D_5+OH}[D_5][OH] - k_{VOPi+OH}[VOP_i][OH] \quad (7)$$

The fitted $k_{VOPi+OH}$ values for each VOP are on the order of $\sim 10^{-12}\,cm^3\,s^{-1}$ (Table S7) but faster than k_{D_5+OH}, which suggests that these VOPs have atmospheric lifetimes shorter than that of D_5. Alton and Browne (2022) have estimated these VOPs to be volatile with quantitative structure–activity relationship models. However, there are uncertainties in those models, and the VOPs may have lower-saturation mass concentrations than expected. Moreover, the chemical mechanism might be more complex than the one outlined with simple Reactions (R4) and (R5). Consequently, we present these $k_{VOPi+OH}$ values as estimates for secondary chemistry in this simplified reaction scheme, and future work using quantitative measurements should improve the calculated lifetimes of these intermediate $D_5 + OH$ products in the atmosphere.

3.1.2 Formaldehyde (HCHO) yields

As shown in Table S8 and Fig. 3, the experimental molar yields of HCHO (Y_{HCHO}, $\Delta HCHO/\Delta D_5$ in $ppb\,ppb^{-1}$) exceed 100 % at low OH_{exp} and decrease with higher OH_{exp}. We attribute the decreasing Y_{HCHO} with increasing OH_{exp} to HCHO removal by OH in the PAM-OFR. HCHO has a lifetime of 0.91 d at $[OH]_{avg} = 1.5 \times 10^6\,cm^{-3}$ (Atkinson et al., 2006) or 78 s at $[OH] = 1.5 \times 10^9\,cm^{-3}$. In such high-[OH] conditions, some HCHO is oxidized while being produced, which is consistent with the decreasing Y_{HCHO} with increasing OH_{exp} (Fig. 3a). However, HCHO formation likely occurs over multiple oxidation steps (Fu et al., 2020), and how VOP + OH branches to produce HCHO and the rate coefficients for those reactions are not experimentally constrained.

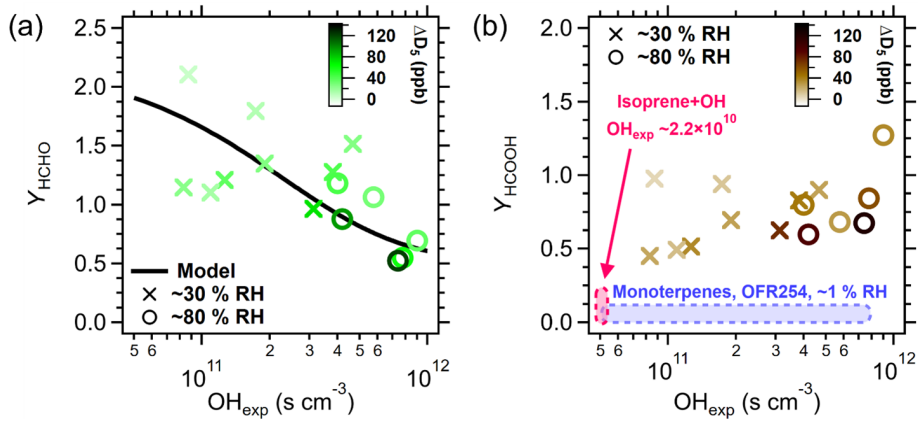


Figure 3. Experimental molar yields of selected VOPs: **(a)** HCHO and **(b)** HCOOH as functions of OH_{exp}. The blue shaded area in **(b)** is the range of Y_{HCOOH} (< 10 %) measured by Friedman and Farmer (2018) with monoterpenes under low-RH and low-NO_x conditions. The pink shaded area refers to Y_{HCOOH} from isoprene + OH chamber experiments (Link et al., 2020) at lower OH_{exp}.

Consequently, we implement a simplified mechanism (Reactions R6–R8) where D_5+ OH produces a representative VOP (VOP_{rep}) and yields HCHO at each oxidation step. The subsequent VOP_{rep}+ OH reactions share the same rate coefficient as D_5+ OH and produce HCHO with the same yield (γ_{HCHO}). This γ_{HCHO} is the cumulative molar yield of HCHO or the molar yield of HCHO as $OH_{exp} \rightarrow 0$. This γ_{HCHO} is also used to correlate satellite column retrievals of HCHO with VOC emissions (Millet et al., 2006) where an empirical value can be used to constrain uncertainty.

$$D_5 + OH \rightarrow VOP_{rep} + \gamma_{HCHO}HCHO \quad \left(k_{D_5+OH} = 2.0 \times 10^{-12}\,cm^3\,s^{-1}\right) \quad (R6)$$

$$VOP_{rep} + OH \rightarrow VOP_{rep} + \gamma_{HCHO}HCHO \quad (k_{D_5+OH}) \quad (R7)$$

$$HCHO + OH \rightarrow \quad (k_{HCHO+OH} = 8.5 \times 10^{-12}\,cm^3\,s^{-1}) \quad (R8)$$

We fit γ_{HCHO} to be 223 % (black line in Fig. 3a), assuming a constant [OH] in the PAM-OFR and that HCHO removal via partitioning or reactive uptake is negligible. This γ_{HCHO} is consistent with the modeled yields of those for VOCs used by Millet et al. (2006), who used γ_{HCHO} from chemical models ranging from 60 %–230 % for a variety of VOCs. Thus, D_5 has a comparable γ_{HCHO} to that of isoprene or aromatic VOCs. An improved mechanism and additional rate coefficients are needed to accurately model HCHO formation.

Fu et al. (2020) proposed a mechanism for D_3 siloxane where high Y_{HCHO} is produced under low-NO / HO_2 conditions. In that mechanism, RO_2 rearrangement and RO H shift is fast, and HCHO is produced at each rearrangement step. The γ_{HCHO} exceeding 100 % in these D_5 experiments is consistent with HCHO production over multiple rapid oxidation steps. The results we report suggest that a similar HCHO production mechanism exists for D_5.

Mao et al. (2009) found that models under-predicted tropospheric HCHO during their aircraft campaign studying Asian pollution outflows into the Pacific Ocean. This discrepancy between the measurements and calculations was pronounced near the surface and up to 2 km. They proposed that there is some missing OH reactivity and that the unaccounted species would be reactive with OH and yield HCHO when oxidized. Based on the D_5 experiments present here, the inclusion of siloxane species may reduce the HCHO formation gap; Coggon et al. (2021) already noted that including volatile chemical products in their model would increase HCHO production.

The large formation of HCHO may entail D_5 siloxane contributing to O_3 formation, albeit indirectly. We were unable to observe O_3 enhancement due to the high concentrations of O_3 produced from the PAM-OFR internal chemistry itself and the lack of NO_x. Given that k_{D_5+OH} is relatively slow compared to that of other common anthropogenic VOCs, we suspect that the oxidation of D_5 will occur downwind of urban sources in low-NO_x conditions or in cases of air stagnation. Whether D_5 has a net positive or negative effect on O_3 formation in these VOC / NO_x scenarios needs to be assessed with models. To get a rough estimate of O_3 production, we consider a case where 20 ppt of D_5 reacts with OH to form 40 ppt of HCHO, which also fully reacts. This D_5 concentration is within the range reported by Coggon et al. (2018) in ambient urban air. The molar maximum incremental reactivity of HCHO under high-NO_x conditions is ∼ 20 % (Carter et al., 1995), which makes HCHO a prominent precursor for tropospheric O_3. By multiplying the maximum incremental reactivity with the HCHO reacted with OH, we can estimate an O_3 formation potential of 8 ppt from D_5 in urban air.

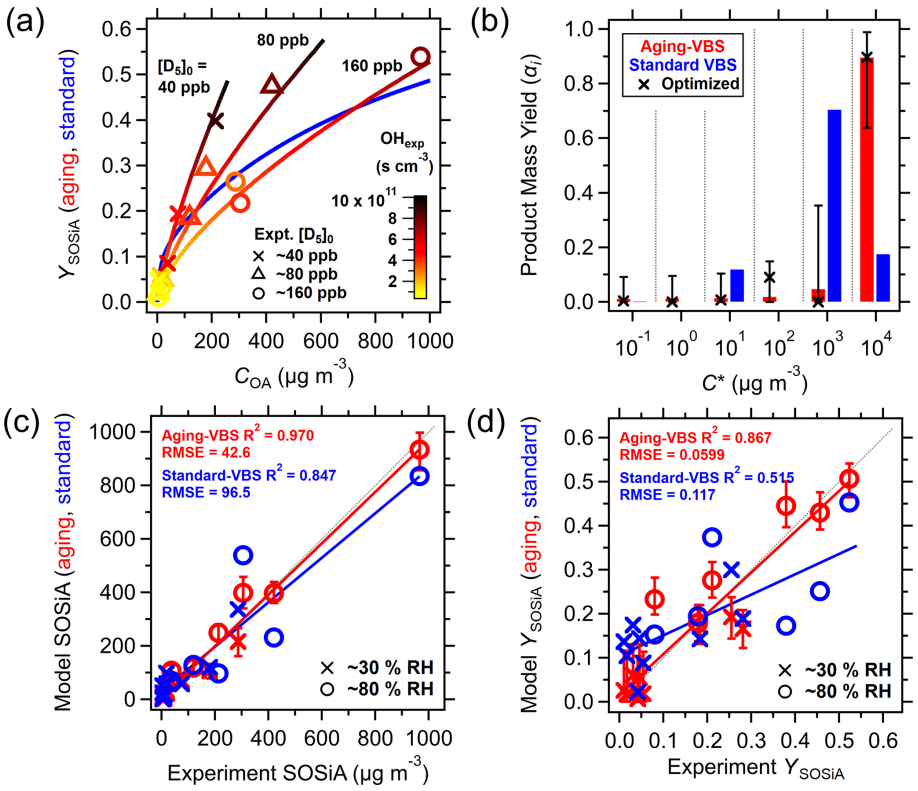


Figure 4. Application of standard-VBS and aging-VBS models to experimental data. **(a)** Y_{SOSiA} as a function of C_{OA}, where the Y_{SOSiA} appears to be correlated with OH_{exp}. The standard-VBS model is shown in blue, and the aging-VBS model is shown with OH_{exp} (color scale) as it is a kinetic model. **(b)** VBS product mass yields for each volatility bin. For the aging-VBS model, the values are those of the first-generation products. **(c)** Comparison of SOSiA mass concentrations and **(d)** comparison of Y_{SOSiA} between the aging-VBS and standard-VBS models against measurements. The error bars indicate the minimum and maximum values from the parameter fit ensemble. The aging-VBS model shows a lower RMSE and higher R^2.

3.1.3 Formic acid (HCOOH) yields

We find molar yields of HCOOH (Y_{HCOOH}, $\Delta HCOOH/\Delta D_5$ ppb ppb^{-1}) between 45 %–127 %, as shown in Fig. 3b, although a trend with OH_{exp} is not obvious (Fig. 3b). We assume HCOOH loss via OH oxidation to be minor given the rate coefficient of $k_{HCOOH+OH} = 4.5 \times 10^{-13}$ cm^3 s^{-1} at 298.15 K (Atkinson et al., 2006), which corresponds to 17 d of OH_{exp} at $[OH]_{avg} = 1.5 \times 10^6$ cm^{-3} or an OH-oxidation lifetime of 440 s in our highest-OH_{exp} experiment. In addition to D_4T(OCHO) hydrolysis, HCOOH may have been produced by heterogeneous reactions of HCHO at the surface of the SOSiA or the OFR walls in these humid experiments. In the atmosphere, HCOOH is presumed to form heterogeneously from HCHO and methanediol ($HOCH_2OH$) in the presence of wet particles (Franco et al., 2021).

The Y_{HCOOH} values from D_5+ OH we report are higher than the values from isoprene + OH (Link et al., 2020) or monoterpene + OH reported by Friedman and Farmer (2018), who quantified the Y_{HCOOH} of seven monoterpenes at varying OH_{exp} without NO_x. The range of Y_{HCOOH} values from these references is shown as shaded areas in Fig. 3b. The Y_{HCOOH} from D_5 is on par with the humid isoprene ozonolysis cases reported by Link et al. (2020). Friedman and Farmer (2018) also used a PAM-OFR, but with 254 nm UV lamps in dry conditions (∼ 1 % RH), and Link et al. (2020) used a reaction chamber, which limits a direct comparison with our results. Nevertheless, Friedman and Farmer (2018) found Y_{HCOOH} of 0.64 %–8.5 % at $OH_{exp} = 2.0 \times 10^{11}$ s cm^{-3}. Aside from the different precursor VOCs and mechanism, Friedman and Farmer (2018) may have encountered less heterogenous production of HCOOH due to the dry OFR conditions. While D_5+ OH may produce more HCOOH than isoprene + OH, the global emissions of D_5 (McLachlan et al., 2010) are about 4 orders of magnitude smaller than those of isoprene (Guenther et al., 2012). Nevertheless, the product class of siloxanes may constitute a minor atmospheric HCOOH source in urban locations, especially if emissions were to increase.

3.2 SOSiA mass yields

3.2.1 Volatility basis set parameterization

The Odum two-product model does not accurately capture the Y_{SOSiA} in the literature in the high C_{OA} range (Sect. S4), so we apply a VBS model. Figure 4a shows the fitted aerosol mass yield curve (blue line) using a standard-VBS model (Eq. 4), but the experimental Y_{SOSiA} (y axis) appears to depend on both C_{OA} (x axis) and OH_{exp} (color scale). To address whether accounting for the varying OH_{exp} in these experiments would improve the VBS model outputs, we fit the produced SOSiA mass using a standard-VBS model (Eq. 4) and a kinetic model with VBS and chemical aging rate coefficients ("aging-VBS model", Reactions R1–R3) based on OH_{exp} and $[D5]_0$ (Table 1).

We fit $k_{age,gas}$ and $k_{age,particle}$ in the aging-VBS model to be 2.2×10^{-12} cm^3 s^{-1} and 2.0×10^{-12} cm^3 s^{-1}, respectively. The fitted aging-VBS model parameters are summarized in Table S11. Figure 4a also shows the aerosol mass yield curves calculated with the aging-VBS model over varying OH_{exp}. Since the aging-VBS model is kinetic, the Y_{SOSiA} values are dependent on both $[D_5]_0$ and OH_{exp}, and we calculate three yield curves using the approximate experimental $[D_5]_0$. The yield curves generated with the aging-VBS model are more consistent with the experiments and show how Y_{SOSiA}, $[D_5]_0$, and OH_{exp} are intertwined in the proposed aging mechanism.

Secondary organic aerosol (SOA) mass yield often exhibits a maximum as a function of OH_{exp}, after which the yield decreases due to fragmentation becoming dominant at high OH_{exp} (Isaacman-VanWertz et al., 2018). We do not find such a maximum in the range of OH_{exp} studied, which suggests that an even higher Y_{SOSiA} could have been found at higher OH_{exp}. Moreover, SOSiA is reported to be non-hygroscopic compared to SOA (Janechek et al., 2019), and we do not see an obvious relationship between the experiment humidity conditions and aerosol formation.

In both the standard and aging-VBS model fits (blue and red, respectively, in Fig. 4b), ~ 95 % of the D_5+ OH product mass is in the gas phase at a C_{OA} of 10 µg m^{-3}. The high fraction of gaseous products is consistent with low Y_{SOSiA} in the lower-OH_{exp} experiments, whereas additional oxidation in the higher-OH_{exp} experiments leads to a shift towards products that partition into the particle phase, thus increasing Y_{SOSiA}. The optimized α_i values for the aging-VBS model are shown as markers in Fig. 4b. The error bars indicate the minimum and maximum values of the fitted α_i in the ensemble parameter sets, which are further expanded in Fig. S12a. The fit ensemble suggests that products from D_5+ OH must be largely volatile ($C^* \geq 10^3$ µg m^{-3}) in order to reproduce the experimental SOSiA yields.

Figure 4c and d show comparisons of the standard and aging-VBS models with experimental SOSiA mass concentrations and Y_{SOSiA}. The error bars indicate the range of

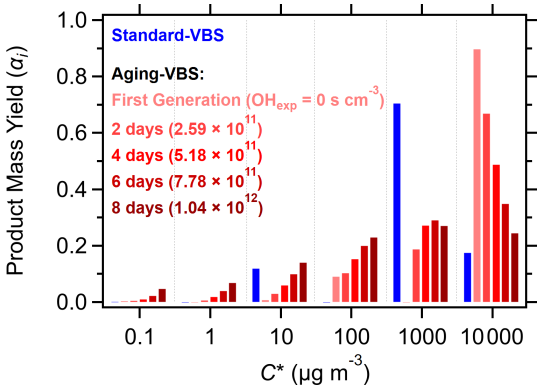


Figure 5. Evolution of the volatility distribution with OH_{exp}. The standard-VBS model parameterization (blue bars) is dominated by the $C^* = 1000$ µg m^{-3} volatility bin. In the aging-VBS model, the first-generation volatility distribution is dominated by the highest-volatility bin ($C^* = 10\,000$ µg m^{-3}) but decreases with increasing OH_{exp} (red bars).

model outcomes within the fit ensemble. We see an improvement in the RMSE and R^2 with the aging-VBS model over the standard-VBS model, suggesting that incorporating OH_{exp} into the yield parameterization improves model performance. Figure 5 compares the standard-VBS model with the aging-VBS model for a range of OH_{exp}, showing that product volatility gradually decreases with increasing OH_{exp} in the aging-VBS model. The high volatility of the initial products is consistent with the lack of the rapid formation of low-volatile species, such as highly oxygenated molecules known to form SOA (Isaacman-VanWertz et al., 2018).

We find that the model is sensitive to $k_{age,particle}$, and a larger rate coefficient results in higher SOSiA formation (Fig. S11a). When fitting the model with deactivated particle-phase aging ($k_{age,particle} = 0$), model-experiment RMSE is slightly increased (Fig. S11b). Thus, the fitting process provides a weak constraint on the parameter value (Fig. S12c). The numerical value of the fitted $k_{age,particle}$ is physically reasonable as it corresponds to an effective uptake coefficient of OH molecules colliding with the particle surface in the range of 0.1–1 (Sect. S1.6). On the other hand, $k_{age,gas}$ is very influential on the model output and tightly constraint in the ensemble of model fits around a value of 2×10^{-12} cm^3 s^{-1} (Fig. S12b). We hence postulate that multi-generational aging of in the gas phase is likely an important process for SOSiA formation, while particle-phase aging may only play a minor role under the investigated conditions.

3.2.2 Consolidating literature Y_{SOSiA}

To address the variation in the literature Y_{SOSiA} and to generate parameters for air-quality models, we fit the parameters in the aging-VBS model with all available data in the literature and those from our experiments. Given that the literature

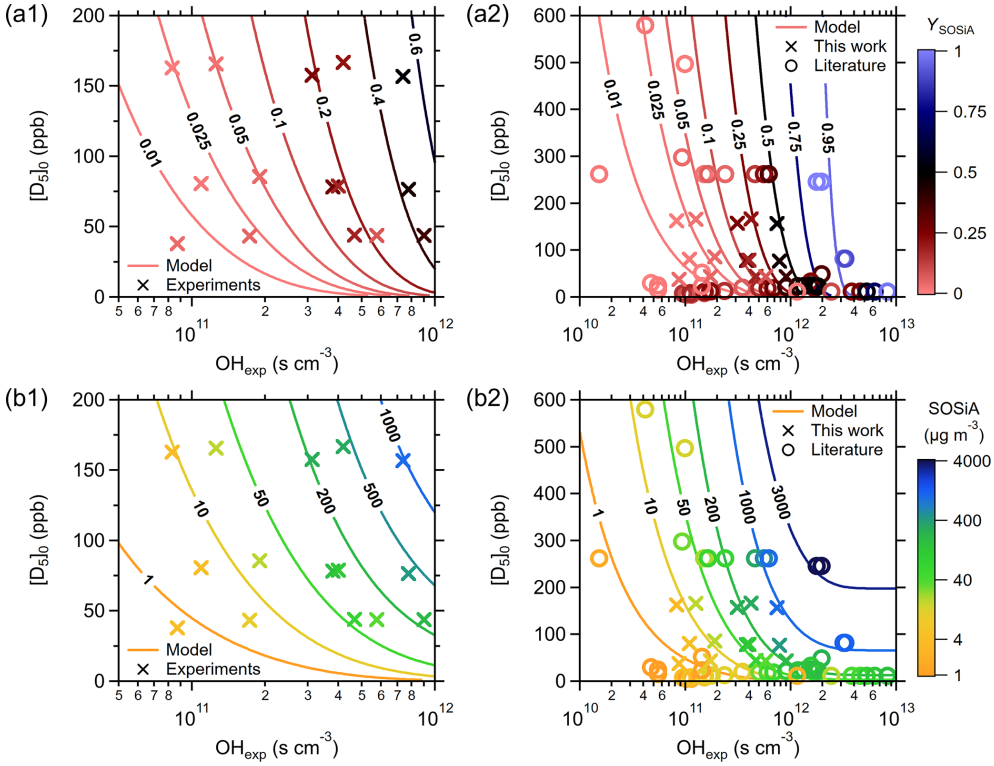


Figure 6. Comparison of experiments, model results, and literature values: **(a)** Y_{SOSiA} and **(b)** SOSiA mass concentrations as a function of $[D_5]_0$ and OH_{exp}. The aging-VBS model is fit using experimental data from (1) this study and (2) those in the literature. SOSiA formation generally increases with $[D_5]_0$ and OH_{exp}. The aging-VBS model can capture the broad range of Y_{SOSiA} reported in the literature.

used differing ρ_{SOSiA} values to calculate Y_{SOSiA} from SMPS data, we adjust the Y_{SOSiA} and C_{OA} reported in the literature to that of the ρ_{SOSiA} used here ($\rho_{SOSiA} = 1.07\,g\,cm^{-3}$). Similarly, we re-calculate the OH_{exp} in the literature using Eq. (2) and the $[D_5]_0$ and $[D_5]_{final}$ values.

Figure 6 shows experimental values (markers) and model outputs (contours) of Y_{SOSiA} (panels a1 and a2) and SOSiA mass concentrations (panels b1 and b2) as a function of $[D_5]_0$ and OH_{exp}. Figure 6a1 and b1 are generated using the aging-VBS model fit using only data from experiments presented in this study, while Fig. 6a2 and b2 show a fit including data from the literature. The aging-VBS model captures the increasing Y_{SOSiA} with increasing $[D_5]_0$ and OH_{exp}. At a given $[D_5]_0$, Y_{SOSiA} and the SOSiA mass concentrations increase with higher OH_{exp}. Figure 6a2 shows that the relatively high Y_{SOSiA} ($> 50\,\%$) is feasible at $OH_{exp} > 10^{12}\,s\,cm^3$. Moreover, the aging-VBS model predicts that Y_{SOSiA} is almost negligible ($< 5\,\%$) under atmospheric concentrations of D_5 and OH_{exp}.

Figure S8 shows that the aging-VBS model used here leads to a much higher correlation between modeled and experimental values for SOSiA mass concentration compared to the same analysis with a standard-VBS model (RMSE = 189 vs. 378). The better correlation suggests that the volatility distribution evolves with OH_{exp} and that chemical aging should be considered when evaluating the volatility distribution of SOSiA from $D_5 + OH$.

We note that bulk-phase chemistry is more complex than logarithmic shifts in volatility with OH_{exp} and is not fully captured in the proposed aging-VBS parameterization. For example, Wu and Johnston (2017), Avery et al. (2023), and Chen et al. (2023) characterized $D_5 + OH$ SOSiA with mass spectrometry and found spectra indicative of oligomers. The formation of oligomers may reduce the bulk volatility by more than one bin and change the gas–particle equilibrium timescales (Berkemeier et al., 2020). Here, we incorporate $k_{age,gas}$ and a simple bin hopping approach to illustrate that a change in the volatility distribution with OH_{exp} can adequately capture the Y_{SOSiA} variation in the literature. Future work with more sophisticated chemical models should close that gap further.

4 Conclusions and atmospheric implications

With a PAM-OFR, PTR-MS, and SMPS, we studied the formation of VOPs and SOSiA under various OH_{exp} conditions. Using a simplified VOP oxidation scheme (Reactions R4 and R5), we find that the VOPs of tentatively identified siloxanols and formate esters have shorter OH-oxidation lifetimes than their precursor D_5 (Table S7). In addition, we find the mass

yield of HCHO of D_5 comparable to that of isoprene or aromatics (Millet et al., 2006), suggesting that D_5 siloxane is a potential O_3-contributing species in downwind scenarios. We find Y_{HCOOH} ranging from 45 %–127 %, which suggests that D_5+ OH is a source of atmospheric HCOOH, albeit smaller than isoprene, which is emitted in higher amounts by orders of magnitude.

An aging-VBS model incorporating OH_{exp} and chemical aging adequately describes gas–particle partitioning at atmospheric OH_{exp} and C_{OA}. Based on these experiments, low-NO_x Y_{SOSiA} should be < 5 % under commonly observed atmospheric $OH_{exp} < 5 \times 10^{11}$ s cm^{-3} (Fig. 6a1). The first-generation products of D_5+ OH are likely volatile, but their volatility decreases with increasing OH_{exp} (Fig. 5). This evolution in volatility suggests that further oxidation of secondary products would reduce the volatility enough to form SOSiA. Unlike α-pinene (Isaacman-VanWertz et al., 2018) or other precursors for SOA, D_5+ OH does not appear to produce low-volatile species within a single oxidation step. Instead, additional OH_{exp} is needed to form aerosol, which suggests that multiple oxidation steps lead to a gradual decrease of product volatility. Hence, concepts that can be successfully applied to SOA formation may not accurately capture SOSiA formation, for which models must consider chemical aging. In the atmosphere, SOSiA from D_5+ OH may be easier to detect downwind of urban sources due to the higher OH_{exp} and dilution and/or removal of competing OH-reactive species.

Based on KinSim calculations (Sect. S5), we expect that the RO_2 fate is dominated by RO_2+ HO_2 and RO_2+ OH, which is consistent with the calculations performed by Avery et al. (2023). However, we note that the reaction rate coefficients of RO_2 and its subsequent products are uncertain for D_5, and we cannot directly address the atmospheric relevance of these calculated RO_2 fates at this time. To improve Y_{SOSiA} parameterizations for the atmosphere, there is a need to study the impact NO_x has on siloxane RO_2 chemistry, given that siloxanes are likely emitted from urban sources where [NO_x] is high. In such scenarios, RO_2+ NO_x is likely an important fate (Peng et al., 2019; Newland et al., 2021). Han et al. (2022) found that the addition of N_2O into their OFR would reduce Y_{SOSiA}, although the cause is unclear. However, Charan et al. (2022) did not find Y_{SOSiA} to change with NO_x in their chamber experiments, which is consistent with rapid RO formation across RO_2 fates. Quantifying secondary species across RO_2 fates and identifying their subsequent oxidation reactions may also be useful to adapt the D_5 oxidation mechanism into more sophisticated chemical kinetics models.

We find that the aging-VBS model is very sensitive to $k_{age,gas}$ (Fig. S12), suggesting that photochemical aging in the gas phase should be considered in these models. The condensation timescale calculations suggest that the loss of low-volatile species to the wall is small (Sect. S1.3); however, these calculations assume a high mass accommodation coefficient for SOSiA and do not account for particle nucleation. Should particle nucleation be delayed or happen slowly, the gas wall loss may be higher than expected, leading to under-quantification of SOSiA. Furthermore, the aging-VBS model assumes that $k_{age,gas}$ is uniform across products or that chemical aging results in a 10-fold decrease in volatility.

While the proposed model assumes that the particles are internally well mixed, the high [OH] used in OFRs may induce faster radical reactions and dimerization near the particle surface (Zhao et al., 2019), which affects particle composition and equilibrium timescales. While dimers and oligomers have been found in SOSiA (Wu and Johnston, 2017; Avery et al., 2023; Chen et al., 2023), the model currently does not account for particle-phase oligomer formation. How oligomerization in the D_5+ OH SOSiA system evolves the volatility distribution and particle properties is currently not considered in the aging-VBS model. Moreover, high degrees of oxidation should lead to fragmentation and increasing volatility (Isaacman-VanWertz et al., 2018), which is also not considered in the aging-VBS model. Hence, multiphase modeling to evaluate SOSiA chemistry and translate experimental findings to atmospheric conditions remains a direction for future research.

Appendix A: Abbreviations

C_{OA}:	organic aerosol mass loading
C^*:	effective saturation mass concentration
D_5:	decamethylcyclopentasiloxane
EVR:	extended volatility range
I_{254}, I_{185}:	flux of 254 and 185 nm photons
ncps:	normalized counts per second
NO_x:	nitric oxide and nitrogen dioxide
OA:	organic aerosol
OFR:	oxidation flow reactor
OH:	hydroxyl radical
$[OH]_{avg}$:	24 h average daily hydroxyl radical concentration
OH_{exp}:	hydroxyl radical exposure
OHR_{ext}:	external hydroxyl radical reactivity
O_3:	ozone
PAM:	potential aerosol mass
PTR:	proton transfer reaction
PTR-MS:	proton transfer reaction mass spectrometer
RH:	relative humidity
RMSE:	root mean square error
RO:	alkoxyl radical
RO_2:	peroxyl radical
SMPS:	scanning mobility particle sizer
SOA:	secondary organic aerosol
SOSiA:	secondary organosiloxane aerosol
UV:	ultraviolet radiation
VBS:	volatility basis set
VOPs:	volatile oxidation products
Y_{HCHO}:	formaldehyde molar yield from D_5
Y_{HCOOH}:	formic acid molar yield from D_5
$Y_{rel,VOP}$:	relative molar yield of VOP from D_5
Y_{SOSiA}:	SOSiA mass yield from D_5
γ :	molar yields extrapolated to when $OH_{exp} \rightarrow 0$
ρ_{SOSiA}:	SOSiA aerosol mass density
τ_{res}:	residence time

Data availability. Summary data are available in the Supplement. Additional data will be provided upon reasonable request.

Supplement. The supplement related to this article is available online at: https://doi.org/10.5194/acp-23-14307-2023-supplement.

Author contributions. HGK, YC, and YP conducted the experiments. YP performed the offline calibrations of OH exposure on the PAM-OFR. HGK analyzed the data. HGK and TB developed the kinetic models. HGK, TB, and HK wrote the manuscript with contributions from all co-authors. HK supervised the experiments, and TB supervised the model analyses.

Competing interests. At least one of the (co-)authors is a member of the editorial board of *Atmospheric Chemistry and Physics*. The peer-review process was guided by an independent editor, and the authors also have no other competing interests to declare.

Disclaimer. Instruments and products used in the research are listed for reference and not as endorsements.

Publisher's note: Copernicus Publications remains neutral with regard to jurisdictional claims made in the text, published maps, institutional affiliations, or any other geographical representation in this paper. While Copernicus Publications makes every effort to include appropriate place names, the final responsibility lies with the authors.

Acknowledgements. This work was supported by the FRIEND Project (Fine Particle Research Initiative in East Asia Considering National Differences), which is funded by the National Research Foundation (NRF) of Korea and the Ministry of Science and ICT of South Korea (2022M3G1A1020858). This work was also funded by the NRF under NRF-2021R1A2C2004365. Hyun Gu Kang is supported by the Max Planck Graduate Center with Johannes Gutenberg University Mainz. The authors thank APM Engineering (Gyeonggi-do, South Korea) for PTR-MS renting and for maintaining it. The authors acknowledge the two anonymous reviewers for their comments, which can be found on the EGUsphere website.

Financial support. This research has been supported by the National Research Foundation of Korea (grant nos. NRF-2021R1A2C2004365 and 2022M3G1A1020858).

The article processing charges for this open-access publication were covered by the Max Planck Society.

Review statement. This paper was edited by Allan Bertram and reviewed by two anonymous referees.

References

Alton, M. W. and Browne, E. C.: Atmospheric Chemistry of Volatile Methyl Siloxanes: Kinetics and Products of Oxidation by OH Radicals and Cl Atoms, Environ. Sci. Technol., 54, 5992–5999, https://doi.org/10.1021/acs.est.0c01368, 2020.

Alton, M. W. and Browne, E. C.: Atmospheric Degradation of Cyclic Volatile Methyl Siloxanes: Radical Chemistry and Oxidation Products, ACS Environmental Au, https://doi.org/10.1021/acsenvironau.1c00043, 2022.

Arata, C., Misztal, P. K., Tian, Y., Lunderberg, D. M., Kristensen, K., Novoselac, A., Vance, M. E., Farmer, D. K., Nazaroff, W. W., and Goldstein, A. H.: Volatile organic compound emissions during HOMEChem, Indoor Air, 31, 2099–2117, https://doi.org/10.1111/ina.12906, 2021.

Atkinson, R.: Kinetics of the gas-phase reactions of a series of organosilicon compounds with hydroxyl and nitrate(NO3) radicals and ozone at 297 ± 2 K, Environ. Sci. Technol., 25, 863–866, https://doi.org/10.1021/es00017a005, 1991.

Atkinson, R., Baulch, D. L., Cox, R. A., Crowley, J. N., Hampson, R. F., Hynes, R. G., Jenkin, M. E., Rossi, M. J., Troe, J., and IUPAC Subcommittee: Evaluated kinetic and photochemical data for atmospheric chemistry: Volume II – gas phase reactions of organic species, Atmos. Chem. Phys., 6, 3625–4055, https://doi.org/10.5194/acp-6-3625-2006, 2006.

Avery, A. M., Alton, M. W., Canagaratna, M. R., Krechmer, J. E., Sueper, D. T., Bhattacharyya, N., Hildebrandt Ruiz, L., Brune, W. H., and Lambe, A. T.: Comparison of the Yield and Chemical Composition of Secondary Organic Aerosol Generated from the OH and Cl Oxidation of Decamethylcyclopentasiloxane, ACS Earth Space Chem., https://doi.org/10.1021/acsearthspacechem.2c00304, 2023.

Berkemeier, T., Ammann, M., Krieger, U. K., Peter, T., Spichtinger, P., Pöschl, U., Shiraiwa, M., and Huisman, A. J.: Technical note: Monte Carlo genetic algorithm (MCGA) for model analysis of multiphase chemical kinetics to determine transport and reaction rate coefficients using multiple experimental data sets, Atmos. Chem. Phys., 17, 8021–8029, https://doi.org/10.5194/acp-17-8021-2017, 2017.

Berkemeier, T., Takeuchi, M., Eris, G., and Ng, N. L.: Kinetic modeling of formation and evaporation of secondary organic aerosol from NO3 oxidation of pure and mixed monoterpenes, Atmos. Chem. Phys., 20, 15513–15535, https://doi.org/10.5194/acp-20-15513-2020, 2020.

Berkemeier, T., Mishra, A., Mattei, C., Huisman, A. J., Krieger, U. K., and Pöschl, U.: Ozonolysis of Oleic Acid Aerosol Revisited: Multiphase Chemical Kinetics and Reaction Mechanisms, ACS Earth Space Chem., 5, 3313–3323, https://doi.org/10.1021/acsearthspacechem.1c00232, 2021.

Brown, P., Watts, P., Märk, T. D., and Mayhew, C. A.: Proton transfer reaction mass spectrometry investigations on the effects of reduced electric field and reagent ion internal energy on product ion branching ratios for a series of saturated alcohols, Int. J. Mass Spectrom., 294, 103–111, https://doi.org/10.1016/j.ijms.2010.05.028, 2010.

Carter, W. P. L., Pierce, J. A., Malkina, I. L., Luo, D., and Long, W. D.: Environmental Chamber Studies of Maximum Incremental Reactivities of Volatile Organic Compounds, Statewide Air Pollution Research Center, University of California Riverside, 227 pp., 1993.

Carter, W. P. L., Pierce, J. A., Luo, D., and Malkina, I. L.: Environmental chamber study of maximum incremental reactivities of volatile organic compounds, Atmos. Environ., 29, 2499–2511, https://doi.org/10.1016/1352-2310(95)00149-S, 1995.

Chandramouli, B. and Kamens, R. M.: The photochemical formation and gas–particle partitioning of oxidation products of decamethyl cyclopentasiloxane and decamethyl tetrasiloxane in the atmosphere, Atmos. Environ., 35, 87–95, https://doi.org/10.1016/S1352-2310(00)00289-2, 2001.

Charan, S. M., Huang, Y., Buenconsejo, R. S., Li, Q., Cocker III, D. R., and Seinfeld, J. H.: Secondary organic aerosol formation from the oxidation of decamethylcyclopentasiloxane at atmospherically relevant OH concentrations, Atmos. Chem. Phys., 22, 917–928, https://doi.org/10.5194/acp-22-917-2022, 2022.

Chen, X., Millet, D. B., Neuman, J. A., Veres, P. R., Ray, E. A., Commane, R., Daube, B. C., McKain, K., Schwarz, J. P., Katich, J. M., Froyd, K. D., Schill, G. P., Kim, M. J., Crounse, J. D., Allen, H. M., Apel, E. C., Hornbrook, R. S., Blake, D. R., Nault, B. A., Campuzano-Jost, P., Jimenez, J. L., and Dibb, J. E.: HCOOH in the Remote Atmosphere: Constraints from Atmospheric Tomography (ATom) Airborne Observations, ACS Earth Space Chem., 5, 1436–1454, https://doi.org/10.1021/acsearthspacechem.1c00049, 2021.

Chen, Y., Park, Y., Kang, H. G., Jeong, J., and Kim, H.: Chemical characterization and formation of secondary organosiloxane aerosol (SOSiA) from OH oxidation of decamethylcyclopentasiloxane, Environ. Sci. Atmos., 3, 662–671, https://doi.org/10.1039/D2EA00161F, 2023.

Cheng, Z., Qiu, X., Shi, X., and Zhu, T.: Identification of organosiloxanes in ambient fine particulate matters using an untargeted strategy via gas chromatography and time-of-flight mass spectrometry, Environ. Pollut., 271, 116128, https://doi.org/10.1016/j.envpol.2020.116128, 2021.

Coggon, M. M., McDonald, B. C., Vlasenko, A., Veres, P. R., Bernard, F., Koss, A. R., Yuan, B., Gilman, J. B., Peischl, J., Aikin, K. C., DuRant, J., Warneke, C., Li, S.-M., and de Gouw, J. A.: Diurnal Variability and Emission Pattern of Decamethylcyclopentasiloxane (D5) from the Application of Personal Care Products in Two North American Cities, Environ. Sci. Technol., 52, 5610–5618, https://doi.org/10.1021/acs.est.8b00506, 2018.

Coggon, M. M., Gkatzelis, G. I., McDonald, B. C., Gilman, J. B., Schwantes, R. H., Abuhassan, N., Aikin, K. C., Arend, M. F., Berkoff, T. A., Brown, S. S., Campos, T. L., Dickerson, R. R., Gronoff, G., Hurley, J. F., Isaacman-VanWertz, G., Koss, A. R., Li, M., McKeen, S. A., Moshary, F., Peischl, J., Pospisilova, V., Ren, X., Wilson, A., Wu, Y., Trainer, M., and Warneke, C.: Volatile chemical product emissions enhance ozone and modulate urban chemistry, P. Natl. Acad. Sci. USA, 118, e2026653118, https://doi.org/10.1073/pnas.2026653118, 2021.

de Gouw, J. and Warneke, C.: Measurements of volatile organic compounds in the earth's atmosphere using proton-transfer-reaction mass spectrometry, Mass Spectrom. Rev., 26, 223–257, https://doi.org/10.1002/mas.20119, 2007.

de Gouw, J., Warneke, C., Karl, T., Eerdekens, G., van der Veen, C., and Fall, R.: Sensitivity and specificity of atmospheric trace gas detection by proton-transfer-reaction mass spectrometry, Int. J. Mass Spectrom., 223–224, 365–382, https://doi.org/10.1016/S1387-3806(02)00926-0, 2003.

Derwent, R. G., Jenkin, M. E., and Saunders, S. M.: Photochemical ozone creation potentials for a large number of reactive hydrocarbons under European conditions, Atmos. Environ., 30, 181–199, https://doi.org/10.1016/1352-2310(95)00303-G, 1996.

Donahue, N. M., Robinson, A. L., Stanier, C. O., and Pandis, S. N.: Coupled partitioning, dilution, and chemical aging of semivolatile organics, Environ. Sci. Technol., 40, 2635–2643, https://doi.org/10.1021/es052297c, 2006.

Franco, B., Blumenstock, T., Cho, C., Clarisse, L., Clerbaux, C., Coheur, P.-F., de Mazière, M., de Smedt, I., Dorn, H.-P., Emmerichs, T., Fuchs, H., Gkatzelis, G., Griffith, D. W. T., Gromov, S., Hannigan, J. W., Hase, F., Hohaus, T., Jones, N., Kerkweg, A., Kiendler-Scharr, A., Lutsch, E., Mahieu, E., Novelli, A., Ortega, I., Paton-Walsh, C., Pommier, M., Pozzer, A., Reimer, D., Rosanka, S., Sander, R., Schneider, M., Strong, K., Tillmann, R.,

van Roozendael, M., Vereecken, L., Vigouroux, C., Wahner, A., and Taraborrelli, D.: Ubiquitous atmospheric production of organic acids mediated by cloud droplets, Nature, 593, 233–237, https://doi.org/10.1038/s41586-021-03462-x, 2021.

Friedman, B. and Farmer, D. K.: SOA and gas phase organic acid yields from the sequential photooxidation of seven monoterpenes, Atmos. Environ., 187, 335–345, https://doi.org/10.1016/j.atmosenv.2018.06.003, 2018.

Fu, Z., Xie, H.-B., Elm, J., Guo, X., Fu, Z., and Chen, J.: Formation of Low-Volatile Products and Unexpected High Formaldehyde Yield from the Atmospheric Oxidation of Methylsiloxanes, Environ. Sci. Technol., 54, 7136–7145, https://doi.org/10.1021/acs.est.0c01090, 2020.

Gkatzelis, G. I., Coggon, M. M., McDonald, B. C., Peischl, J., Aikin, K. C., Gilman, J. B., Trainer, M., and Warneke, C.: Identifying Volatile Chemical Product Tracer Compounds in U.S. Cities, Environ. Sci. Technol., 55, 188–199, https://doi.org/10.1021/acs.est.0c05467, 2021.

Graiver, D., Farminer, K. W., and Narayan, R.: A Review of the Fate and Effects of Silicones in the Environment, J. Polym. Environ., 11, 129–136, https://doi.org/10.1023/A:1026056129717, 2003.

Guenther, A. B., Jiang, X., Heald, C. L., Sakulyanontvittaya, T., Duhl, T., Emmons, L. K., and Wang, X.: The Model of Emissions of Gases and Aerosols from Nature version 2.1 (MEGAN2.1): an extended and updated framework for modeling biogenic emissions, Geosci. Model Dev., 5, 1471–1492, https://doi.org/10.5194/gmd-5-1471-2012, 2012.

Han, C., Yang, H., Li, K., Lee, P., Liggio, J., Leithead, A., and Li, S.-M.: Secondary organic aerosols from OH oxidation of cyclic volatile methyl siloxanes as an important Si source in the atmosphere, Atmos. Chem. Phys., 22, 10827–10839, https://doi.org/10.5194/acp-22-10827-2022, 2022.

Hazra, M. K., Francisco, J. S., and Sinha, A.: Hydrolysis of Glyoxal in Water-Restricted Environments: Formation of Organic Aerosol Precursors through Formic Acid Catalysis, J. Phys. Chem. A, 118, 4095–4105, https://doi.org/10.1021/jp502126m, 2014.

Horii, Y., Nojiri, K., Minomo, K., Motegi, M., and Kannan, K.: Volatile methylsiloxanes in sewage treatment plants in Saitama, Japan: Mass distribution and emissions, Chemosphere, 233, 677–686, https://doi.org/10.1016/j.chemosphere.2019.05.247, 2019.

Howard, P. H. and Muir, D. C. G.: Identifying New Persistent and Bioaccumulative Organics Among Chemicals in Commerce, Environ. Sci. Technol., 44, 2277–2285, https://doi.org/10.1021/es903383a, 2010.

Isaacman-VanWertz, G., Massoli, P., O'Brien, R., Lim, C., Franklin, J. P., Moss, J. A., Hunter, J. F., Nowak, J. B., Canagaratna, M. R., Misztal, P. K., Arata, C., Roscioli, J. R., Herndon, S. T., Onasch, T. B., Lambe, A. T., Jayne, J. T., Su, L., Knopf, D. A., Goldstein, A. H., Worsnop, D. R., and Kroll, J. H.: Chemical evolution of atmospheric organic carbon over multiple generations of oxidation, Nat. Chem., 10, 462–468, https://doi.org/10.1038/s41557-018-0002-2, 2018.

Janechek, N. J., Marek, R. F., Bryngelson, N., Singh, A., Bullard, R. L., Brune, W. H., and Stanier, C. O.: Physical properties of secondary photochemical aerosol from OH oxidation of a cyclic siloxane, Atmos. Chem. Phys., 19, 1649–1664, https://doi.org/10.5194/acp-19-1649-2019, 2019.

Jordan, A., Haidacher, S., Hanel, G., Hartungen, E., Märk, L., Seehauser, H., Schottkowsky, R., Sulzer, P., and Märk, T. D.: A high resolution and high sensitivity proton-transfer-reaction time-of-flight mass spectrometer (PTR-TOF-MS), Int. J. Mass Spectrom., 286, 122–128, https://doi.org/10.1016/j.ijms.2009.07.005, 2009.

Kaikiti, C., Stylianou, M., and Agapiou, A.: TD-GC/MS analysis of indoor air pollutants (VOCs, PM) in hair salons, Chemosphere, 294, 133691, https://doi.org/10.1016/j.chemosphere.2022.133691, 2022.

Kang, E., Root, M. J., Toohey, D. W., and Brune, W. H.: Introducing the concept of Potential Aerosol Mass (PAM), Atmos. Chem. Phys., 7, 5727–5744, https://doi.org/10.5194/acp-7-5727-2007, 2007.

Katz, E. F., Lunderberg, D. M., Brown, W. L., Day, D. A., Jimenez, J. L., Nazaroff, W. W., Goldstein, A. H., and DeCarlo, P. F.: Large Emissions of Low-Volatility Siloxanes during Residential Oven Use, Environ. Sci. Technol. Lett., 8, 519–524, https://doi.org/10.1021/acs.estlett.1c00433, 2021.

Kessler, S. H., Nah, T., Daumit, K. E., Smith, J. D., Leone, S. R., Kolb, C. E., Worsnop, D. R., Wilson, K. R., and Kroll, J. H.: OH-Initiated Heterogeneous Aging of Highly Oxidized Organic Aerosol, J. Phys. Chem. A, 116, 6358–6365, https://doi.org/10.1021/jp212131m, 2012.

Kim, J. and Xu, S.: Quantitative structure-reactivity relationships of hydroxyl radical rate constants for linear and cyclic volatile methylsiloxanes, Environ. Toxicol. Chem., 36, 3240–3245, https://doi.org/10.1002/etc.3914, 2017.

Kroll, J. H., Lim, C. Y., Kessler, S. H., and Wilson, K. R.: Heterogeneous Oxidation of Atmospheric Organic Aerosol: Kinetics of Changes to the Amount and Oxidation State of Particle-Phase Organic Carbon, J. Phys. Chem. A, 119, 10767–10783, https://doi.org/10.1021/acs.jpca.5b06946, 2015.

Le Breton, M., McGillen, M. R., Muller, J. B. A., Bacak, A., Shallcross, D. E., Xiao, P., Huey, L. G., Tanner, D., Coe, H., and Percival, C. J.: Airborne observations of formic acid using a chemical ionization mass spectrometer, Atmos. Meas. Tech., 5, 3029–3039, https://doi.org/10.5194/amt-5-3029-2012, 2012.

Lee, S., Moon, H.-B., Song, G.-J., Ra, K., Lee, W.-C., and Kannan, K.: A nationwide survey and emission estimates of cyclic and linear siloxanes through sludge from wastewater treatment plants in Korea, Sci. Total Environ., 497–498, 106–112, https://doi.org/10.1016/j.scitotenv.2014.07.083, 2014.

Lei, Y. D., Wania, F., and Mathers, D.: Temperature-Dependent Vapor Pressure of Selected Cyclic and Linear Polydimethylsiloxane Oligomers, J. Chem. Eng. Data, 55, 5868–5873, https://doi.org/10.1021/je100835n, 2010.

Link, M. F., Nguyen, T. B., Bates, K., Müller, J.-F., and Farmer, D. K.: Can Isoprene Oxidation Explain High Concentrations of Atmospheric Formic and Acetic Acid over Forests?, ACS Earth Space Chem., 4, 730–740, https://doi.org/10.1021/acsearthspacechem.0c00010, 2020.

Lu, D., Tan, J., Yang, X., Sun, X., Liu, Q., and Jiang, G.: Unraveling the role of silicon in atmospheric aerosol secondary formation: a new conservative tracer for aerosol chemistry, Atmos. Chem. Phys., 19, 2861–2870, https://doi.org/10.5194/acp-19-2861-2019, 2019.

Mao, J., Ren, X., Brune, W. H., Olson, J. R., Crawford, J. H., Fried, A., Huey, L. G., Cohen, R. C., Heikes, B., Singh, H. B., Blake,

D. R., Sachse, G. W., Diskin, G. S., Hall, S. R., and Shetter, R. E.: Airborne measurement of OH reactivity during INTEX-B, Atmos. Chem. Phys., 9, 163–173, https://doi.org/10.5194/acp-9-163-2009, 2009.

McLachlan, M. S., Kierkegaard, A., Hansen, K. M., van Egmond, R., Christensen, J. H., and Skjøth, C. A.: Concentrations and Fate of Decamethylcyclopentasiloxane (D_5) in the Atmosphere, Environ. Sci. Technol., 44, 5365–5370, https://doi.org/10.1021/es100411w, 2010.

Meng, T., Su, S., Cheng, J., Zhong, F., and Tang, Z.: Methylsiloxanes in street dust from Hefei, China: Distribution, sources, and human exposure, Environ. Res., 201, 111513, https://doi.org/10.1016/j.envres.2021.111513, 2021.

Milani, A., Al-Naiema, I. M., and Stone, E. A.: Detection of a secondary organic aerosol tracer derived from personal care products, Atmos. Environ., 246, 118078, https://doi.org/10.1016/j.atmosenv.2020.118078, 2021.

Millet, D. B., Jacob, D. J., Turquety, S., Hudman, R. C., Wu, S., Fried, A., Walega, J., Heikes, B. G., Blake, D. R., Singh, H. B., Anderson, B. E., and Clarke, A. D.: Formaldehyde distribution over North America: Implications for satellite retrievals of formaldehyde columns and isoprene emission, J. Geophys. Res.-Atmos., 111, D24S02, https://doi.org/10.1029/2005JD006853, 2006.

Millet, D. B., Baasandorj, M., Farmer, D. K., Thornton, J. A., Baumann, K., Brophy, P., Chaliyakunnel, S., de Gouw, J. A., Graus, M., Hu, L., Koss, A., Lee, B. H., Lopez-Hilfiker, F. D., Neuman, J. A., Paulot, F., Peischl, J., Pollack, I. B., Ryerson, T. B., Warneke, C., Williams, B. J., and Xu, J.: A large and ubiquitous source of atmospheric formic acid, Atmos. Chem. Phys., 15, 6283–6304, https://doi.org/10.5194/acp-15-6283-2015, 2015.

Müller, M., Mikoviny, T., and Wisthaler, A.: Detector aging induced mass discrimination and non-linearity effects in PTR-ToF-MS, Int. J. Mass Spectrom., 365–366, 93–97, https://doi.org/10.1016/j.ijms.2013.12.008, 2014.

Newland, M. J., Bryant, D. J., Dunmore, R. E., Bannan, T. J., Acton, W. J. F., Langford, B., Hopkins, J. R., Squires, F. A., Dixon, W., Drysdale, W. S., Ivatt, P. D., Evans, M. J., Edwards, P. M., Whalley, L. K., Heard, D. E., Slater, E. J., Woodward-Massey, R., Ye, C., Mehra, A., Worrall, S. D., Bacak, A., Coe, H., Percival, C. J., Hewitt, C. N., Lee, J. D., Cui, T., Surratt, J. D., Wang, X., Lewis, A. C., Rickard, A. R., and Hamilton, J. F.: Low-NO atmospheric oxidation pathways in a polluted megacity, Atmos. Chem. Phys., 21, 1613–1625, https://doi.org/10.5194/acp-21-1613-2021, 2021.

Odum, J. R., Hoffmann, T., Bowman, F., Collins, D., Flagan, R. C., and Seinfeld, J. H.: Gas/Particle Partitioning and Secondary Organic Aerosol Yields, Environ. Sci. Technol., 30, 2580–2585, https://doi.org/10.1021/es950943+, 1996.

Palm, B. B., Campuzano-Jost, P., Ortega, A. M., Day, D. A., Kaser, L., Jud, W., Karl, T., Hansel, A., Hunter, J. F., Cross, E. S., Kroll, J. H., Peng, Z., Brune, W. H., and Jimenez, J. L.: In situ secondary organic aerosol formation from ambient pine forest air using an oxidation flow reactor, Atmos. Chem. Phys., 16, 2943–2970, https://doi.org/10.5194/acp-16-2943-2016, 2016.

Peng, Z. and Jimenez, J. L.: Radical chemistry in oxidation flow reactors for atmospheric chemistry research, Chem. Soc. Rev., 49, 2570–2616, https://doi.org/10.1039/C9CS00766K, 2020.

Peng, Z., Lee-Taylor, J., Orlando, J. J., Tyndall, G. S., and Jimenez, J. L.: Organic peroxy radical chemistry in oxidation flow reactors and environmental chambers and their atmospheric relevance, Atmos. Chem. Phys., 19, 813–834, https://doi.org/10.5194/acp-19-813-2019, 2019.

Pennington, E. A., Seltzer, K. M., Murphy, B. N., Qin, M., Seinfeld, J. H., and Pye, H. O. T.: Modeling secondary organic aerosol formation from volatile chemical products, Atmos. Chem. Phys., 21, 18247–18261, https://doi.org/10.5194/acp-21-18247-2021, 2021.

Piel, F., Müller, M., Winkler, K., Skytte af Sätra, J., and Wisthaler, A.: Introducing the extended volatility range proton-transfer-reaction mass spectrometer (EVR PTR-MS), Atmos. Meas. Tech., 14, 1355–1363, https://doi.org/10.5194/amt-14-1355-2021, 2021.

Robinson, A. L., Donahue, N. M., Shrivastava, M. K., Weitkamp, E. A., Sage, A. M., Grieshop, A. P., Lane, T. E., Pierce, J. R., and Pandis, S. N.: Rethinking Organic Aerosols: Semivolatile Emissions and Photochemical Aging, Science (1979), 315, 1259–1262, https://doi.org/10.1126/science.1133061, 2007.

Rücker, C. and Kümmerer, K.: Environmental Chemistry of Organosiloxanes, Chem. Rev., 115, 466–524, https://doi.org/10.1021/cr500319v, 2015.

Safron, A., Strandell, M., Kierkegaard, A., and Macleod, M.: Rate Constants and Activation Energies for Gas-Phase Reactions of Three Cyclic Volatile Methyl Siloxanes with the Hydroxyl Radical, Int. J. Chem. Kinet., 47, 420–428, https://doi.org/10.1002/kin.20919, 2015.

Schweigkofler, M. and Niessner, R.: Determination of Siloxanes and VOC in Landfill Gas and Sewage Gas by Canister Sampling and GC-MS/AES Analysis, Environ. Sci. Technol., 33, 3680–3685, https://doi.org/10.1021/es9902569, 1999.

Seltzer, K. M., Pennington, E., Rao, V., Murphy, B. N., Strum, M., Isaacs, K. K., and Pye, H. O. T.: Reactive organic carbon emissions from volatile chemical products, Atmos. Chem. Phys., 21, 5079–5100, https://doi.org/10.5194/acp-21-5079-2021, 2021a.

Seltzer, K. M., Murphy, B. N., Pennington, E. A., Allen, C., Talgo, K., and Pye, H. O. T.: Volatile Chemical Product Enhancements to Criteria Pollutants in the United States, Environ. Sci. Technol., 56, 6905–6913, https://doi.org/10.1021/acs.est.1c04298, 2021b.

Sommerlade, R., Parlar, H., Wrobel, D., and Kochs, P.: Product analysis and kinetics of the gas-phase reactions of selected organosilicon compounds with OH radicals using a smog chamber-mass spectrometer system, Environ. Sci. Technol., 27, 2435–2440, https://doi.org/10.1021/es00048a019, 1993.

Sommers, J. M., Stroud, C. A., Adam, M. G., O'Brien, J., Brook, J. R., Hayden, K., Lee, A. K. Y., Li, K., Liggio, J., Mihele, C., Mittermeier, R. L., Stevens, R. G., Wolde, M., Zuend, A., and Hayes, P. L.: Evaluating SOA formation from different sources of semi- and intermediate-volatility organic compounds from the Athabasca oil sands, Environ. Sci.-Atmos., 2, 469–490, https://doi.org/10.1039/D1EA00053E, 2022.

Song, K., Gong, Y., Guo, S., Lv, D., Wang, H., Wan, Z., Yu, Y., Tang, R., Li, T., Tan, R., Zhu, W., Shen, R., and Lu, S.: Investigation of partition coefficients and fingerprints of atmospheric gas- and particle-phase intermediate volatility and semi-volatile organic compounds using pixel-based approaches, J. Chromatogr. A, 1665, 462808, https://doi.org/10.1016/j.chroma.2022.462808, 2022.

Spivack, J. L., Pohl, E. R., and Kochs, P.: Organoalkoxysilanes, Organosilanols, and Organosiloxanols, in: Organosilicon Materials, edited by: Chandra, G., Springer Berlin Heidelberg, Berlin, Heidelberg, 105–135, https://doi.org/10.1007/978-3-540-68331-5_5, 1997.

Stevens, C.: Environmental degradation pathways for the breakdown of polydimethylsiloxanes, J. Inorg. Biochem., 69, 203–207, https://doi.org/10.1016/S0162-0134(97)10019-8, 1998.

Tang, X., Misztal, P. K., Nazaroff, W. W., and Goldstein, A. H.: Siloxanes Are the Most Abundant Volatile Organic Compound Emitted from Engineering Students in a Classroom, Environ. Sci. Technol. Lett., 2, 303–307, https://doi.org/10.1021/acs.estlett.5b00256, 2015.

Tansel, B. and Surita, S. C.: Historical and projected trends of siloxane use in consumer products, associated impacts on municipal solid waste and landfill gas utilization, Int. J. Environ. Sci. Technol., 14, 795–802, https://doi.org/10.1007/s13762-016-1186-x, 2017.

Tran, T. M. and Kannan, K.: Occurrence of cyclic and linear siloxanes in indoor air from Albany, New York, USA, and its implications for inhalation exposure, Sci. Total Environ., 511, 138–144, https://doi.org/10.1016/j.scitotenv.2014.12.022, 2015.

TSI Inc.:Measuring Nanoparticle Size Distributions in Real-time: Key Factors for Accuracy, TSI Incorporated, Application Note SMPS-003, 7 pp., 2012.

Wang, N., Ernle, L., Bekö, G., Wargocki, P., and Williams, J.: Emission Rates of Volatile Organic Compounds from Humans, Environ. Sci. Technol., 56, 4838–4848, https://doi.org/10.1021/acs.est.1c08764, 2022.

Whelan, M. J. and Kim, J.: Application of multimedia models for understanding the environmental behavior of volatile methylsiloxanes: Fate, transport, and bioaccumulation, Integr. Environ. Assess. Manag., 18, 599–621, https://doi.org/10.1002/ieam.4507, 2021.

Whelan, M. J., Estrada, E., and van Egmond, R.: A modelling assessment of the atmospheric fate of volatile methyl siloxanes and their reaction products, Chemosphere, 57, 1427–1437, https://doi.org/10.1016/j.chemosphere.2004.08.100, 2004.

Wu, Y. and Johnston, M. V: Aerosol Formation from OH Oxidation of the Volatile Cyclic Methyl Siloxane (cVMS) Decamethylcyclopentasiloxane, Environ. Sci. Technol., 51, 4445–4451, https://doi.org/10.1021/acs.est.7b00655, 2017.

Xiang, X., Liu, N., Xu, L., and Cai, Y.: Review of recent findings on occurrence and fates of siloxanes in environmental compartments, Ecotoxicol Environ. Saf., 224, 112631, https://doi.org/10.1016/j.ecoenv.2021.112631, 2021.

Xiao, R., Zammit, I., Wei, Z., Hu, W.-P., MacLeod, M., and Spinney, R.: Kinetics and Mechanism of the Oxidation of Cyclic Methylsiloxanes by Hydroxyl Radical in the Gas Phase: An Experimental and Theoretical Study, Environ. Sci. Technol., 49, 13322–13330, https://doi.org/10.1021/acs.est.5b03744, 2015.

Xu, J., Harrison, R. M., Song, C., Hou, S., Wei, L., Fu, P., Li, H., Li, W., and Shi, Z.: $PM_{2.5}$-bound silicon-containing secondary organic aerosols (Si-SOA) in Beijing ambient air, Chemosphere, 288, 132377, https://doi.org/10.1016/j.chemosphere.2021.132377, 2022.

Xu, N. and Collins, D. R.: Design and characterization of a new oxidation flow reactor for laboratory and long-term ambient studies, Atmos. Meas. Tech., 14, 2891–2906, https://doi.org/10.5194/amt-14-2891-2021, 2021.

Yu, S.: Role of organic acids (formic, acetic, pyruvic and oxalic) in the formation of cloud condensation nuclei (CCN): a review, Atmos. Res., 53, 185–217, https://doi.org/10.1016/S0169-8095(00)00037-5, 2000.

Yuan, B., Veres, P. R., Warneke, C., Roberts, J. M., Gilman, J. B., Koss, A., Edwards, P. M., Graus, M., Kuster, W. C., Li, S.-M., Wild, R. J., Brown, S. S., Dubé, W. P., Lerner, B. M., Williams, E. J., Johnson, J. E., Quinn, P. K., Bates, T. S., Lefer, B., Hayes, P. L., Jimenez, J. L., Weber, R. J., Zamora, R., Ervens, B., Millet, D. B., Rappenglück, B., and de Gouw, J. A.: Investigation of secondary formation of formic acid: urban environment vs. oil and gas producing region, Atmos. Chem. Phys., 15, 1975–1993, https://doi.org/10.5194/acp-15-1975-2015, 2015.

Zhao, B., Wang, S., Donahue, N. M., Chuang, W., Hildebrandt Ruiz, L., Ng, N. L., Wang, Y., and Hao, J.: Evaluation of One-Dimensional and Two-Dimensional Volatility Basis Sets in Simulating the Aging of Secondary Organic Aerosol with Smog-Chamber Experiments, Environ. Sci. Technol., 49, 2245–2254, https://doi.org/10.1021/es5048914, 2015.

Zhao, Z., Tolentino, R., Lee, J., Vuong, A., Yang, X., and Zhang, H.: Interfacial Dimerization by Organic Radical Reactions during Heterogeneous Oxidative Aging of Oxygenated Organic Aerosols, J. Phys. Chem. A, 123, 10782–10792, https://doi.org/10.1021/acs.jpca.9b10779, 2019.

2.3. Multiphase chemistry and phase state explain nonlinear effects in the formation and evaporation of SOA from mixed monoterpene precursors

This section has been published as a research article in the journal *ACS ES&T Air*, where I am the first author. Under the supervision of Dr. Thomas Berkemeier, I further developed the model and VBS mechanism based on previous studies and ported the model into the KM-MEMO and KM3C frameworks. I also developed the adaptive layer resizing and moving-boundary algorithms under the supervision of Dr. Thomas Berkemeier. I performed all model calculations and global optimization of parameters. I also produced the figures and the text with input from co-authors. The supplement to this work can be found in Appendix B.2.

Kang, H. G., Takeuchi, M., Ng, N. L., Pöschl, U., and Berkemeier, T.: Multiphase Chemistry and Phase State Explain Nonlinear Effects in the Formation and Evaporation of SOA from Mixed Monoterpene Precursors. ***ACS ES&T Air*****, *in press* (2026).**

This modeling study describes the condensation, evaporation, and particle-phase diffusion of SOA from α-pinene and limonene + NO_3, where the data came from previous studies (Berkemeier et al., 2020; Takeuchi et al., 2022). To resolve difficulties with the numerical treatment of evaporating aerosols, we developed KM3C. We concluded that the slow evaporation of SOA in these chamber experiments was due to the formation of a viscous surface crust, which arose as higher-volatile species evaporated from the particle surface. This viscous crust kinetically limited the evaporation of volatile species. Furthermore, we found that cross reactions between the α-pinene- and limonene-derived intermediates that lead to accretion products explain the nonlinear Y_{SOA} found in multiprecursor experiments.

ACS ES&T Air

Open Access

This article is licensed under CC-BY 4.0

pubs.acs.org/estair

Article

Multiphase Chemistry and Phase State Explain Nonlinear Effects in the Formation and Evaporation of SOA from Mixed Monoterpene Precursors

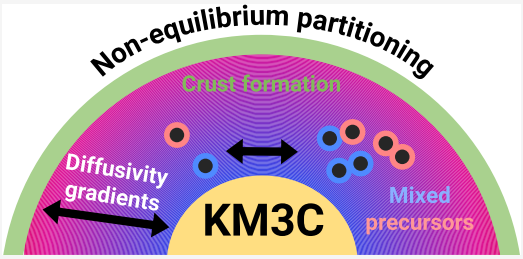
Hyun Gu Kang, Masayuki Takeuchi, Nga L. Ng, Ulrich Pöschl, and Thomas Berkemeier*

Cite This: https://doi.org/10.1021/acsestair.5c00438

Read Online

ACCESS | Metrics & More | Article Recommendations | Supporting Information

ABSTRACT: A large fraction of airborne particulate matter consists of secondary organic aerosol (SOA), which can be highly viscous, leading to kinetic limitations in gas−particle partitioning and chemical reactivity. The underlying processes, however, have not been fully resolved and quantified in computational models. We use experimental data and the kinetic multilayer model of multiphase chemistry (KM3C) to investigate SOA formation by oxidation of limonene and α-pinene with the nitrate radical (NO_3). The model explicitly treats gas−wall loss, gas−particle partitioning, as well as gas- and particle-phase chemistry, and includes a novel method for parametrizing bulk diffusivity from particle composition. KM3C utilizes and reproduces the temporal evolution of particle mass and thermal desorption mass spectrometry data (FIGAERO-CIMS) obtained in chamber experiments. The model can explain the observed slow evaporation of limonene SOA through slow bulk diffusivity and predicts the formation of a viscous surface crust. In mixed-precursor experiments, KM3C attributes nonadditive SOA mass yields to cross-reactions between α-pinene- and limonene-derived intermediates, leading to accretion products. We conclude that particle phase state, oligomerization, and multiprecursor effects have to be resolved to accurately describe and predict atmospheric SOA formation.



KEYWORDS: *organic aerosol, diffusion, partitioning, viscosity, oligomerization*

1. INTRODUCTION

Air quality models use absorptive partitioning theory to estimate organic aerosol (OA) formation.[1] Donahue et al.[2] built on absorptive partitioning theory to introduce the volatility basis set (VBS), which parametrizes secondary organic aerosol (SOA) formation by categorizing volatile organic compound (VOC) oxidation products by their vapor pressures. A VBS can be derived using SOA growth data from oxidation reactors or thermal desorption data from instruments such as the filter inlet for gases and aerosols chemical ionization mass spectrometer (FIGAERO-CIMS).[3,4] While absorptive partitioning theory assumes rapid gas and particle equilibria and homogeneous particles,[1] particles from experiments and ambient air can be viscous and may not reach equilibrium with the surrounding gas phase within their atmospheric lifetimes.[5−7]

Berkemeier et al.[8] reacted α-pinene and limonene with the nitrate radical (NO_3) in the Georgia Tech Environmental Chamber (GTEC), which can be temperature-controlled between 5 and 42 °C. They derived the oxidation product volatility distribution using the SOA growth and evaporation data with a kinetic model. However, the model considered only data from a scanning mobility particle sizer (SMPS), and the effects of a viscous particle phase state were only explored in a sensitivity study. As a consequence, the model required rapid and near-complete oligomerization of the limonene SOA to fit the experimental data. Schobesberger et al.[3] developed a model to calculate FIGAERO-CIMS thermograms from volatility but assumed that the particle bulk is well-mixed. Here, we describe SOA growth and evaporation in a reaction chamber and parallel thermal desorption measurements with FIGAERO-CIMS using a single kinetic multilayer model and a single kinetic parameter set and explicitly account for the evolution of the particle phase state over time.

Typical accretion reactions in the particle phase of SOA are peroxyhemiacetal formation from hydroperoxides and carbonyls, esterification from alcohols and carboxylic acids,[9−11] and acid-catalyzed aldol condensation.[12,13] Bakker-Arkema and Ziemann[9] mixed extracted SOA from α-pinene + O_3 with a hydroperoxide probe molecule and found that the oligomerization equilibrium was reached within an hour. However, there are remaining uncertainties in both oligomerization rates and equilibrium constants, and a wide range of oligomer mass

Received: November 3, 2025
Revised: March 23, 2026
Accepted: March 24, 2026

Downloaded via MPI CHEMIE on April 8, 2026 at 05:59:06 (UTC).
See https://pubs.acs.org/sharingguidelines for options on how to legitimately share published articles.

ACS Publications

© XXXX The Authors. Published by American Chemical Society

fractions have been reported, such as >50% for α-pinene + O_3 SOA.[14,15]

Kinetic multilayer models can account for how bulk diffusivity (D_b) affects chemistry[16−18] and partitioning.[19,20] In such models, the particle bulk is divided into layers in the form of spherical shells, which can exchange mass through diffusional transport. Kinetic multilayer models have been used previously to study the effects of diffusivity in SOA growth and evaporation,[8,20−25] in addition to related applications such as the cloud formation ability,[19] oxidative aging,[18,26−28] and photochemical aging of OA.[16,29,30] This multilayer bulk structure better explains scenarios where rapid mixing of the particle bulk cannot be assumed,[31−33] but the computational expense of the model increases steeply with the number of bulk layers. Especially for SOA formation chemistry, where hundreds of chemical reactions and oxidation products play a role, a multilayer treatment of aerosol particles can quickly become infeasible.

VBS-based chemical mechanisms can help reduce the number of chemical compounds that must be considered when modeling the formation of SOA. VBS approaches often presume that each precursor VOC oxidizes to form products independent of the presence of other VOCs, thus assuming that the total SOA mass yield (Y_{SOA}) is the sum of the yields of the individual precursors.[34] However, experiments have found Y_{SOA} to not be a linear sum.[8,35−37] Takeuchi et al.[36] used FIGAERO-CIMS thermograms and Y_{SOA} collected during chamber experiments similar to those described in Berkemeier et al.[8] to conclude that reactions between the condensed α-pinene and limonene oxidation products lead to nonadditive Y_{SOA}. The authors proposed that cross-reactions between gas-phase intermediates or particle-phase products of the two monoterpenes may cause the nonlinearity, but such chemistry was not explicitly modeled.

The oxidation of gaseous species tends to reduce the vapor pressure of these species by adding functional groups onto their molecular backbones.[38] In a VBS-based model, such oxidative aging can be reflected through shifts in the volatility distribution toward products with lower effective saturation mass concentrations (C^*).[2,39] This "volatility bin-hopping" has been used to model the shift in the volatility distribution of siloxane oxidation products[40] and oil sand emissions[41] by photochemical aging.

In this study, we use the kinetic multilayer model for multiphase chemistry (KM3C) to model the SOA growth and evaporation data from Berkemeier et al.[8] and the FIGAERO-CIMS thermograms reported in Takeuchi et al.[36] with a single chemical mechanism and a set of kinetic model parameters. We explore the effects of mixed-precursor dimer production from gas-phase peroxy radical reactions (RO_2 + RO_2), oligomerization in the particle bulk, gas-phase NO_3 aging, and composition-dependent diffusivity. The Monte Carlo genetic algorithm (MCGA)[42] is used to derive optimal model parameters from the experimental data.

2. METHODS

2.1. Experiments

Details on the experiments conducted at the Georgia Tech Environmental Chamber (GTEC) facility are described in Berkemeier et al.[8] and Takeuchi et al.[36] In brief, α-pinene and/or limonene reacted with NO_3 via molar excess injections of N_2O_5 (4:1 of N_2O_5 to double bond) into a dry and dark Teflon chamber in the presence of ammonium sulfate seed particles. Since α-pinene has lower Y_{SOA} than limonene when reacted with NO_3, experiments were performed with higher concentrations of α-pinene than those of limonene to achieve similar SOA mass loadings.

Experiments started at a temperature of about 5 °C that increased to 42 °C in two steps over the course of hours. A scanning mobility particle sizer (SMPS) was used to monitor SOA growth and evaporation, and the data was adjusted for particle−wall loss.[43] Four types of experiments were conducted: two where each monoterpene was oxidized separately (APN and LIM), one where both monoterpenes were oxidized together (MIX), and one sequential experiment where limonene was oxidized after α-pinene (SEQ).

A filter inlet for gases and aerosols chemical ionization mass spectrometer (FIGAERO-CIMS) was used to collect and thermally desorb particles on a Teflon filter in intervals of 60 min throughout the course of the experiment. We use a FIGAERO-CIMS thermogram from each chamber temperature set point (5, 25, and 42 °C), which is three thermograms for each experiment, for kinetic modeling.

2.2. Kinetic Multilayer Model for Multiphase Chemistry (KM3C)

The kinetic multilayer model for multiphase chemistry (KM3C) explicitly describes the temporal evolution of a multiphase chemical system by solving ordinary differential equations (ODEs) that contain transport fluxes and rates of chemical production and losses. The differential equations were solved using Matlab software (ode15s solver). The model builds on the earlier work by Shiraiwa and co-workers.[32,44] The model code is automatically generated using the kinetic multiphase meta-model (KM-MEMO) code generator, which is a Matlab package program developed in-house to produce model files based on user inputs without having to manually compose the model code.[30]

We build on the model from Berkemeier et al.,[8] where the previous model assumed that particles are well-mixed, by having multiple bulk layers to account for D_b. We also incorporate adaptive layer resizing and moving−boundary algorithms, which allow for the particles to grow and shrink dynamically while avoiding numerical stiffness. As for the model compartment structure, we follow the one in Berkemeier et al.,[8] which subdivided a reaction chamber into the wall, gas-phase, and particle-phase compartments. Thin gas layers surrounding the chamber wall and the particle bulk allow for the treatment of gas diffusion. Gas−wall loss is treated following Huang et al.[45] Separate chemical mechanisms are employed in the gas and particle phases. The particle bulk was further subdivided into thin diffusion layers.

The depth of the near-surface particle bulk layer increases and decreases as the organic species adsorb and desorb. When the near-surface bulk layer becomes very thin due to evaporation, numerical stiffness increases sharply, which often leads to failure of the numerical ODE solver. We address this issue by adopting an adaptive layer resizing algorithm (Figure 1b), which merges adjacent bulk layers when the volume of a layer falls below a lower threshold. Likewise, the algorithm splits a layer when it exceeds an upper volume threshold, resulting in a dynamic number of bulk layers.

Note that the merging of bulk layers can lead to numerical diffusion,[46] i.e., increased transport of matter compared to the real physical system, if concentrations in neighboring layers are different. The impact of numerical diffusion can generally be minimized by using a sufficient number of bulk layers so that concentrations between neighboring layers differ only slightly. The systems investigated in this study, however, exhibit steep concentration gradients at the particle surface, and merging of the topmost into the second bulk layer then leads to a sudden increase in evaporation of volatile species that were trapped under the near-surface layer. To resolve this issue, we incorporate a moving-boundary algorithm, similar to that used by Couvidat and Sartelet,[46] where the volume of the near-surface layer does not shrink as a result of net desorption at the surface (Figures S1 and S2). The moving-boundary algorithm is described in detail in Section S1.

KM3C is also used to model thermal desorption in FIGAERO-CIMS explicitly. The model runs are initiated with the exact

https://doi.org/10.1021/acsestair.5c00438
ACS EST Air XXXX, XXX, XXX−XXX

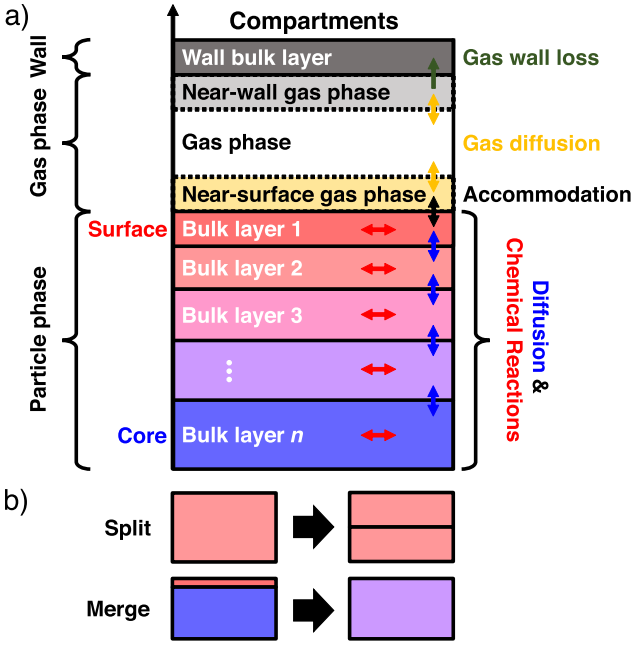


Figure 1. (a) Compartments and processes in the kinetic multilayer model KM3C and (b) illustration of the adaptive layer resizing scheme. KM3C subdivides a reaction chamber into the wall, gas, and particle phase compartments and models mass transport between and reactions inside each model layer. Particle-phase bulk layers split or merge as they exceed upper or lower size thresholds, respectively, leading to a dynamic number of layers throughout the calculation.

composition of particles (including internal diffusion gradients) from the chamber model runs, taken at a specific experimental time that coincides with the sampling interval of the FIGAERO-CIMS thermogram. The thermal desorption behavior of the particles when flowing pure nitrogen gas into the FIGAERO device is then simulated. KM-MEMO is also equipped with parameter optimization algorithms, including the Monte Carlo Genetic Algorithm (MCGA),[42] which is used in this study to obtain globally fitting kinetic parameter sets (Section S4) using the chamber experiment bulk mass time series and the FIGAERO thermograms. In the first step, we use MCGA to optimize all kinetic parameters necessary to describe the pure precursor systems on the respective experimental data (APN and LIM). The parameters exclusive to the mixed precursor systems (i.e., properties of heterodimers) are optimized in a second optimization step only to the mixed precursor experimental data (MIX, SEQ). A sensitivity study of the optimized model parameters is shown and discussed in Section S5.

2.2.1. Chemical Mechanism. The reaction mechanism used in this study builds on the mechanism presented in Berkemeier et al.,[8] which was based on Master Chemical Mechanism v3 (MCM).[47] The semiexplicit mechanism bins intermediates and oxidation products into categories based on molecular structural features (e.g., alkoxy radicals RO, peroxy radicals RO_2) and volatility, respectively. We simplify aspects of the Berkemeier et al.[8] mechanism by removing the distinction between the non-nitrated and nitrated organic species. Instead, all products are distributed across a single volatility basis set (VBS), which significantly reduces the number of model parameters and calculation time. We set logarithmically spaced volatility bins for condensing monomers in the range $C^*_{298} = 1 \times 10^{-4} - 1 \times 10^{3}$ $\mu g\ m^{-3}$, where C^*_{298} is the effective saturation mass concentration at 298 K.[2] We also assign a separate bin for high-volatile species that do not partition. The C^* are adjusted for temperature following Epstein et al.[48] From the FIGAERO-CIMS data, we find that a large fraction (>80%) of detected ions in each experiment contain nitrogen (Figure S16) and so use a single VBS for nitrated and non-nitrated chemical species.

The precursor VOCs react with NO_3 to form peroxy radicals (RO_2), which undergo further radical chemistry until they eventually terminate into stable oxidation products that are represented by VBS species. Specific details are available in Section S3, and a schematic of the mechanism is shown in Figure S3. The mechanism also includes dimer formation through $RO_{2,apn} + RO_{2,lim} \rightarrow ROOR_{het}$ reactions, where the volatility bin branching is linearly interpolated and the C^*_{298} of $ROOR_{het}$ is optimized for between those of $ROOR_{apn}$ and $ROOR_{lim}$. To address potential nonlinear effects in heterodimer formation, we include a fit adjustment factor ($\gamma_{RO2+RO2}$) for the $RO_{2,apn} + RO_{2,lim}$ reaction, eq 1. We set the bounds of $\gamma_{RO2+RO2}$ to be within an order of magnitude of $k_{RO2+RO2,lim}$, which covers the range between $k_{RO2+RO2,apn}$ and $k_{RO2+RO2,lim}$ and reflects the wide range of $k_{RO2+RO2}$ reported in the literature.[49−51]

$$k_{RO2+RO2,het} = k_{RO2+RO2,lim} \times \gamma_{RO2+RO2} \quad (1)$$

The gas-phase chemical mechanism includes aging of oxidation products with NO_3 by the volatility bin assigned to them. We assume that hydrogen abstraction by NO_3 adds a functional group, such as −OH or−OOH, to the molecule and reduces the molecule's C^*_{298} by 2 orders of magnitude.[38] We optimize for the NO_3-aging rate coefficient (k_{aging}) for each monoterpene precursor in a range consistent with aliphatic species.[52,53]

In the particle phase, oxidation products can react to form oligomers, which we presume do not evaporate. Following Berkemeier et al.,[8] we assume reverse oligomerization to occur as first-order reactions and the forward oligomerization as second-order reactions by multiplying a first-order rate coefficient with the mass fraction of monomeric reaction partners in a given model layer (M_f). We fit the forward and reverse oligomerization rate coefficients ($k_{fwd,olig}$ and $k_{rev,olig}$) and energies of activation ($E_{a,fwd}$ and $E_{a,rev}$). Oligomers decompose into the original monomers, and the mechanism includes reactions between α-pinene and limonene monomers to form particle-phase hetero-oligomers. The rate coefficients for the hetero-oligomer formation and dissociation are assumed to lie between the values for the pure α-pinene and limonene systems (eqs 2 and 3), which we denote as "scale" in the below equations. We include a fitted adjustment factor ($\gamma_{fwd,olig}$ and $\gamma_{rev,olig}$) to the rate coefficients to address nonlinear effects.

$$k_{fwd,olig,het} = \gamma_{fwd,olig} \times \text{scale}(k_{fwd,olig,apn}, k_{fwd,olig,lim}) \times M_f \times \exp\left(\frac{E_{a,fwd,het}}{R} \times \left(\frac{1}{298} - \frac{1}{T}\right)\right) \quad (2)$$

$$k_{rev,olig,het} = \gamma_{rev,olig} \times \text{scale}(k_{rev,olig,apn}, k_{rev,olig,lim}) \times \exp\left(\frac{E_{a,rev,het}}{R} \times \left(\frac{1}{298} - \frac{1}{T}\right)\right) \quad (3)$$

2.2.2. Composition-Dependent Bulk Diffusivity (D_b). Kinetic multilayer models allow assigning distinct D_b for every model layer based on molecular composition.[16,19] A gradient of diffusivity based on composition has been proposed for systems analogous to SOA,[54,55] and SOA with higher fractions of low-volatiles have been observed to be more viscous.[56]

Previous studies found a log−log relationship between vapor pressure and viscosity, where less volatile species tend to have higher viscosities.[57−61] We thus prescribe a linear relationship between the decadal logarithms of the effective saturation mass concentration of species i at 298 K, $C^*_{298,i}$, and the self-diffusivity at 298 K, $D_{b,298,i}$.

$$\log 10(D_{b,298,i}) = m \times \log 10(C^*_{298,i}) + b \quad (4)$$

The slope (m) and intercept (b) of this log−log relationship (eq 4) are obtained by fitting to the experimental data, and we use the same relationship to calculate the $D_{b,298,i}$ of the monomers and dimers (Figure S4). As oligomers are nonvolatile in this model, they are assumed to contribute with a $D_{b,298,i}$ that is a fraction x_{olig} of the $D_{b,298,i}$ from the lowest volatility bin of the model.

https://doi.org/10.1021/acsestair.5c00438
ACS EST Air XXXX, XXX, XXX−XXX

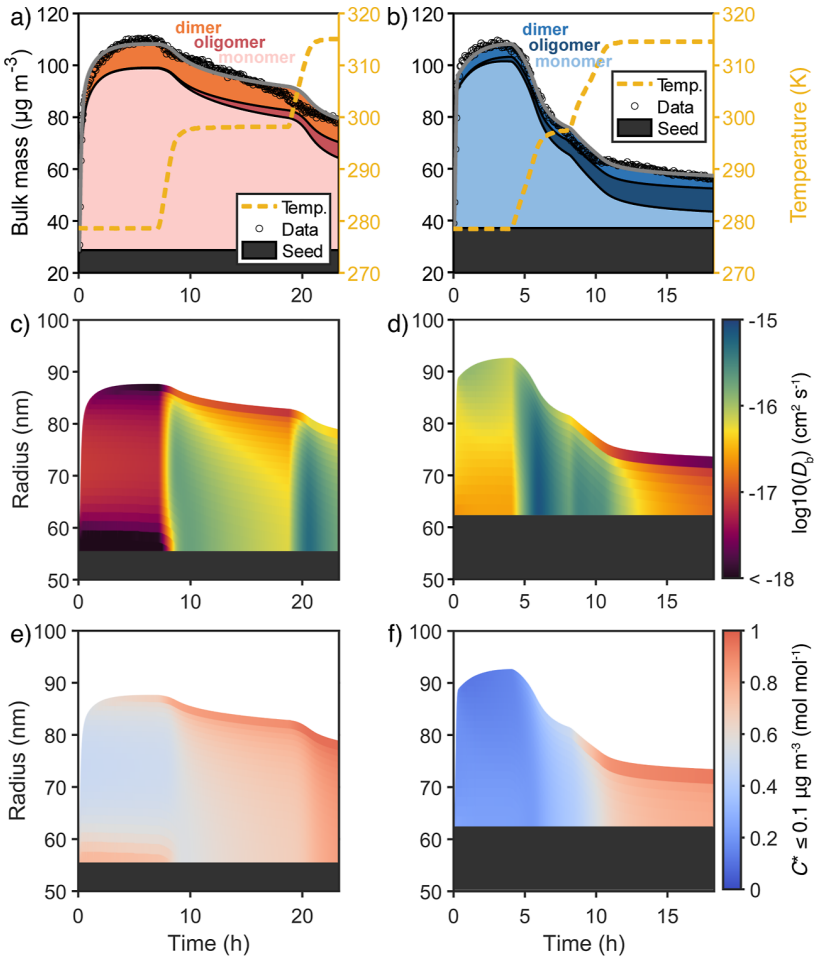


Figure 2. SOA mass concentrations and model results for bulk composition in the chamber for LIM (left column) and APN experiments (right column). Panels (a,b) show the time evolution of SOA mass concentrations obtained from SMPS data (markers) and the model (gray line). Subdivisions of the filled area underneath the modeled SOA mass concentrations denote the contribution of monomers, gas-phase dimers, and particle-phase oligomers to the total mass. The temperature during the model runs is shown as an orange dashed line. Panels (c,d) use color-coding and subdivision of the filled area underneath the modeled SOA mass concentrations into individual model layers to show the composition-dependent D_b for each bulk layer. Likewise, panels (e,f) display the molar fraction of all low-volatile species and oligomers ($C^*_{298,i} \leq 0.1$ μg m^3) in each bulk layer. The model shows surface crust formation for both pure monoterpene precursors, which can be accredited to the increased concentration of low-volatile species and oligomers at the particle surface.

To calculate the diffusivity of a given bulk layer l at 298 K ($D_{b,298,l}$) from the composition of that bulk layer, we use the Vignes equation[18,62] (eq 5), which is a logarithmic mixing rule that weighs $D_{b,298,i}$ with the molar fraction $x_{i,l}$ of species i inside layer l.

$$D_{b,298,l} = \prod (D_{b,298,i})^{x_{i,l}} \tag{5}$$

We adjust D_b for temperature with the Clausius–Clapeyron eq (eq 6), where ΔH^{dif} is the effective enthalpy of diffusion and R is the gas constant. We fit ΔH^{dif} between 50 and 150 kJ mol^{-1}, a range consistent with that of water–sucrose solutions.[63]

$$D_{b,l} = D_{b,298,l} \times \exp\left(-\frac{\Delta H^{dif}}{R}\left(\frac{1}{T} - \frac{1}{298}\right)\right) \tag{6}$$

3. RESULTS AND DISCUSSION

3.1. Phase State Effects on SOA Growth and Evaporation

The time series of SOA mass concentrations in the pure precursor experiments (LIM, APN) is well-captured by the kinetic model, including the evaporation upon increase in chamber temperature (Figure 2a,b). The APN experiment shows sensitivity to k_{aging} due to the higher percentage of products of higher volatility (Figure S12); the model is sensitive to the monomer volatility distributions in both, APN and LIM, experiments (Figure S10). While Berkemeier et al.[8] also achieved a good fit with the SOA mass, the previous model did so with a rapid and high degree of oligomerization. Here, the optimized model has a lower degree of oligomerization. The formation and evaporation occur more gradually for limonene SOA than for α-pinene SOA. The model finds that the bulk diffusivity in the APN experiment (Figure 2d) is initially higher than in the LIM experiment (Figure 2c) and that evaporation of α-pinene SOA is initially not diffusion-limited. In both experiments, diffusivity in the particle phase decreases with time as semivolatiles evaporate. Especially, the D_b of the near-surface bulk layer becomes suppressed compared to the underlying layers upon an increase in chamber temperature. The model suggests this surface crust forms by accumulation of low-volatile species and non-partitioning oligomers at the surface (Figure 2e,f). A viscous surface crust ($D_b \approx 1 \times 10^{-17}$ cm^2 s^{-1}) forms upon the first increase in chamber temperature to 25 °C for the LIM

https://doi.org/10.1021/acsestair.5c00438
ACS EST Air XXXX, XXX, XXX–XXX

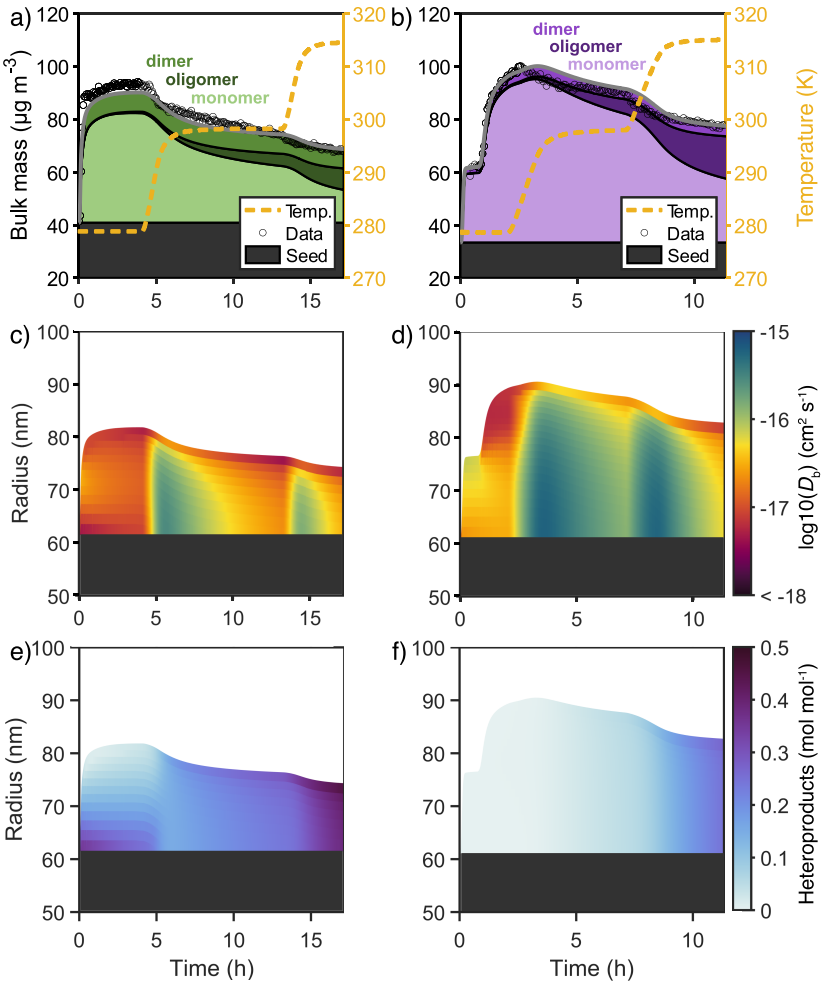


Figure 3. SOA mass concentrations and model results for bulk composition in the chamber for MIX (left column) and SEQ experiments (right column). Panels (a,b) show the time evolution of SOA mass concentrations obtained from SMPS data (markers) and the model (gray line). Subdivisions of the filled area underneath the modeled SOA mass concentrations denote the contribution of monomers, gas-phase dimers, and particle-phase oligomers to the total mass. The temperature during the model runs is shown as an orange dashed line. Panels (c,d) use color-coding and subdivision of the filled area underneath the modeled SOA mass concentrations into individual model layers to show the composition-dependent D_b for each bulk layer. The model slightly underpredicts Y_{SOA} in the MIX experiment. (e,f) show the sum of the molar fractions of heterodimers and hetero-oligomers.

experiment and upon the second increase in chamber temperature to 42 °C in the APN experiment, each time slowing evaporation considerably. The formation of the crust in APN at higher temperatures coincides with oligomerization and the evaporation of more volatile species. These crusts delay the evaporation of underlying species, similar to the diffusion-limited evaporation found in polymer−solvent systems.[55]

Li et al.[64] used EPISuite to calculate the glass transition temperatures and vapor pressures of organic compounds and provided an empirical relationship between glass transition temperature and vapor pressure (Section S6). The $D_b - C^*$ relationship (eq 4) is largely consistent with the data analyzed by Li et al. (2020) for the range of C^*_{298} in this study and does not require an upper viscosity limit (Figure S11). However, the data set is sparse for low C^*_{298} species, and KM3C is sensitive to the composition-dependent bulk diffusivity parameters (Section S5, Figure S15). Thus, further research is needed to better constrain the relationship between viscosity and volatility of organic compounds.

The model also fits the MIX and SEQ experiments with reasonable accuracy (Figure 3a,b), using the same kinetic model parameters as for the pure precursor experiments, APN and LIM. In the MIX experiment, the model finds that the surface crust forms early on (Figure 3c), like with LIM, and the distribution of α-pinene and limonene species throughout the particle is more homogeneous compared with that of SEQ (Figure S5). Note that we find α-pinene oxidation products to condense slightly before the monomeric limonene oxidation products due to the faster oxidation chemistry of α-pinene in the gas phase (Figure S5a,b). Furthermore, accretion products of oxidation products from both monoterpenes (hetero-oligomers) form efficiently, which titrate away the less numerous monomeric limonene oxidation products near the core of the particle (Figure 3e). For SEQ, the model finds that a more viscous limonene SOA phase forms on the top of the less viscous α-pinene SOA (Figure 3d) and that heterodimers do not initially form. At 5 °C, both phases hardly mix, as hypothesized by Boyd et al.,[65] and this division persists until the chamber temperature is increased to 25 °C where mixing happens of both phases occurs (Figure 3f). Consequently, the

https://doi.org/10.1021/acsestair.5c00438
ACS EST Air XXXX, XXX, XXX−XXX

more volatile α-pinene species are trapped under the limonene species at the start, and hetero-oligomers do not form until the particle mixes (Figure S5). Both systems show formation of a viscous surface crust upon heating.

To test the effect that slow bulk diffusion has on partitioning, we run the model with a single well-mixed bulk layer but otherwise the same model parameters (Figure 4 and Figure S6). The model is sensitive to both slope and intercept of the $D_b - C^*$ relationship (eq 4), where slower diffusion generally results in slower evaporation (Figure S11). In the case of LIM (Figure 4), gas–particle equilibrium is rapidly achieved in the monolayer model, not capturing the observed gradual decrease in particle mass. The SOA mass after 24 h, however, is very similar in both simulations. A monolayer model run for the APN experiment is fairly comparable with the result of the multilayer model (Figure S6), which is consistent with the earlier finding that evaporation of fresh α-pinene SOA is not diffusion-limited. However, we note crust formation in the model is a consequence of the $D_b - C^*$ relationship (eq 4), where a steeper slope would result in a less diffusive crust. In the absence of additional data, we cannot definitively assert whether slow bulk mixing or diffusivity gradient formation are unique solutions to explain the observed data. Nevertheless, diffusion-limited evaporation via crust formation is proposed in other particle systems[55] and offers a plausible explanation for the slow SOA evaporation examined in this manuscript.

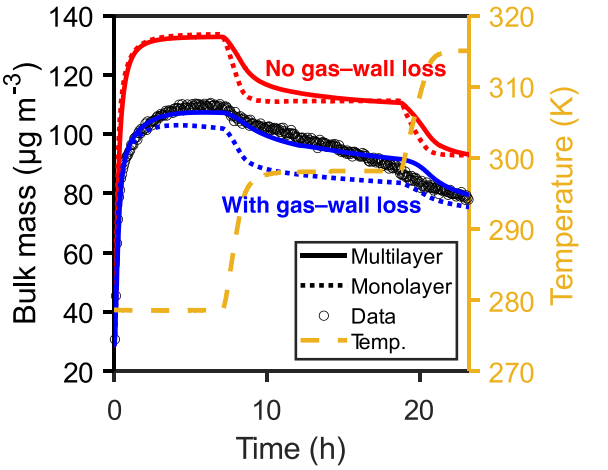


Figure 4. Effect of gas–wall loss and bulk diffusivity on SOA formation in LIM. Solid and dotted lines are results from the full multilayer model and a simplified monolayer version, respectively. When the particle is well-mixed in the monolayer model, less SOA is formed as repartitioning of species to the gas phase is facilitated, leading to gradual loss to the chamber walls. In the full multilayer model, slow bulk diffusivity can shield semivolatile species from being lost to the walls.

Furthermore, we find that peak Y_{SOA} is higher in the simulation with the multilayer model. This result is counter-intuitive as semivolatile organics on the surface of a viscous particle may be incorporated more slowly into the particle bulk, which may result in slower SOA growth. As shown in Figure 4, there is more SOA formation in LIM without gas–wall loss (red solid and dotted lines), and there is no significant effect of bulk diffusion on peak Y_{SOA}. The reason that slow bulk diffusion can increase Y_{SOA} in chamber experiments is that gas–particle repartitioning is slowed by bulk diffusion and thus semivolatile species are shielded from gas–wall loss, and similar results are found with the other scenarios (Figure S7). This result highlights the findings in McVay et al.,[66] where both kinetically limited condensation and gas–wall loss time scales need to be considered when modeling SOA formation.

3.2. Nonadditivity of Y_{SOA}

Figure 5 compares the SOA mass yield (Y_{SOA}) obtained with the kinetic model to the data reported in Berkemeier et al.[8] and in Takeuchi et al.[36] We generate the yield curves by adjusting the initial VOC and N_2O_5 concentrations while keeping the ratio $[VOC]/[N_2O_5]$ constant. We report total Y_{SOA} for all experiments. For the mixed precursor experiments (MIX, SEQ), we also report yields for the individual precursors, attributing the gas- and particle-phase heterodimers in equal parts to α-pinene and limonene.

When accounting for cross-reactions between α-pinene and limonene oxidation products to form heterodimers, we find that the modeled Y_{SOA} agrees well with the experimental results. The model reproduces a small enhancement in the SOA yield of α-pinene in the MIX experiment compared to that in the APN experiment, but the same enhancement is not found in the SEQ experiment (Figure 5a). The model suggests that mixing between the monoterpene products is initially limited in the SEQ experiment, causing a limonene SOA shell to form around an α-pinene core (Figure S5d,e). The spatial separation of oxidation products in the particle phase and the temporal separation of peroxy radicals in the gas phase leads to reduced formation of heterodimers from cross-reactions (Figure 3f). Previous studies[67,68] suggested that incomplete mixing or phase separation may affect Y_{SOA} in multiprecursor experiments. Here, the model assumes full thermodynamic miscibility between limonene and α-pinene oxidation products, and spatial separation is only due to diffusion limitations in the particle phase.

The model returns a decrease in limonene SOA yield in the SEQ experiment (Figure 5a), in line with the experimental observations by Takeuchi et al.[36] This is due to a shift in the product spectrum toward a lower abundance of gas-phase dimers in the particle phase (Figures 3b) caused by lower limonene precursor (and thus RO_2) concentrations. Surprisingly, while limonene oxidation products do not fully mix into the existing α-pinene SOA particles, the viscous phase state does not reduce limonene SOA yield in the SEQ experiment (Figure S8a). This is because of the effect of shielding semivolatiles from gas–wall loss discussed for the LIM experiment above (Figure 4), which leads to an overall increase in SOA yield due to the viscous phase state. Note that the partitioning of low-volatile species, which almost fully condense, is hardly affected by particle phase state in the model.

When the heterogeneous reaction parameters are linearly interpolated between α-pinene and limonene, there is a marked reduction in the simulated SOA mass throughout the MIX experiment, while the SEQ experiment shows faster evaporation at the 42 °C temperature set point (Figure 5b,c). Thus, based on the global optimization results in this study (Section S4), we propose that the reaction rate coefficients of cross-reactions between α-pinene and limonene oxidation products must be faster than one would obtain from linear combination of the same reactions leading to the homodimers. The MCM assigns a $k_{RO2+RO2}$ of 9.20×10^{-14} cm^3 s^{-1} for the pure systems of α-pinene and limonene. The global model

https://doi.org/10.1021/acsestair.5c00438
ACS EST Air XXXX, XXX, XXX–XXX

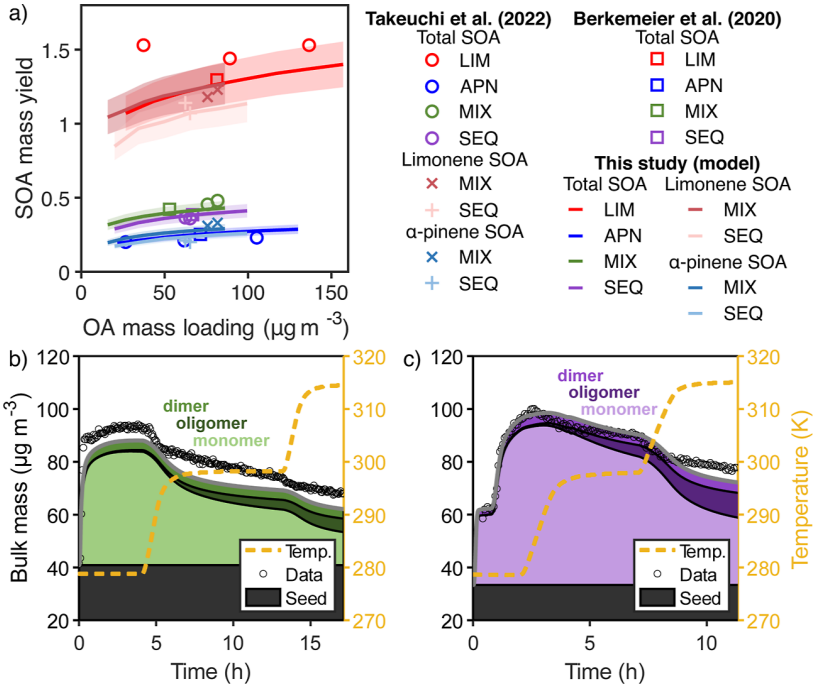


Figure 5. (a) SOA mass yield (Y_{SOA}) curves (lines) obtained using KM3C and compared to measured values (markers) from Berkemeier et al.[8] and Takeuchi et al.[36] The shaded areas indicate the modeled uncertainty assuming ±10% error in the initial VOC and N_2O_5 concentrations. Total refers to Y_{SOA} calculated with the sum of α-pinene and limonene mass reacted. For SEQ and MIX, Takeuchi et al.[36] used mass spectra to separate the α-pinene and limonene SOA, and we draw Y_{SOA} for each monoterpene. SOA mass concentrations in the chamber for (b) MIX and (c) SEQ experiments in modified model simulations in which the rate coefficient parameters for the heteroproduct formation reactions are linearly interpolated between those of α-pinene and limonene. For the MIX experiment, model results are notably lower than experimental measurements, which indicates nonlinear effects in the rate coefficients of cross-reactions.

optimization in this study suggests an enhanced rate coefficient for the gas-phase cross-reaction, $RO_{2,apn}$ + $RO_{2,lim}$, of 7.18 × 10^{-13} cm^3 s^{-1}.

Reported RO_2 + RO_2 rate coefficients vary widely in the literature and depend on the molecular structures.[49,50] Some of the enhancement in the rate coefficient we infer from the model results may be reflective of the differences in the structures between $RO_{2,apn}$ and $RO_{2,lim}$. For instance, Franzon et al.[51] find that $k_{RO2+RO2}$ for reactions involving an acyl peroxy radical can reach 10^{-11} cm^3 s^{-1}. The particle-phase oligomerization parameters are summarized in Table 1. The

Table 1. (a) Optimized First-Order Rate Coefficients (s^{-1}) and Energies of Activation (kJ mol^{-1}) for Forward and Reverse Oligomerization Reactions

	α-pinene	limonene	heterogeneous
$k_{fwd,olig}$	1.11 × 10^{-5}	3.00 × 10^{-6}	9.52 × 10^{-6}
$k_{rev,olig}$	3.03 × 10^{-6}	3.53 × 10^{-5}	8.08 × 10^{-7}
$E_{a,fwd}$	55.0	98.6	98.4
$E_{a,rev}$	42.1	44.2	43.1

current optimized values suggest that the rate coefficients for the formation of heterodimers are more consistent with the slightly higher formation rate of α-pinene homodimers than with the formation rate of limonene homodimers. We find that the model is sensitive to heterodimer formation in the MIX experiment (Figure S14), where stronger formation of heterodimer results in stronger initial SOA growth. As a consequence, the MIX experiment shows a higher oligomer content than the LIM experiment.

In the ambient atmosphere, many VOCs are oxidized simultaneously; thus, atmospheric conditions likely resemble more the MIX experiment than the SEQ experiment. Nonlinearity of Y_{SOA} has been found in other VOC mixtures.[69,70] As part of the nonadditivity arises from gas-phase dimer formation, future studies should look into the effects of RO_2 fate[49] on Y_{SOA} in precursor mixtures. Nevertheless, we find that Y_{SOA} nonlinearity is not only due to gas-phase kinetics but also due to the phase state of the particles as the formation of heterodimers can be limited by slow diffusion, as shown in the SEQ experiment. We conclude that particle phase state needs to be considered in order to accurately model the growth and fate of atmospheric SOA, which is particularly relevant in dry and cold environments.[7] Although the relationship between bulk diffusivity and volatility presented in this study applies directly to SOA under dry conditions, the plasticizing effects of water, which increase diffusivity coefficients, must be considered at higher relative humidities.[6,71] An approximate mathematical description has previously been achieved using the κ-Köhler theory and the Gordon−Taylor equation;[19,64,72,73] however, a full description of the relationships of volatility, hygroscopicity, and diffusivity in SOA−water mixtures remains to be determined and is a subject of future studies.

3.3. Thermal Desorption

We use KM3C to model FIGAERO-CIMS sum thermograms based on the composition calculated during SOA growth and evaporation in the chamber experiment. The model is overall able to capture the FIGAERO-CIMS thermogram shapes and their temporal evolution (Figure 6). We show one thermogram

https://doi.org/10.1021/acsestair.5c00438
ACS EST Air XXXX, XXX, XXX−XXX

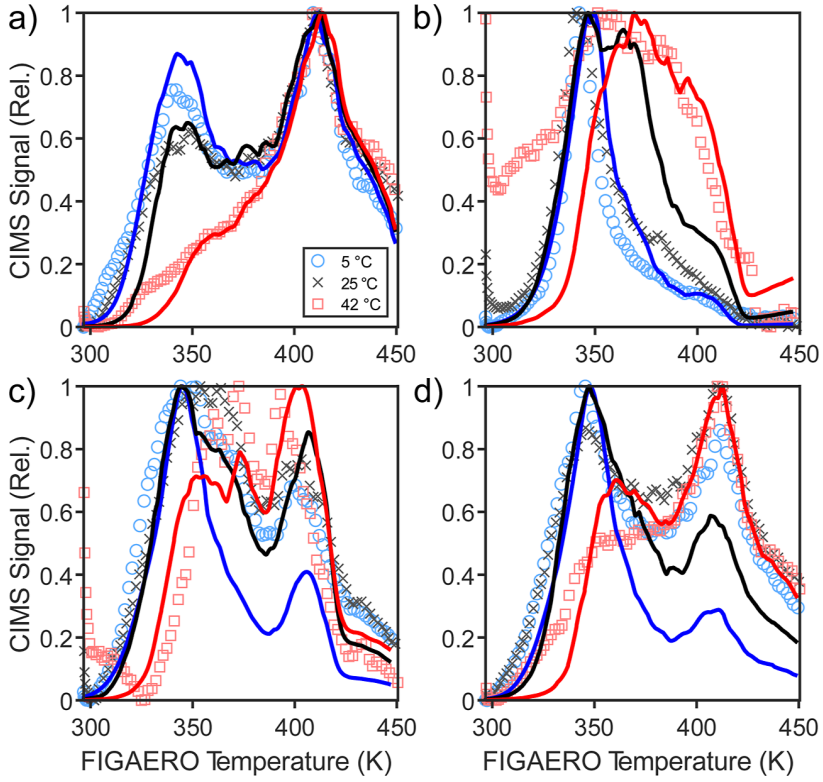


Figure 6. FIGAERO-CIMS thermograms of (a) LIM, (b) APN, (c) MIX, and (d) SEQ experiments. Lines and markers indicate the model and normalized data from the three temperature steps in the chamber experiment (5 °C: blue, 25 °C: black, 42 °C: red). The legend refers to the temperatures in the chamber during the sampling period.

from each temperature step, where the black, red, and blue colors correspond to the 5, 25, and 42 °C temperature set points in the chamber, respectively. Overall lower desorption temperatures in the thermogram for the APN experiment (Figure 6b) suggest that SOA is composed of more volatile species compared to SOA in the LIM experiment (Figure 6a). The thermogram distribution shifts to higher temperatures as the experiment progresses. While the APN thermogram exhibits a single peak, the LIM, MIX, and SEQ thermograms show two peaks. In the model, the first thermogram peak results from the desorption of semivolatile monomers and the second peak in the thermograms results from the evaporation of low-volatile monomers, dimers, and dissociating oligomers. When describing FIGAERO-CIMS data, the model is sensitive to the activation energies of the forward and reverse oligomerization reactions, $E_{a,fwd}$ and $E_{a,rev}$ (Figure S13), as oligomer decomposition is driven by these parameters at the higher temperatures of the FIGAERO. The first peak generally decreases relative to the second peak with every heating step, which is consistent with the model result that semivolatile monomers evaporate predominantly. Notably, α-pinene SOA shows pronounced particle-phase oligomerization in the model when heated to 42 °C, causing a shoulder of the first peak to develop. We note that different chemical species can have different sensitivities to the iodide CIMS,[74] which is not accounted for in this study and may explain part of the discrepancy between the model and the experiment. For instance, Song et al.[75] found that iodide CIMS sensitivity increases with the addition of polar functional groups. The addition of such functional groups onto a molecule decreases the molecule's vapor pressure,[38] and such low-volatile molecules likely desorb at higher temperatures in the FIGAERO. Accordingly, the second desorption peak seen in the LIM, MIX, and SEQ experiments may include a greater number of such highly functionalized molecules that the iodide CIMS is more sensitive to, which may skew the fitted model toward low-volatile species.

While KM3C predicts a surface crust as a reason for slow evaporation in the LIM experiment, Berkemeier et al.[8] achieved a good fit to the SOA mass data with a model that assumes a well-mixed particle bulk. This monolayer bulk model attributed the slow evaporation to the decomposition of particle-phase oligomers. When refitting KM3C with a single bulk layer, we reproduce this result from the earlier study (Figure S9a). However, the FIGAERO thermograms simulated with the particle composition from these well-mixed bulk calculations do not exhibit the double-peak behavior observed in the LIM experiment. Instead, the high degree of oligomerization results in a single peak desorbing at high temperatures (Figure S9b). Thus, the addition of FIGAERO-CIMS data adds a strong and important constraint on the model parameter space, further building evidence that the bulk diffusivity can have a pronounced effect on the evaporation of SOA. Furthermore, the KM3C model results show how slow bulk diffusion can affect the mechanistic interpretation of SOA evolution in chamber experiments. Here, KM3C attributes the slow evaporation of limonene SOA in the chamber to kinetically limited evaporation caused by formation of a viscous surface crust, while a model that was fitted to the data without accounting for slow bulk diffusion[8] attributed the phenomenon to strong oligomer formation and decomposition.

https://doi.org/10.1021/acsestair.5c00438
ACS EST Air XXXX, XXX, XXX−XXX

In addition to laboratory chamber experiments, bulk diffusivity affects cloud formation and chemical fate in the atmosphere.[18,19] Zaveri et al.[76] studied urban plume measurements from aircraft campaigns over the Amazon and found that the growth of sub-10 nm particles into cloud condensation nuclei (CCN) is driven by the partitioning of semivolatile oxidation products of biogenic precursors into viscous particles. The authors modeled the impact that this enhancement of CCN has on cloud formation and found that the transition of shallow to deep convective cloud is enhanced while precipitation is suppressed. Furthermore, Shiraiwa et al.[7] found that gas−particle interactions in viscous particles may be kinetically limited. This effect would also increase ice nucleation and enable regional transport of pollutants that are trapped in the particles.[77] Thus, to accurately model cloud formation and chemical exposure, air quality models may need to consider effects of high viscosity and slow bulk diffusion.

■ ASSOCIATED CONTENT

Supporting Information

The Supporting Information is available free of charge at https://pubs.acs.org/doi/10.1021/acsestair.5c00438.

Moving-boundary algorithm, adsorption and desorption rate coefficients, chemical mechanism, optimized parameters and MCGA, model sensitivity to parameters, comparison of the $D_b - C^*$ relationship with data, and related data illustrations and schematics (PDF)

■ AUTHOR INFORMATION

Corresponding Author

Thomas Berkemeier − *Multiphase Chemistry Department, Max Planck Institute for Chemistry, 55218 Mainz, Germany;* orcid.org/0000-0001-6390-6465; Email: t.berkemeier@mpic.de

Authors

Hyun Gu Kang − *Multiphase Chemistry Department, Max Planck Institute for Chemistry, 55218 Mainz, Germany;* orcid.org/0000-0002-3320-9447

Masayuki Takeuchi − *School of Civil and Environmental Engineering, Georgia Institute of Technology, Atlanta, Georgia 30332, United States of America;* Present Address: Department of Mechanical Engineering, 613 University of Colorado Boulder, Boulder, Colorado 80309, United States of America; orcid.org/0000-0002-9327-6748

Nga L. Ng − *School of Chemical and Bimolecular Engineering, School of Civil and Environmental Engineering, and School of Earth and Atmospheric Sciences, Georgia Institute of Technology, Atlanta, Georgia 30332, United States of America;* Present Address: Division of Engineering and Applied Science, California Institute of Technology, Pasadena, California 91125, United States of America; orcid.org/0000-0001-8460-4765

Ulrich Pöschl − *Multiphase Chemistry Department, Max Planck Institute for Chemistry, 55218 Mainz, Germany;* orcid.org/0000-0003-1412-3557

Complete contact information is available at: https://pubs.acs.org/10.1021/acsestair.5c00438

Funding

Open access funded by Max Planck Society.

Notes

The authors declare no competing financial interest.

■ ACKNOWLEDGMENTS

The experimental data used in this study were originally generated with the support of the National Science Foundation (NSF) CAREER AGS-1555034, the National Oceanic and Atmospheric Administration (NOAA) NA18OAR4310112, and the Eckert Postdoctoral Fellowship from the School of Chemical and Biomolecular Engineering at Georgia Institute of Technology. The FIGAERO-HR-ToF-CIMS has been purchased through the NSF Major Research Instrumentation (MRI) Grant 1428738. Hyun Gu Kang is supported by the Max Planck Graduate Center with the Johannes Gutenberg University Mainz (MPGC). The authors are grateful for computing time on the supercomputer RAVEN at the Max Planck Computing and Data Facility (MPCDF). The authors thank Zhiqiang Zhang and Siegfried Schobesberger for insightful discussions.

■ REFERENCES

(1) Pankow, J. F. An absorption model of gas/particle partitioning of organic compounds in the atmosphere. *Atmos. Environ.* **1994**, *28*, 185−188.

(2) Donahue, N. M.; Robinson, A. L.; Stanier, C. O.; Pandis, S. N. Coupled Partitioning, Dilution, and Chemical Aging of Semivolatile Organics. *Environ. Sci. Technol.* **2006**, *40*, 2635−2643.

(3) Schobesberger, S.; D'Ambro, E. L.; Lopez-Hilfiker, F. D.; Mohr, C.; Thornton, J. A. A model framework to retrieve thermodynamic and kinetic properties of organic aerosol from composition-resolved thermal desorption measurements. *Atmos. Chem. Phys.* **2018**, *18*, 14757−14785.

(4) Ylisirniö, A.; Barreira, L. M. F.; Pullinen, I.; Buchholz, A.; Jayne, J.; Krechmer, J. E.; Worsnop, D. R.; Virtanen, A.; Schobesberger, S. On the calibration of FIGAERO-ToF-CIMS: importance and impact of calibrant delivery for the particle-phase calibration. *Atmos. Meas. Technol.* **2021**, *14*, 355−367.

(5) Virtanen, A.; Joutsensaari, J.; Koop, T.; Kannosto, J.; Yli-Pirilä, P.; Leskinen, J.; Mäkelä, J. M.; Holopainen, J. K.; Pöschl, U.; Kulmala, M.; Worsnop, D. R.; Laaksonen, A. An amorphous solid state of biogenic secondary organic aerosol particles. *Nature* **2010**, *467*, 824−827.

(6) Koop, T.; Bookhold, J.; Shiraiwa, M.; Pöschl, U. Glass transition and phase state of organic compounds: dependency on molecular properties and implications for secondary organic aerosols in the atmosphere. *Phys. Chem. Chem. Phys.* **2011**, *13*, 19238.

(7) Shiraiwa, M.; Li, Y.; Tsimpidi, A. P.; Karydis, V. A.; Berkemeier, T.; Pandis, S. N.; Lelieveld, J.; Koop, T.; Pöschl, U. Global distribution of particle phase state in atmospheric secondary organic aerosols. *Nat. Commun.* **2017**, *8*, 15002.

(8) Berkemeier, T.; Takeuchi, M.; Eris, G.; Ng, N. L. Kinetic modeling of formation and evaporation of secondary organic aerosol from NO_3 oxidation of pure and mixed monoterpenes. *Atmos. Chem. Phys.* **2020**, *20*, 15513−15535.

(9) Bakker-Arkema, J. G.; Ziemann, P. J. Measurements of Kinetics and Equilibria for the Condensed Phase Reactions of Hydroperoxides with Carbonyls to Form Peroxyhemiacetals. *ACS Earth Space Chem.* **2020**, *4*, 467−475.

(10) Maben, H. K.; Ziemann, P. J. Kinetics of oligomer-forming reactions involving the major functional groups present in atmospheric secondary organic aerosol particles. *Environ. Sci.: Processes Impacts* **2023**, *25*, 214−228.

(11) Kenseth, C. M.; Hafeman, N. J.; Rezgui, S. P.; Chen, J.; Huang, Y.; Dalleska, N. F.; Kjaergaard, H. G.; Stoltz, B. M.; Seinfeld, J. H.;

Wennberg, P. O. Particle-phase accretion forms dimer esters in pinene secondary organic aerosol. *Science* **2023**, *382*, 787−792.
(12) Tolocka, M. P.; Jang, M.; Ginter, J. M.; Cox, F. J.; Kamens, R. M.; Johnston, M. V. Formation of Oligomers in Secondary Organic Aerosol. *Environ. Sci. Technol.* **2004**, *38*, 1428−1434.
(13) Casale, M.; Richman, A.; Elrod, M.; Garland, R.; Beaver, M.; Tolbert, M. Kinetics of acid-catalyzed aldol condensation reactions of aliphatic aldehydes. *Atmos. Environ.* **2007**, *41*, 6212−6224.
(14) Hall, W. A.; Johnston, M. V. Oligomer Content of α -Pinene Secondary Organic Aerosol. *Aerosol Sci. Technol.* **2011**, *45*, 37−45.
(15) Rodigast, M.; Mutzel, A.; Herrmann, H. A quantification method for heat-decomposable methylglyoxal oligomers and its application on 1,3,5-trimethylbenzene SOA. *Atmos. Chem. Phys.* **2017**, *17*, 3929−3943.
(16) Pfrang, C.; Shiraiwa, M.; Pöschl, U. Chemical ageing and transformation of diffusivity in semi-solid multi-component organic aerosol particles. *Atmos. Chem. Phys.* **2011**, *11*, 7343−7354.
(17) Hosny, N. A.; Fitzgerald, C.; Vyšniauskas, A.; Athanasiadis, A.; Berkemeier, T.; Uygur, N.; Pöschl, U.; Shiraiwa, M.; Kalberer, M.; Pope, F. D.; Kuimova, M. K. Direct imaging of changes in aerosol particle viscosity upon hydration and chemical aging. *Chem. Sci.* **2016**, *7*, 1357−1367.
(18) Berkemeier, T.; Steimer, S. S.; Krieger, U. K.; Peter, T.; Pöschl, U.; Ammann, M.; Shiraiwa, M. Ozone uptake on glassy, semi-solid and liquid organic matter and the role of reactive oxygen intermediates in atmospheric aerosol chemistry. *Phys. Chem. Chem. Phys.* **2016**, *18*, 12662−12674.
(19) Berkemeier, T.; Shiraiwa, M.; Pöschl, U.; Koop, T. Competition between water uptake and ice nucleation by glassy organic aerosol particles. *Atmos. Chem. Phys.* **2014**, *14*, 12513−12531.
(20) Zaveri, R. A.; et al. Growth Kinetics and Size Distribution Dynamics of Viscous Secondary Organic Aerosol. *Environ. Sci. Technol.* **2018**, *52*, 1191−1199.
(21) Shiraiwa, M.; Yee, L. D.; Schilling, K. A.; Loza, C. L.; Craven, J. S.; Zuend, A.; Ziemann, P. J.; Seinfeld, J. H. Size distribution dynamics reveal particle-phase chemistry in organic aerosol formation. *Proc. Natl. Acad. Sci. U.S.A.* **2013**, *110*, 11746−11750.
(22) Roldin, P.; Eriksson, A. C.; Nordin, E. Z.; Hermansson, E.; Mogensen, D.; Rusanen, A.; Boy, M.; Swietlicki, E.; Svenningsson, B.; Zelenyuk, A.; Pagels, J. Modelling non-equilibrium secondary organic aerosol formation and evaporation with the aerosol dynamics, gas- and particle-phase chemistry kinetic multilayer model ADCHAM. *Atmos. Chem. Phys.* **2014**, *14*, 7953−7993.
(23) Yli-Juuti, T.; Pajunoja, A.; Tikkanen, O.; Buchholz, A.; Faiola, C.; Väisänen, O.; Hao, L.; Kari, E.; Peräkylä, O.; Garmash, O.; Shiraiwa, M.; Ehn, M.; Lehtinen, K.; Virtanen, A. Factors controlling the evaporation of secondary organic aerosol from α -pinene ozonolysis. *Geophys. Res. Lett.* **2017**, *44*, 2562−2570.
(24) Ingram, S.; Rovelli, G.; Song, Y.-C.; Topping, D.; Dutcher, C. S.; Liu, S.; Nandy, L.; Shiraiwa, M.; Reid, J. P. Accurate Prediction of Organic Aerosol Evaporation Using Kinetic Multilayer Modeling and the Stokes-Einstein Equation. *J. Phys. Chem. A* **2021**, *125*, 3444−3456.
(25) Sartelet, K.; Wang, Z.; Kim, Y.; Lannuque, V.; Couvidat, F. Advanced modeling of gas chemistry and aerosol dynamics with SSH-aerosol v2.0. *Geosci. Model Dev.* **2026**, *19*, 389−421.
(26) Schnitzler, E. G.; Abbatt, J. P. D. Heterogeneous OH oxidation of secondary brown carbon aerosol. *Atmos. Chem. Phys.* **2018**, *18*, 14539−14553.
(27) Berkemeier, T.; Mishra, A.; Mattei, C.; Huisman, A. J.; Krieger, U. K.; Pöschl, U. Ozonolysis of Oleic Acid Aerosol Revisited: Multiphase Chemical Kinetics and Reaction Mechanisms. *ACS Earth Space Chem.* **2021**, *5*, 3313−3323.
(28) Milsom, A.; Lees, A.; Squires, A. M.; Pfrang, C. MultilayerPy (v1.0): a Python-based framework for building, running and optimizing kinetic multi-layer models of aerosols and films. *Geosci. Model Dev.* **2022**, *15*, 7139−7151.
(29) Alpert, P. A.; Dou, J.; Corral Arroyo, P.; Schneider, F.; Xto, J.; Luo, B.; Peter, T.; Huthwelker, T.; Borca, C. N.; Henzler, K. D.; et al. Photolytic radical persistence due to anoxia in viscous aerosol particles. *Nat. Commun.* **2021**, *12*, 1769.
(30) Mishra, A.; Kilchhofer, K.; Iezzi, L.; Pöschl, U.; Alpert, P. A.; Ammann, M.; Berkemeier, T. Photochemical Degradation of Iron Citrate in Anoxic Viscous Films Enhanced by Redox Cascades. *ACS Earth Space Chem.* **2025**, *9*, 689−698.
(31) Pöschl, U.; Rudich, Y.; Ammann, M. Kinetic model framework for aerosol and cloud surface chemistry and gas-particle interactions - Part 1: General equations, parameters, and terminology. *Atmos. Chem. Phys.* **2007**, *7*, 5989−6023.
(32) Shiraiwa, M.; Pfrang, C.; Koop, T.; Pöschl, U. Kinetic multi-layer model of gas-particle interactions in aerosols and clouds (KM-GAP): linking condensation, evaporation and chemical reactions of organics, oxidants and water. *Atmos. Chem. Phys.* **2012**, *12*, 2777−2794.
(33) Masoud, C. G.; Li, Y.; Wang, D. S.; Katz, E. F.; DeCarlo, P. F.; Farmer, D. K.; Vance, M. E.; Shiraiwa, M.; Hildebrandt Ruiz, L. Molecular composition and gas-particle partitioning of indoor cooking aerosol: Insights from a FIGAERO-CIMS and kinetic aerosol modeling. *Aerosol Sci. Technol.* **2022**, *56*, 1156−1173.
(34) Appel, K. W.; et al. Description and evaluation of the Community Multiscale Air Quality (CMAQ) modeling system version 5.1. *Geosci. Model Dev.* **2017**, *10*, 1703−1732.
(35) McFiggans, G.; et al. Secondary organic aerosol reduced by mixture of atmospheric vapours. *Nature* **2019**, *565*, 587−593.
(36) Takeuchi, M.; Berkemeier, T.; Eris, G.; Ng, N. L. Non-linear effects of secondary organic aerosol formation and properties in multi-precursor systems. *Nat. Commun.* **2022**, *13*, 7883.
(37) Khalaj, F.; Gu, S.; Mehra, A.; Williams, L. R.; Krechmer, J.; Lambe, A.; Perraud, V.; Faiola, C. L. Aerosol chemistry of oxygenated terpenes in simple and complex chemical systems. *Aerosol Sci. Technol.* **2025**, *59*, 470−486.
(38) Pankow, J. F.; Asher, W. E. SIMPOL.1: a simple group contribution method for predicting vapor pressures and enthalpies of vaporization of multifunctional organic compounds. *Atmos. Chem. Phys.* **2008**, *8*, 2773−2796.
(39) Robinson, A. L.; Donahue, N. M.; Shrivastava, M. K.; Weitkamp, E. A.; Sage, A. M.; Grieshop, A. P.; Lane, T. E.; Pierce, J. R.; Pandis, S. N. Rethinking Organic Aerosols: Semivolatile Emissions and Photochemical Aging. *Science* **2007**, *315*, 1259−1262.
(40) Kang, H. G.; Chen, Y.; Park, Y.; Berkemeier, T.; Kim, H. Volatile oxidation products and secondary organosiloxane aerosol from D_5 + OH at varying OH exposures. *Atmos. Chem. Phys.* **2023**, *23*, 14307−14323.
(41) Sommers, J. M.; Stroud, C. A.; Adam, M. G.; O'Brien, J.; Brook, J. R.; Hayden, K.; Lee, A. K. Y.; Li, K.; Liggio, J.; Mihele, C.; Mittermeier, R. L.; Stevens, R. G.; Wolde, M.; Zuend, A.; Hayes, P. L. Evaluating SOA formation from different sources of semi- and intermediate-volatility organic compounds from the Athabasca oil sands. *Environ. Sci.: Atmos.* **2022**, *2*, 469−490.
(42) Berkemeier, T.; Ammann, M.; Krieger, U. K.; Peter, T.; Spichtinger, P.; Pöschl, U.; Shiraiwa, M.; Huisman, A. J. Technical note: Monte Carlo genetic algorithm (MCGA) for model analysis of multiphase chemical kinetics to determine transport and reaction rate coefficients using multiple experimental data sets. *Atmos. Chem. Phys.* **2017**, *17*, 8021−8029.
(43) Nah, T.; McVay, R. C.; Pierce, J. R.; Seinfeld, J. H.; Ng, N. L. Constraining uncertainties in particle-wall deposition correction during SOA formation in chamber experiments. *Atmos. Chem. Phys.* **2017**, *17*, 2297−2310.
(44) Shiraiwa, M.; Pfrang, C.; Pöschl, U. Kinetic multi-layer model of aerosol surface and bulk chemistry (KM-SUB): the influence of interfacial transport and bulk diffusion on the oxidation of oleic acid by ozone. *Atmos. Chem. Phys.* **2010**, *10*, 3673−3691.
(45) Huang, Y.; Zhao, R.; Charan, S. M.; Kenseth, C. M.; Zhang, X.; Seinfeld, J. H. Unified Theory of Vapor-Wall Mass Transport in Teflon-Walled Environmental Chambers. *Environ. Sci. Technol.* **2018**, *52*, 2134−2142.

https://doi.org/10.1021/acsestair.5c00438
ACS EST Air XXXX, XXX, XXX−XXX

(46) Couvidat, F.; Sartelet, K. The Secondary Organic Aerosol Processor (SOAP v1.0) model: a unified model with different ranges of complexity based on the molecular surrogate approach. *Geosci. Model Dev.* **2015**, *8*, 1111−1138.
(47) Saunders, S. M.; Jenkin, M. E.; Derwent, R. G.; Pilling, M. J. Protocol for the development of the Master Chemical Mechanism, MCM v3 (Part A): tropospheric degradation of non-aromatic volatile organic compounds. *Atmos. Chem. Phys.* **2003**, *3*, 161−180.
(48) Epstein, S. A.; Riipinen, I.; Donahue, N. M. A Semiempirical Correlation between Enthalpy of Vaporization and Saturation Concentration for Organic Aerosol. *Environ. Sci. Technol.* **2010**, *44*, 743−748.
(49) Ziemann, P. J.; Atkinson, R. Kinetics, products, and mechanisms of secondary organic aerosol formation. *Chem. Soc. Rev.* **2012**, *41*, 6582.
(50) Jenkin, M. E.; Valorso, R.; Aumont, B.; Rickard, A. R. Estimation of rate coefficients and branching ratios for reactions of organic peroxy radicals for use in automated mechanism construction. *Atmos. Chem. Phys.* **2019**, *19*, 7691−7717.
(51) Franzon, L.; Camredon, M.; Valorso, R.; Aumont, B.; Kurtén, T. Ether and ester formation from peroxy radical recombination: a qualitative reaction channel analysis. *Atmos. Chem. Phys.* **2024**, *24*, 11679−11699.
(52) D'Anna, B.; Andresen, A.~; Gefen, Z.; Nielsen, C. J. Kinetic study of OH and NO_3 radical reactions with 14 aliphatic aldehydes. *Phys. Chem. Chem. Phys.* **2001**, *3*, 3057−3063.
(53) Moreno, A.; Salgado, M. S.; Martín, M. P.; Martínez, E.; Cabañas, B. Kinetic Study of the Gas Phase Reactions of a Series of Alcohols with the NO_3 Radical. *J. Phys. Chem. A* **2012**, *116*, 10383−10389.
(54) Salmon, J.-B.; Doumenc, F.; Guerrier, B. Humidity-insensitive water evaporation from molecular complex fluids. *Phys. Rev. E* **2017**, *96*, 032612.
(55) Huisman, M.; Poon, W. C. K.; Warren, P. B.; Titmuss, S.; Marenduzzo, D. Diffusive evaporation dynamics in polymer solutions is ubiquitous. *Soft Matter* **2025**, *21*, 1508−1515.
(56) Champion, W. M.; Rothfuss, N. E.; Petters, M. D.; Grieshop, A. P. Volatility and Viscosity Are Correlated in Terpene Secondary Organic Aerosol Formed in a Flow Reactor. *Environ. Sci. Technol. Lett.* **2019**, *6*, 513−519.
(57) Mitra, S. S. Relation between Vapor Pressure and Viscosity of Liquids. *J. Chem. Phys.* **1954**, *22*, 349−350.
(58) Woodman, A. L.; Murbach, W. J.; Kaufman, M. H. Vapor pressure and viscosity relationships for a homologous series of α, ω-dinitriles. *J. Phys. Chem.* **1960**, *64*, 658−660.
(59) Frank, A. Viscosity-vapor pressure correlation of alcohols, methyl ketones and alkyl halides. M.Sc. thesis; American Chemical Society, 1962.
(60) Johnston, W. G.; Sargent, L. B. The Determination of Vapor Pressures of Low Viscosity Lubricants from Distillation Data. *ASLE Transactions* **1970**, *13*, 304−310.
(61) Rothfuss, N. E.; Petters, M. D. Influence of Functional Groups on the Viscosity of Organic Aerosol. *Environ. Sci. Technol.* **2017**, *51*, 271−279.
(62) Vignes, A. Diffusion in Binary Solutions. Variation of Diffusion Coefficient with Composition. *Ind. Eng. Chem. Fundam.* **1966**, *5*, 189−199.
(63) Kiland, K. J.; Maclean, A. M.; Kamal, S.; Bertram, A. K. Diffusion of Organic Molecules as a Function of Temperature in a Sucrose Matrix (a Proxy for Secondary Organic Aerosol). *J. Phys. Chem. Lett.* **2019**, *10*, 5902−5908.
(64) Li, Y.; Day, D. A.; Stark, H.; Jimenez, J. L.; Shiraiwa, M. Predictions of the glass transition temperature and viscosity of organic aerosols from volatility distributions. *Atmos. Chem. Phys.* **2020**, *20*, 8103−8122.
(65) Boyd, C. M.; Nah, T.; Xu, L.; Berkemeier, T.; Ng, N. L. Secondary Organic Aerosol (SOA) from Nitrate Radical Oxidation of Monoterpenes: Effects of Temperature, Dilution, and Humidity on Aerosol Formation, Mixing, and Evaporation. *Environ. Sci. Technol.* **2017**, *51*, 7831−7841.
(66) McVay, R. C.; Cappa, C. D.; Seinfeld, J. H. Vapor-Wall Deposition in Chambers: Theoretical Considerations. *Environ. Sci. Technol.* **2014**, *48*, 10251−10258.
(67) Shilling, J. E.; Zawadowicz, M. A.; Liu, J.; Zaveri, R. A.; Zelenyuk, A. Photochemical Aging Alters Secondary Organic Aerosol Partitioning Behavior. *ACS Earth Space Chem.* **2019**, *3*, 2704−2716.
(68) Mahrt, F.; Peng, L.; Zaks, J.; Huang, Y.; Ohno, P. E.; Smith, N. R.; Gregson, F. K. A.; Qin, Y.; Faiola, C. L.; Martin, S. T.; Nizkorodov, S. A.; Ammann, M.; Bertram, A. K. Not all types of secondary organic aerosol mix: two phases observed when mixing different secondary organic aerosol types. *Atmos. Chem. Phys.* **2022**, *22*, 13783−13796.
(69) Chen, T.; Zhang, P.; Chu, B.; Ma, Q.; Ge, Y.; Liu, J.; He, H. Secondary organic aerosol formation from mixed volatile organic compounds: Effect of RO_2 chemistry and precursor concentration. *npj Clim. Atmos. Sci.* **2022**, *5*, 95.
(70) Voliotis, A.; Du, M.; Wang, Y.; Shao, Y.; Alfarra, M. R.; Bannan, T. J.; Hu, D.; Pereira, K. L.; Hamilton, J. F.; Hallquist, M.; Mentel, T. F.; McFiggans, G. Chamber investigation of the formation and transformation of secondary organic aerosol in mixtures of biogenic and anthropogenic volatile organic compounds. *Atmos. Chem. Phys.* **2022**, *22*, 14147−14175.
(71) Shiraiwa, M.; Ammann, M.; Koop, T.; Pöschl, U. Gas uptake and chemical aging of semisolid organic aerosol particles. *Proc. Natl. Acad. Sci. U.S.A.* **2011**, *108*, 11003−11008.
(72) Petters, M. D.; Kreidenweis, S. M. A single parameter representation of hygroscopic growth and cloud condensation nucleus activity. *Atmos. Chem. Phys.* **2007**, *7*, 1961−1971.
(73) Dette, H. P.; Qi, M.; Schröder, D. C.; Godt, A.; Koop, T. Glass-Forming Properties of 3-Methylbutane-1,2,3-tricarboxylic Acid and Its Mixtures with Water and Pinonic Acid. *J. Phys. Chem. A* **2014**, *118*, 7024−7033.
(74) Bi, C.; Krechmer, J. E.; Frazier, G. O.; Xu, W.; Lambe, A. T.; Claflin, M. S.; Lerner, B. M.; Jayne, J. T.; Worsnop, D. R.; Canagaratna, M. R.; Isaacman-VanWertz, G. Quantification of isomer-resolved iodide chemical ionization mass spectrometry sensitivity and uncertainty using a voltage-scanning approach. *Atmos. Meas. Technol.* **2021**, *14*, 6835−6850.
(75) Song, M.; He, S.; Li, X.; Liu, Y.; Lou, S.; Lu, S.; Zeng, L.; Zhang, Y. Optimizing the iodide-adduct chemical ionization mass spectrometry (CIMS) quantitative method for toluene oxidation intermediates: experimental insights into functional-group differences. *Atmos. Meas. Technol.* **2024**, *17*, 5113−5127.
(76) Zaveri, R. A.; Wang, J.; Fan, J.; Zhang, Y.; Shilling, J. E.; Zelenyuk, A.; Mei, F.; Newsom, R.; Pekour, M.; Tomlinson, J.; et al. Rapid growth of anthropogenic organic nanoparticles greatly alters cloud life cycle in the Amazon rainforest. *Sci. Adv.* **2022**, *8*, No. eabj0329.
(77) Mu, Q.; Shiraiwa, M.; Octaviani, M.; Ma, N.; Ding, A.; Su, H.; Lammel, G.; Pöschl, U.; Cheng, Y. Temperature effect on phase state and reactivity controls atmospheric multiphase chemistry and transport of PAHs. *Sci. Adv.* **2018**, *4*, No. eaap7314.

https://doi.org/10.1021/acsestair.5c00438
ACS EST Air XXXX, XXX, XXX−XXX

2.4. Surface crust formation controls evaporation kinetics of secondary organic aerosols

This section has been published as a research article in the journal *Environmental Science and Technology*, where I am the second author. Under the supervision of Dr. Thomas Berkemeier, I performed model calculations and global optimization with the limonene SOA data originally reported in Berkemeier et al. (2020). I contributed to the production of the figures and the writing. The supplement to this work can be found in Appendix B.3.

Schervish, M., Kang, H. G., Wingen, L. M., Nguyen, K., Begay, C., Wilson, J., Shrivastava, M., Chen, Y., Schilling, J. E., Ng, N. L., Pöschl, U., Berkemeier, T., Zelenyuk, A., Shiraiwa, M.: Surface Crust Formation Controls Evaporation Kinetics of Secondary Organic Aerosols *Environ. Sci. Technol.* 60, 7995-8006 (2026).

This study used kinetic multilayer models to show the interwined effects of particle composition, diffusion, and evaporation. Co-authors studied the evaporation of SOA from α-pinene + O_3 and polyethylene glycol (PEG) nanoparticles, and we contributed the limonene SOA model, where the evaporation in the chamber was slow. Unlike the model in Section 2.2, the limonene SOA model in this section used an empirical T_g–C^* relationship, which resulted in a much less-diffusive crust. We concluded that a surface crust emerged as lower-volatile compounds accumulated at the particle surface while higher-volatile species evaporated, which explains the near size-independent evaporation.

Environmental Science & Technology

pubs.acs.org/est

Article

Surface Crust Formation Controls Evaporation Kinetics of Secondary Organic Aerosols

Meredith Schervish, Hyun Gu Kang, Lisa M. Wingen, Kieudiem Nguyen, Cheyenne Begay, Jacqueline Wilson, Manish Shrivastava, Yuzhi Chen, John E. Shilling, Nga L. Ng, Ulrich Pöschl, Thomas Berkemeier,* Alla Zelenyuk,* and Manabu Shiraiwa*

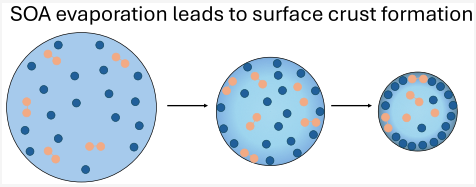
Cite This: *Environ. Sci. Technol.* 2026, 60, 7995−8006

Read Online

ACCESS | Metrics & More | Article Recommendations | Supporting Information

Downloaded via MPI CHEMIE on March 30, 2026 at 14:34:28 (UTC).
See https://pubs.acs.org/sharingguidelines for options on how to legitimately share published articles.

ABSTRACT: Gas-particle partitioning is critical for the evolution of secondary organic aerosols (SOA) in the atmosphere. SOA particles evaporate more slowly than expected at nearly size-independent rates, but the underlying mechanism remains controversial. Here, we apply kinetic multilayer modeling to simulate evaporation of α-pinene SOA, demonstrating that surface crust formation, emerging from accumulation of low-volatility compounds at the particle surface, leads to slow evaporation and reduced size dependence of the evaporation rate. While evaporation induced by decomposition of oligomers would naturally lead to size-independent evaporation rates, we observe and simulate nearly size-independent slow evaporation of polyethylene glycol mixture particles containing polymeric species that do not decompose, confirming the relevance of composition-dependent diffusivity for size-independent, slow evaporation. Slow evaporation of limonene SOA was also observed in environmental chamber experiments, and model simulations demonstrate strong surface crust formation with bulk diffusivity being depressed by up to 5 orders of magnitude compared to the inner bulk. We present experimental evidence using a surface-based mass spectrometry technique that shows that the particle surface becomes enriched in high molecular weight compounds upon evaporation of monomers. Our findings imply that viscous surface crusts may also limit the growth and chemical transformation of SOA particles, influencing their impacts on air quality and climate.



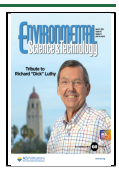
KEYWORDS: *secondary organic aerosol partitioning, phase state, heterogeneous chemistry, kinetic modeling*

INTRODUCTION

Secondary organic aerosols (SOA), formed from oxidation of volatile organic compounds and gas-particle partitioning of the oxidation products, account for a large fraction of atmospheric particulate matter, impacting climate, air quality, and public health.[1,2] The evolution of SOA is a complex multistep process that involves chemical reactions and mass transport in the gas phase, at the particle surface, and in the particle bulk.[2] The multiphase chemistry of SOA is one of the most challenging problems in the current understanding of atmospheric aerosol processes.[3] Despite extensive research efforts, SOA processes and properties still represent major uncertainties in atmospheric models investigating aerosol effects on clouds, radiation, climate, air quality, and public health.[4,5]

Traditionally, SOA particles were assumed to be well-mixed liquid droplets, but laboratory and field measurements have shown that SOA particles can exist in highly viscous semisolid or amorphous solid phase states depending on chemical composition and environmental conditions.[6,7] High viscosity can lead to slow evaporation or condensation, resulting in long equilibration time scales in the gas-particle partitioning of semivolatile species.[8] For example, SOA particles derived from α-pinene and limonene were observed to evaporate very slowly, which was attributed to a highly viscous phase state.[9−11] While slow SOA evaporation was mostly observed at low RH,[11,12] Wilson et al. also observed limited evaporation even at high RH.[9] Notably, SOA evaporation rates were observed to be nearly independent of particle size, which was unexpected, as smaller particles with larger surface area-to-volume ratios should evaporate faster relative to their initial size even prior to reaching sizes small enough for large Kelvin effects. The evaporation kinetics of SOA are influenced by the volatility distribution of the SOA constituents as low-volatility compounds evaporate more slowly,[11,13−15] and by the decomposition of oligomers that precedes the evaporation of more volatile monomers. Oligomers are high molecular weight molecules with low volatility and high viscosity, and can be formed in the gas phase via peroxy radical accretion reactions or in the condensed phase via particle-phase chemistry such as esterification.[16] Some particle-phase oligomers are also

Received: August 10, 2025
Revised: February 17, 2026
Accepted: February 19, 2026
Published: February 27, 2026



ACS Publications © 2026 American Chemical Society

susceptible to decomposition both thermally and chemically on time scales of hours.[17]

Attempts have been made to simulate slow evaporation of SOA with computational models by including slow decomposition of oligomers,[18] by using obstruction theory that treats oligomers as nondiffusing species, and by using reduced mass accommodation coefficients.[14,19] In a complex mixture of organic compounds with different volatilities, evaporation of the more volatile species leads to an increase in the viscosity of the particle over time, as suggested by modeling studies that resolve time-dependent viscosity but assume a homogeneous particle bulk.[11,20] Previous modeling work has shown that during condensation, concentration gradients can persist in viscous particles even beyond the time scale for gas-particle equilibration.[21,22] Therefore, the SOA particle bulk may become heterogeneous in composition and bulk diffusivity upon partitioning, but modeling attempts rarely have been made to simulate SOA evaporation by resolving bulk profiles, often due to the computational demands of such simulations.[18,23,24] Despite its importance for SOA fate and burden in the atmosphere, there is still a lack of mechanistic and process-level understanding of SOA evaporation including the relative contribution of viscous phase state and oligomer decomposition and the potential role of particle inhomogeneity on evaporation kinetics.[23,25]

In this work, we present new experimental results on evaporation of hexaethylene glycol (HEG, $C_{12}H_{26}O_7$), where we observe the expected size-dependent evaporation, and polyethylene glycols (PEGs, mixtures of polymers with a range of chain lengths with different average molecular weights), which exhibit nearly size-independent evaporation. By applying a kinetic multilayer model that resolves the time-dependent evolution of radial bulk diffusivity in radial profiles, we demonstrate that the diminishment of size-dependent evaporation is caused by the faster increase in viscosity of smaller particles due to faster relative change in composition during the evaporation of compounds with higher volatility and accumulation of compounds with lower volatility. We then simulate the evaporation of α-pinene and limonene SOA with a higher viscosity at the onset of evaporation, showing the formation of a surface crust made up of lower volatility compounds. Finally, we present experimental evidence of surface crust formation by measuring the evolution of surface composition upon evaporation of α-pinene SOA.

MATERIALS AND METHODS

PEG and SOA Particle Generation and Analysis

PEG 200, 300, and 400 particles were generated by atomization of the neat liquids, while PEG 1000 particles were generated by atomization of PEG 1000 solution in nanopure water and subsequently dried using a silica gel diffusion dryer. α-pinene SOA particles were formed by homogeneous nucleation initiated by injecting 200 ppb of α-pinene, ~500 ppb of ozone, and ~250 ppm of cyclohexane, used as an OH scavenger, into a clean 100 L Teflon bag filled with zero air. Particles were size-selected with a differential mobility analyzer, passed through two activated charcoal denuders, and loaded into the 7 L stainless steel evaporation chamber, partially filled with activated charcoal. Activated charcoal was used to continuously remove gas-phase organics and avoid the gas−wall repartitioning. Low particle number concentrations in the chamber (~10−150 particles cm^{-3}) provide the means to follow room-temperature evaporation kinetics of individual size-selected aerosol particles. A single-particle mass spectrometer, SPLAT II or miniSPLAT, was used to measure vacuum aerodynamic diameter (d_{va}), density, shape, and mass spectra of individual particles as a function of evaporation time, as described elsewhere by Vaden et al.[10,26] Particle evaporation kinetics was quantified by measuring changes in particle d_{va} with 0.5% accuracy and precision.

KM-GAP

The kinetic multilayer model of gas-particle interactions in aerosols and clouds (KM-GAP) is used to simulate the evaporation of different organic aerosol particles. The details of KM-GAP can be found in previous work,[27] so here we will give a brief description as well as the updates and specific implementation in this study. KM-GAP explicitly treats the processes of gas-phase diffusion, adsorption and desorption, surface-bulk exchange, and bulk diffusion within the particle. KM-GAP consists of a gas phase, a near-surface gas phase, and a particle phase with a sorption layer, a near-surface bulk layer, and several bulk layers. The number of bulk layers is set such that the outer half of the particle volume initially consists of layers of 1 nm thickness for high resolution near the surface, while the inner half of the particle volume contains 5 layers for computational efficiency. Gas-phase diffusion from near-surface bulk to the gas phase is resolved, and vapor loss to activated charcoal in the evaporation chamber is treated as a first-order irreversible process. KM-GAP does not require the simplification of assumptions about steady-state conditions and homogeneous radial mixing, which are often applied in other aerosol models. KM-GAP allows for the implementation of a time-dependent, composition-dependent diffusivity in each layer of the particle bulk.

We simulated the composition-dependent diffusivities by assigning glass transition temperature values to each individual species and assigning the T_g in each layer using a mass fraction weighted average. The viscosity of each layer is then calculated using the modified Vogel−Fulcher−Tammann (VFT) equation and subsequently the diffusivity in each layer is calculated using the Stokes−Einstein equation[28,29] (see Supporting Information (SI) for details). We carried out an additional PEG 400 evaporation simulation using a number fraction-based approach as in Vignes et al., discussed in the SI to show a similar fit can be achieved using this method (Figure S5).

For simulation of the PEG mixtures and α-pinene SOA evaporation experiments, the total number concentration of monodisperse particles was set to 100 cm^{-3} to match the low number concentrations (10−150 cm^{-3}) in those experiments. A set of parameters for each species were optimized using the Monte Carlo Genetic Algorithm (MCGA) as described in the SI.[30] These parameters include the glass transition temperature, volatility, and initial mass fractions for four semivolatile and one nonvolatile species (Tables S1 and S2). In these cases, the volatility was optimized separately independently from the glass transition temperature to allow for variability not provided in a parametrization given the good agreement of the best fit with measured glass transition temperature values as discussed in the Results and Discussion section. For the α-pinene SOA evaporation simulation, the first-order rate constant for oligomer decomposition was also determined by fitting.

The KM-GAP model for simulation of limonene oxidation uses a chemical mechanism based on Berkemeier et al.,[30] which in turn was modified after the Master Chemical Mechanism,[31] incorporating gaseous dimer formation from $RO_2 + RO_2$ and oligomerization in the particle phase. Product volatility is described using a volatility basis set (VBS) approach.[32] We modify the model and chemical mechanism from Berkemeier et al. with an aging mechanism in which reaction of NO_3 with a gas-phase organic oxidation product reduces the species' volatility by 2 orders of magnitude.[33,34] We further simplify the product VBS by combining organonitrates and non-nitrated organics into a single volatility distribution. Further details of the model, as well as a full list of model optimization parameters, are given in the SI (Table S3).

SOA Surface Composition Measurements

Ozonolysis of α-pinene was carried out in the presence of glutaric acid particles, which act as both a condensation surface and a soft ionization matrix. The evolution of the SOA coating during evaporation was measured with matrix-assisted ionization in vacuum (MAIV)-mass spectrometry. Particles were generated in a flow reactor with a volume of 1.6 L (4.6 cm ID x 95 cm length). A syringe pump

https://doi.org/10.1021/acs.est.5c11018
Environ. Sci. Technol. 2026, 60, 7995−8006

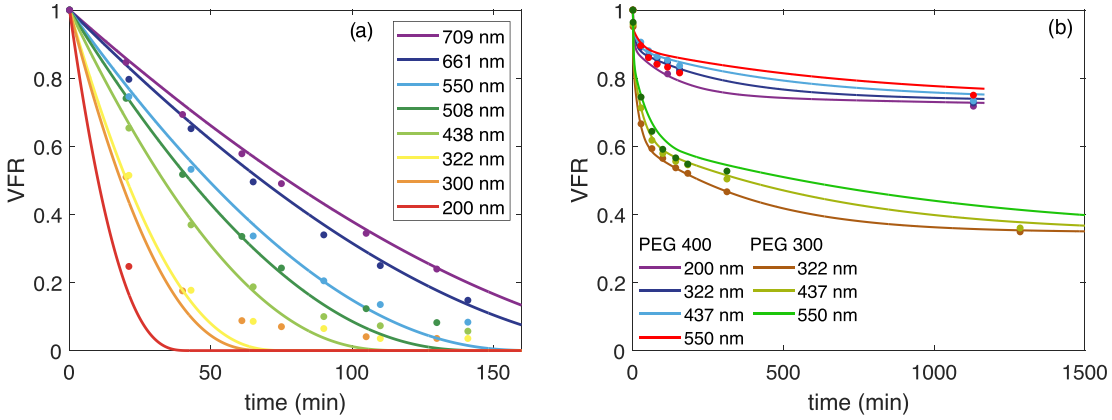


Figure 1. (a) Volume fraction remaining (VFR) during evaporation of size-selected single-component HEG particles in the evaporation chamber (measured data points) and simulated using KM-GAP (lines). (b) VFR during evaporation of size-selected PEG 300 and PEG 400 particles in the evaporation chamber (measured data points) and simulated using KM-GAP (lines) with a dynamic diffusivity.

was used to introduce liquid (+)-α-pinene (Sigma-Aldrich, ≥99%) into a flow of 0.7 L min^{-1} clean air to evaporate the liquid before it entered the flow system. α-pinene was further purified before use by passing the liquid through a small column of alumina powder to remove potential oxidation products. Ozone was generated by flowing oxygen (Praxair, 99.993%) through a mercury Pen-Ray lamp (UVP, model 11SC-2) and introduced at a rate of 0.3 L min^{-1}. Glutaric acid (GA) matrix particles used for MAIV mass spectrometry were atomized from a solution of 30 mM GA (Sigma-Aldrich, 99%) in water (Nanopure, 18 MΩ·cm) and dried with two silica gel diffusion dryers (TSI, model 3076) before entering the flow system at 3.5 L min^{-1}. The initial concentrations of α-pinene and O_3 were both ~7 ppm in a total air flow of 4.5 L min^{-1}.

While uncoated GA matrix particles exhibit a number of peaks (Figure S15a), SOA particles without the matrix are not detected with MAIV (Figure S15b) and α-pinene vapors alone are also not detected (Figure S15c). MAIV measurements in the absence of GA matrix particles used a flow of 3.5 L min^{-1} of clean air in place of the particle flow to maintain the same total flow rate of 4.5 L min^{-1}. Evaporation of the particles was carried out by passing the particles through several honeycomb charcoal denuders (Novacarb; Mast Carbon, Ltd. and Aerodyne) at room temperature. The evaporation times achieved at this flow rate are on the order of seconds.

RESULTS AND DISCUSSION

PEG Evaporation

Evaporation experiments were performed at room temperature in an evaporation chamber and particle size was measured periodically using a single-particle mass spectrometer.[10] Figure 1a shows the observed volume fraction remaining (VFR, the ratio of particle volume to initial particle volume, $V_p/V_{p,0}$) of HEG particles with different initial particle diameters varying from 200 to 709 nm. HEG is composed of a semivolatile species with a measured volatility from literature (C^*) of 3 μg m^{-3} and molecular weight of 282 g mol^{-1}, adopting a liquid phase state.[35] As expected in this single-component and liquid system, we observe size-dependent evaporation rates, where the relative change of the particle volume $\left(\frac{dVFR}{dt}\right)$ is faster for smaller particles than for larger particles, similar to the observations of evaporation kinetics of liquid dioctyl phthalate particles measured using the same experimental approach.[10] Thus, while larger particles will lose mass and volume faster due to their larger surface area, smaller particles will exhibit a faster relative change in volume due to their larger surface-area-to-volume ratios.

We simulated the observed evaporation kinetics using the kinetic multilayer model of gas and particle interactions (KM-GAP), which explicitly treats the processes of mass transport between the gas and particle phases.[27] The particle bulk is divided into multiple layers to simulate mass transport based on the bulk phase diffusivity, which is assumed to be 10^{-8} cm^2 s^{-1}, characteristic of liquid particles. As shown by solid lines, the model reproduces the size-dependent evaporation very well. As HEG particles are only composed of a single species, evaporation does not lead to a change in viscosity, and evaporation is driven by the volatility and surface area, with smaller particles evaporating more rapidly due to their larger surface area-to-volume ratios.

We also investigate the evaporation of multiple PEG systems, including PEG 200, PEG 300, PEG 400, and PEG 1000, which are mixtures of polyethylene glycol polymers with average molecular weights of 200, 300, 400, and 1000 g mol^{-1}, respectively. These multicomponent mixtures include larger polymers that do not decompose at or near room temperature.[36] Figure 1b shows the evaporation kinetics of PEG 400 and PEG 300, which exhibit fast initial evaporation, followed by slow evaporation over time. PEG 300 has a similar average molecular weight to HEG; however, the PEG 300 particles evaporate to ~50% of their initial volume after 5 h and to ~35% of their initial volume after ~1 day, in contrast to HEG particles that evaporate to 0−10% of their initial volume in 50−150 min, depending on initial size. PEG 200 particles evaporate to ~10% of their initial volume within 2−3 h, while PEG 400 particles evaporate to ~80% of their initial volume, and PEG 1000 particles evaporate only to approximately 90% of their initial volume in the same time frame (Figure S1). Size-selected PEG 200, PEG 300, PEG 400, and PEG 1000 particles are all observed to evaporate with much smaller size dependence compared to HEG. Especially stark is the similarity in the change in VFR for the 322 and 550 nm PEG 300 particles compared to the same sizes of HEG. Given the similar average molecular weights of PEG 300 and HEG, we would expect similar average volatilities, which highlights the importance of the multicomponent nature of PEG 300 (i.e., the presence of longer polymers) in reducing both the magnitude and size dependence of the evaporation rate. Note that opposed to the relative volume evaporation rates $\left(\frac{dVFR}{dt}\right)$, the absolute volume change rates $\left(\frac{dV_p}{dt}\right)$ of all investigated

https://doi.org/10.1021/acs.est.5c11018
Environ. Sci. Technol. 2026, 60, 7995−8006

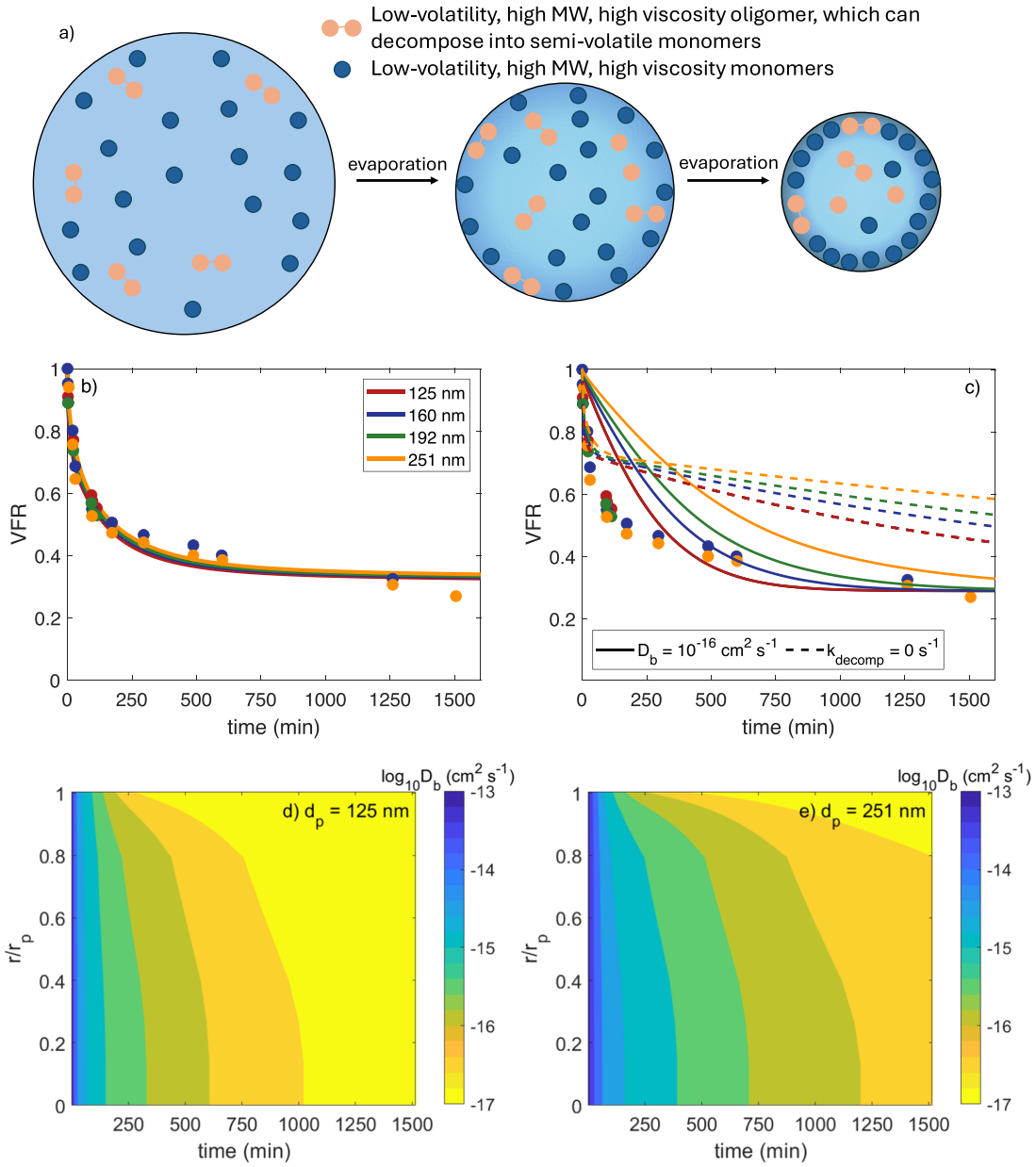


Figure 2. (a) Schematic of evaporation of SOA with low-volatility monomers (dark blue circles), semivolatile species (light blue), and oligomers that may decompose to semivolatile compounds (orange, shown as dimers). As evaporation proceeds, the particle shrinks due to volatilization of the semivolatile species and the low-volatility compounds are left at the surface forming a crust. (b, c) Volume fraction remaining (VFR) during α-pinene SOA evaporation for four initial particle sizes. Data points are from Vaden et al. Panel b shows the best fit with dynamic diffusivity and oligomer decomposition. Panel c shows cases with a constant diffusivity (D_b = 10^{-16} cm^2 s^{-1}) and oligomer decomposition (solid lines) and no oligomer decomposition with a dynamic diffusivity (dashed lines). Different colored points and lines are for evaporation experiments of different particles sizes. (d, e) Time evolution of radial profiles of bulk diffusivity upon evaporation of α-pinene SOA particles with initial particle diameter of (d) 125 nm and (e) 251 nm, as simulated by KM-GAP. The y-axis (r/r_p) is the distance from the particle center normalized by the particle radius (r/r_p = 1 at the surface).

particles are clearly size-dependent as shown in Figure S2. A detailed discussion of the evaporation kinetics of HEG, PEG 300, and PEG 400 particles is given in the SI and shown in Figures S2−S4.

The solid lines in Figure 1b show modeling results obtained with KM-GAP, which captures the evaporation kinetics with reduced size dependence for PEG 300 and PEG 400 particles. We treat PEG mixtures as four semivolatile species and one nonvolatile species each with different volatility (C^*) and glass transition temperature (T_g). The initial mole fractions of these five species, as well as their C^* and T_g, were determined by fitting the model to the observations using the Monte Carlo Genetic Algorithm.[30] The estimated volatilities of PEG 400 components were in the range of ∼0.007 to 105 μg m^{-3}, which is consistent with measured range of volatilities.[37] PEG 300 is overall more volatile and less viscous than PEG 400, consistent with the lower average molecular weight of PEG 300. The estimated T_g values are in the range of 117−220 K, corresponding to an initial bulk diffusivity of ∼10^{-7} cm^2 s^{-1} for PEG 300 and ∼10^{-8} cm^2 s^{-1} for PEG 400, which would

https://doi.org/10.1021/acs.est.5c11018
Environ. Sci. Technol. 2026, 60, 7995−8006

correspond to a liquid phase state consistent with measurements of PEG 300 and PEG 400 viscosity at room temperature.[38,39]

We find that in smaller particles, bulk diffusivity decreases more rapidly and thus leads to an earlier reduction in evaporation rate compared to the larger particles, which causes the relative evaporation rates of these particles to become similar. Over ∼20 h of evaporation, the average diffusivity of each PEG 400 particle decreases by approximately 1 order of magnitude, with the smaller particles becoming more viscous more rapidly than the larger particles (Figure S6). The different behaviors of the rates of change of particle diameter for the multicomponent PEG 300 and PEG 400 systems compared to the single-component HEG system, shown in Figure S2, indicate that the composition change of the multicomponent systems drive the differences between the evaporation behavior of HEG in Figure 1a and PEG 300 and PEG 400 in Figure 1b. HEG particles exhibit the same evaporation behavior at a specific size, independent of initial size of the particle. PEG 300 and PEG 400 particles evaporate differently at the same size depending on their initial size because of different compositions at that size. When the bulk diffusivity is fixed throughout evaporation and homogeneous throughout the particle bulk, even allowing for different volatilities and mass fractions does not lead to a reasonable fit, and the relative volume change depends more on particle size, as shown for PEG 400 particles in Figure S8. Thus, composition-dependent diffusivity was essential to fully reproduce the experimental data with the kinetic model.

α-Pinene SOA Evaporation

We simulate the observed evaporation kinetics of SOA generated via α-pinene ozonolysis.[10] A schematic of evaporation with oligomer decomposition is shown in Figure 2a, showing the surface enrichment of high viscosity compounds upon evaporative depletion of low viscosity compounds. The measurements of Vaden et al. show that α-pinene SOA initially evaporates rapidly, losing about 10% volume in the first few minutes.[10] Evaporation then proceeds more slowly with the particles losing approximately 50% of their volume after ∼2 h, with about 30% of the volume fraction remaining (VFR) after 24 h (Figure 2b). The model estimates that α-pinene SOA contains 29% of nonvolatile species by mass, leading to the convergence of all of the different initial size particles to the same VFR after ∼10 h (Figure 2b). While the PEG systems shown in Figure 1b will also converge to their nonvolatile fraction, we observe more rapid convergence in the α-pinene SOA system due to oligomer decomposition. This relative evaporation rate was observed to be nearly size-independent for particles with diameters between 125 and 251 nm. Using KM-GAP, we simulate the evaporation of the α-pinene SOA by resolving the dynamic evolution of bulk diffusivity profiles and oligomer decomposition.

As α-pinene SOA is known to contain oligomers, the effect of oligomer decomposition must be considered. In a particle with no mass transport limitations, the evaporation rate may be controlled by the oligomer decomposition rate, which should be size-independent. Here, oligomer decomposition is treated as a first-order process with a low-volatility oligomer (species 4 in Table S1) decomposing into two semivolatile species (species 1 and 2 in Table S1). This was done so as not to increase the number of species adding additional complexity to an already multiparameter fit. It should be noted that due to the wide range of measured SOA oligomer decomposition rates and product pathways and with no measurements in the observations to constrain this process, this simplified approach represents a limitation in this work. Note that we found little to no difference in the fit by instead choosing the two middle volatility species as the decomposition products, indicating that the precise value of the decomposition product volatility was not critical for achieving a good model fit. We represent α-pinene SOA with four semi- to low-volatility species and one nonvolatile species by assigning volatility, glass transition temperature, and initial mass fraction (see Table S1). The best fit reproduces the full time series with slow evaporation at later times due to increased bulk diffusion limitations and slow evaporation of lower volatility species. A zoom-in of the initial 200 min of evaporation is shown in Figure S9.

The fit parameters for this case are broadly consistent with experimental measurements for the α-pinene SOA. T_g for the monomer species are estimated to be in the range of 187−236 K and those for the oligomer species are in the range of 250−301 K, which is consistent with the T_g values measured and predicted for α-pinene SOA species.[29,40,41] Given this good agreement and the variability in T_g values for species with a given C^0 value, we optimized these parameters separately for α-pinene SOA. The best fit volatility distribution contains almost 75% low-volatility to nonvolatile species by mass, with the roughly 25% remaining mass being semivolatile species. The high mass fraction of low-volatility species is consistent with previous studies of volatility and oligomer content for α-pinene SOA.[42,43]

Figure 2b shows the best fit case for α-pinene SOA evaporation, and Figure 2d,e shows the evolution of the bulk diffusivity over the course of evaporation for the smallest and largest particle size. All particles have an initial bulk diffusivity of 4×10^{-13} cm^2 s^{-1}, characteristic of a semisolid phase state, which facilitates fast initial evaporation of semivolatile species. This process leaves behind oligomers and low-volatility species at the surface, leading to a decrease in bulk diffusivity, as shown in the schematic in Figure 2a. In contrast to the PEG 400 case, the lower initial D_b of α-pinene SOA leads to significant mass transfer limitations in the particle as it evaporates, resulting in large inhomogeneities in the radial composition profile of the particle bulk. We refer to the region at the surface with low bulk diffusivity and high viscosity as a "surface crust," which hinders semivolatile species in the inner particle bulk from evaporation. Note that this "surface crust" is distinct from an organic shell in a phase-separated core−shell particle, as it requires organic phase heterogeneities in composition, unlike in a phase-separated particle where the organic phase may be fully homogeneous. Additionally, a surface crust may be formed through fully kinetic processes rather than the thermodynamic phase separation of immiscible species. We calculate the time for the outermost layer to reach a diffusivity below 10^{-15} cm^2 s^{-1} as previous experimental and computational work observed significant bulk diffusion limitation to partitioning with bulk diffusivities below ∼10^{-15} cm^2 s^{-1}.[8,12,44,45] This diffusivity is achieved at the surface in ∼85 and ∼101 min for the 125 and 251 nm particles, respectively (Figure 2d,e). The reduced size dependence of the relative evaporation rate is due to a surface crust forming at different times for different particle sizes: small particles evaporate quickly leading to more rapid surface enrichment in high viscosity compounds, limiting additional evaporation. Larger particles will evaporate slower leading to slower surface

https://doi.org/10.1021/acs.est.5c11018
Environ. Sci. Technol. 2026, 60, 7995−8006

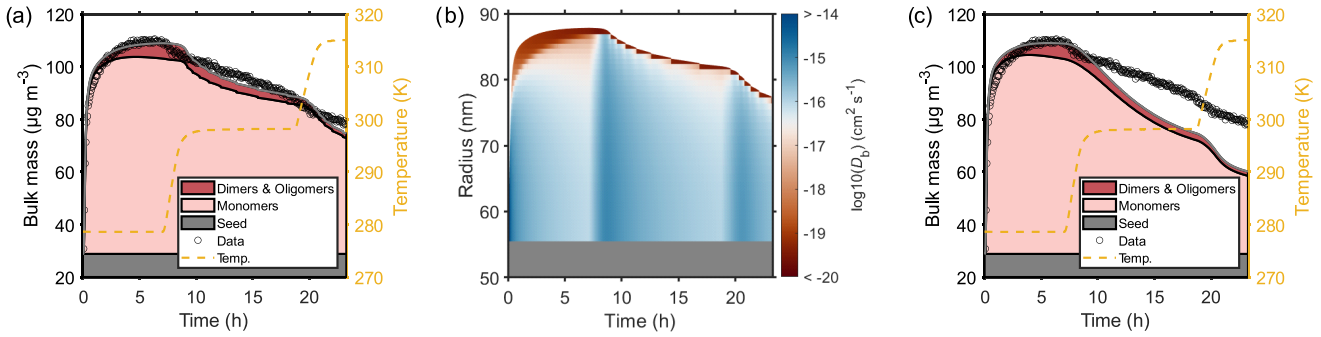


Figure 3. Modeled formation and evaporation of limonene SOA in an environmental chamber experiment with varying temperature. Panel (a) shows SOA mass concentrations, (b) shows the particle radius, and (c) shows faster particle evaporation when the bulk has a uniform $D_{b,298K}$ of 1×10^{-16} cm^2 s^{-1}. Colors in panel (a and c) distinguish monomers and dimers/oligomers and in panel (b) indicate the composition-dependent bulk diffusion coefficient, log 10(D_b). The model suggests that a layer of low diffusivity at the particle surface can be formed, preventing volatile species from evaporating.

enrichment, allowing them to catch up to the smaller particles. At the onset of surface crust formation in the 251 nm particles, the innermost particle bulk layer has a diffusivity ~5 times higher than the outermost bulk layer and then will grow to over an order of magnitude difference within a few minutes of surface crust formation in each initial size case. Once a surface crust forms, different diffusivities for different particle sizes in the more viscous outer layers control the evaporation rate. It should be noted that the whole particle bulk viscosity has also increased gradually with the surface crust formation, leading to a gradient in particle bulk diffusivity near the surface (Figure 2d,e). As evaporation proceeds to longer time scales, some semivolatile species trapped in the particle bulk can reach the surface and evaporate, leading to more viscous inner particle bulk layers. Inhomogeneity in the particle bulk persists even after 24 h, consistent with experimental observations of semivolatile species trapped in α-pinene SOA during evaporation.[9,44] At its minimum, the surface diffusivity of the 251 nm particles reaches ~10^{-18} cm^2 s^{-1} after 1500 min of evaporation. The innermost layer at this time has a diffusivity approximately a factor of 50 higher, and diffusion limitations then persist throughout the entire particle bulk, leading to hindered mass transport even in the innermost layers. While limited evaporation throughout the evaporative process is due to all of these factors in combination and reproducing the observations requires an increased viscosity of the entire particle bulk over time, the diffusivity is lowest at the surface, and evaporation is controlled by transport to the particle surface.

In Figure 2c in solid lines, we use the volatilities and mass fraction from the best fit case shown in Figure 2b, but fix the diffusivity to be 10^{-16} cm^2 s^{-1} to be consistent with previous measurements of α-pinene SOA viscosity at <5% RH.[44,46] The presence of bulk diffusion limitations and the large proportion of low-volatility species still let the model match the measurements at long observation times, but the size-independent evaporation phenomenon cannot be reproduced at this viscosity, despite using the same parameters for oligomer content and decomposition. A case with a fixed diffusivity of 10^{-15} cm^2 s^{-1} is shown in the Figure S9c, but still does not reproduce the measurements. In Figure 2c in dashed lines, composition-dependent diffusivity is implemented but the oligomer decomposition rate constant is set to 0 s^{-1} to remove the effect of oligomer decomposition. Evaporation is rapid initially as higher volatility species evaporate but slows down once these are depleted leading to slower evaporation of lower volatility species. The extent of evaporation is hindered as oligomers are low volatility and do not fully evaporate on this time scale. Despite this lack of agreement, there is still a reduction in the size dependence with the implementation of a composition-dependent diffusivity compared to the fixed diffusivity. The results in Figure 2c indicate that both oligomer decomposition and the resulting changes in bulk diffusivity are needed to accurately simulate the evaporation of α-pinene SOA particles.

Overall, we show that surface crust formation and oligomer decomposition, in concert, can explain the observed, limited, and nearly size-independent evaporation behavior of α-pinene SOA at low RH. While these low RH conditions are uncommon in the atmosphere, observations of evaporation at high RH show similar size-independence, indicating that a low viscosity of α-pinene SOA at the onset of evaporation due to the high RH can also lead to size-independent evaporation,[9] similar to the PEG system. Experimental results have observed limited and size-independent evaporation for other systems as well, including limonene ozonolysis SOA at both low and high RHs, indicating that surface crust formation is likely to occur in other types of SOA.[9] Other studies, however, have observed that diffusion limitations diminish at high RH, leading to rapid evaporation of SOA.[11,12,17,47] While not the direct focus of this work, treating a heterogeneous particle bulk with dynamic diffusivity is key to resolving this discrepancy in observations.

Limonene SOA Evaporation

Slow evaporation of SOA was also observed in the environmental chamber experiments of the NO_3 radical-initiated oxidation of limonene.[18,48] In these experiments, the chamber temperature was increased in two steps from 5 to 25 °C and from 25 to 42 °C over the course of 23 h. Evaporation of limonene SOA mass did not follow the temperature−time-profile, which was explained by slow decomposition of particle-phase oligomers in previous model simulations.[18] We use KM-GAP to simulate the growth and evaporation of SOA in the limonene + NO_3 chamber experiments and test whether slow diffusion and surface crust formation would explain the observed SOA growth and evaporation kinetics.

We fit a range of KM-GAP model parameters, including a volatility basis set with 8 bins and reaction rate coefficients of particle-phase oligomerization, to match model outputs of SOA mass to the experimental data measured by a Scanning

https://doi.org/10.1021/acs.est.5c11018
Environ. Sci. Technol. 2026, 60, 7995−8006

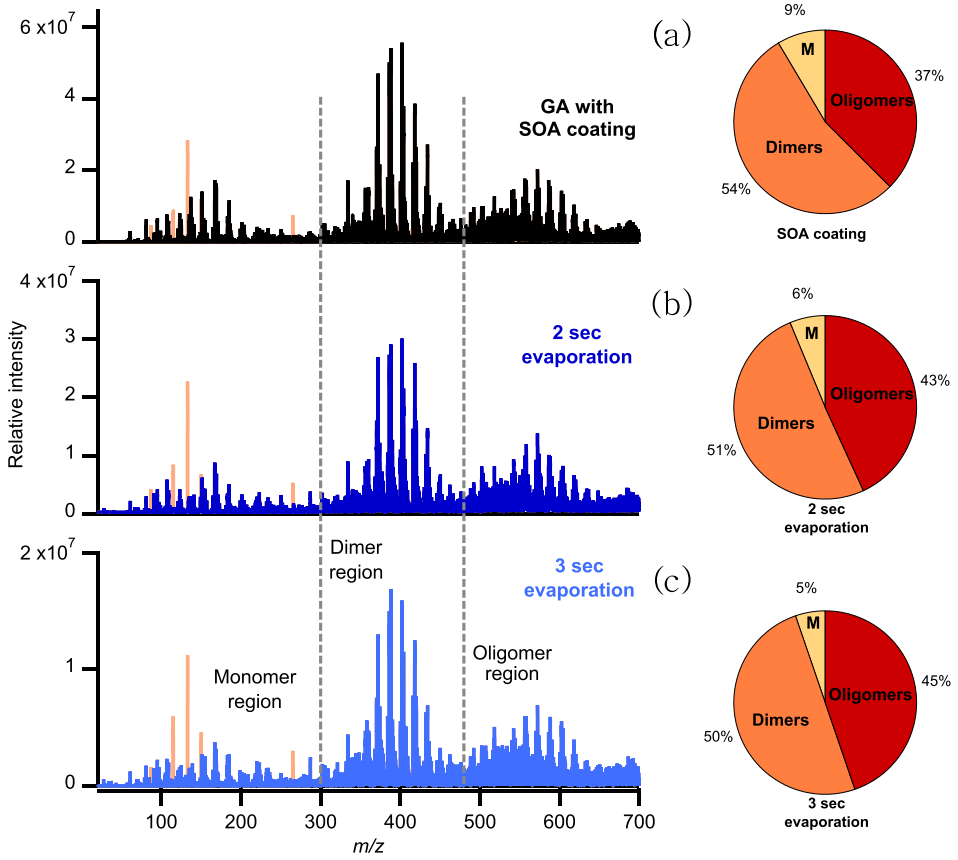


Figure 4. MAIV mass spectra of matrix particles coated with α-pinene SOA products. Dashed lines indicate the monomer (M), dimer, and oligomer regions after evaporation times of (a) 0 s, (b) 2 s, and (c) 3 s. Pie charts to the right of each spectrum show the corresponding fraction of each region remaining in the SOA coating. Glutaric acid matrix peaks in each spectrum are indicated in light orange and are not included in the pie chart fractions.

Mobility Particle Sizer (SMPS). We correct the SMPS particle size distributions for wall loss using a particle size-dependent correction method and explicitly model vapor-wall partitioning to account for gas-wall-loss effects.[49,50] The model assumes that the particles have a uniform effective radius. The initial particle size is calculated using the seed particle mass and number concentrations. Composition-dependent diffusivity is calculated using a polynomial relationship between T_g and log(C^*) as proposed by Li et al.[51] The model captures the time evolution of particle growth and evaporation (Figure 3a) and shows strong surface crust formation throughout the simulation, with diffusion coefficients in the first bulk layer being depressed by up to 5 orders of magnitude compared to the inner bulk layers of the particle (Figure 3b). The model finds that SVOCs evaporating from the surface result in low-volatility monomers ($C^* \leq 0.1$ μg m^{-3}), dimers, and oligomers accruing at the surface, forming a crust (Figure 3b). If the model is run with uniform $D_{b,298K}$ of 1×10^{-16} cm^2 s^{-1} (Figure 3c) a crust does not form and particles equilibrate faster, which shows that a surface crust increases equilibrium time scales. Once again, as in the α-pinene SOA case, the relatively low initial bulk diffusivity of limonene SOA can lead to a sufficiently low surface diffusivity to form a large gradient in bulk diffusivity, in contrast to the less viscous PEG mixtures. Note that bulk diffusivity generally decreases throughout the particle during the constant temperature phases and increases during temperature ramping phases, providing evidence that a surface crust can form even when evaporation is driven by an increase in temperature rather than dilution of the surrounding air at room temperature, as in the α-pinene SOA evaporation case.

To address whether the experimental data can also be reconciled without oligomerization, we performed a global model optimization with oligomerization disabled. We find that the model can fit to the data well while also exhibiting crust formation (Figure S12). However, the model is also able to achieve fits without crust formation when using a modified T_g and C^* relationship (Figure S13). The strength of surface crust formation in this system is a consequence of the slope in the T_g vs C^* relationship, with a stronger dependence leading to stronger crust formation. This highlights the need for future research into the relationship between volatility and viscosity. Nevertheless, the limonene SOA model with the established relationship between T_g and C^* shows clear formation of a surface crust.[51] Prior studies have found additional evidence for nonequilibrium partitioning of SOA from limonene + NO_3.[52] We find that surface crust formation is a plausible explanation for the slow evaporation of limonene SOA in environmental chamber experiments, which was previously only possible using oligomer decomposition as the sole cause. Future experiments with size-dependent evaporation should help quantify the impacts of oligomerization and surface crust formation.

https://doi.org/10.1021/acs.est.5c11018
Environ. Sci. Technol. 2026, 60, 7995−8006

Experimental Evidence for Surface Crust Formation

To provide further experimental evidence of surface crust formation, matrix-assisted ionization in vacuum—mass spectrometry (MAIV-MS) was used to detect the surface composition of α-pinene SOA condensed onto matrix particles in real-time before and after passing the particles through carbon denuders.[53] This unique technique allows us to probe only the surface and near-surface-bulk composition of SOA particles without being influenced by inner bulk composition. Details on the MAIV-MS technique are provided in the Supporting Information. As shown in Figure 4, the low molecular weight condensed-phase SOA products in the monomer region initially contribute 9% of the total intensity (Figure 4a), while after evaporation at room temperature for 3 s, low molecular weight species decrease to about half their initial value (Figure 4c). The relative peak intensities in the higher molecular weight dimer and oligomer regions are not significantly impacted during evaporation, and the oligomer contribution to the total spectrum increases from 37% to 45% (Figure 4c). While the short evaporation time scale does not result in decreases in diameter (Figure S14), it demonstrates a change in surface composition toward a more oligomeric coating. As the film composition evolves during evaporation, there is a progressive loss of total ion intensity from both the matrix particles and α-pinene oxidation products (Figures 4 and S16), suggesting that the composition of the remaining coating inhibits underlying matrix evaporation and ionization. These experimental results clearly demonstrate the transition to a higher molecular weight surface composition upon the rapid evaporation of low molecular weight compounds and the accumulation of high molecular weight compounds.

Implications

In this work, we provide evidence for surface crust formation upon the evaporation of multiple SOA over a wide range of time scales, causing nearly size-independent evaporation kinetics. The formed surface crust should affect subsequent condensation and growth of the particles. Chen et al. observed that isoprene SOA, that was evaporated for 20 min and subsequently exposed to fresh isoprene semivolatile organic compounds (SVOCs), grew much slower than the initial SOA formation rate.[20] Using KM-GAP, we achieve good agreement between observed and simulated organic aerosol concentrations of isoprene SOA when a surface crust is formed during evaporation (Figure S17 and Table S4). The subsequent growth of isoprene SOA was reproduced by considering dynamic evolution of bulk diffusivity; particle growth is initially hindered by the surface crust, but the growth is facilitated as the surface becomes softened upon condensation of SVOCs acting as plasticizers.[23,54] If particles are assumed to be homogeneously liquid or semisolid with constant diffusivity after evaporation, condensation can be significantly over- or underestimated, respectively, as shown in Figure S17. In Chen et al., growth of isoprene SOA after evaporation is reproduced well by assuming a constant diffusivity that is lower than that during the initial growth period. In this work, we show that size-independent evaporation can be explained by surface crust formation during the evaporation of a range of multicomponent systems. Thus, it is likely that a surface crust was formed in the isoprene SOA experiments by Chen et al. as well. Garofalo et al. observed the appearance of a bimodal size distribution during the oxidation of catechol by O_3 and NO_3, but they were unable to determine whether the different growth rates of different size were due to thermodynamic immiscibility between the oxidation products or kinetic limitations at the surface[55]: in this case, condensation might have led to particle-phase heterogeneities with surface crust formation. A proper consideration of particle heterogeneity, composition-dependent diffusivity, and thus the potential for surface crust formation is necessary to accurately simulate all aspects of SOA evolution beyond just total mass; further studies are warranted to elucidate the effect of surface crust on the particle size distribution dynamics and chemical composition of SOA particles.

The nearly size-independent and slow evaporation of SOA particles has implications for the probability of small particles remaining active as cloud condensation nuclei (CCN). We show that small particles can become more viscous or form a surface crust more rapidly than larger particles, limiting further evaporation. This will allow small particles to survive during atmospheric transport and dilution. Additionally, Zaveri et al. showed that diffusion limitations in larger particles can facilitate growth of small particles to CCN-relevant sizes, impacting cloud formation and precipitation.[56]

In addition to evaporation, a surface crust can also be formed due to heterogeneous reactions, as shown by several previous studies. Particle viscosity heterogeneity and the formation of viscous surfaces have been observed during ozonolysis of oleic acid particles via fluorescence lifetime imaging microscopy[57,58] and Raman microscopy.[59] Kinetic modeling has suggested that heterogeneous ozonolysis of fatty acid particles and films leads to solidification and crust formation at the particle surface.[60] Similarly, it was demonstrated that reactive uptake of ammonia by α-pinene SOA particles resulted in the formation of ~4 nm thick solid crust that inhibited further ammonia uptake and prevented coagulating particles from coalescing for over 2 days; a depth-profiling approach was used to demonstrate the differences in composition, viscosity, and volatility of crust as compared to the particle inner volume.[45] Multiphase reactivity of polycyclic aromatic hydrocarbons (PAHs) against ozone was shown to be controlled by phase separation to form a highly viscous surface layer that causes bulk diffusion limitations.[61] The surface crust and high viscosity of SOA can protect PAHs from further multiphase degradation and evaporative loss,[62,63] facilitating a long-range transport as has been demonstrated by chemical transport modeling.[64,65]

Ozone uptake by biomass burning organic aerosols (BBOA) can lead to whitening of brown carbon and this time scale can be extended with the increasing viscosity of the outer hydrophobic shell.[66] Limited ozone uptake was observed upon photoirradiation of BBOA due to an increase of particle viscosity.[67] It has also been shown that exposure to UV irradiation and photoaging can increase SOA particle viscosity substantially.[68] BBOA has been observed to contain oligomers generated through particle-phase chemistry.[69] Dilution in biomass burning plumes causing evaporation of semivolatile species could therefore lead to surface crust formation and subsequent hindering of whitening of brown carbon in the particle bulk. Thus, surface crust formation may impact atmospheric loading of aerosol particles and the CCN budget. While our work focuses on evaporation-driven surface crust formation which is likely to occur via atmospheric dilution, surface crust formation may also occur under a broad array of atmospheric processes including heterogeneous and multiphase reactions.[55,61] Further laboratory experiments, field

https://doi.org/10.1021/acs.est.5c11018
Environ. Sci. Technol. 2026, 60, 7995−8006

observations, and large-scale chemical transport modeling are required to probe and quantify the extent of such effects in future studies.

■ ASSOCIATED CONTENT

Supporting Information

The Supporting Information is available free of charge at https://pubs.acs.org/doi/10.1021/acs.est.5c11018.

Includes additional description of methods, analysis of evaporation rates of PEG particles, and simulation of isoprene SOA condensation and evaporation (PDF)

■ AUTHOR INFORMATION

Corresponding Authors

Thomas Berkemeier − *Multiphase Chemistry Department, Max Planck Institute for Chemistry, Mainz 55128, Germany;* orcid.org/0000-0001-6390-6465; Email: t.berkemeier@mpic.de

Alla Zelenyuk − *Pacific Northwest National Laboratory, Richland, Washington 99354, United States;* orcid.org/0000-0002-0674-0910; Email: Alla.Zelenyuk-Imre@pnnl.gov

Manabu Shiraiwa − *Department of Chemistry, University of California, Irvine, California 92697, United States;* orcid.org/0000-0003-2532-5373; Email: m.shiraiwa@uci.edu

Authors

Meredith Schervish − *Department of Chemistry, University of California, Irvine, California 92697, United States;* Present Address: Department of Veterinary Physiology and Pharmacology, College of Veterinary Medicine and Biomedical Sciences, Texas A&M University, College Station, Texas 77843, United States; orcid.org/0009-0002-3365-9007

Hyun Gu Kang − *Multiphase Chemistry Department, Max Planck Institute for Chemistry, Mainz 55128, Germany;* orcid.org/0000-0002-3320-9447

Lisa M. Wingen − *Department of Chemistry, University of California, Irvine, California 92697, United States;* orcid.org/0000-0001-5847-9913

Kieudiem Nguyen − *Department of Chemistry, University of California, Irvine, California 92697, United States*

Cheyenne Begay − *Department of Chemistry, University of California, Irvine, California 92697, United States*

Jacqueline Wilson − *Pacific Northwest National Laboratory, Richland, Washington 99354, United States;* Present Address: UK Health Security Agency, Oak Park Lane, Cookridge, Leeds, West Yorkshire LS16 6RW, UK.

Manish Shrivastava − *Pacific Northwest National Laboratory, Richland, Washington 99354, United States;* orcid.org/0000-0002-9053-2400

Yuzhi Chen − *Pacific Northwest National Laboratory, Richland, Washington 99354, United States;* orcid.org/0000-0002-2547-8428

John E. Shilling − *Pacific Northwest National Laboratory, Richland, Washington 99354, United States;* orcid.org/0000-0002-3728-0195

Nga L. Ng − *School of Chemical and Biomolecular Engineering, School of Earth and Atmospheric Sciences, School of Civil and Environmental Engineering, Georgia Institute of Technology, Atlanta, Georgia 30332, United States;* orcid.org/0000-0001-8460-4765

Ulrich Pöschl − *Multiphase Chemistry Department, Max Planck Institute for Chemistry, Mainz 55128, Germany;* orcid.org/0000-0003-1412-3557

Complete contact information is available at: https://pubs.acs.org/10.1021/acs.est.5c11018

Notes

The authors declare no competing financial interest.

■ ACKNOWLEDGMENTS

This work was funded by the U.S. Department of Energy (DE-SC0022139), U.S. National Science Foundation (AGS-2246502), and Atmospheric System Research (ASR) program as part of the DOE Office of Biological and Environmental Research. L.M.W. wishes to acknowledge support from the US National Science Foundation (grant # 2331523). J.W., M.Shr, Y.C., and A.Z. were supported by the Atmospheric System Research (ASR) program as part of the DOE BER under PNNL ICLASS project KP1701010/57131. Pacific Northwest National Laboratory is operated by DOE by the Battelle Memorial Institute under Contract DE-A06-76RLO1830. H.G.K. is supported by the Max Planck Graduate Center with the Johannes Gutenberg University Mainz (MPGC). T.B. and N.L.N. acknowledge support from the U.S. National Science Foundation (AGS-1555034) and the Eckert Fellowship at the Georgia Institute of Technology.

■ REFERENCES

(1) Jimenez, J. L.; Canagaratna, M. R.; Donahue, N. M.; Prevot, A. S. H.; Zhang, Q.; Kroll, J. H.; DeCarlo, P. F.; Allan, J. D.; Coe, H.; Ng, N. L.; Aiken, A. C.; Docherty, K. S.; Ulbrich, I. M.; Grieshop, A. P.; Robinson, A. L.; Duplissy, J.; Smith, J. D.; Wilson, K. R.; Lanz, V. A.; Hueglin, C.; Sun, Y. L.; Tian, J.; Laaksonen, A.; Raatikainen, T.; Rautiainen, J.; Vaattovaara, P.; Ehn, M.; Kulmala, M.; Tomlinson, J. M.; Collins, D. R.; Cubison, M. J. E.; Dunlea, J.; Huffman, J. A.; Onasch, T. B.; Alfarra, M. R.; Williams, P. I.; Bower, K.; Kondo, Y.; Schneider, J.; Drewnick, F.; Borrmann, S.; Weimer, S.; Demerjian, K.; Salcedo, D.; Cottrell, L.; Griffin, R.; Takami, A.; Miyoshi, T.; Hatakeyama, S.; Shimono, A.; Sun, J. Y.; Zhang, Y. M.; Dzepina, K.; Kimmel, J. R.; Sueper, D.; Jayne, J. T.; Herndon, S. C.; Trimborn, A. M.; Williams, L. R.; Wood, E. C.; Middlebrook, A. M.; Kolb, C. E.; Baltensperger, U.; Worsnop, D. R. Evolution of Organic Aerosols in the Atmosphere. *Science* **2009**, *326* (5959), 1525−1529.

(2) Pöschl, U.; Shiraiwa, M. Multiphase Chemistry at the Atmosphere−Biosphere Interface Influencing Climate and Public Health in the Anthropocene. *Chem. Rev.* **2015**, *115* (10), 4440−4475.

(3) Carlton, A. G.; Christiansen, A. E.; Flesch, M. M.; Hennigan, C. J.; Sareen, N. Multiphase Atmospheric Chemistry in Liquid Water: Impacts and Controllability of Organic Aerosol. *Acc. Chem. Res.* **2020**, *53* (9), 1715−1723.

(4) Shrivastava, M.; Cappa, C. D.; Fan, J.; Goldstein, A. H.; Guenther, A. B.; Jimenez, J. L.; Kuang, C.; Laskin, A.; Martin, S. T.; Ng, N. L.; Petaja, T.; Pierce, J. R.; Rasch, P. J.; Roldin, P.; Seinfeld, J. H.; Shilling, J.; Smith, J. N.; Thornton, J. A.; Volkamer, R.; Wang, J.; Worsnop, D. R.; Zaveri, R. A.; Zelenyuk, A.; Zhang, Q. Recent Advances in Understanding Secondary Organic Aerosol: Implications for Global Climate Forcing. *Rev. Geophys.* **2017**, *55* (2), 509−559.

(5) Heald, C. L.; Kroll, J. H. The Fuel of Atmospheric Chemistry: Toward a Complete Description of Reactive Organic Carbon. *Sci. Adv.* **2020**, *6* (6), No. eaay8967.

(6) Koop, T.; Bookhold, J.; Shiraiwa, M.; Pöschl, U. Glass Transition and Phase State of Organic Compounds: Dependency on Molecular

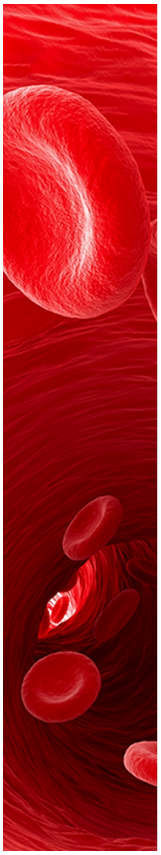
Properties and Implications for Secondary Organic Aerosols in the Atmosphere. *Phys. Chem. Chem. Phys.* **2011**, *13* (43), 19238−19255.
(7) Reid, J. P.; Bertram, A. K.; Topping, D. O.; Laskin, A.; Martin, S. T.; Petters, M. D.; Pope, F. D.; Rovelli, G. The Viscosity of Atmospherically Relevant Organic Particles. *Nat. Commun.* **2018**, *9* (1), No. 956.
(8) Schervish, M.; Donahue, N. M.; Shiraiwa, M. Effects of Volatility, Viscosity, and Non-Ideality on Particle−Particle Mixing Timescales of Secondary Organic Aerosols. *Aerosol Sci. Technol.* **2024**, *58* (4), 411−426.
(9) Wilson, J.; Imre, D.; Beránek, J.; Shrivastava, M.; Zelenyuk, A. Evaporation Kinetics of Laboratory-Generated Secondary Organic Aerosols at Elevated Relative Humidity. *Environ. Sci. Technol.* **2015**, *49* (1), 243−249.
(10) Vaden, T. D.; Imre, D.; Beránek, J.; Shrivastava, M.; Zelenyuk, A. Evaporation Kinetics and Phase of Laboratory and Ambient Secondary Organic Aerosol. *Proc. Natl. Acad. Sci. U.S.A.* **2011**, *108* (6), 2190−2195.
(11) Yli-Juuti, T.; Pajunoja, A.; Tikkanen, O.; Buchholz, A.; Faiola, C.; Väisänen, O.; Hao, L.; Kari, E.; Peräkylä, O.; Garmash, O.; Shiraiwa, M.; Ehn, M.; Lehtinen, K.; Virtanen, A. Factors Controlling the Evaporation of Secondary Organic Aerosol from A-pinene Ozonolysis. *Geophys. Res. Lett.* **2017**, *44* (5), 2562−2570.
(12) Li, Z.; Tikkanen, O.-P.; Buchholz, A.; Hao, L.; Kari, E.; Yli-Juuti, T.; Virtanen, A. Effect of Decreased Temperature on the Evaporation of α-Pinene Secondary Organic Aerosol Particles. *ACS Earth Space Chem.* **2019**, *3* (12), 2775−2785.
(13) Saleh, R.; Donahue, N. M.; Robinson, A. L. Time Scales for Gas-Particle Partitioning Equilibration of Secondary Organic Aerosol Formed from Alpha-Pinene Ozonolysis. *Environ. Sci. Technol.* **2013**, *47* (11), 5588−5594.
(14) Roldin, P.; Eriksson, A. C.; Nordin, E. Z.; Hermansson, E.; Mogensen, D.; Rusanen, A.; Boy, M.; Swietlicki, E.; Svenningsson, B.; Zelenyuk, A.; Pagels, J. Modelling Non-Equilibrium Secondary Organic Aerosol Formation and Evaporation with the Aerosol Dynamics, Gas- and Particle-Phase Chemistry Kinetic Multilayer Model ADCHAM. *Atmos. Chem. Phys.* **2014**, *14* (15), 7953−7993.
(15) Kolesar, K. R.; Li, Z.; Wilson, K. R.; Cappa, C. D. Heating-Induced Evaporation of Nine Different Secondary Organic Aerosol Types. *Environ. Sci. Technol.* **2015**, *49* (20), 12242−12252.
(16) Kenseth, C. M.; Hafeman, N. J.; Rezgui, S. P.; Chen, J.; Huang, Y.; Dalleska, N. F.; Kjaergaard, H. G.; Stoltz, B. M.; Seinfeld, J. H.; Wennberg, P. O. Particle-Phase Accretion Forms Dimer Esters in Pinene Secondary Organic Aerosol. *Science* **2023**, *382* (6672), 787−792.
(17) D'Ambro, E. L.; Schobesberger, S.; Zaveri, R. A.; Shilling, J. E.; Lee, B. H.; Lopez-Hilfiker, F. D.; Mohr, C.; Thornton, J. A. Isothermal Evaporation of α-Pinene Ozonolysis SOA: Volatility, Phase State, and Oligomeric Composition. *ACS Earth Space Chem.* **2018**, *2* (10), 1058−1067.
(18) Berkemeier, T.; Takeuchi, M.; Eris, G.; Ng, N. L. Kinetic Modeling of Formation and Evaporation of Secondary Organic Aerosol from NO_3 Oxidation of Pure and Mixed Monoterpenes. *Atmos. Chem. Phys.* **2020**, *20* (24), 15513−15535.
(19) Shrivastava, M.; Zelenyuk, A.; Imre, D.; Easter, R.; Beranek, J.; Zaveri, R. A.; Fast, J. Implications of Low Volatility SOA and Gas-Phase Fragmentation Reactions on SOA Loadings and Their Spatial and Temporal Evolution in the Atmosphere. *J. Geophys. Res.: Atmos.* **2013**, *118* (8), 3328−3342.
(20) Chen, Y.; Zaveri, R. A.; Vandergrift, G. W.; Cheng, Z.; China, S.; Zelenyuk, A.; Shilling, J. E. Nonequilibrium Behavior in Isoprene Secondary Organic Aerosol. *Environ. Sci. Technol.* **2023**, *57* (38), 14182−14193.
(21) Li, Y.; Shiraiwa, M. Timescales of Secondary Organic Aerosols to Reach Equilibrium at Various Temperatures and Relative Humidities. *Atmos. Chem. Phys.* **2019**, *19* (9), 5959−5971.
(22) Schervish, M.; Shiraiwa, M. Impact of Phase State and Non-Ideal Mixing on Equilibration Timescales of Secondary Organic Aerosol Partitioning. *Atmos. Chem. Phys.* **2023**, *23* (1), 221−233.
(23) O'Meara, S.; Topping, D. O.; Zaveri, R. A.; McFiggans, G. An Efficient Approach for Treating Composition-Dependent Diffusion within Organic Particles. *Atmos. Chem. Phys.* **2017**, *17* (17), 10477−10494.
(24) Tikkanen, O.-P.; Hämäläinen, V.; Rovelli, G.; Lipponen, A.; Shiraiwa, M.; Reid, J. P.; Lehtinen, K. E. J.; Yli-Juuti, T. Optimization of Process Models for Determining Volatility Distribution and Viscosity of Organic Aerosols from Isothermal Particle Evaporation Data. *Atmos. Chem. Phys.* **2019**, *19* (14), 9333−9350.
(25) Huisman, M.; Poon, W. C. K.; Warren, P. B.; Titmuss, S.; Marenduzzo, D. Diffusive Evaporation Dynamics in Polymer Solutions Is Ubiquitous. *Soft Matter* **2025**, *21* (8), 1508−1515.
(26) Zelenyuk, A.; Imre, D.; Wilson, J.; Zhang, Z.; Wang, J.; Mueller, K. Airborne Single Particle Mass Spectrometers (SPLAT II & miniSPLAT) and New Software for Data Visualization and Analysis in a Geo-Spatial Context. *J. Am. Soc. Mass Spectrom.* **2015**, *26* (2), 257−270.
(27) Shiraiwa, M.; Pfrang, C.; Koop, T.; Pöschl, U. Kinetic Multi-Layer Model of Gas-Particle Interactions in Aerosols and Clouds (KM-GAP): Linking Condensation, Evaporation and Chemical Reactions of Organics, Oxidants and Water. *Atmos. Chem. Phys.* **2012**, *12* (5), 2777−2794.
(28) Shiraiwa, M.; Li, Y.; Tsimpidi, A. P.; Karydis, V. A.; Berkemeier, T.; Pandis, S. N.; Lelieveld, J.; Koop, T.; Pöschl, U. Global Distribution of Particle Phase State in Atmospheric Secondary Organic Aerosols. *Nat. Commun.* **2017**, *8* (1), No. 15002.
(29) DeRieux, W.-S. W.; Li, Y.; Lin, P.; Laskin, J.; Laskin, A.; Bertram, A. K.; Nizkorodov, S. A.; Shiraiwa, M. Predicting the Glass Transition Temperature and Viscosity of Secondary Organic Material Using Molecular Composition. *Atmos. Chem. Phys.* **2018**, *18* (9), 6331−6351.
(30) Berkemeier, T.; Ammann, M.; Krieger, U. K.; Peter, T.; Spichtinger, P.; Pöschl, U.; Shiraiwa, M.; Huisman, A. J. Technical Note: Monte Carlo Genetic Algorithm (MCGA) for Model Analysis of Multiphase Chemical Kinetics to Determine Transport and Reaction Rate Coefficients Using Multiple Experimental Data Sets. *Atmos. Chem. Phys.* **2017**, *17* (12), 8021−8029.
(31) Saunders, S. M.; Jenkin, M. E.; Derwent, R. G.; Pilling, M. J. Protocol for the Development of the Master Chemical Mechanism, MCM v3 (Part A): Tropospheric Degradation of Non-Aromatic Volatile Organic Compounds. *Atmos. Chem. Phys.* **2003**, *3* (1), 161−180.
(32) Donahue, N. M.; Robinson, A. L.; Stanier, C. O.; Pandis, S. N. Coupled Partitioning, Dilution, and Chemical Aging of Semivolatile Organics. *Environ. Sci. Technol.* **2006**, *40* (8), 2635−2643.
(33) Robinson, A. L.; Donahue, N. M.; Shrivastava, M. K.; Weitkamp, E. A.; Sage, A. M.; Grieshop, A. P.; Lane, T. E.; Pierce, J. R.; Pandis, S. N. Rethinking Organic Aerosols: Semivolatile Emissions and Photochemical Aging. *Science* **2007**, *315* (5816), 1259−1262.
(34) Kang, H. G.; Chen, Y.; Park, Y.; Berkemeier, T.; Kim, H. Volatile Oxidation Products and Secondary Organosiloxane Aerosol from D5+OH at Varying OH Exposures. *Atmos. Chem. Phys.* **2023**, *23* (22), 14307−14323.
(35) Bannan, T. J.; Le Breton, M.; Priestley, M.; Worrall, S. D.; Bacak, A.; Marsden, N. A.; Mehra, A.; Hammes, J.; Hallquist, M.; Alfarra, M. R.; Krieger, U. K.; Reid, J. P.; Jayne, J.; Robinson, W.; McFiggans, G.; Coe, H.; Percival, C. J.; Topping, D. A Method for Extracting Calibrated Volatility Information from the FIGAERO-HR-ToF-CIMS and Its Experimental Application. *Atmos. Meas. Tech.* **2019**, *12* (3), 1429−1439.
(36) Madorsicy, S. L.; Straus, S. Thermal Degradation of Polyethylene Oxide and Polypropylene Oxide. *J. Polym. Sci.* **1959**, *36* (130), 183−194.
(37) Krieger, U. K.; Siegrist, F.; Marcolli, C.; Emanuelsson, E. U.; Gøbel, F. M.; Bilde, M.; Marsh, A.; Reid, J. P.; Huisman, A. J.; Riipinen, I.; Hyttinen, N.; Myllys, N.; Kurtén, T.; Bannan, T.; Percival, C. J.; Topping, D. A Reference Data Set for Validating Vapor

https://doi.org/10.1021/acs.est.5c11018
Environ. Sci. Technol. 2026, 60, 7995−8006

Pressure Measurement Techniques: Homologous Series of Polyethylene Glycols. *Atmos. Meas. Tech.* **2018**, *11* (1), 49−63.
(38) Zhang, K.; Yang, J.; Yu, X.; Zhang, J.; Wei, X. Densities and Viscosities for Binary Mixtures of Poly(Ethylene Glycol) 400 + Dimethyl Sulfoxide and Poly(Ethylene Glycol) 600 + Water at Different Temperatures. *J. Chem. Eng. Data* **2011**, *56* (7), 3083−3088.
(39) Zhang, N.; Zhang, J.; Zhang, Y.; Bai, J.; Huo, T.; Wei, X. Excess Molar Volumes and Viscosities of Poly(Ethylene Glycol) 300 + Water at Different Temperatures. *Fluid Phase Equilib.* **2012**, *313*, 7−10.
(40) Petters, S. S.; Kreidenweis, S. M.; Grieshop, A. P.; Ziemann, P. J.; Petters, M. D. Temperature- and Humidity-Dependent Phase States of Secondary Organic Aerosols. *Geophys. Res. Lett.* **2019**, *46* (2), 1005−1013.
(41) Berkemeier, T.; Shiraiwa, M.; Pöschl, U.; Koop, T. Competition between Water Uptake and Ice Nucleation by Glassy Organic Aerosol Particles. *Atmos. Chem. Phys.* **2014**, *14* (22), 12513−12531.
(42) Fuentes, E.; McFiggans, G. A Modeling Approach to Evaluate the Uncertainty in Estimating the Evaporation Behaviour and Volatility of Organic Aerosols. *Atmos. Meas. Tech.* **2012**, *5* (4), 735−757.
(43) Ye, Q.; Wang, M.; Hofbauer, V.; Stolzenburg, D.; Chen, D.; Schervish, M.; Vogel, A.; Mauldin, R. L.; Baalbaki, R.; Brilke, S.; Dada, L.; Dias, A.; Duplissy, J.; El Haddad, I.; Finkenzeller, H.; Fischer, L.; He, X.; Kim, C.; Kürten, A.; Lamkaddam, H.; Lee, C. P.; Lehtipalo, K.; Leiminger, M.; Manninen, H. E.; Marten, R.; Mentler, B.; Partoll, E.; Petäjä, T.; Rissanen, M.; Schobesberger, S.; Schuchmann, S.; Simon, M.; Tham, Y. J.; Vazquez-Pufleau, M.; Wagner, A. C.; Wang, Y.; Wu, Y.; Xiao, M.; Baltensperger, U.; Curtius, J.; Flagan, R.; Kirkby, J.; Kulmala, M.; Volkamer, R.; Winkler, P. M.; Worsnop, D.; Donahue, N. M. Molecular Composition and Volatility of Nucleated Particles from α-Pinene Oxidation between − 50 °C and + 25 °C. *Environ. Sci. Technol.* **2019**, *53* (21), 12357−12365.
(44) Abramson, E.; Imre, D.; Beránek, J.; Wilson, J.; Zelenyuk, A. Experimental Determination of Chemical Diffusion within Secondary Organic Aerosol Particles. *Phys. Chem. Chem. Phys.* **2013**, *15* (8), 2983−2991.
(45) Bell, D. M.; Imre, D.; Martin, S. T.; Zelenyuk, A. The Properties and Behavior of α-Pinene Secondary Organic Aerosol Particles Exposed to Ammonia under Dry Conditions. *Phys. Chem. Chem. Phys.* **2017**, *19* (9), 6497−6507.
(46) Zhang, Y.; Sanchez, M. S.; Douet, C.; Wang, Y.; Bateman, A. P.; Gong, Z.; Kuwata, M.; Renbaum-Wolff, L.; Sato, B. B.; Liu, P. F.; Bertram, A. K.; Geiger, F. M.; Martin, S. T. Changing Shapes and Implied Viscosities of Suspended Submicron Particles. *Atmos. Chem. Phys.* **2015**, *15* (14), 7819−7829.
(47) Li, Z.; Buchholz, A.; Ylisirniö, A.; Barreira, L.; Hao, L.; Schobesberger, S.; Yli-Juuti, T.; Virtanen, A. Evolution of Volatility and Composition in Sesquiterpene-Mixed and α-Pinene Secondary Organic Aerosol Particles during Isothermal Evaporation. *Atmos. Chem. Phys.* **2021**, *21* (24), 18283−18302.
(48) Takeuchi, M.; Berkemeier, T.; Eris, G.; Ng, N. L. Non-Linear Effects of Secondary Organic Aerosol Formation and Properties in Multi-Precursor Systems. *Nat. Commun.* **2022**, *13* (1), No. 7883.
(49) Nah, T.; McVay, R. C.; Pierce, J. R.; Seinfeld, J. H.; Ng, N. L. Constraining Uncertainties in Particle-Wall Deposition Correction during SOA Formation in Chamber Experiments. *Atmos. Chem. Phys.* **2017**, *17* (3), 2297−2310.
(50) Huang, Y.; Zhao, R.; Charan, S. M.; Kenseth, C. M.; Zhang, X.; Seinfeld, J. H. Unified Theory of Vapor−Wall Mass Transport in Teflon-Walled Environmental Chambers. *Environ. Sci. Technol.* **2018**, *52* (4), 2134−2142.
(51) Li, Y.; Day, D. A.; Stark, H.; Jimenez, J. L.; Shiraiwa, M. Predictions of the Glass Transition Temperature and Viscosity of Organic Aerosols from Volatility Distributions. *Atmos. Chem. Phys.* **2020**, *20* (13), 8103−8122.
(52) Boyd, C. M.; Nah, T.; Xu, L.; Berkemeier, T.; Ng, N. L. Secondary Organic Aerosol (SOA) from Nitrate Radical Oxidation of Monoterpenes: Effects of Temperature, Dilution, and Humidity on Aerosol Formation, Mixing, and Evaporation. *Environ. Sci. Technol.* **2017**, *51* (14), 7831−7841.
(53) Qin, Y.; Wingen, L. M.; Finlayson-Pitts, B. J. Toward a Molecular Understanding of the Surface Composition of Atmospherically Relevant Organic Particles. *Proc. Natl. Acad. Sci. U.S.A.* **2022**, *119* (35), No. e2209134119.
(54) Li, Y.; Lakey, P. S. J.; Ezell, M. J.; Johnson, K. N.; Shiraiwa, M.; Finlayson-Pitts, B. J. Distinct Temperature Trends in the Uptake of Gaseous N-Butylamine on Two Solid Diacids. *ACS ES&T Air* **2024**, *1* (1), 52−61.
(55) Garofalo, L. A.; He, Y.; Jathar, S. H.; Pierce, J. R.; Fredrickson, C. D.; Palm, B. B.; Thornton, J. A.; Mahrt, F.; Crescenzo, G. V.; Bertram, A. K.; Draper, D. C.; Fry, J. L.; Orlando, J.; Zhang, X.; Farmer, D. K. Heterogeneous Nucleation Drives Particle Size Segregation in Sequential Ozone and Nitrate Radical Oxidation of Catechol. *Environ. Sci. Technol.* **2021**, *55* (23), 15637−15645.
(56) Zaveri, R. A.; Wang, J.; Fan, J.; Zhang, Y.; Shilling, J. E.; Zelenyuk, A.; Mei, F.; Newsom, R.; Pekour, M.; Tomlinson, J.; Comstock, J. M.; Shrivastava, M.; Fortner, E.; Machado, L. A. T.; Artaxo, P.; Martin, S. T. Rapid Growth of Anthropogenic Organic Nanoparticles Greatly Alters Cloud Life Cycle in the Amazon Rainforest. *Sci. Adv.* **2022**, *8* (2), No. eabj0329.
(57) Hosny, N. A.; Fitzgerald, C.; Vyšniauskas, A.; Athanasiadis, A.; Berkemeier, T.; Uygur, N.; Pöschl, U.; Shiraiwa, M.; Kalberer, M.; Pope, F. D.; Kuimova, M. K. Direct Imaging of Changes in Aerosol Particle Viscosity upon Hydration and Chemical Aging. *Chem. Sci.* **2016**, *7* (2), 1357−1367.
(58) Xu, S.; Mahrt, F.; Gregson, F. K. A.; Bertram, A. K. Possible Effects of Ozone Chemistry on the Phase Behavior of Skin Oil and Cooking Oil Films and Particles Indoors. *ACS Earth Space Chem.* **2022**, *6* (7), 1836−1845.
(59) Milsom, A.; Squires, A. M.; Ward, A. D.; Pfrang, C. The Impact of Molecular Self-Organisation on the Atmospheric Fate of a Cooking Aerosol Proxy. *Atmos. Chem. Phys.* **2022**, *22* (7), 4895−4907.
(60) Pfrang, C.; Shiraiwa, M.; Pöschl, U. Chemical Ageing and Transformation of Diffusivity in Semi-Solid Multi-Component Organic Aerosol Particles. *Atmos. Chem. Phys.* **2011**, *11* (14), 7343−7354.
(61) Zhou, S.; Hwang, B. C. H.; Lakey, P. S. J.; Zuend, A.; Abbatt, J. P. D.; Shiraiwa, M. Multiphase Reactivity of Polycyclic Aromatic Hydrocarbons Is Driven by Phase Separation and Diffusion Limitations. *Proc. Natl. Acad. Sci. U. S. A.* **2019**, *116* (24), 11658−11663.
(62) Zelenyuk, A.; Imre, D.; Beránek, J.; Abramson, E.; Wilson, J.; Shrivastava, M. Synergy between Secondary Organic Aerosols and Long-Range Transport of Polycyclic Aromatic Hydrocarbons. *Environ. Sci. Technol.* **2012**, *46* (22), 12459−12466.
(63) Zelenyuk, A.; Imre, D. G.; Wilson, J.; Bell, D. M.; Suski, K. J.; Shrivastava, M.; Beránek, J.; Alexander, M. L.; Kramer, A. L.; Simonich, S. L. M. The Effect of Gas-Phase Polycyclic Aromatic Hydrocarbons on the Formation and Properties of Biogenic Secondary Organic Aerosol Particles. *Faraday Discuss.* **2017**, *200* (0), 143−164.
(64) Shrivastava, M.; Lou, S.; Zelenyuk, A.; Easter, R. C.; Corley, R. A.; Thrall, B. D.; Rasch, P. J.; Fast, J. D.; Massey Simonich, S. L.; Shen, H.; Tao, S. Global Long-Range Transport and Lung Cancer Risk from Polycyclic Aromatic Hydrocarbons Shielded by Coatings of Organic Aerosol. *Proc. Natl. Acad. Sci. U.S.A.* **2017**, *114* (6), 1246−1251.
(65) Mu, Q.; Shiraiwa, M.; Octaviani, M.; Ma, N.; Ding, A.; Su, H.; Lammel, G.; Pöschl, U.; Cheng, Y. Temperature Effect on Phase State and Reactivity Controls Atmospheric Multiphase Chemistry and Transport of PAHs. *Sci. Adv.* **2018**, *4* (3), No. eaap7314.
(66) Gregson, F. K. A.; Gerrebos, N. G. A.; Schervish, M.; Nikkho, S.; Schnitzler, E. G.; Schwartz, C.; Carlsten, C.; Abbatt, J. P. D.; Kamal, S.; Shiraiwa, M.; Bertram, A. K. Phase Behavior and Viscosity in Biomass Burning Organic Aerosol and Climatic Impacts. *Environ. Sci. Technol.* **2023**, *57* (39), 14548−14557.

https://doi.org/10.1021/acs.est.5c11018
Environ. Sci. Technol. 2026, 60, 7995−8006

(67) Al-Mashala, H. H.; Betz, K. L.; Calvert, C. T.; Barton, J. A.; Bruce, E. E.; Schnitzler, E. G. Ultraviolet Irradiation Can Increase the Light Absorption and Viscosity of Primary Brown Carbon from Biomass Burning. *ACS Earth Space Chem.* **2023**, *7* (10), 1882−1889.
(68) Baboomian, V. J.; Crescenzo, G. V.; Huang, Y.; Mahrt, F.; Shiraiwa, M.; Bertram, A. K.; Nizkorodov, S. A. Sunlight Can Convert Atmospheric Aerosols into a Glassy Solid State and Modify Their Environmental Impacts. *Proc. Natl. Acad. Sci. U.S.A.* **2022**, *119* (43), No. e2208121119.
(69) Gilardoni, S.; Massoli, P.; Paglione, M.; Giulianelli, L.; Carbone, C.; Rinaldi, M.; Decesari, S.; Sandrini, S.; Costabile, F.; Gobbi, G. P.; Pietrogrande, M. C.; Visentin, M.; Scotto, F.; Fuzzi, S.; Facchini, M. C. Direct Observation of Aqueous Secondary Organic Aerosol from Biomass-Burning Emissions. *Proc. Natl. Acad. Sci. U.S.A.* **2016**, *113* (36), 10013−10018.


CAS BIOFINDER DISCOVERY PLATFORM™
CAS BIOFINDER HELPS YOU FIND YOUR NEXT BREAKTHROUGH FASTER
Navigate pathways, targets, and diseases with precision
Explore CAS BioFinder
CAS
A division of the American Chemical Society

https://doi.org/10.1021/acs.est.5c11018
Environ. Sci. Technol. 2026, 60, 7995−8006

2.5. Temperature-dependent multiphase chemical kinetics explain uniform atmospheric nanoparticle growth rates

This section is a draft manuscript, where I am the second author. Under the supervision of Dr. Thomas Berkemeier and Prof. Dr. Ulrich Pöschl, Dr. Zhiqiang Zhang and I developed the KM3C model code building on previous studies, and I applied the adaptive layer resizing and moving-boundary algorithms. I also contributed to the figures and text, and after further revisions with co-authors, the manuscript will be submitted to a peer-reviewed journal.

Zhang, Z., Kang, H. G., Pöschl, U., Berkemeier, T.: Temperature-dependent multiphase chemical kinetics explain uniform atmospheric nanoparticle growth rates, *in preparation*.

We used KM3C to explain the uniform growth rates of newly-formed particles found in α-pinene + O_3 chamber experiments performed at different temperatures and in boreal forest air, despite differing gas-phase OOM concentrations (Stolzenburg et al., 2018, 2025). We found that the initial growth was kinetically limited by diffusion and that the OOM composition and volatility changed with temperature. The slower particle growth from the more-volatile OOM formed at lower temperatures was effectively balanced by the faster growth with the less-volatile OOM in higher temperatures. This interplay has led to an apparent near-constant growth rate of nanoparticles.

Abstract

Aerosols have a profound influence on weather, climate, and human health, but new particle formation in the atmosphere has remained a scientific conundrum. In particular, the growth rates of atmospheric nanoparticles are often smaller and less dependent on condensable vapor concentrations than expected.

Here, we take a new approach to analyze observational data from field measurements in Hyytiälä, Finland, and from the CERN CLOUD experiment. We show that atmospheric nanoparticle growth can be accurately predicted when the distribution of chemical species and volatilities, the multiphase mass transport kinetics including particle phase state and bulk concentration profiles, and the relevant temperature dependencies are taken into account. The previously unexplained observations can be reconciled by inclusion of vapors that fall into the semi- and intermediate volatility ranges at room temperature, but are sufficiently low-volatile to contribute to particle growth at low temperatures. Furthermore, the rates of vapor uptake and particle growth can be limited by slow bulk accommodation due to diffusion-limited surface-to-bulk transport in semi-solid particles.

This study reveals an important fundamental dynamic in atmospheric aerosol growth, where oxidation chemistry at lower temperatures leads to less oxidized molecules, which is effectively balanced by lower volatility, leading to a convergence of nanoparticle growth rates.

1 Introduction

Atmospheric aerosols consisting of airborne particles in the nanometer to micrometer size range have a strong influence on air quality, public health, and climate (Team et al., 2023; World Health Organization, 2023). Large fractions of airborne fine particulate matter consist of secondary organic aerosols (SOA) formed by gas-to-particle conversion of organic precursor molecules in the atmosphere (Jimenez et al., 2009; Riipinen et al., 2011). Over the past decades, numerous studies have been performed to elucidate and characterize the processes and effects of atmospheric new particle formation and growth (Kulmala et al., 2004, 2014). The rates of nanoparticle growth, however, have remained elusive/enigmatic and constitute a major gap in the scientific understanding and assessment of atmospheric aerosols and their effects on health and climate (Gordon et al., 2017). In particular, the growth rates of SOA nanoparticles observed in field measurements and laboratory experiments could not be explained by the traditional kinetic models applied in earlier studies (Stolzenburg et al., 2023, 2025). These models describe the uptake of condensable organic vapors at the particle surface, but they do not resolve mass transport and concentration gradients for different species inside the particle. Here, we develop and utilize a new kinetic multilayer model of multiphase chemistry (KM3C) (Kang et al., 2026), which fully resolves the reactivity, diffusivity,

and differential concentration gradients of different chemical species across the gas phase, interface, and condensed phase. We analyze observational data from field measurements and laboratory experiments, and we find that SOA nanoparticle growth can be accurately predicted when the relevant processes, properties, and temperature dependencies are taken into account.

2 Results

2.1 Slow nanoparticle growth in ambient air

Figure 1 illustrates how previously unexplained discrepancies between field measurements and model predictions of condensable organic vapor concentrations and nanoparticle growth rates can be reconciled by elucidating condensed phase diffusivity and concentration gradients. As reported by Stolzenburg et al. (Stolzenburg et al., 2025) and illustrated in Figure 1a, the previous kinetic model failed to capture the field measurements of relatively low growth rates, despite accounting for systematic uncertainties from the quantification of measured condensable vapors, activity coefficients, decomposition reactions as well as limited bulk diffusion. Incomplete mass closure in atmospheric nanoparticle growth rates have been reported, and including potentially unaccounted oxygenated organic molecules (OOMs), modelling results would further deviate upward form measurements.

In this study, by reducing the bulk diffusion to ($D_{b,298K}$ = 8 $\times$ 10^{-20} cm^2 s^{-1}), a general mass closure in nanoparticle growth rates is achieved. SOA particles can exist in an amorphous glassy phase state, leading to low diffusivity in the condensed phase(Virtanen et al., 2010). Further incorporating measurement uncertainty by shifting full VBS by $\pm$ 1 bin, we could reliably capture measured nanoparticle growth rates right after nucleation. As shown in Figure 1b, there are differential concentration gradients within modelled nanoparticle. In the process of nanoparticle growth, growth rates are primarily governed by surface to bulk transportation, and surface to bulk transportation rate is proportional to diffusivity in particle phase, which substantially slow down nanoparticle growth rates compared to high particle phase diffusivity ($D_{\mathrm{b,\,298\,K}}$ = 10^{-15} cm^2 s^{-1}) scenario as shown in Figure S1.

2.2 Weak concentration-dependence of nanoparticle growth

Figure 2 shows the laboratory experiments of dark α-pinene ozonolysis conducted at the Cosmics Leaving Outdoor Droplets (CLOUD) chamber at the European Organization for Nuclear Research (CERN) (Stolzenburg et al., 2018). Experiments were performed at three different temperatures (25, 5, and -25 °C). Proton transfer reaction (PTR3) and nitrate chemical ionization mass spectrometers (nitrate-CI) were used to measure the gas-phase species. At 25 °C, the nitrate-CI could measure the majority of the OOMs in

the condensed phase following absorptive partitioning theory (Pankow, 1994). However, at -25 °C, only a minority of the OOMs was measured by the nitrate-CI.

As shown in Figure S2, KM3C is unable to reproduce the observed nanoparticle growth rates when constrained solely by the concentration of OOMs measured by nitrate-CI. The discrepancy is most pronounced at -25 °C, where nitrate-CI detects only a minor fraction of OOMs and relatively high-volatility species (SVOCs) can increasingly contribute to particle growth. By additionally incorporating OOMs measured by PTR3, KM3C can generally capture most of the measured nanoparticle growth rates (Figure 3). Furthermore, particle phase diffusivity is a crucial factor to achieve an even better mass closure in nanoparticle growth rates (Figure 3), particularly the nanoparticles from cluster size (diameter from 1.5 nm to 3 nm), which is the decisive stage for nanoparticles becoming climate-relevant.

A positive correlation between OOMs concentration and temperature was observed in field studies across China (Tang et al., 2025), which could be explained by high temperature often accompanied by enhanced solar radiation likely increase OOMs concentration (Bianchi et al., 2019). However, alternatively, lower apparent OOM concentrations at lower temperatures may result from undetected species, as indicated in Figure 2 (Stolzenburg et al., 2018; Tröstl et al., 2016). Figure 4 shows that in low-temperature environments, incorporating undetected OOMs measured by PTR3 (Figure 2), in addition to those captured by nitrate-CI, reconciles previously underestimated nanoparticle growth rates (indicated by the bottom left arrow in Figure 4). Under warmer conditions, as found in previous studies (Stolzenburg et al., 2025; Cai et al., 2026), observed growth rates are slower than the previous simpler modelling results. In this study, by taking low bulk diffusivity into consideration, slower growth rates can be reproduced (indicated by the upper right arrow in Figure 4).

By accounting for variations in particle-phase diffusivity and measurement uncertainty, the majority of observed field nanoparticle growth rates can be captured , as indicated by the grey shaded area in Figure 4. The upper bound of the shading area corresponds to high particle-phase diffusivity combined with a -1 bin shift of the full VBS, which offers a mechanistic explanation for the empirical scarcity of atmospheric nanoparticle growth rates exceeding 10 nm h^{-1}. Whereas the lower bound represents low particle-phase diffusivity with +1 bin shift. Very low growth rates not captured may result from even lower particle-phase diffusivity, right-shifted VBS bins, or measurement uncertainties. The modelling results in this study (solid line and grey shading area) shows an apparent independence of nanoparticle growth rate on OOMs concentration incompletely measured by nitrate-CI. This behavior can be attributed to temperature-dependent volatility, contributions from undetected OOMs as noted in few previous studies, and, critically, the low particle-phase diffusivity explicitly accounted for in our kinetic modelling.

2.3 Atmospheric implication

Nanoparticle growth from cluster size immediately after nucleation represents the decisive stage to become climate-relevant. This study resolves the long-standing scientific conundrum of atmospheric nanoparticle growth by reconciling discrepancies between theoretical predictions and chamber and field measurements with KM3C kinetic multilayer model. We demonstrate that the apparent observed near-constant growth rates result from a complex interplay between measurement uncertainty, temperature dependence on volatility, and diffusion limitation in the particle phase.

This study yields critical insights into the mechanisms governing secondary organic aerosol formation mechanism. We demonstrate that while lower temperatures lead to less oxidized organic molecules, this is effectively balanced by a decrease in saturation vapor pressure. Semi-volatile organic compounds, often undetected by nitrate-CI can contribute significantly to growth at low temperatures, leading to mass closure in nanoparticle growth. Our model highlights the decisive role of the particle phase state and particle phase diffusivity. Incorporating low bulk diffusivity ($D_{\mathrm{b,\,298\,K}}$ = 8 $\times$ 10^{-20} $\mathrm{cm^2\ s^{-1}}$) reproduces the suppressed growth rates observed under warmer conditions, which traditional simpler models previously would overestimate. The internal concentration gradients caused by surface-to-bulk mass-transfer limitations are essential for capturing the growth kinetics of nanometer-sized particles. This study also provides a mechanistic explanation for the empirical scarcity of growth rates exceeding 10 $\mathrm{nm\,h^{-1}}$. In summary, accurate characterization of nanoparticle growth and its climatic implications necessitates the integration of advanced measurement techniques with explicit modelling of multiphase transport processes.

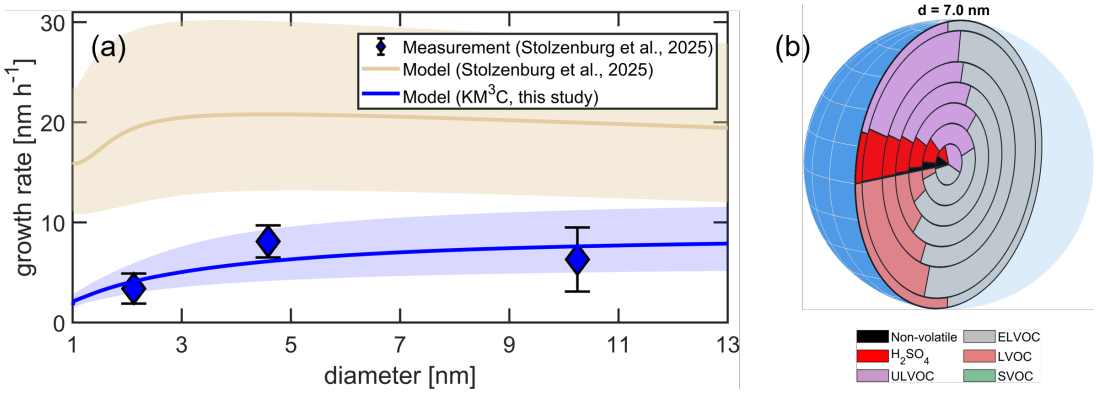


Figure 1: *Atmospheric nanoparticle growth rates observed in a field experiment (Hyytiälä, 17th August 2020). (A) Aerosol size distributions were measured in combination with condensable vapor concentrations (Stolzenburg et al., 2025). Observed growth rates (blue diamond markers and error bars representing arithmetic mean values and standard deviations) were substantially lower than the vapor concentration-based predictions obtained with a traditional kinetic model (Stolzenburg et al. 2025; brown line and shading for best estimate and uncertainty range by shifting full VBS by ± 1 bin). In contrast, the new multiphase kinetic model resolving the diffusivity and differential concentration gradients of different species inside the particles (KM3C; blue line and shading for best estimate and uncertainty range by shifting full VBS by ± 1 bin) correctly predicts the observed growth rates within experimental and model uncertainties. (B) Differential concentration gradients inside growing nanoparticles, where ultra-low and extremely low volatile organic compounds (ULVOC + ELVOC) are enriched in the particle core with very low diffusivity, while low volatile organic compounds (LVOC) with relatively higher volatility, diffusivity, and gas phase abundance are enriched near the surface. These differential gradients effectively delay the penetration and equilibrium uptake of species with relatively higher volatility and abundance (LVOC), thus keeping the growth rate lower than expected under the assumption of a well-mixed and thus rapidly equilibrating condensed/particle phase.*

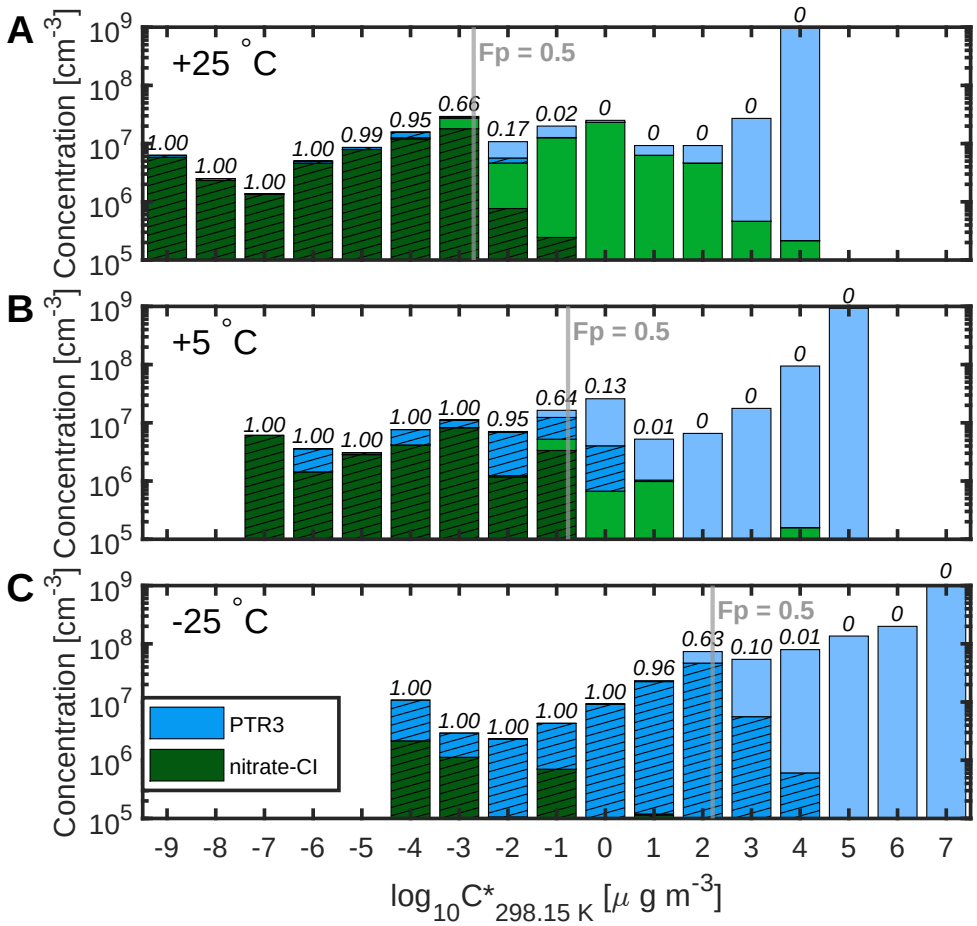


Figure 2: *Volatility distributions of three experiments in the CERN CLOUD chamber. Experiments were conducted at (A) 25 °C, (B) 5 °C and (C) -25 °C reported by Stolzenburg et al. (2018). Shaded areas and numbers above the bars indicate fractions that partition into the particle phase (F_p) at an aerosol mass loading of 0.002 $\mu g\ m^{-3}$, corresponding to 10^5 particles cm^{-3} with 3 nm diameter, and the grey vertical lines indicate the volatility where F_p = 0.5.*

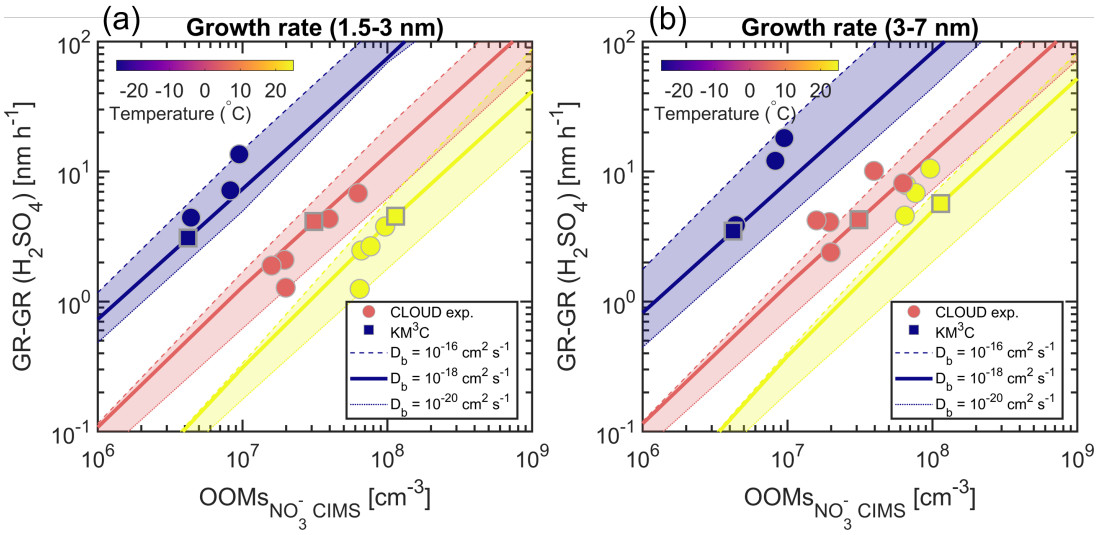


Figure 3: *KM3C captures measured nanoparticle growth rates in CERN CLOUD chamber. Nanoparticle growth rates (GR) in laboratory chamber experiments in the CERN CLOUD chamber (circular markers) and in the KM3C kinetic model (square markers, colored solid lines). Data is plotted against the concentration of oxygenated organic molecules (OOMs) as measured by nitrate-CI, which are a subset of the total condensable organic matter. Colored solid lines are obtained by linearly scaling the combined OOM concentrations (nitrate-CI + PTR3) in the model at the three respective temperatures (-25, 5 and 25°C). Upper and lower boundaries of the shaded areas are obtained by scaling the bulk diffusion coefficient* $D_{b,298K}$ *within the semi-solid phase state range.*

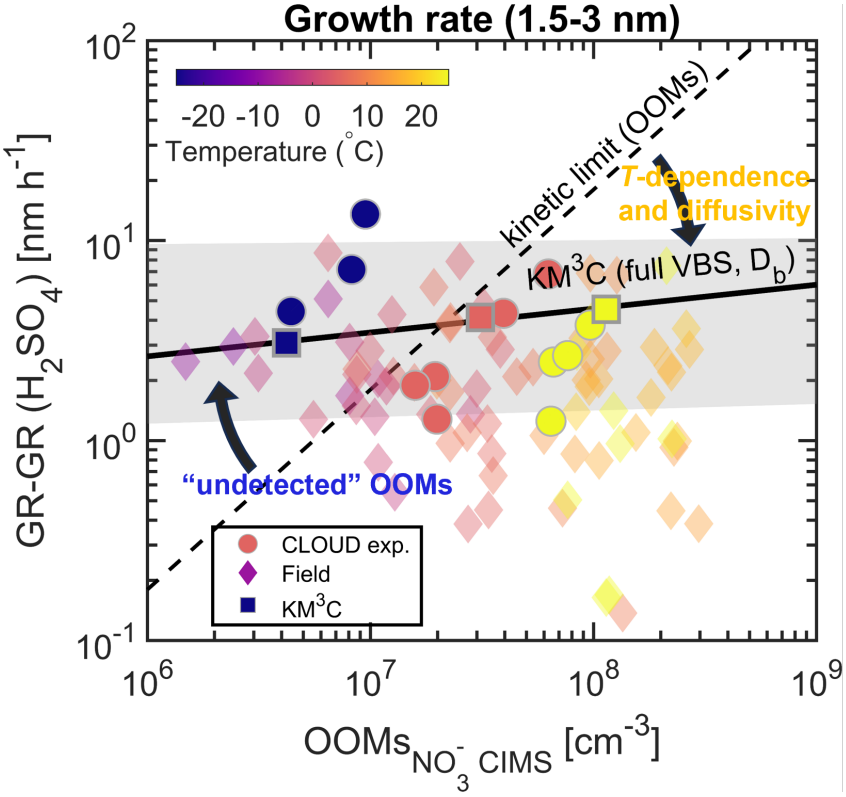


Figure 4: *KM3C captures apparent independence of nanoparticle growth rates on OOMs concentration. Illustration of the consequence of using the full volatility basis set (VBS), temperature-dependence and diffusivity in the kinetic multilayer model of multiphase chemistry (KM3C, black solid line and square markers), leading to an apparent independence of nanoparticle growth rate as a function of concentration of oxygenated organic molecules (OOMs) as seen in laboratory (circular markers) and field data (diamond markers), which is not captured by simpler kinetic models (black dashed line).*

8

3 References

Bianchi, F., Kurtén, T., Riva, M., Mohr, C., Rissanen, M. P., Roldin, P., Berndt, T., Crounse, J. D., Wennberg, P. O., Mentel, T. F., Wildt, J., Junninen, H., Jokinen, T., Kulmala, M., Worsnop, D. R., Thornton, J. A., Donahue, N., Kjaergaard, H. G., and Ehn, M.: Highly Oxygenated Organic Molecules (HOM) from Gas-Phase Autoxidation Involving Peroxy Radicals: A Key Contributor to Atmospheric Aerosol, Chemical Reviews, 119, 3472–3509, 2019.

Cai, R., Li, X., Li, Y., Blichner, S., Stolzenburg, D., Zha, Q., Cai, J., Nie, W., Yan, C., Huang, D. D., Wang, Z., Wu, J., Yin, R., Sarnela, N., Huang, W., Tuovinen, S., Holm, S., Ahonen, L., Yao, L., Ding, A., Bianchi, F., Liu, Y., Winkler, P. M., Petäjä, T., Chen, J., Kerminen, V.-M., Wang, L., Worsnop, D., Jiang, J., Kulmala, M., and Kangasluoma, J.: The key role of nanoparticle concentration gradient in aerosol initial growth, Nature Communications, 2026.

Gordon, H., Kirkby, J., Baltensperger, U., Bianchi, F., Breitenlechner, M., Curtius, J., Dias, A., Dommen, J., Donahue, N. M., Dunne, E. M., Duplissy, J., Ehrhart, S., Flagan, R. C., Frege, C., Fuchs, C., Hansel, A., Hoyle, C. R., Kulmala, M., Kürten, A., Lehtipalo, K., Makhmutov, V., Molteni, U., Rissanen, M. P., Stozkhov, Y., Tröstl, J., Tsagkogeorgas, G., Wagner, R., Williamson, C., Wimmer, D., Winkler, P. M., Yan, C., and Carslaw, K. S.: Causes and importance of new particle formation in the present-day and preindustrial atmospheres, Journal of Geophysical Research: Atmospheres, 122, 8739–8760, 2017.

Jimenez, J. L., Canagaratna, M. R., Donahue, N. M., Prevot, A. S. H., Zhang, Q., Kroll, J. H., DeCarlo, P. F., Allan, J. D., Coe, H., Ng, N. L., Aiken, A. C., Docherty, K. S., Ulbrich, I. M., Grieshop, A. P., Robinson, A. L., Duplissy, J., Smith, J. D., Wilson, K. R., Lanz, V. A., Hueglin, C., Sun, Y. L., Tian, J., Laaksonen, A., Raatikainen, T., Rautiainen, J., Vaattovaara, P., Ehn, M., Kulmala, M., Tomlinson, J. M., Collins, D. R., Cubison, M. J., Dunlea, J., Huffman, J. A., Onasch, T. B., Alfarra, M. R., Williams, P. I., Bower, K., Kondo, Y., Schneider, J., Drewnick, F., Borrmann, S., Weimer, S., Demerjian, K., Salcedo, D., Cottrell, L., Griffin, R., Takami, A., Miyoshi, T., Hatakeyama, S., Shimono, A., Sun, J. Y., Zhang, Y. M., Dzepina, K., Kimmel, J. R., Sueper, D., Jayne, J. T., Herndon, S. C., Trimborn, A. M., Williams, L. R., Wood, E. C., Middlebrook, A. M., Kolb, C. E., Baltensperger, U., and Worsnop, D. R.: Evolution of Organic Aerosols in the Atmosphere, Science, 326, 1525–1529, 2009.

Kang, H. G., Takeuchi, M., Ng, N. L., Pöschl, U., and Berkemeier, T.: Multiphase Chemistry and Phase State Explain Nonlinear Effects in the Formation and Evaporation of SOA from Mixed Monoterpene Precursors, ACS ESamp;T Air, 2026.

Kulmala, M., Vehkamäki, H., Petäjä, T., Dal Maso, M., Lauri, A., Kerminen, V.-M., Birmili, W., and McMurry, P.: Formation and growth rates of ultrafine atmospheric particles: a review of observations, Journal of Aerosol Science, 35, 143–176, 2004.

Kulmala, M., Petäjä, T., Ehn, M., Thornton, J., Sipilä, M., Worsnop, D., and Kerminen, V.-M.: Chemistry of Atmospheric Nucleation: On the Recent Advances on Precursor Characterization and Atmospheric Cluster Composition in Connection with Atmospheric New Particle Formation, Annual Review of Physical Chemistry, 65, 21–37, 2014.

Riipinen, I., Pierce, J. R., Yli-Juuti, T., Nieminen, T., Häkkinen, S., Ehn, M., Junninen, H., Lehtipalo, K., Petäjä, T., Slowik, J., Chang, R., Shantz, N. C., Abbatt, J., Leaitch, W. R., Kerminen, V.-M., Worsnop, D. R., Pandis, S. N., Donahue, N. M., and Kulmala, M.: Organic condensation: a vital link connecting aerosol formation to cloud condensation nuclei (CCN) concentrations, Atmospheric Chemistry and Physics, 11, 3865–3878, 2011.

Stolzenburg, D., Fischer, L., Vogel, A. L., Heinritzi, M., Schervish, M., Simon, M., Wagner, A. C., Dada, L., Ahonen, L. R., Amorim, A., Baccarini, A., Bauer, P. S., Baumgartner, B., Bergen, A., Bianchi, F., Breitenlechner, M., Brilke, S., Buenrostro Mazon, S., Chen, D., Dias, A., Draper, D. C., Duplissy, J., El Haddad, I., Finkenzeller, H., Frege, C., Fuchs, C., Garmash, O., Gordon, H., He, X., Helm, J., Hofbauer, V., Hoyle, C. R., Kim, C., Kirkby, J., Kontkanen, J., Kürten, A., Lampilahti, J., Lawler, M., Lehtipalo, K., Leiminger, M., Mai, H., Mathot, S., Mentler, B., Molteni, U., Nie, W., Nieminen, T., Nowak, J. B., Ojdanic, A., Onnela, A., Passananti, M., Petäjä, T., Quéléver, L. L. J., Rissanen, M. P., Sarnela, N., Schallhart, S., Tauber, C., Tomé, A., Wagner, R., Wang, M., Weitz, L., Wimmer, D., Xiao, M., Yan, C., Ye, P., Zha, Q., Baltensperger, U., Curtius, J., Dommen, J., Flagan, R. C., Kulmala, M., Smith, J. N., Worsnop, D. R., Hansel, A., Donahue, N. M., and Winkler, P. M.: Rapid growth of organic aerosol nanoparticles over a wide tropospheric temperature range, Proceedings of the National Academy of Sciences, 115, 9122–9127, 2018.

Stolzenburg, D., Cai, R., Blichner, S. M., Kontkanen, J., Zhou, P., Makkonen, R., Kerminen, V.-M., Kulmala, M., Riipinen, I., and Kangasluoma, J.: Atmospheric nanoparticle growth, Reviews of Modern Physics, 95, 2023.

Stolzenburg, D., Sarnela, N., Bianchi, F., Cai, J., Cai, R., Cheng, Y., Dada, L., Donahue, N. M., Grothe, H., Holm, S., Kerminen, V.-M., Lehtipalo, K., Petäjä, T., Sulo, J., Winkler, P. M., Yan, C., Kangasluoma, J., and Kulmala, M.: Incomplete mass closure in atmospheric nanoparticle growth, npj Climate and Atmospheric Science, 8, 2025.

Tang, L., Feng, Z., Shang, D., Zeng, L., Wu, Z., Wang, H., Chen, S., Li, X., Zeng, L., Hu, J., and Hu, M.: Ongoing uncoordinated anthropogenic emission abatement promotes atmospheric new particle growth in a Chinese megacity, Nature Communications, 16, 2025.

Team, C. W., Lee, H., and Romero, J., eds.: Climate Change 2023: Synthesis Report. Contribution of Working Groups I, II and III to the Sixth Assessment Report of the Intergovernmental Panel on Climate Change, IPCC, Geneva, Switzerland, 2023.

10

Tröstl, J., Chuang, W. K., Gordon, H., Heinritzi, M., Yan, C., Molteni, U., Ahlm, L., Frege, C., Bianchi, F., Wagner, R., Simon, M., Lehtipalo, K., Williamson, C., Craven, J. S., Duplissy, J., Adamov, A., Almeida, J., Bernhammer, A.-K., Breitenlechner, M., Brilke, S., Dias, A., Ehrhart, S., Flagan, R. C., Franchin, A., Fuchs, C., Guida, R., Gysel, M., Hansel, A., Hoyle, C. R., Jokinen, T., Junninen, H., Kangasluoma, J., Keskinen, H., Kim, J., Krapf, M., Kürten, A., Laaksonen, A., Lawler, M., Leiminger, M., Mathot, S., Möhler, O., Nieminen, T., Onnela, A., Petäjä, T., Piel, F. M., Miettinen, P., Rissanen, M. P., Rondo, L., Sarnela, N., Schobesberger, S., Sengupta, K., Sipilä, M., Smith, J. N., Steiner, G., Tomè, A., Virtanen, A., Wagner, A. C., Weingartner, E., Wimmer, D., Winkler, P. M., Ye, P., Carslaw, K. S., Curtius, J., Dommen, J., Kirkby, J., Kulmala, M., Riipinen, I., Worsnop, D. R., Donahue, N. M., and Baltensperger, U.: The role of low-volatility organic compounds in initial particle growth in the atmosphere, Nature, 533, 527–531, 2016.

Virtanen, A., Joutsensaari, J., Koop, T., Kannosto, J., Yli-Pirilä, P., Leskinen, J., Mäkelä, J. M., Holopainen, J. K., Pöschl, U., Kulmala, M., Worsnop, D. R., and Laaksonen, A.: An amorphous solid state of biogenic secondary organic aerosol particles, Nature, 467, 824–827, 2010.

World Health Organization: Health workforce support and safeguards list 2023, Tech. rep., World Health Organization, Geneva, Switzerland, accessed: 2026 April 1, 2023.

3. Conclusions and outlook

Through this PhD project, we conclude that the viscous phase states of secondary organic aerosol (SOA) drastically lengthen gas-particle partitioning equilibrium timescales. Longer equilibrium timescales violate a key assumption in absorptive partitioning theory (Pankow, 1994), which presumes that particles are well-mixed and that gas-particle partitioning is fast. We showed with KM3C that the evaporation of higher-volatile organics from the surfaces of SOA from limonene + NO_3 leaves behind a viscous surface crust, under which higher-volatile species were trapped. We report that the chemical composition of SOA changes when partitioning is kinetically limited by diffusion. We also find that the initial growth rates of newly-formed viscous particles are kinetically limited by surface-bulk transfer, and particle phase state ought to be considered when modeling sub-10 nm nanoparticle growth.

In addition, cross reactions between the oxidation products originating from different VOC alter the resulting product volatility distribution by changing RO_2 fates and accretion product formation. We showed that accretion products from cross reactions explain the nonlinear Y_{SOA} found in multiprecursor experiments, which is consistent with other studies (Ahlberg et al., 2017; McFiggans et al., 2019). However, some experiments have found that linear additions of Y_{SOA} from different VOC can adequately describe SOA formation (Odum et al., 1996; Emanuelsson et al., 2013). Clarifying the cross reactions and fate of intermediate oxidation products from different VOC and revising chemical mechanisms in air quality models to include those cross reactions may improve model estimates of SOA formation.

Lastly, we conclude that the wide range of secondary organosiloxane aerosol (SOSiA) formation reported in previous studies (Wu and Johnston, 2017; Janechek et al., 2019; Charan et al., 2022) is the result of the different OH exposures (OH_{exp}, [OH] $\times$ time). We found that the immediate oxidation products of D_5 siloxane, which is an emerging anthropogenic pollutant, is too volatile to form secondary organosiloxane aerosol (SOSiA). We used a kinetic box model and chemical mechanism that incorporates chemical-aging reactions, where progressive oxidation of the D_5 + OH products reduces the volatility of those products, to conclude that the high SOSiA formation reported in previous studies (Wu and Johnston, 2017; Janechek et al., 2019; Charan et al., 2022) was driven by high OH_{exp}. While such high OH_{exp} are feasible in laboratory experiments, in the atmosphere, these conditions are more representative of air downwind of D_5 emissions sources. Thus, SOSiA is not likely a contributor to urban PM but may contribute to PM in downwind air. We recommend future D_5 + OH experiments consider the impact of multigenerational chemical aging on SOSiA formation, and ambient measurements searching for SOSiA should target the downwind of emissions sources. Furthermore,

we detected the production of HCHO in these experiments, which has been predicted for similar siloxanes by Fu et al. (2020), and quantified experimental HCHO yields upwards of 200 %. HCHO is known to contribute to tropospheric O_3 formation (Carter et al., 1993), and further study is needed to assess the effects of D_5 on air quality.

In this PhD project, we were able to use empirical D_b–C^* and T_g–C^* relationships (Frank, 1962; Li et al., 2020) to calculate the composition-based D_b in the model. However, the self-diffusivity data of the low C^* species these parameterizations are based on is sparse, and the calculated D_b can be better constrained with improved parameterizations. Furthermore, SOA is generally hygroscopic, and many parts of the global atmosphere are humid (Shiraiwa et al., 2017), while the experiments modeled here were dry. The plasticizing effects of water increases particle-phase diffusion (Berkemeier et al., 2016), and a full description of the relationships between SOA volatility, hygroscopicity, and diffusivity in SOA–water mixtures needs to be developed to account for particle phase affects in the the global atmosphere. Future studies thus will be able to reduce uncertainty in the modeling of organic aerosol phase state by by providing diffusivity coefficients through direct measurements (e.g., Evoy et al., 2021) or through simulations, such as molecular dynamics (e.g., Siachouli et al., 2025), with a focus on more complex mixtures and changing relative humidity.

4. Bibliography

Abbatt, J. P. D. and Ravishankara, A. R.: Opinion: Atmospheric multiphase chemistry – past, present, and future, Atmos. Chem. Phys., 23, 9765–9785, 2023.

Ahlberg, E., Falk, J., Eriksson, A., Holst, T., Brune, W. H., Kristensson, A., Roldin, P., and Svenningsson, B.: Secondary organic aerosol from VOC mixtures in an oxidation flow reactor, Atmos. Environ., 161, 210–220, 2017.

Aumont, B., Valorso, R., Mouchel-Vallon, C., Camredon, M., Lee-Taylor, J., and Madronich, S.: Modeling SOA formation from the oxidation of intermediate volatility *n* -alkanes, Atmos. Chem. Phys., 12, 7577–7589, 2012.

Berkemeier, T. and Pöschl, U.: Carbon Nanoparticle Oxidation by NO_2 and O_2 : Chemical Kinetics and Reaction Pathways, Angew. Chem. Int. Ed., 63, e202413 325, 2024.

Berkemeier, T., Shiraiwa, M., Pöschl, U., and Koop, T.: Competition between water uptake and ice nucleation by glassy organic aerosol particles, Atmos. Chem. Phys., 14, 12 513–12 531, 2014.

Berkemeier, T., Steimer, S. S., Krieger, U. K., Peter, T., Pöschl, U., Ammann, M., and Shiraiwa, M.: Ozone uptake on glassy, semi-solid and liquid organic matter and the role of reactive oxygen intermediates in atmospheric aerosol chemistry, Phys. Chem. Chem. Phys., 18, 12 662–12 674, 2016.

Berkemeier, T., Ammann, M., Krieger, U. K., Peter, T., Spichtinger, P., Pöschl, U., Shiraiwa, M., and Huisman, A. J.: Technical note: Monte Carlo genetic algorithm (MCGA) for model analysis of multiphase chemical kinetics to determine transport and reaction rate coefficients using multiple experimental data sets, Atmos. Chem. Phys., 17, 8021–8029, 2017.

Berkemeier, T., Takeuchi, M., Eris, G., and Ng, N. L.: Kinetic modeling of formation and evaporation of secondary organic aerosol from NO_3 oxidation of pure and mixed monoterpenes, Atmos. Chem. Phys., 20, 15 513–15 535, 2020.

Berkemeier, T., Mishra, A., Mattei, C., Huisman, A. J., Krieger, U. K., and Pöschl, U.: Ozonolysis of Oleic Acid Aerosol Revisited: Multiphase Chemical Kinetics and Reaction Mechanisms, ACS Earth Space Chem., 5, 3313–3323, 2021.

Brunet, C. E., Marek, R. F., Stanier, C. O., and Hornbuckle, K. C.: Concentrations of Volatile Methyl Siloxanes in New York City Reflect Emissions from Personal Care and Industrial Use, Environ. Sci. Technol., 58, 8835–8845, 2024.

Bufalini, J. J., Walter, T. A., and Bufalini, M. M.: Ozone formation potential of organic compounds, Environ. Sci. Technol., 10, 908–912, 1976.

Calvin, K., Dasgupta, D., Krinner, G., Mukherji, A., Thorne, P. W., Trisos, C., Romero, J., Aldunce, P., Barrett, K., Blanco, G., Cheung, W. W., Connors, S., Denton, F., Diongue-Niang, A., Dodman, D., Garschagen, M., Geden, O., Hayward, B., Jones, C., Jotzo, F., Krug, T., Lasco, R., Lee, Y.-Y., Masson-Delmotte, V., Meinshausen, M., Mintenbeck, K., Mokssit, A., Otto, F. E., Pathak, M., Pirani, A., Poloczanska, E., Pörtner, H.-O., Revi, A., Roberts, D. C., Roy, J., Ruane, A. C., Skea, J., Shukla, P. R., Slade, R., Slangen, A., Sokona, Y., Sörensson, A. A., Tignor, M., Van Vuuren, D., Wei, Y.-M., Winkler, H., Zhai, P., Zommers, Z., Hourcade, J.-C., Johnson, F. X., Pachauri, S., Simpson, N. P., Singh, C., Thomas, A., Totin, E., Alegría, A., Armour, K., Bednar-Friedl, B., Blok, K., Cissé, G., Dentener, F., Eriksen, S., Fischer, E., Garner, G., Guivarch, C., Haasnoot, M., Hansen, G., Hauser, M., Hawkins, E., Hermans, T., Kopp, R., Leprince-Ringuet, N., Lewis, J., Ley, D., Ludden, C., Niamir, L., Nicholls, Z., Some, S., Szopa, S., Trewin, B., Van Der Wijst, K.-I., Winter, G., Witting, M., Birt, A., Ha, M., Arias, P., Bustamante, M., Elgizouli, I., Flato, G., Howden, M., Méndez-Vallejo, C., Pereira, J. J., Pichs-Madruga, R., Rose, S. K., Saheb, Y., Sánchez Rodríguez, R., Ürge Vorsatz, D., Xiao, C., Yassaa, N., Romero, J., Kim, J., Haites, E. F., Jung, Y., Stavins, R., Birt, A., Ha, M., Orendain, D. J. A., Ignon, L., Park, S., Park, Y., Reisinger, A., Cammaramo, D., Fischlin, A., Fuglestvedt, J. S., Hansen, G., Ludden, C., Masson-Delmotte, V., Matthews, J. R., Mintenbeck, K., Pirani, A., Poloczanska, E., Leprince-Ringuet, N., and Péan, C.: IPCC, 2023: Climate Change 2023: Synthesis Report. Contribution of Working Groups I, II and III to the Sixth Assessment Report of the Intergovernmental Panel on Climate Change [Core Writing Team, H. Lee and J. Romero (eds.)]. IPCC, Geneva, Switzerland., Tech. rep., Intergovernmental Panel on Climate Change, 2023.

Carter, W. P. L., Pierce, J. A., Malkina, I. L., Luo, D., and Long, W. D.: Environmental Chamber Studies of Maximum Incremental Reactivities of Volatile Organic Compounds, Tech. rep., Statewide Air Pollution Research Center, University of California at Riverside, Riverside, CA 92521, 1993.

Charan, S. M., Huang, Y., Buenconsejo, R. S., Li, Q., Cocker Iii, D. R., and Seinfeld, J. H.: Secondary organic aerosol formation from the oxidation of decamethylcyclopentasiloxane at atmospherically relevant OH concentrations, Atmos. Chem. Phys., 22, 917–928, 2022.

Chen, J. and Luo, D.: Ozone formation potentials of organic compounds from different emission sources in the South Coast Air Basin of California, Atmos. Environ., 55, 448–455, 2012.

Coggon, M. M., Gkatzelis, G. I., McDonald, B. C., Gilman, J. B., Schwantes, R. H., Abuhassan, N., Aikin, K. C., Arend, M. F., Berkoff, T. A., Brown, S. S., Campos, T. L., Dickerson, R. R., Gronoff, G., Hurley, J. F., Isaacman-VanWertz, G., Koss, A. R., Li, M., McKeen, S. A., Moshary, F., Peischl, J., Pospisilova, V., Ren, X., Wilson, A., Wu, Y.,

Trainer, M., and Warneke, C.: Volatile chemical product emissions enhance ozone and modulate urban chemistry, Proc. Natl. Acad. Sci. U.S.A., 118, e2026653 118, 2021.

Compernolle, S., Ceulemans, K., and Müller, J.-F.: EVAPORATION: a new vapour pressure estimation methodfor organic molecules including non-additivity and intramolecular interactions, Atmos. Chem. Phys., 11, 9431–9450, 2011.

Donahue, N. M., Robinson, A. L., Stanier, C. O., and Pandis, S. N.: Coupled Partitioning, Dilution, and Chemical Aging of Semivolatile Organics, Environ. Sci. Technol., 40, 2635–2643, 2006.

Einstein, A.: Über die von der molekularkinetischen Theorie der Wärme geforderte Bewegung von in ruhenden Flüssigkeiten suspendierten Teilchen, Ann. Phys., 322, 549–560, 1905.

Emanuelsson, E. U., Hallquist, M., Kristensen, K., Glasius, M., Bohn, B., Fuchs, H., Kammer, B., Kiendler-Scharr, A., Nehr, S., Rubach, F., Tillmann, R., Wahner, A., Wu, H.-C., and Mentel, T. F.: Formation of anthropogenic secondary organic aerosol (SOA) and its influence on biogenic SOA properties, Atmos. Chem. Phys., 13, 2837–2855, 2013.

Evoy, E., Kiland, K. J., Huang, Y., Schnitzler, E. G., Maclean, A. M., Kamal, S., Abbatt, J. P. D., and Bertram, A. K.: Diffusion Coefficients and Mixing Times of Organic Molecules in β-Caryophyllene Secondary Organic Aerosol (SOA) and Biomass Burning Organic Aerosol (BBOA), ACS Earth Space Chem., 5, 3268–3278, 2021.

Feng, Y., Ramanathan, V., and Kotamarthi, V. R.: Brown carbon: a significant atmospheric absorber of solar radiation?, Atmos. Chem. Phys., 13, 8607–8621, 2013.

Frank, A.: Viscosity-vapor pressure correlation of alcohols, methyl ketones and alkyl halides, Master's thesis, Newark College of Engineering, Newark, New Jersey, 1962.

Fu, Z., Xie, H.-B., Elm, J., Guo, X., Fu, Z., and Chen, J.: Formation of Low-Volatile Products and Unexpected High Formaldehyde Yield from the Atmospheric Oxidation of Methylsiloxanes, Environ. Sci. Technol., 54, 7136–7145, 2020.

Galeazzo, T., Aumont, B., Camredon, M., Valorso, R., Lim, Y. B., Ziemann, P. J., and Shiraiwa, M.: Secondary organic aerosols derived from intermediate-volatility n-alkanes adopt low-viscous phase state, Atmos. Chem. Phys., 24, 5549–5565, 2024.

George, C., Ammann, M., D'Anna, B., Donaldson, D. J., and Nizkorodov, S. A.: Heterogeneous Photochemistry in the Atmosphere, Chem. Rev., 115, 4218–4258, 2015.

George, I. J. and Abbatt, J. P. D.: Heterogeneous oxidation of atmospheric aerosol particles by gas-phase radicals, Nat. Chem., 2, 713–722, 2010.

Hall, W. A. and Johnston, M. V.: The Thermal-Stability of Oligomers in Alpha-Pinene Secondary Organic Aerosol, Aerosol Sci. Technol., 46, 983–989, 2012.

Heitto, A., Lehtinen, K., Petäjä, T., Lopez-Hilfiker, F., Thornton, J. A., Kulmala, M., and Yli-Juuti, T.: Effects of oligomerization and decomposition on the nanoparticle growth: a model study, Atmos. Chem. Phys., 22, 155–171, 2022.

Huang, C., Wang, H. L., Li, L., Wang, Q., Lu, Q., De Gouw, J. A., Zhou, M., Jing, S. A., Lu, J., and Chen, C. H.: VOC species and emission inventory from vehicles and their SOA formation potentials estimation in Shanghai, China, Atmos. Chem. Phys., 15, 11 081–11 096, 2015.

Janechek, N. J., Marek, R. F., Bryngelson, N., Singh, A., Bullard, R. L., Brune, W. H., and Stanier, C. O.: Physical properties of secondary photochemical aerosol from OH oxidation of a cyclic siloxane, Atmos. Chem. Phys., 19, 1649–1664, 2019.

Jimenez, J. L., Canagaratna, M. R., Donahue, N. M., Prevot, A. S. H., Zhang, Q., Kroll, J. H., DeCarlo, P. F., Allan, J. D., Coe, H., Ng, N. L., Aiken, A. C., Docherty, K. S., Ulbrich, I. M., Grieshop, A. P., Robinson, A. L., Duplissy, J., Smith, J. D., Wilson, K. R., Lanz, V. A., Hueglin, C., Sun, Y. L., Tian, J., Laaksonen, A., Raatikainen, T., Rautiainen, J., Vaattovaara, P., Ehn, M., Kulmala, M., Tomlinson, J. M., Collins, D. R., Cubison, M. J., E., Dunlea, J., Huffman, J. A., Onasch, T. B., Alfarra, M. R., Williams, P. I., Bower, K., Kondo, Y., Schneider, J., Drewnick, F., Borrmann, S., Weimer, S., Demerjian, K., Salcedo, D., Cottrell, L., Griffin, R., Takami, A., Miyoshi, T., Hatakeyama, S., Shimono, A., Sun, J. Y., Zhang, Y. M., Dzepina, K., Kimmel, J. R., Sueper, D., Jayne, J. T., Herndon, S. C., Trimborn, A. M., Williams, L. R., Wood, E. C., Middlebrook, A. M., Kolb, C. E., Baltensperger, U., and Worsnop, D. R.: Evolution of Organic Aerosols in the Atmosphere, Science, 326, 1525–1529, 2009.

Johnston, W. G. and Sargent, L. B.: The Determination of Vapor Pressures of Low Viscosity Lubricants from Distillation Data, A S L E Transactions, 13, 304–310, 1970.

Jokinen, T., Berndt, T., Makkonen, R., Kerminen, V.-M., Junninen, H., Paasonen, P., Stratmann, F., Herrmann, H., Guenther, A. B., Worsnop, D. R., Kulmala, M., Ehn, M., and Sipilä, M.: Production of extremely low volatile organic compounds from biogenic emissions: Measured yields and atmospheric implications, Proc. Natl. Acad. Sci. U.S.A., 112, 7123–7128, 2015.

Kenagy, H. S., Heald, C. L., Tahsini, N., Goss, M. B., and Kroll, J. H.: Can we achieve atmospheric chemical environments in the laboratory? An integrated model-measurement approach to chamber SOA studies, Sci. Adv., 10, eado1482, 2024.

Koo, B., Knipping, E., and Yarwood, G.: 1.5-Dimensional volatility basis set approach for modeling organic aerosol in CAMx and CMAQ, Atmos. Environ., 95, 158–164, 2014.

Kourtchev, I., Giorio, C., Manninen, A., Wilson, E., Mahon, B., Aalto, J., Kajos, M., Venables, D., Ruuskanen, T., Levula, J., Loponen, M., Connors, S., Harris, N., Zhao, D., Kiendler-Scharr, A., Mentel, T., Rudich, Y., Hallquist, M., Doussin, J.-F., Maenhaut, W., Bäck, J., Petäjä, T., Wenger, J., Kulmala, M., and Kalberer, M.: Enhanced Volatile Organic Compounds emissions and organic aerosol mass increase the oligomer content of atmospheric aerosols, Sci. Rep., 6, 35 038, 2016.

Krüger, M., Galeazzo, T., Eremets, I., Schmidt, B., Pöschl, U., Shiraiwa, M., and Berkemeier, T.: Improved vapor pressure predictions using group contribution-assisted graph convolutional neural networks (GC^2 NN), Geosci. Model Dev., 18, 7357–7371, 2025.

Lannuque, V., Camredon, M., Couvidat, F., Hodzic, A., Valorso, R., Madronich, S., Bessagnet, B., and Aumont, B.: Exploration of the influence of environmental conditions on secondary organic aerosol formation and organic species properties using explicit simulations: development of the VBS-GECKO parameterization, Atmos. Chem. Phys., 18, 13 411–13 428, 2018.

Li, J., Carlson, B. E., Yung, Y. L., Lv, D., Hansen, J., Penner, J. E., Liao, H., Ramaswamy, V., Kahn, R. A., Zhang, P., Dubovik, O., Ding, A., Lacis, A. A., Zhang, L., and Dong, Y.: Scattering and absorbing aerosols in the climate system, Nat. Rev. Earth Environ., 3, 363–379, 2022.

Li, Y., Day, D. A., Stark, H., Jimenez, J. L., and Shiraiwa, M.: Predictions of the glass transition temperature and viscosity of organic aerosols from volatility distributions, Atmos. Chem. Phys., 20, 8103–8122, 2020.

Lopez-Hilfiker, F. D., Mohr, C., Ehn, M., Rubach, F., Kleist, E., Wildt, J., Mentel, T. F., Lutz, A., Hallquist, M., Worsnop, D., and Thornton, J. A.: A novel method for online analysis of gas and particle composition: description and evaluation of a Filter Inlet for Gases and AEROsols (FIGAERO), Atmos. Meas. Tech., 7, 983–1001, 2014.

McDonald, B. C., De Gouw, J. A., Gilman, J. B., Jathar, S. H., Akherati, A., Cappa, C. D., Jimenez, J. L., Lee-Taylor, J., Hayes, P. L., McKeen, S. A., Cui, Y. Y., Kim, S.-W., Gentner, D. R., Isaacman-VanWertz, G., Goldstein, A. H., Harley, R. A., Frost, G. J., Roberts, J. M., Ryerson, T. B., and Trainer, M.: Volatile chemical products emerging as largest petrochemical source of urban organic emissions, Science, 359, 760–764, 2018.

McFiggans, G., Mentel, T. F., Wildt, J., Pullinen, I., Kang, S., Kleist, E., Schmitt, S., Springer, M., Tillmann, R., Wu, C., Zhao, D., Hallquist, M., Faxon, C., Le Breton, M., Hallquist, M., Simpson, D., Bergström, R., Jenkin, M. E., Ehn, M., Thornton, J. A., Alfarra, M. R., Bannan, T. J., Percival, C. J., Priestley, M., Topping, D., and Kiendler-Scharr, A.: Secondary organic aerosol reduced by mixture of atmospheric vapours, Nature, 565, 587–593, 2019.

Mishra, A., Lelieveld, S., Pöschl, U., and Berkemeier, T.: Multiphase Kinetic Modeling of Air Pollutant Effects on Protein Modification and Nitrotyrosine Formation in Epithelial Lining Fluid, Environ. Sci. Technol., 57, 12 642–12 653, 2023.

Mishra, A., Kilchhofer, K., Iezzi, L., Pöschl, U., Alpert, P. A., Ammann, M., and Berkemeier, T.: Photochemical Degradation of Iron Citrate in Anoxic Viscous Films Enhanced by Redox Cascades, ACS Earth Space Chem., 9, 689–698, 2025.

Mitra, S. S.: Relation between Vapor Pressure and Viscosity of Liquids, J. Chem. Phys., 22, 349–350, 1954.

Nault, B. A., Jo, D. S., McDonald, B. C., Campuzano-Jost, P., Day, D. A., Hu, W., Schroder, J. C., Allan, J., Blake, D. R., Canagaratna, M. R., Coe, H., Coggon, M. M., DeCarlo, P. F., Diskin, G. S., Dunmore, R., Flocke, F., Fried, A., Gilman, J. B., Gkatzelis, G., Hamilton, J. F., Hanisco, T. F., Hayes, P. L., Henze, D. K., Hodzic, A., Hopkins, J., Hu, M., Huey, L. G., Jobson, B. T., Kuster, W. C., Lewis, A., Li, M., Liao, J., Nawaz, M. O., Pollack, I. B., Peischl, J., Rappenglück, B., Reeves, C. E., Richter, D., Roberts, J. M., Ryerson, T. B., Shao, M., Sommers, J. M., Walega, J., Warneke, C., Weibring, P., Wolfe, G. M., Young, D. E., Yuan, B., Zhang, Q., De Gouw, J. A., and Jimenez, J. L.: Secondary organic aerosols from anthropogenic volatile organic compounds contribute substantially to air pollution mortality, Atmos. Chem. Phys., 21, 11 201–11 224, 2021.

Oberdörster, G., Sharp, Z., Atudorei, V., Elder, A., Gelein, R., Lunts, A., Kreyling, W., and Cox, C.: Extrapulmonary Translocation of Ultrafine Carbon Particles following Whole-body Inhalation Exposure of Rats, J. Toxicol. Environ. Health Part A, 65, 1531–1543, 2002.

Odum, J. R., Hoffmann, T., Bowman, F., Collins, D., Flagan, R. C., and Seinfeld, J. H.: Gas/Particle Partitioning and Secondary Organic Aerosol Yields, Environ. Sci. Technol., 30, 2580–2585, 1996.

Pankow, J. F.: An absorption model of the gas/aerosol partitioning involved in the formation of secondary organic aerosol, Atmos. Environ., 28, 189–193, 1994.

Pankow, J. F. and Asher, W. E.: SIMPOL.1: a simple group contribution method for predicting vapor pressures and enthalpies of vaporization of multifunctional organic compounds, Atmos. Chem. Phys., 8, 2773–2796, 2008.

Pope, C. A., Coleman, N., Pond, Z. A., and Burnett, R. T.: Fine particulate air pollution and human mortality: 25+ years of cohort studies, Environ. Res., p. 108924, 2019.

Pozzer, A., Reifenberg, S. F., Kumar, V., Franco, B., Kohl, M., Taraborrelli, D., Gromov, S., Ehrhart, S., Jöckel, P., Sander, R., Fall, V., Rosanka, S., Karydis, V., Akritidis, D., Emmerichs, T., Crippa, M., Guizzardi, D., Kaiser, J. W., Clarisse, L., Kiendler-Scharr, A., Tost, H., and Tsimpidi, A.: Simulation of organics in the atmosphere: evaluation of EMACv2.54 with the Mainz Organic Mechanism (MOM) coupled to the ORACLE (v1.0) submodel, Geosci. Model Dev., 15, 2673–2710, 2022.

Pöschl, U.: Atmospheric Aerosols: Composition, Transformation, Climate and Health Effects, Angew. Chem. Int. Ed., 44, 7520–7540, 2005.

Pöschl, U., Rudich, Y., and Ammann, M.: Kinetic model framework for aerosol and cloud surface chemistry and gas-particle interactions – Part 1: General equations, parameters, and terminology, Atmos. Chem. Phys., 7, 5989–6023, 2007.

Ravishankara, A. R.: Heterogeneous and Multiphase Chemistry in the Troposphere, Science, 276, 1058–1065, 1997.

Robinson, A. L., Donahue, N. M., Shrivastava, M. K., Weitkamp, E. A., Sage, A. M., Grieshop, A. P., Lane, T. E., Pierce, J. R., and Pandis, S. N.: Rethinking Organic Aerosols: Semivolatile Emissions and Photochemical Aging, Science, 315, 1259–1262, 2007.

Rücker, C. and Kümmerer, K.: Environmental Chemistry of Organosiloxanes, Chem. Rev., 115, 466–524, 2015.

Safiri, S., Carson-Chahhoud, K., Noori, M., Nejadghaderi, S. A., Sullman, M. J. M., Ahmadian Heris, J., Ansarin, K., Mansournia, M. A., Collins, G. S., Kolahi, A.-A., and Kaufman, J. S.: Burden of chronic obstructive pulmonary disease and its attributable risk factors in 204 countries and territories, 1990-2019: results from the Global Burden of Disease Study 2019, BMJ, 378, e069 679, 2022.

Saunders, S. M., Jenkin, M. E., Derwent, R. G., and Pilling, M. J.: Protocol for the development of the Master Chemical Mechanism, MCM v3 (Part A): tropospheric degradation of non-aromatic volatile organic compounds, Atmos. Chem. Phys., 3, 161–180, publisher: Copernicus GmbH, 2003.

Schmedding, R., Rasool, Q. Z., Zhang, Y., Pye, H. O. T., Zhang, H., Chen, Y., Surratt, J. D., Lopez-Hilfiker, F. D., Thornton, J. A., Goldstein, A. H., and Vizuete, W.: Predicting secondary organic aerosol phase state and viscosity and its effect on multiphase chemistry in a regional-scale air quality model, Atmos. Chem. Phys., 20, 8201–8225, 2020.

Schobesberger, S., D'Ambro, E. L., Lopez-Hilfiker, F. D., Mohr, C., and Thornton, J. A.: A model framework to retrieve thermodynamic and kinetic properties of organic aerosol from composition-resolved thermal desorption measurements, Atmos. Chem. Phys., 18, 14 757–14 785, 2018.

Schraufnagel, D. E.: The health effects of ultrafine particles, Exp. Mol. Med., 52, 311–317, 2020.

Seinfeld, J. H.: Atmospheric Chemistry and Physics: From Air Pollution to Climate Change, New York Academy of Sciences Series, John Wiley & Sons, Incorporated, Newark, 1st ed edn., ISBN 978-1-118-94740-1 978-1-119-22116-6, 2016.

Seltzer, K. M., Pennington, E., Rao, V., Murphy, B. N., Strum, M., Isaacs, K. K., and Pye, H. O. T.: Reactive organic carbon emissions from volatile chemical products, Atmos. Chem. Phys., 21, 5079–5100, 2021.

Shiraiwa, M., Pfrang, C., and Pöschl, U.: Kinetic multi-layer model of aerosol surface and bulk chemistry (KM-SUB): the influence of interfacial transport and bulk diffusion on the oxidation of oleic acid by ozone, Atmos. Chem. Phys., 10, 3673–3691, 2010.

Shiraiwa, M., Ammann, M., Koop, T., and Pöschl, U.: Gas uptake and chemical aging of semisolid organic aerosol particles, Proc. Natl. Acad. Sci. U.S.A., 108, 11 003–11 008, 2011.

Shiraiwa, M., Pfrang, C., Koop, T., and Pöschl, U.: Kinetic multi-layer model of gas-particle interactions in aerosols and clouds (KM-GAP): linking condensation, evaporation and chemical reactions of organics, oxidants and water, Atmos. Chem. Phys., 12, 2777–2794, 2012.

Shiraiwa, M., Zuend, A., Bertram, A. K., and Seinfeld, J. H.: Gas–particle partitioning of atmospheric aerosols: interplay of physical state, non-ideal mixing and morphology, Phys. Chem. Chem. Phys., 15, 11 441–11 453, 2013.

Shiraiwa, M., Li, Y., Tsimpidi, A. P., Karydis, V. A., Berkemeier, T., Pandis, S. N., Lelieveld, J., Koop, T., and Pöschl, U.: Global distribution of particle phase state in atmospheric secondary organic aerosols, Nat. Commun., 8, 15 002, 2017.

Shrivastava, M., Cappa, C. D., Fan, J., Goldstein, A. H., Guenther, A. B., Jimenez, J. L., Kuang, C., Laskin, A., Martin, S. T., Ng, N. L., Petaja, T., Pierce, J. R., Rasch, P. J., Roldin, P., Seinfeld, J. H., Shilling, J., Smith, J. N., Thornton, J. A., Volkamer, R., Wang, J., Worsnop, D. R., Zaveri, R. A., Zelenyuk, A., and Zhang, Q.: Recent advances in understanding secondary organic aerosol: Implications for global climate forcing, Rev. Geophys., 55, 509–559, 2017.

Siachouli, P., Mavrantzas, V. G., and Pandis, S. N.: Predicting and parameterizing the glass transition temperature of atmospheric organic aerosol components *via* molecular dynamics simulations, Soft Matter, 21, 3880–3889, 2025.

Sommers, J. M., Stroud, C. A., Adam, M. G., O'Brien, J., Brook, J. R., Hayden, K., Lee, A. K. Y., Li, K., Liggio, J., Mihele, C., Mittermeier, R. L., Stevens, R. G., Wolde, M., Zuend, A., and Hayes, P. L.: Evaluating SOA formation from different sources of semi- and intermediate-volatility organic compounds from the Athabasca oil sands, Environ. Sci.: Atmos., 2, 469–490, 2022.

Srivastava, D., Vu, T. V., Tong, S., Shi, Z., and Harrison, R. M.: Formation of secondary organic aerosols from anthropogenic precursors in laboratory studies, npj Clim. Atmos. Sci., 5, 22, 2022.

Stolzenburg, D., Fischer, L., Vogel, A. L., Heinritzi, M., Schervish, M., Simon, M., Wagner, A. C., Dada, L., Ahonen, L. R., Amorim, A., Baccarini, A., Bauer, P. S., Baumgartner, B., Bergen, A., Bianchi, F., Breitenlechner, M., Brilke, S., Buenrostro Mazon, S., Chen, D., Dias, A., Draper, D. C., Duplissy, J., El Haddad, I., Finkenzeller, H., Frege, C., Fuchs, C., Garmash, O., Gordon, H., He, X., Helm, J., Hofbauer, V., Hoyle, C. R., Kim, C., Kirkby, J., Kontkanen, J., Kürten, A., Lampilahti, J., Lawler, M., Lehtipalo, K., Leiminger, M., Mai, H., Mathot, S., Mentler, B., Molteni, U., Nie, W., Nieminen, T., Nowak, J. B., Ojdanic, A., Onnela, A., Passananti, M., Petäjä, T., Quéléver, L. L. J., Rissanen, M. P., Sarnela, N., Schallhart, S., Tauber, C., Tomé, A., Wagner, R., Wang, M., Weitz, L., Wimmer, D., Xiao, M., Yan, C., Ye, P., Zha, Q., Baltensperger, U., Curtius, J., Dommen, J., Flagan, R. C., Kulmala, M., Smith, J. N., Worsnop, D. R., Hansel, A., Donahue, N. M., and Winkler, P. M.: Rapid growth of organic aerosol nanoparticles over a wide tropospheric temperature range, Proc. Natl. Acad. Sci. U.S.A., 115, 9122–9127, 2018.

Stolzenburg, D., Wang, M., Schervish, M., and Donahue, N. M.: Tutorial: Dynamic organic growth modeling with a volatility basis set, J. Aerosol Sci., 166, 106 063, 2022.

Stolzenburg, D., Sarnela, N., Bianchi, F., Cai, J., Cai, R., Cheng, Y., Dada, L., Donahue, N. M., Grothe, H., Holm, S., Kerminen, V.-M., Lehtipalo, K., Petäjä, T., Sulo, J., Winkler, P. M., Yan, C., Kangasluoma, J., and Kulmala, M.: Incomplete mass closure in atmospheric nanoparticle growth, npj Clim. Atmos. Sci., 8, 75, 2025.

Takeuchi, M., Berkemeier, T., Eris, G., and Ng, N. L.: Non-linear effects of secondary organic aerosol formation and properties in multi-precursor systems, Nat. Commun., 13, 7883, 2022.

Thoma, M., Bachmeier, F., Gottwald, F. L., Simon, M., and Vogel, A. L.: Mass spectrometry-based *Aerosolomics* : a new approach to resolve sources, composition, and partitioning of secondary organic aerosol, Atmos. Meas. Tech., 15, 7137–7154, 2022.

Woodman, A. L., Murbach, W. J., and Kaufman, M. H.: Vapor pressure and viscosity relationships for a homologous series of α,ω-dinitriles, J. Phys. Chem., 64, 658–660, 1960.

Woody, M. C., Baker, K. R., Hayes, P. L., Jimenez, J. L., Koo, B., and Pye, H. O. T.: Understanding sources of organic aerosol during CalNex-2010 using the CMAQ-VBS, Atmos. Chem. Phys., 16, 4081–4100, 2016.

Wu, Y. and Johnston, M. V.: Aerosol Formation from OH Oxidation of the Volatile Cyclic Methyl Siloxane (cVMS) Decamethylcyclopentasiloxane, Environ. Sci. Technol., 51, 4445–4451, 2017.

Zhang, D., Comstock, J., Sivaraman, C., Mo, K., Krishnamurthy, R., Tian, J., Su, T., Li, Z., and Roldán-Henao, N.: Best estimate of the planetary boundary layer height from multiple remote sensing measurements, Atmos. Meas. Tech., 18, 3453–3475, 2025.

Zhang, Z., Xu, W., Lambe, A. T., Hu, W., Liu, T., and Sun, Y.: Insights Into Formation and Aging of Secondary Organic Aerosol From Oxidation Flow Reactors: A Review, Curr. Pollut. Rep., 10, 387–400, 2024.

Zhao, Y., Yang, X., Du, Y., Chen, L., Dong, J., Hu, T., Sun, N., Sun, Q., Liang, W., Wei, X., and Zhang, Z.: Global cardiovascular disease burden attributable to particulate matter pollution, 1990–2021: an analysis of the global burden of disease study 2021 and forecast to 2045, BMC Cardiovasc. Disord., 25, 401, 2025.

A. Personal List of Publications

Journal Articles

1. Zhang, Z., Kang, H. G., Pöschl, U., Berkemeier, T.: Temperature-dependent multiphase chemical kinetics explain uniform atmospheric nanoparticle growth rates, *in preparation*.

2. Kang, H. G., Takeuchi, M., Ng, N. L., Pöschl, U., and Berkemeier, T.: Multiphase chemistry and phase state explain nonlinear effects in the formation and evaporation of SOA from mixed monoterpene precursors, *ACS ES&T Air*, *in press* (2026).

3. Schervish, M., Kang, H. G., Wingen, L. M., Nguyen, K., Begay, C., Wilson, J., Shrivastava, M., Chen, Y., Schilling, J. E., Ng, N. L., Pöschl, U., Berkemeier, T., Zelenyuk, A., Shiraiwa, M.: Surface crust formation controls evaporation kinetics of secondary organic aerosols, *Environ. Sci. Technol.* **60**, 7995-8006 (2026).

4. Kim, H., Jeong, J., Moon, J., Kang, H. G.: Source-resolved volatility and oxidation state decoupling in wintertime organic aerosols in Seoul, *Atmos. Chem. Phys.* **26**, 1145-1161 (2026).

5. Kang, H. G., Chen, Y., Park, Y., Berkemeier, T., Kim, H.: Volatile oxidation products and secondary organosiloxane aerosol from D_5 + OH at varying OH exposures, *Atmos. Chem. Phys.* **23**, 14307-14323 (2023).

6. Chen, Y., Kang, H. G., Jeong, J., Kim, H.: Chemical characterization and formation of secondary organosiloxane aerosol (SOSiA) from OH oxidation of decamethylcyclopentasiloxane, *Environ. Sci.: Atmos.* **3**, 662-671 (2023).

Oral presentations

1. Kang, H. G., Eremets, I., Leitner, J., Pöschl, U., and Berkemeier, T.: Reaction kinetics and pathways of carbon nanoparticle oxidation and gasification by NO_x, O_2, and H_2O, 13th International Freiberg Conference on Circular Carbon Technologies, Prague, Czechia, 15th - 19th September 2025.

2. Kang, H. G., Takeuchi, M., Ng, N. L., Ylisirniö, A., Schobesberger, S., Pöschl, U., and Berkemeier, T.: A kinetic model for the formation and thermal desorption of

secondary organic aerosol, European Aerosol Conference, Tampere, Finland, 25th - 30th August 2024.

3. Kang, H. G., Chen, Y., Park, Y., Pöschl, U., Berkemeier, T., Kim, H.: Gas-phase Products and Secondary Organosiloxane Aerosol from D_5 + OH in an Oxidation Flow Reactor, 11th International Aerosol Conference, Athens, Greece, 4th - 9th September 2022.

Poster presentations

1. Kang, H. G., Eremets, I., Leitner, J., Pöschl, U., and Berkemeier, T.: Multiphase chemical kinetics of carbon nanoparticle oxidation and synthesis gas production, Max Planck Network on Sustainable Materials Kick-off Workshop, Potsdam, Germany, 21st - 22nd October 2025.

2. Kang, H. G., Takeuchi, M., Ng, N. L., Li, Z., Schobesberger, S., Pöschl, U., and Berkemeier, T.: Intertwined effects between volatility and bulk diffusivity in the growth and evaporation of secondary organic aerosol, 2nd Conference on Multiscale Modeling of Complex Systems, Mainz, Germany, 1st - 5th September 2025.

3. Kang, H. G., Takeuchi, M., Ng, N. L., Pöschl, U., and Berkemeier, T.: Non-linear effects in the formation, evaporation, and thermal desorption of mixed monoterpene secondary organic aerosol, Chemistry of Clouds Conference, Sønderborg, Denmark, 6th - 9th April 2025.

4. Kang, H. G., Chen, Y., Park, Y., Pöschl, U., Berkemeier, T., Kim, H.: Oxidation Products and Aerosol Yields from D_5 Siloxane, an Emerging Urban Pollutant, 782 WE-Heraeus-Seminar: Aerosols, Health and Climate: Gigacity and Future, Bad Honnef, Germany, 20th - 24th March 2023.

B. Supplement

B.1 Supplement of "Volatile oxidation products and secondary organosiloxane aerosol from D_5 + OH at varying OH exposures"

Supplement of Atmos. Chem. Phys., 23, 14307–14323, 2023
https://doi.org/10.5194/acp-23-14307-2023-supplement
© Author(s) 2023. CC BY 4.0 License.



Atmospheric Chemistry and Physics
Open Access
EGU

Supplement of

Volatile oxidation products and secondary organosiloxane aerosol from $D_5 + OH$ at varying OH exposures

Hyun Gu Kang et al.

Correspondence to: Thomas Berkemeier (t.berkemeier@mpic.de) and Hwajin Kim (khj0116@snu.ac.kr)

The copyright of individual parts of the supplement might differ from the article licence.

S1 Experiment and Set Up Details

S1.1 PAM-OFR

Fig. S1 shows the experiment set up. During these experiments, the laboratory room temperatures and pressures were 17 – 21 °C and ~1020 hPa (1 atm) respectively. In this manuscript, we used 1 atm for unit conversions and in KinSim. We passed different flow ratios of dry and humid zero air through the passivated 15 mL glass bulb to get the desired experiment humidity conditions. Mass flow controllers (MFC, MC and MCS series, Alicat Scientific, Tucson, AZ, USA) controlled the input air flow rates. Air coming out of the PAM-OFR and instrument outlets went to the exhaust or through scrubbers to minimize O_3 and aerosol exposure in the room. Ultra-high purity N_2 from a gas cylinder (Sinyang Oxygen Company, Seoul, South Korea) regulated to 30 psig purged the UV lamps.

The PAM-OFR was connected to an O_3 monitor (Model UV-100, 2B Technologies, Boulder, CO, USA) via the outlet side port. For the 120 s τ_{res} experiment, a pump was attached to the outlet side port for additional flow. The PTR-MS inlet and the aerosol sampling line was connected at the OFR outlet center port (Fig. S1). We used perfluoroalkoxy alkane (PFA) tubing (6.35 mm (1/4") OD, 4.35 mm ID, Sungjin Rubber Industrial, Seoul, South Korea) for the connections to the OFR inlet. The OFR was equipped with conductive Teflon flow rings at both the inlet and the outlet side ports, and the D_5 and humid air were injected through the inlet side port.

We used D_5 (97 %, CAS#541-02-6, Sigma-Aldrich, Saint Louis, MO, USA) as the VOC precursor and stored the D_5 in a refrigerator (~1 °C) when not in use. A syringe pump (Fusion 4000, Chemyx, Stafford, TX, USA) equipped with a 10 uL gas-tight microliter syringe (Model 1801, Hamilton, Reno, NV, USA) continuously injected D_5 into the PAM-OFR. The syringe fed into the passivated glass bulb through a polytetrafluoroethylene-faced (PTFE) septa (13 mm, Scilab, Seoul, South Korea) at room temperature. At the injection speeds and air flow rates used, we did not visually observe any D_5 build-up in the bulb.

For cleaning, making atomizer solutions, and generating humid air for the PAM-OFR, we used Type 1 deionized water (DI water, >18.2 MΩ cm resistivity at 25 °C) from a purification system (Milli-Q Direct 16, Merck, Darmstadt, Germany). We rinsed the microliter syringe between experiments with acetone and DI water and dried them at room temperature in the fume hood. The passivated glass bulb was also rinsed with acetone and DI water and heated in a drying oven before the experiments.

Zero air came from a generator (Model 8301P, Acoem Ecotech, Victoria, Australia) coupled with a catalytic converter set to 520 °C (Model HTO-1000HC, Acoem Ecotech, Victoria, Australia). The zero air also passed through scrubbers filled with

activated molecular sieves (4 Å 4 – 8 mesh, Sigma-Aldrich, Saint Louis, MO, USA), $NaMnO_4$ oxidizing media (Purafil SP, Purafil, Doraville, GA, USA), and activated carbon (Purakol, Purafil, Doraville, GA, USA). Lastly, the zero air went through a filtered air supply (Model 3074B, TSI, Shoreview, MN, USA) prior to injection to the PAM-OFR and the Nafion humidifier (FC-100-80-6MKK, Perma Pure, Lakewood, NJ, USA).

To assess the OH_{exp} range, we conducted an offline calibration on the PAM-OFR with calibration CO gas (UnionGas, Gyeonggi-do, South Korea) with a Serinus 30i CO analyzer (Acoem Ecotech, Victoria, Australia). We used humidity conditions close to that of the experiments (Fig. S2). We used the D_5 siloxane trace as a direct measure of OH_{exp} during the experiments themselves and found the OH_{exp} assessed with D_5 to be consistent with the offline calibration with CO. We did not operate the CO analyzer during the experiments to avoid the risk of siloxanes fouling its catalytic converter (Dewil et al., 2006).

S1.2 Aerosol Sampling Line

The aerosol sampling line was connected at the PAM-OFR center outlet port and lead to the SMPS. The sampling line consisted of a O_3 denuder and a Nafion dryer (PD-200T-12MSS, Perma Pure, Lakewood, NJ, USA) with conductive connections and fittings in between. We installed the O_3 denuder in the sampling line to prevent O_3 damage to the SMPS, and it was a diffusion denuder filled with hopcalite pellets (3 mm, Purelyst MD-101, Pure Sphere, Chungcheongnam-do, South Korea). The custom-made diffusion denuder was cylindrical in shape at 52 cm long and 6.5 cm in diameter, and the wet particles would pass through a 12.7 mm (1/2") ID center line made of stainless mesh. Prior to experiments, we passed filtered compressed air through the O_3 denuder at 10 L min^{-1} for ~30 min to remove any loose particles.

We assessed the O_3 removal by comparing the concentrations entering and exiting the O_3 denuder filled with fresh hopcalite pellets. The flow rate through the O_3 denuder matched that of experiments (3.0 L min^{-1}), and we used the same O_3 monitor used on the PAM-OFR. To generate O_3, humid air was fed into the OFR with 185 nm lights on without siloxanes or seed, and the OFR outputted 2.1 ppm of O_3. We found that the denuder would remove ~90 % of the O_3 by concentration at these test conditions.

We used the particle loss calculator (von der Weiden et al., 2009) with the dimensions of the aerosol sampling line to calculate the size dependent losses in the line (Fig. S3). Given that we did not know at what point when the SOSiA was formed in the PAM-OFR, we only applied the particle loss in the aerosol sampling line to correct the Y_{SOSiA}. The particle loss corrections to the Y_{SOSiA} were done by applying the particle loss at the experiment SOSiA volume mode with that from the calculator.

To prevent siloxane contamination from conductive silicone tubing (Timko et al., 2009; Yu et al., 2009; Asbach et al., 2016), we used conductive PFA tubing (6.35 mm (1/4") OD, 4.76 mm (3/16") ID, Fluorotherm Polymers, Parsippany, NJ, USA) and stainless-steel compression fittings for the connections in the aerosol sampling line. In this experiment set up, we only used conductive silicone tubing (12 cm, 9.53 mm (0.375") OD, 4.8 mm (0.19") ID, TSI, Shoreview, MN, USA) at the inlet of the SMPS and for connections between the SMPS components.

S1.3 Condensational Sink and Condensation Lifetimes

We follow the instructions in Section 3.3 of Palm et al. (2016) to calculate the condensational sink (*CS*, s^{-1}) and low-volatile organic compound (LVOC) condensation lifetimes (τ_{CS}, s), where we use the particle number size distribution from the SMPS. In Eq. (S1), *r* is the wet particle radius (m), *N* is the particle number size distribution (m^{-3} at each particle diameter), and β is the dimensionless Fuchs-Sutugin correction factor (Seinfeld and Pandis, 2006). We also use the same gas diffusion coefficient (D_g) used by Palm et al. (2016) of 7×10^{-6} m^2 s^{-1}, which represents LVOC. In Eq. (S3), α is the dimensionless accommodation coefficient that is assumed to be 1 (Liu et al., 2019).

$$CS = 4\pi D_g \int_0^\infty r\beta(r)N(r)dr = 4\pi D_g \sum_0^\infty r\beta(r)N(r) \quad \text{(S1)}$$

$$\tau_{CS} = \frac{1}{CS} \quad \text{(S2)}$$

$$\beta(r) = \frac{Kn+1}{0.377Kn+1+\frac{4}{3}\alpha^{-1}Kn^2+\frac{4}{3}\alpha^{-1}Kn} \quad \text{(S3)}$$

To obtain β, we calculate the dimensionless Knudsen number (*Kn*), the mean free path (λ_g, m), and the mean thermal velocity (ω_{avg}, m s^{-1}) for LVOC at each *r*. In Eq. (S6), *T* refers to the temperature (K) in the PAM-OFR and R is the gas constant (R = 8.3145 kg m^2 s^{-2} K^{-1} mol^{-1}). Since particles were dried before being detected by the SMPS, we obtain *r* in Eq. (S1) and (S4) by multiplying the dry particle radius with the growth factor (*GF*), which is the ratio of the wet particle diameter versus when the particle is dry (Fig. S5).

$$Kn = \frac{\lambda_g}{r} \quad \text{(S4)}$$

$$\lambda_g = \frac{3D_g}{v_{avg}} \quad \text{(S5)}$$

$$\omega_{avg} = \sqrt{\frac{8RT}{\pi M}} \quad \text{(S6)}$$

We find *GF* with Eq. (S7), where κ is the dimensionless hygroscopicity parameter and α_w is the dimensionless water activity approximated via α_w = RH %/100. For κ, Palm et al. (2016) used a value representing that of SOA (κ = 0.13), but Janechek et al. (2019) found SOSiA to be non-hygroscopic (κ = 0.01). Consequently, we calculate the *CS* for both the LVOC and SOSiA cases, with molecular weights (*M*) of LVOC, 0.200 kg mol^{-1}, and of D_5, 0.370 kg mol^{-1}. The calculated *GF* for both cases are shown in Fig. S5 and Table S3.

$$\kappa = (GF^3 - 1)(1 - \alpha_w)\alpha_w^{-1} \quad \text{(S7)}$$

The PAM-OFR has an estimated LVOC eddy diffusion wall loss lifetime (τ_{wall}) of 400 s (Palm et al., 2016), while the calculated τ_{CS} ranged up to ~136 s when using the particle size distribution measured during experiments (Table S3). Palm et al. (2016) recommended using the average of the particle size distributions entering and exiting the OFR, which would double the aforementioned τ_{CS} since we did not use seed aerosol. Either case, we expect the loss of LVOC to the walls to have been small since $\tau_{CS} < \tau_{wall}$.

S1.4 PTR-MS Inlet and Settings

The PTR-MS inlet was made of SilcoNert 2000-coated (SilcoTek, Bellefonte, PA, USA) stainless steel inlet tubing (1.59 mm (1/16") OD, 1.0 mm (0.040") ID) at 1.2 m in length. The PTR-MS was connected immediately at the center outlet of the OFR with SilcoNert 2000-coated fittings (Swagelok, Solon, OH, USA) and conductive PFA tubing (Fluorotherm Polymers, Parsippany, NJ, USA). We set the flow rate into the PTR-MS inlet to 0.43 L min^{-1} using its built-in inlet flow controller and inlet pressure controller. The PTR-MS inlet was equipped with a heating hose set to 60 °C and a dust filter to prevent clogging, especially at the high SOSiA masses. The single stage filter holder was made of PFA (Savillex, Eden Prairie, MN, USA) and held a 25 mm PTFE filter (5 µm pore, Synspec, Groningen, Netherlands) that was replaced daily.

The mass spectrometer extraction time and maximum flight times were 2.0 and 20.0 µs respectively, with the maximum mass at *m/z* 632.0. The mass spectra were integrated and recorded every 1000 ms. For the PTR-MS mass scale calibration, we used $(H_2{}^{18}O)H^+$ (*m/z* 21.0221), $(H_2O)_2H^+$ (*m/z* 37.0284), $(C_6H_4I)H^+$ (*m/z* 203.9431), and $(C_6H_4I_2)H^+$ (*m/z* 330.8475) during the data analysis. We used ioniTOF 4.0 to control the instrument and PTR-MS Viewer 3.4.4 (Ionicon Analytik, Innsbruck, Austria) to process the PTR-MS mass spectra.

S1.5 PTR-MS Mass Spectra Interpretation

D_5 has isotopologues (Fig. 1) whose ion masses overlap with those of VOP. Additionally, large alcohols fragment during the PTR (Brown et al., 2010), and the reported siloxanol ($D_4T(OH)$) or siloxanediol ($D_3T_2(OH)_2$) may have fragmented if they

behave like saturated organic alcohols. Since we did not have siloxanol calibration standards, we opt to use the -H_2O fragmentation behavior of organic alcohols to assess the qualitative trends of the proposed VOP.

We use the -H_2O fragment of $[D_4T(OH)]H^+$ at *m/z* 355, the -H_2O fragment of $D_3T_2(OH)_2$ at *m/z* 357, and the -H_2O fragment of $[D_3T_2(OH)(OCHO)]H^+$ at *m/z* 385 to assess the relative trends of these VOP (Table S4). However, the signal at *m/z* 355 overlaps with the -CH_4 fragment of protonated D_5 $[C_9H_{27}O_5Si_5]^+$, as noted by Coggon et al. (2018). As for *m/z* 357, this signal overlaps with an isotopologue of the -CH_4 fragment of $[D_5]H^+$ and the -H_2O fragment of $[D_4T(OH)]H^+$. To retrieve the signal of $D_4T(OH)$ and $D_3T_2(OH)_2$, we subtract the fragment and/or isotopologue signals from the total signal at the designated ion masses. For *m/z* 355, we subtract the -CH_4 fragment of $[D_5]H^+$ using the signal ratios of D_5 at *m/z* 355 and *m/z* 371 found prior to each experiment. For *m/z* 357, we subtract the $[C_9H_{27}O_5Si_5]^+$ isotopologue signal fraction.

For the quantification of D_5, we opt to use the main D_5 ion ($[C_{10}H_{30}Si_5]H^+$) at *m/z* 371, as opposed to the -CH_4 fragment ion at *m/z* 355. Coggon et al. (2018) used the fragment ion for their ambient air measurements due to higher ion counts there. $[C_9H_{27}O_5Si_5]^+$ had a higher ion count than $[C_{10}H_{30}Si_5]H^+$ during our calibrations and experiments as well, but the D_5 concentrations in these experiments are sufficiently high for quantification at *m/z* 371. Additionally, Since the -H_2O fragment ion of $[D_4T(OH)]H^+$ has the same elemental composition of the -CH_4 fragment of $[D_5]H^+$, we choose the *m/z* 371 ion to avoid potential overlaps in the D_5 quantification.

The PTR-MS is limited in the species it can detect and resolve. The PTR-MS configuration restricts the volatility range of identifiable species, where species are not fragmented during the PTR or lost on the surfaces of the instrument and inlet. Moreover, the PTR is known to fragment peroxides (Li et al., 2022), which limits their detection. Saturated alcohols larger than ethanol and unsaturated alcohols are also known to undergo fragmentation during ionization in the PTR-MS (Brown et al., 2010; Demarcke et al., 2010). Consequently, we cannot rule out that some D_5 VOP fragments are being misattributed in the trends that we report.

For example, methanediol ($CH_2(OH)_2$) is the hydrated form of HCHO and has been observed to largely fragment to a -H_2O PTR ion that overlaps at *m/z* 31 (Franco et al., 2021). Although $CH_2(OH)_2$ may be formed in the gas phase through HCHO + H_2O via HCOOH catalysis (Hazra et al., 2013), the gaseous compound is thought to have evaporated after being formed heterogeneously (Franco et al., 2021). Franco et al. (2021) also fitted the gaseous unimolecular dehydration ($CH_2(OH)_2 \rightarrow$ HCHO + H_2O) rate coefficient $k_{CH2(OH)2}$ to be 8.5×10^{-5} s^{-1}, which gives the species a unimolecular dehydration lifetime of 0.14 days, which is longer than the experiment residence times of the PAM-OFR. The dominant products from $CH_2(OH)_2$ + OH are HCOOH and HO_2 via the decomposition of the RO_2, and so this diol is practically an intermediate between HCHO and HCOOH.

Given the humid PAM-OFR conditions, $CH_2(OH)_2$ may have been present, and the -H_2O fragment ion may have led to the over-quantification of HCHO; the fragmentation of $CH_2(OH)_2$ during the PTR needs to be characterized to constrain this uncertainty. However, Franco et al. (2021) found that $CH_2(OH)_2$ + OH has a rate coefficient of $k_{CH2(OH)2+OH}$ = ~7.5 × 10^{-12} cm^3 s^{-1}, and so we expect $CH_2(OH)_2$ to have a OH-oxidation lifetime less than that of τ_{res} at the [OH] in the PAM-OFR. Consequently, we do not expect the $CH_2(OH)_2$ -H_2O fragment interference to the HCHO quantification to be large.

S1.6 Upper Limit Estimation of $k_{age,particle}$

Surface and bulk accommodation processes are not explicitly resolved in the kinetic model and $k_{age,particle}$ acts on the concentrations of particle-phase products per unit air volume. To address whether the numerical value of the fitted $k_{age,particle}$ is reasonable, we calculate its upper physical limit as the collision flow of OH onto the particles in one cm^3 of air ($F_{coll,OH}$, cm^{-3} s^{-1}) derived from gas kinetic theory (Pöschl et al., 2007).

$$F_{\mathrm{coll,OH}} = \frac{\omega_{\mathrm{OH}}}{4} A_{\mathrm{particle}} [\mathrm{OH}] \tag{S8}$$

Here, ω_{OH} is the mean thermal velocity of OH in cm s^{-1} (Eq. (S6)) and $A_{particle}$ is the particle surface area density (cm^2 cm^{-3}) measured with the SMPS at the outlet of the PAM-OFR. This flow must always be larger than the heterogeneous reaction flow of OH with the particle surface in one cm^3 of air ($F_{het,OH}$, cm^{-3} s^{-1}).

$$F_{\mathrm{het,OH}} = k_{\mathrm{age,particle}}\, c_{\mathrm{particle}}\, [\mathrm{OH}] \tag{S9}$$

Accordingly, we find the following condition for $k_{age,particle}$.

$$k_{\mathrm{age,particle}} < \frac{\omega_{\mathrm{OH}}}{4\, c_{\mathrm{particle}}} A_{\mathrm{particle}} \tag{S10}$$

Here, $c_{particle}$, (cm^{-3}) denotes the concentration of total SOSiA products in the particle phase in one cm^3 of air. The estimated upper limit $k_{age,particle}$ are summarized in Table S12.

S2 SOSiA Mass Density (ρ_{SOSiA})

In a separate series of experiments, we collected SOSiA filter samples from the PAM-OFR on pre-weighed PTFE filters (47 mm, 2 μm pore, PT48P-KR, MTL, Minneapolis, MN, USA), where we also operated the SMPS. Then, we stored the filter samples in a desiccator placed inside of a temperature and humidity-controlled micro-balance room for a day to remove mass interference from condensed water. Each filter was weighed ten times on a semi-micro balance (± 0.01 mg, ME204, Mettler

Toledo, Columbus, OH, USA), and we calculate the mean ρ_{SOSiA} by dividing the masses of SOSiA (300 – 740 µg) over integrated SMPS volumes.

From five filter samples, we find a mean (± standard deviation) ρ_{SOSiA} of 1.07 ± 0.08 g cm^{-3}. We note that existing publications used discrepant ρ_{SOSiA} values, which are summarized in Table S9. That range includes those representing SOA (Charan et al., 2022) or D_5 itself (Janechek et al., 2019). Wu and Johnston (2017) did not explicitly state the ρ_{SOSiA} they used. Han et al. (2022) used particle size and mass data from an SMPS and an AMS to get ρ_{SOSiA} of 1.6 – 1.8 g cm^{-3} for SOSiA from different siloxane precursors. Avery et al. (2023) used the SOSiA elemental ratios from the AMS with the method described by Kuwata et al. (2012) to obtain ρ_{SOSiA} of 1.59 – 1.78 g cm^{-3}.

For reference, Fytas and Wang (1984) measured the density of several methylphenylsiloxane oligomers, which ranged from 0.99 – 1.10 g cm^{-3}, while He et al. (1988) used a polydimethylsiloxane density parameterization based on molecular weight that maximizes to 0.97 g cm^{-3}. Dee et al. (1992) measured the densities of polydimethylsiloxane oligomers and found values between 1 to 1.14 g cm^{-3}. One of the silanols formed in the siloxane degradation process is dimethylsilanediol (DMSD, $C_2H_8O_2Si$), and Mazzoni et al. (1997) calculated DMSD to have a density of 1.023 g cm^{-3} at 20 °C using a group contribution method. Lamers et al. (2021) found that dimethylsiloxane oligomers of varying lengths would have densities of ~1 g cm^{-3}.

While the ρ_{SOSiA} we report are in line with literature siloxane/silanol densities, they are lower than those reported by Han et al. (2022) and Avery et al. (2023). Some of the difference between their and our ρ_{SOSiA} measurements may be explained by the different experiment conditions, such as OH_{exp}, since aerosol density is expected to increase with higher oxygenation (Kuwata et al., 2012; Nakao et al., 2013). Moreover, Han et al. (2022), Avery et al. (2023), and this study uses different methods to measure ρ_{SOSiA}. Lastly, volatile species may have evaporated from the collected particles while the filters were in the desiccator, which would lead to an undermeasurement of the particle masses and thus SOSiA density.

S3 PTR-MS Calibration

For HCHO, we used a paraformaldehyde permeation tube (CAS#30525-89-4, VICI Metronics, Poulsbo, WA, USA) and a calibration gas generator (Model 150 Dynacalibrator, VICI Metronics, Poulsbo, WA, USA) set to 70 °C to produce HCHO calibration gas with ultra-high purity N_2 as the carrier gas. To achieve a steady output, we conditioned the permeation tube in the calibration gas generator for a week at the temperature and carrier gas flow rate to be used during the calibration. The HCHO calibration gas was diluted dynamically to achieve target concentrations with zero/humid air and MFCs, and we correct the HCHO quantification for humidity using Eq. (S11) from Vlasenko et al. (2010), where k_{rev} is the fitted reverse

PTR rate coefficient ($cm^3\ s^{-1}$), $[H_2O]_{dry}$ is the H_2O concentration (cm^{-3}) in the drift tube when sample air is dry, $[H_2O]$ is the water concentration (cm^{-3}) in the drift tube when sample air is humid, and Δt is the drift tube reaction time (9.4×10^{-5} s).

$$\frac{\text{Sensitivity}_{\text{meas}}}{\text{Sensitivity}_{\text{dry}}} = \frac{[\text{H}_2\text{O}]_{\text{dry}}\left(1-e^{-k_{\text{rev}}[\text{H}_2\text{O}]\Delta t}\right)}{[\text{H}_2\text{O}]\left(1-e^{-k_{\text{rev}}[\text{H}_2\text{O}]_{\text{dry}}\Delta t}\right)} \quad \text{(S11)}$$

To obtain $[H_2O]_{dry}$, we follow the method described in Vlasenko et al. (2010), where we fit a quadratic polynomial (Eq. (S12)) to $(H_2O)_2H^+$ (ncps) against the sample air absolute humidity (Fig. S6.B3). Then, we take the fitted y-intercept (≈ 4000) and linearly approximated the corresponding absolute humidity at 2×y-intercept, which comes to be ~0.005 mol/mol. Lastly, we convert the $[H_2O]_{dry}$ mixing ratio to cm^{-3} using the drift tube pressure (2.30 mbar) and temperature (80 °C).

$$I_{(H2O)2H+} = A + Bx + Cx^2 \quad \text{(S12)}$$

For HCOOH, a 1 % (w/w) aqueous solution of HCOOH (>98.0 %, CAS#64-18-6, Tokyo Chemical Industry, Tokyo, Japan) was injected into the VOC bulb with a syringe pump and zero/humid air flowing through the bulb. Like Baasandorj et al. (2015), we find the PTR-MS sensitivity at *m/z* 47 to be affected by humidity, with sensitivity decreasing with higher RH at 137 Td. Consequently, we adjust the HCOOH quantification for H_2O cluster effects with the method outlined in Baasandorj et al. (2015). We fit the parameters in Eq. (S13), where x is $I_{(H2O)2H+}/I_{(H2O)H+}$.

$$\text{Sensitivity} = A \times \left(B_1 exp(C_1 x) + B_2 exp(C_2 x)\right) \quad \text{(S13)}$$

S4 Odum two-product Model

Eq. (S14) shows the Odum two-product parameterization (Odum et al., 1996) for aerosol mass yields, in this case for SOSiA. Janechek et al. (2019) and Charan et al. (2022) fitted their data, and we also parameterize the experimental Y_{SOSiA} with the two-product model in Eq. (S14) for comparison. The partitioning coefficient (K, $m^3\ \mu g^{-1}$) is the inverse of the saturation mass concentration C^* ($\mu g\ m^{-3}$), C_{OA} is the OA mass loading ($\mu g\ m^{-3}$), and α is the product yield for each corresponding K. The fitted values and the literature comparison is shown in Fig. S7, and the Y_{SOSiA} have been adjusted for ρ_{SOSiA} = 1.07 g cm^{-3}.

$$Y_{\text{SOSiA}} = C_{\text{OA}}\left(\frac{\alpha_1 K_1}{1+K_1 C_{\text{OA}}} + \frac{\alpha_2 K_2}{1+K_2 C_{\text{OA}}}\right) \quad \text{(S14)}$$

We fit the two-product model with the ρ_{SOSiA}-adjusted data from Han et al. (2022), Avery et al. (2023), and all literature values combined, including those we report. The existing literature values and fit two-product model parameters are

summarized in Tables S9 and S10. As shown in Fig. 4, the two-product model parameters provided by Charan et al. (2022) are consistent with those of Han et al. (2022) and Avery et al. (2023) at ambient surface C_{OA} (0 – 30 μg m^{-3}) with low Y_{SOSiA}. However, the two-product model fit of Janechek et al. (2019) predicts less volatile products, resulting in higher Y_{SOSiA} at those C_{OA}. Our two-product model fit predicts more volatile products, which is consistent with that of Charan et al. (2022), Han et al. (2022), and Avery et al. (2023).

However, for the high C_{OA} cases, the literature diverges with experimental Y_{SOSiA} ranging from 10 to 100 % at ~200 μg m^{-3}, and our Y_{SOSiA} yield curve lies between the curves from the literature (Fig. S7). The intercorrelation of OH_{exp} with Y_{SOSiA} is also visible in Fig. S7, where the higher Y_{SOSiA} measurements occur not only when C_{OA} is high, but also as OH_{exp} increases (color scale). The two-product model here does not explicitly account for chemical aging with OH_{exp}, so we use the aging-VBS approach.

S5 Modeling RO_2 Pathways with KinSim

A potential explanation for the Y_{SOSiA} discrepancies in the literature is the RO_2 fate, where high [OH] in OFR experiments may have pushed the RO_2 fate towards a pathway that forms more condensing species. However, Alton and Browne (2022) found in their chamber that RO_2 + HO_2, RO_2 + NO, and unimolecular pathways would yield similar fractions of siloxanol and formate ester, suggesting these pathways make similar products, likely through RO; Alton and Browne (2022) suggests that the dominant products of RO_2 + HO_2 are RO, OH, and O_2, instead of ROOH.

In OFR185, the RO_2 + OH pathway is feasible due to high [OH] and the atmospheric relevance of this pathway is debated (Peng and Jimenez, 2020). However, Fittschen (2019) suggests that RO_2 + OH is an atmospherically relevant pathway in low-NO_x environments, and the dominant product is expected to be RO (+ HO_2). That being said, Assaf et al. (2018) found that the dominant product of RO_2 + OH is ROOOH for RO_2 with more than 3 carbon atoms, but we are unaware of any documentation of siloxane RO_2 forming ROOOH. The dominance of RO products across RO_2 fates leading to comparable aerosol mass yields has been reported with monoterpene nitrate oxidation as well (Day et al., 2022).

To assess the RO_2 fates in these experiments, we adopt analogous reactions from the literature and added those RO_2 fates into an OFR mechanism template (Peng and Jimenez, 2020) for KinSim 4.16, a chemical kinetics simulator (Peng and Jimenez, 2019). Table S5 shows the additional RO_2 reactions and rate coefficients appended to the OFR mechanism. The results suggest that RO_2 + HO_2 and RO_2 + OH pathways dominated across the experiments, but we encounter an issue reconciling the measured OH_{exp} using (2) and the OH_{exp} from KinSim.

To input the 254 and 185 nm photon fluxes (I_{254} and I_{185}) in KinSim, we follow the recommendations in Rowe et al. (2020) with I_{254max} = 3.0 × 10^{15} cm^{-2} s^{-1} and I_{185max}:I_{254max} = 0.0664. Next, we multiply I_{254max} and I_{185max} by 0.1 to account for the shrink wrap lamp covers and by the ratios of the experiment irradiance and O_3 outputs versus the maximum values at 8V (Table S6). However, we find that with the above photon flux inputs, KinSim calculated the OH_{exp} to be too high and $[D_5]_{final}$ to be too low compared with measurements, although the modeled $[O_3]$ are consistent with measurements (Fig. S9).

Given that we are interested in probing the RO_2 fates, we multiply I_{185} and I_{254} by a factor of 0.1 to bring the OH_{exp} and $[D_5]_{final}$ in line with measurements. We use I_{185} of 3 × 10^{11} – 2 × 10^{12} and I_{254} of 1 × 10^{12} – 3 × 10^{13} cm^{-2} s^{-1} in the case where I_{185} and I_{254} are multiplied by a factor of 0.1, and the initial fluxes are summarized in Table S6. However, this adjustment leads to the output $[O_3]$ being underestimated. To assess the impact of the adjustment on RO_2 fates, we model both cases where I_{185} and I_{254} are and are not adjusted (Fig. S10).

In both UV flux cases, KinSim finds RO_2 + HO_2 and RO_2 + OH to be the dominant reaction pathways across the experiments (Fig. S10). A potential explanation for the OH_{exp} discrepancy is the formation of secondary products that are also reactive with OH, which are not included in OHR_{ext} calculated with injected D_5. Since we observe the formation of OH-reactive species like HCHO and the proposed VOP appear to be removed with OH_{exp}, we suspect that the KinSim mechanism is incomplete, and that a more complete mechanism with subsequent OH-reactive species should improve the KinSim calculations.

For these experiments, we expect RO_2 + HO_2 and RO_2 + OH to have been the dominant pathways across the experiments, based on the findings by Alton and Browne (2022) and the KinSim calculations. Avery et al. (2023) also found similar RO_2 fates with KinSim for their experiments, and the common product of these pathways is RO. We note that the inclusion of VOP into the OFR mechanism or when calculating OHR_{ext} may be needed to reconcile measured OH_{exp} and model expectations. Peng and Jimenez (2020) suggest that using measured OH_{exp} is preferred over modelled values due to uncertainties in the OFR residence time, mixing, and OH recycling. We also use RO_2 reactions and rate coefficients in the OFR mechanism based on those of organics, and that the RO_2 fates are subject to change as the D_5 + OH system is further constrained.

References

Alton, M. W. and Browne, E. C.: Atmospheric Chemistry of Volatile Methyl Siloxanes: Kinetics and Products of Oxidation by OH Radicals and Cl Atoms, Environ Sci Technol, 54, 5992–5999, https://doi.org/10.1021/acs.est.0c01368, 2020.

Alton, M. W. and Browne, E. C.: Atmospheric Degradation of Cyclic Volatile Methyl Siloxanes: Radical Chemistry and Oxidation Products, ACS Environmental Au, https://doi.org/10.1021/acsenvironau.1c00043, 2022.

Asbach, C., Kaminski, H., Lamboy, Y., Schneiderwind, U., Fierz, M., and Todea, A. M.: Silicone sampling tubes can cause drastic artifacts in measurements with aerosol instrumentation based on unipolar diffusion charging, Aerosol Science and Technology, 50, 1375–1384, https://doi.org/10.1080/02786826.2016.1241858, 2016.

Assaf, E., Schoemaecker, C., Vereecken, L., and Fittschen, C.: Experimental and theoretical investigation of the reaction of RO2 radicals with OH radicals: Dependence of the HO2 yield on the size of the alkyl group, Int J Chem Kinet, 50, 670–680, https://doi.org/https://doi.org/10.1002/kin.21191, 2018.

Atkinson, R.: Kinetics of the gas-phase reactions of a series of organosilicon compounds with hydroxyl and nitrate(NO3) radicals and ozone at 297 +- 2 K, Environ Sci Technol, 25, 863–866, https://doi.org/10.1021/es00017a005, 1991.

Atkinson, R., Baulch, D. L., Cox, R. A., Crowley, J. N., Hampson, R. F., Hynes, R. G., Jenkin, M. E., Rossi, M. J., Troe, J., and Subcommittee, I.: Evaluated kinetic and photochemical data for atmospheric chemistry: Volume II – gas phase reactions of organic species, Atmos Chem Phys, 6, 3625–4055, https://doi.org/10.5194/acp-6-3625-2006, 2006.

Avery, A. M., Alton, M. W., Canagaratna, M. R., Krechmer, J. E., Sueper, D. T., Bhattacharyya, N., Hildebrandt Ruiz, L., Brune, W. H., and Lambe, A. T.: Comparison of the Yield and Chemical Composition of Secondary Organic Aerosol Generated from the OH and Cl Oxidation of Decamethylcyclopentasiloxane, ACS Earth Space Chem, https://doi.org/10.1021/acsearthspacechem.2c00304, 2023.

Baasandorj, M., Millet, D. B., Hu, L., Mitroo, D., and Williams, B. J.: Measuring acetic and formic acid by proton-transfer-reaction mass spectrometry: sensitivity, humidity dependence, and quantifying interferences, Atmos Meas Tech, 8, 1303–1321, https://doi.org/10.5194/amt-8-1303-2015, 2015.

Brown, P., Watts, P., Märk, T. D., and Mayhew, C. A.: Proton transfer reaction mass spectrometry investigations on the effects of reduced electric field and reagent ion internal energy on product ion branching ratios for a series of saturated alcohols, Int J Mass Spectrom, 294, 103–111, https://doi.org/https://doi.org/10.1016/j.ijms.2010.05.028, 2010.

Charan, S. M., Huang, Y., Buenconsejo, R. S., Li, Q., Cocker III, D. R., and Seinfeld, J. H.: Secondary organic aerosol formation from the oxidation of decamethylcyclopentasiloxane at atmospherically relevant OH concentrations, Atmos Chem Phys, 22, 917–928, https://doi.org/10.5194/acp-22-917-2022, 2022.

Coggon, M. M., McDonald, B. C., Vlasenko, A., Veres, P. R., Bernard, F., Koss, A. R., Yuan, B., Gilman, J. B., Peischl, J., Aikin, K. C., DuRant, J., Warneke, C., Li, S.-M., and de Gouw, J. A.: Diurnal Variability and Emission Pattern of Decamethylcyclopentasiloxane (D5) from the Application of Personal Care Products in Two North American Cities, Environ Sci Technol, 52, 5610–5618, https://doi.org/10.1021/acs.est.8b00506, 2018.

Day, D. A., Fry, J. L., Kang, H. G., Krechmer, J. E., Ayres, B. R., Keehan, N. I., Thompson, S. L., Hu, W., Campuzano-Jost, P., Schroder, J. C., Stark, H., DeVault, M. P., Ziemann, P. J., Zarzana, K. J., Wild, R. J., Dubè, W. P., Brown, S. S., and Jimenez, J. L.: Secondary Organic Aerosol Mass Yields from NO3 Oxidation of α-Pinene and Δ-Carene: Effect of RO2 Radical Fate, J Phys Chem A, 126, 7309–7330, https://doi.org/10.1021/acs.jpca.2c04419, 2022.

Dee, G. T., Ougizawa, T., and Walsh, D. J.: The pressure-volume-temperature properties of polyethylene, poly(dimethyl siloxane), poly(ethylene glycol) and poly(propylene glycol) as a function of molecular weight, Polymer (Guildf), 33, 3462–3469, https://doi.org/https://doi.org/10.1016/0032-3861(92)91104-A, 1992.

Demarcke, M., Amelynck, C., Schoon, N., Dhooghe, F., Rimetz-Planchon, J., van Langenhove, H., and Dewulf, J.: Laboratory studies in support of the detection of biogenic unsaturated alcohols by proton transfer reaction-mass spectrometry, Int J Mass Spectrom, 290, 14–21, https://doi.org/https://doi.org/10.1016/j.ijms.2009.11.005, 2010.

Dewil, R., Appels, L., and Baeyens, J.: Energy use of biogas hampered by the presence of siloxanes, Energy Convers Manag, 47, 1711–1722, https://doi.org/https://doi.org/10.1016/j.enconman.2005.10.016, 2006.

Fittschen, C.: The reaction of peroxy radicals with OH radicals, Chem Phys Lett, 725, 102–108, https://doi.org/https://doi.org/10.1016/j.cplett.2019.04.002, 2019.

Franco, B., Blumenstock, T., Cho, C., Clarisse, L., Clerbaux, C., Coheur, P.-F., de Mazière, M., de Smedt, I., Dorn, H.-P., Emmerichs, T., Fuchs, H., Gkatzelis, G., Griffith, D. W. T., Gromov, S., Hannigan, J. W., Hase, F., Hohaus, T., Jones, N.,

Kerkweg, A., Kiendler-Scharr, A., Lutsch, E., Mahieu, E., Novelli, A., Ortega, I., Paton-Walsh, C., Pommier, M., Pozzer, A., Reimer, D., Rosanka, S., Sander, R., Schneider, M., Strong, K., Tillmann, R., van Roozendael, M., Vereecken, L., Vigouroux, C., Wahner, A., and Taraborrelli, D.: Ubiquitous atmospheric production of organic acids mediated by cloud droplets, Nature, 593, 233–237, https://doi.org/10.1038/s41586-021-03462-x, 2021.

Fytas, G. and Wang, C. H.: Studies of siloxane oligomers by depolarized Rayleigh scattering, J Am Chem Soc, 106, 4392–4396, https://doi.org/10.1021/ja00328a017, 1984.

Han, C., Yang, H., Li, K., Lee, P., Liggio, J., Leithead, A., and Li, S.-M.: Secondary organic aerosols from OH oxidation of cyclic volatile methyl siloxanes as an important Si source in the atmosphere, Atmos Chem Phys, 22, 10827–10839, https://doi.org/10.5194/acp-22-10827-2022, 2022.

Hazra, M. K., Francisco, J. S., and Sinha, A.: Gas Phase Hydrolysis of Formaldehyde To Form Methanediol: Impact of Formic Acid Catalysis, J Phys Chem A, 117, 11704–11710, https://doi.org/10.1021/jp4008043, 2013.

He, X. W., Widmaier, J. M., Herz, J. E., and Meyer, G. C.: Competition between polycondensation of α,ω-dihydroxy polydimethylsiloxane and its condensation with alkoxy silane: A kinetic approach, Eur Polym J, 24, 1145–1148, https://doi.org/https://doi.org/10.1016/0014-3057(88)90100-0, 1988.

Janechek, N. J., Marek, R. F., Bryngelson, N., Singh, A., Bullard, R. L., Brune, W. H., and Stanier, C. O.: Physical properties of secondary photochemical aerosol from OH oxidation of a cyclic siloxane, Atmos Chem Phys, 19, 1649–1664, https://doi.org/10.5194/acp-19-1649-2019, 2019.

Kim, J. and Xu, S.: Quantitative structure-reactivity relationships of hydroxyl radical rate constants for linear and cyclic volatile methylsiloxanes, Environ Toxicol Chem, 36, 3240–3245, https://doi.org/https://doi.org/10.1002/etc.3914, 2017.

Kuwata, M., Zorn, S. R., and Martin, S. T.: Using Elemental Ratios to Predict the Density of Organic Material Composed of Carbon, Hydrogen, and Oxygen, Environ Sci Technol, 46, 787–794, https://doi.org/10.1021/es202525q, 2012.

Lamers, B. A. G., de Waal, B. F. M., and Meijer, E. W.: The iterative synthesis of discrete dimethylsiloxane oligomers: A practical guide, Journal of Polymer Science, 59, 1142–1150, https://doi.org/https://doi.org/10.1002/pol.20200649, 2021.

Li, H., Almeida, T. G., Luo, Y., Zhao, J., Palm, B. B., Daub, C. D., Huang, W., Mohr, C., Krechmer, J. E., Kurtén, T., and Ehn, M.: Fragmentation inside proton-transfer-reaction-based mass spectrometers limits the detection of ROOR and ROOH peroxides, Atmos Meas Tech, 15, 1811–1827, https://doi.org/10.5194/amt-15-1811-2022, 2022.

Liu, X., Day, D. A., Krechmer, J. E., Brown, W., Peng, Z., Ziemann, P. J., and Jimenez, J. L.: Direct measurements of semi-volatile organic compound dynamics show near-unity mass accommodation coefficients for diverse aerosols, Commun Chem, 2, 98, https://doi.org/10.1038/s42004-019-0200-x, 2019.

Mazzoni, S. M., Roy, S., and Grigoras, S.: Eco-Relevant Properties of Selected Organosilicon Materials, in: Organosilicon Materials, edited by: Chandra, G., Springer Berlin Heidelberg, Berlin, Heidelberg, 53–81, https://doi.org/10.1007/978-3-540-68331-5_3, 1997.

Nakao, S., Tang, P., Tang, X., Clark, C. H., Qi, L., Seo, E., Asa-Awuku, A., and Cocker, D.: Density and elemental ratios of secondary organic aerosol: Application of a density prediction method, Atmos Environ, 68, 273–277, https://doi.org/https://doi.org/10.1016/j.atmosenv.2012.11.006, 2013.

Odum, J. R., Hoffmann, T., Bowman, F., Collins, D., Flagan, R. C., and Seinfeld, J. H.: Gas/Particle Partitioning and Secondary Organic Aerosol Yields, Environ Sci Technol, 30, 2580–2585, https://doi.org/10.1021/es950943+, 1996.

Otkjær, R. V., Jakobsen, H. H., Tram, C. M., and Kjaergaard, H. G.: Calculated Hydrogen Shift Rate Constants in Substituted Alkyl Peroxy Radicals, J Phys Chem A, 122, 8665–8673, https://doi.org/10.1021/acs.jpca.8b06223, 2018.

Palm, B. B., Campuzano-Jost, P., Ortega, A. M., Day, D. A., Kaser, L., Jud, W., Karl, T., Hansel, A., Hunter, J. F., Cross, E. S., Kroll, J. H., Peng, Z., Brune, W. H., and Jimenez, J. L.: In situ secondary organic aerosol formation from ambient pine forest air using an oxidation flow reactor, Atmos Chem Phys, 16, 2943–2970, https://doi.org/10.5194/acp-16-2943-2016, 2016.

Peng, Z. and Jimenez, J. L.: KinSim: A Research-Grade, User-Friendly, Visual Kinetics Simulator for Chemical-Kinetics and Environmental-Chemistry Teaching, J Chem Educ, 96, 806–811, https://doi.org/10.1021/acs.jchemed.9b00033, 2019.

Peng, Z. and Jimenez, J. L.: Radical chemistry in oxidation flow reactors for atmospheric chemistry research, Chem. Soc. Rev., 49, 2570–2616, https://doi.org/10.1039/C9CS00766K, 2020.

Porter, W. C., Jimenez, J. L., and Barsanti, K. C.: Quantifying Atmospheric Parameter Ranges for Ambient Secondary Organic Aerosol Formation, ACS Earth Space Chem, 5, 2380–2397, https://doi.org/10.1021/acsearthspacechem.1c00090, 2021.

Pöschl, U., Rudich, Y., and Ammann, M.: Kinetic model framework for aerosol and cloud surface chemistry and gas-particle interactions – Part 1: General equations, parameters, and terminology, Atmos Chem Phys, 7, 5989–6023, https://doi.org/10.5194/acp-7-5989-2007, 2007.

Rowe, J. P., Lambe, A. T., and Brune, W. H.: Technical Note: Effect of varying the λ=185 and 254nm photon flux ratio on radical generation in oxidation flow reactors, Atmos Chem Phys, 20, 13417–13424, https://doi.org/10.5194/acp-20-13417-2020, 2020.

Safron, A., Strandell, M., Kierkegaard, A., and Macleod, M.: Rate Constants and Activation Energies for Gas-Phase Reactions of Three Cyclic Volatile Methyl Siloxanes with the Hydroxyl Radical, Int J Chem Kinet, 47, 420–428, https://doi.org/https://doi.org/10.1002/kin.20919, 2015.

Seinfeld, J. H. and Pandis, S. N.: Atmospheric Chemistry and Physics: From Air Pollution to Climate Change, 1203 pp., 2006.

Timko, M. T., Yu, Z., Kroll, J., Jayne, J. T., Worsnop, D. R., Miake-Lye, R. C., Onasch, T. B., Liscinsky, D., Kirchstetter, T. W., Destaillats, H., Holder, A. L., Smith, J. D., and Wilson, K. R.: Sampling Artifacts from Conductive Silicone Tubing, Aerosol Science and Technology, 43, 855–865, https://doi.org/10.1080/02786820902984811, 2009.

Vlasenko, A., Macdonald, A. M., Sjostedt, S. J., and Abbatt, J. P. D.: Formaldehyde measurements by Proton transfer reaction – Mass Spectrometry (PTR-MS): correction for humidity effects, Atmos Meas Tech, 3, 1055–1062, https://doi.org/10.5194/amt-3-1055-2010, 2010.

von der Weiden, S.-L., Drewnick, F., and Borrmann, S.: Particle Loss Calculator – a new software tool for the assessment of the performance of aerosol inlet systems, Atmos Meas Tech, 2, 479–494, https://doi.org/10.5194/amt-2-479-2009, 2009.

Wu, Y. and Johnston, M. V: Aerosol Formation from OH Oxidation of the Volatile Cyclic Methyl Siloxane (cVMS) Decamethylcyclopentasiloxane, Environ Sci Technol, 51, 4445–4451, https://doi.org/10.1021/acs.est.7b00655, 2017.

Xiao, R., Zammit, I., Wei, Z., Hu, W.-P., MacLeod, M., and Spinney, R.: Kinetics and Mechanism of the Oxidation of Cyclic Methylsiloxanes by Hydroxyl Radical in the Gas Phase: An Experimental and Theoretical Study, Environ Sci Technol, 49, 13322–13330, https://doi.org/10.1021/acs.est.5b03744, 2015.

Yu, Y., Liz Alexander, M., Perraud, V., Bruns, E. A., Johnson, S. N., Ezell, M. J., and Finlayson-Pitts, B. J.: Contamination from electrically conductive silicone tubing during aerosol chemical analysis, Atmos Environ, 43, 2836–2839, https://doi.org/https://doi.org/10.1016/j.atmosenv.2009.02.014, 2009.

Ziemann, P. J. and Atkinson, R.: Kinetics, products, and mechanisms of secondary organic aerosol formation, Chem Soc Rev, 41, 6582, https://doi.org/10.1039/c2cs35122f, 2012.

Table S1. Summary of literature D_5 + OH rate coefficients and measurement methods. We used the empirical values to calculate the average k_{D5+OH}. GC-FID: gas chromatography-flame ionization detector. GC-MS: gas chromatography-mass spectrometry. CIMS: chemical ionization mass spectrometry.

Reference	Method	k_{D5+OH} at ~298 K (cm^3 s^{-1})
Atkinson (1991)	CH_3NO_2 + UV in 6400 L Teflon chamber, GC-FID, rate relative to cyclohexane.	1.55×10^{-12}
Safron et al. (2015)	O_3/H_2O + UV in 140 mL quartz chamber, GC-MS, rate relative to cyclohexane.	2.6×10^{-12}
Xiao et al. (2015)	O_3/H_2O + UV in 140 mL quartz chamber, GC-MS, rate relative to trimethylpentane.	2.46×10^{-12}
	Computed with Spartan 10 and Merck Molecular Force Field molecular mechanics.	~~2.90×10^{-12}~~
Kim and Xu (2017)	O_3/H_2O + UV in 134 L SilcoNert-coated stainless steel chamber, GC-MS, rate relative to n-hexane.	1.46×10^{-12}
Alton and Browne (2020)	O_3/H_2O + UV in 1000 L Teflon chamber, CIMS, rate relative to propionic acid/MEK.	2.1×10^{-12}
Average		**2.0×10^{-12}**

Table S2. Summary of PAM OFR experiment conditions.

Experiment	τ_{res} (sec)	Lamp Voltage	RH (%)	T (°C)	O_3 (ppm)	Irradiance (μW cm^{-2})	Volume mode (nm)	Surface mode (nm)	Aerosol sampling line loss (%)	Particle number concentration (cm^{-3})
1	180	2.4	33.27 ± 0.07	22.44 ± 0.07	2.18 ± 0.02	0.95 ± 0.05	68.5	57.3	8.49	9.17×10^4
2	180	2.4	33.53 ± 0.07	21.09 ± 0.09	2.37 ± 0.02	0.93 ± 0.05	85.1	66.1	6.74	1.21×10^5
3	180	2.4	32.45 ± 0.03	19.84 ± 0.16	2.29 ± 0.03	0.83 ± 0.08	82	66.1	6.96	1.34×10^5
4	180	2.4	82.47 ± 0.20	20.39 ± 0.12	1.80 ± 0.02	0.56 ± 0.05	98.2	79.1	5.82	3.24×10^5
5	180	2.4	81.96 ± 0.11	21.37 ± 0.08	1.98 ± 0.03	0.84 ± 0.08	131	101.8	4.33	3.83×10^5
6	180	2.4	82.34 ± 0.11	21.57 ± 0.06	1.82 ± 0.02	0.61 ± 0.03	151.2	121.9	3.80	3.83×10^5
7	180	8.0	28.67 ± 0.30	21.66 ± 0.22	12.62 ± 0.15	12.36 ± 0.11	88.2	71	6.52	1.60×10^5
8	180	8.0	28.82 ± 0.16	21.63 ± 0.22	10.65 ± 0.12	9.37 ± 0.11	140.7	113.4	4.02	1.84×10^5
9	180	8.0	28.58 ± 0.17	23.08 ± 0.19	11.04 ± 0.05	9.80 ± 0.07	187.7	145.9	3.15	2.14×10^5
10	180	8.0	75.62	21.61	8.88 ±	12.18 ±	121.9	101.8	4.67	4.62×10^5

			± 0.51	± 0.29	0.08	0.08				
11	180	8.0	74.91 ± 0.33	23.03 ± 0.18	8.00 ± 0.06	9.68 ± 0.06	151.2	117.6	3.80	5.18×10^5
12	180	8.0	75.64 ± 0.34	23.40 ± 0.20	8.03 ± 0.04	9.67 ± 0.10	194.6	151.2	3.04	6.64×10^5
13	120	2.4	30.57 ± 0.13	20.15 ± 0.14	1.69 ± 0.01	0.87 ± 0.03	51.4	42.9	11.7	6.30×10^4
14	120	2.4	28.97 ± 0.07	21.16 ± 0.08	1.62 ± 0.01	0.84 ± 0.06	55.2	47.8	10.7	5.56×10^4
15	120	2.4	28.48 ± 0.05	21.10 ± 0.06	1.54 ± 0.01	0.69 ± 0.05	57.3	49.6	10.4	4.39×10^4

Table S3. Summary of experiment condensational sinks, LVOC condensation lifetimes, and growth factors calculated with the particle size distribution exiting the PAM-OFR as described in Section S1.3.

Parameters	SOA, LVOC κ = 0.13, M = 0.200 kg mol^{-1}			SOSiA, D_5 κ = 0.01, M = 0.370 kg mol^{-1}		
Experiment	***CS*** **(s^{-1})**	**τ_{CS} (s)**	**Growth Factor**	***CS*** **(s^{-1})**	**τ_{CS} (s)**	**Growth Factor**
1	2.57×10^{-2}	38.8	1.02	1.88×10^{-2}	53.3	1.00
2	3.99×10^{-2}	25.1	1.02	2.92×10^{-2}	34.3	1.00
3	3.88×10^{-2}	25.76	1.02	2.84×10^{-2}	35.2	1.00
4	0.173	5.77	1.17	0.101	9.85	1.02
5	0.303	3.30	1.17	0.182	5.50	1.02
6	0.394	2.54	1.17	0.239	4.19	1.02
7	6.68×10^{-2}	15.0	1.02	4.95×10^{-2}	20.2	1.00
8	0.138	7.27	1.02	0.104	9.63	1.00
9	0.250	3.99	1.02	0.192	5.20	1.00
10	0.338	2.95	1.12	0.217	4.61	1.01
11	0.522	1.92	1.12	0.342	2.93	1.01
12	0.913	1.09	1.12	0.605	1.65	1.01
13	1.25×10^{-2}	80.1	1.02	9.06×10^{-3}	110	1.00
14	1.23×10^{-2}	81.3	1.02	8.96×10^{-3}	112	1.00
15	1.01×10^{-2}	99.3	1.02	7.35×10^{-3}	136	1.00

Table S4. Proposed PTR-MS VOP ions and identities. Here, "D" and "T" refer to silicon center atoms bonded to two and three oxygen atoms respectively.

Ion Formula	Ion Unit Mass (*m/z*)	Description
$[HCHO]H^+$	31	Formaldehyde
$[HCOOH]H^+$	47	Formic acid
$[C_9H_{27}O_5Si_5]^+$	355	$[D_5\text{-}CH_4]^+$ and $[D_4T(OH)\text{-}H_2O]^+$
$[C_8H_{25}O_6Si_5]^+$	357	$[D_3T_2(OH)_2\text{-}H_2O]^+$
$[C_{10}H_{30}O_5Si_5]H^+$	371	$[D_5]H^+$ dominant isotope
$[C_9H_{28}O_6Si_5]H^+$	373	$[D_4T(OH)]H^+$ dominant isotope or H_2O cluster of *m/z* 355
$[C_8H_{26}O_7Si_5]H^+$	375	$[D_3T_2(OH)_2]H^+$ dominant isotope
$[C_9H_{25}O_7Si_5]^+$	385	$[D_3T_2(OH)(OCHO)\text{-}H_2O]^+$
$[C_{10}H_{28}O_7Si_5]H^+$	401	$[D_4T(OCHO)]H^+$ dominant isotope

Table S5. Reactions and rate coefficients added to the KinSim OFR mechanism template. The rate coefficients (*k*) have units of $cm^3\ s^{-1}$ and s^{-1} for bimolecular and unimolecular reactions respectively. Ziemann and Atkinson (2012) notes that the rates of RO_2 + RO_2 varies by orders of magnitude depending on the structure of the RO_2 and that the products are uncertain. Here, we assumed that the initial RO_2 from D_5 + OH is analogous to secondary alkyl RO_2. Alton and Browne (2022) proposes the majority product of RO_2 + HO_2 is RO. The RO_2 + OH rate is for the propylperoxy radical (Fittschen, 2019). For isomerization, we used a value in the range of calculated 1,5 H-shift rates in alkanes, which can vary by orders of magnitude depending on the molecule's functionalization (Otkjær et al., 2018).

Reference	Reaction	Products	*k*
Alton and Browne (2022)	$RO_2 + HO_2$	$RO + O_2 + OH$ (90 %) ROOH (10 %)	1.7×10^{-11}
Ziemann and Atkinson (2012)	$RO_2 + RO_2$	ROH + R=O $2RO + O_2$ $ROOR + O_2$	5×10^{-15}
Fittschen (2019)	$RO_2 + OH$	ROOOH $RO + HO_2$	1.4×10^{-10}
Alton and Browne (2022)	RO_2 rearrangement	RO + HCHO	8.0×10^{-3}
Otkjær et al. (2018)	RO_2 isomerization	$R'O_2$	1×10^{-3}
Atkinson et al. (2006)	HCHO + OH	$HO_2 + CO$	8.5×10^{-12}
Atkinson et al. (2006)	CO + OH	$HO_2 + CO_2$	1.5×10^{-13}

Table S6. Input UV fluxes (cm^{-2} s^{-1}) for KinSim.

Experiment	$[O_3]$ matched		OH_{exp} matched	
	I_{185}	I_{254}	I_{185}	I_{254}
1	3.441×10^{12}	2.375×10^{13}	3.441×10^{11}	2.375×10^{12}
2	3.741×10^{12}	2.325×10^{13}	3.741×10^{11}	2.325×10^{12}
3	3.615×10^{12}	2.075×10^{13}	3.615×10^{11}	2.075×10^{12}
4	4.038×10^{12}	1.400×10^{13}	4.038×10^{11}	1.400×10^{12}
5	4.442×10^{12}	2.100×10^{13}	4.442×10^{11}	2.100×10^{12}
6	4.083×10^{12}	1.525×10^{13}	4.083×10^{11}	1.525×10^{12}
7	1.992×10^{13}	3.090×10^{14}	1.992×10^{12}	3.090×10^{13}
8	1.681×10^{13}	2.343×10^{14}	1.681×10^{12}	2.343×10^{13}
9	1.743×10^{13}	2.450×10^{14}	1.743×10^{12}	2.450×10^{13}
10	1.992×10^{13}	3.045×10^{14}	1.992×10^{12}	3.045×10^{13}
11	1.795×10^{13}	2.420×10^{14}	1.795×10^{12}	2.420×10^{13}
12	1.801×10^{13}	2.418×10^{14}	1.801×10^{12}	2.418×10^{13}
13	5.534×10^{12}	2.175×10^{13}	5.534×10^{11}	2.175×10^{12}
14	5.304×10^{12}	2.100×10^{13}	5.304×10^{11}	2.100×10^{12}
15	5.042×10^{12}	1.725×10^{13}	5.042×10^{11}	1.725×10^{12}

Table S7. Fit first generation relative molar yields (γ_i) and $k_{VOPi+OH}$ of proposed VOP. Here, "D" and "T" refer to silicon center atoms bonded to two and three oxygen atoms respectively.

Proposed VOP	γ_i	$k_{VOPi+OH}$ ($cm^3\ s^{-1}$)
$D_4T(OCHO)$ (*m/z* 401)	0.0514	4.57×10^{-12}
$D_3T_2(OH)(OCHO)$ (*m/z* 385)	0.518	5.26×10^{-12}
$D_3T_2(OH)_2$ (*m/z* 357)	0.343	5.73×10^{-12}
$D_4T(OH)$ (*m/z* 355)	1.11	7.53×10^{-12}

Table S8. Experimental molar yields of HCHO and HCOOH. As these species are formed in the OFR at an unknown point, there may be some loss through oxidation with OH. Consequently, the OH_{exp} determined with D_5 may not represent the OH_{exp} these VOP experienced.

Experiment	ΔHCHO/ΔD_5 (ppb/ppb)	ΔHCOOH/ΔD_5 (ppb/ppb)
1	1.79 ± 0.25	0.94 ± 0.15
2	1.35 ± 0.15	0.69 ± 0.09
3	1.21 ± 0.21	0.52 ± 0.09
4	1.52 ± 0.11	0.90 ± 0.09
5	1.28 ± 0.11	0.83 ± 0.09
6	0.96 ± 0.06	0.62 ± 0.05
7	1.06 ± 0.06	0.68 ± 0.05
8	1.18 ± 0.09	0.80 ± 0.07
9	0.88 ± 0.04	0.60 ± 0.04
10	0.69 ± 0.03	1.27 ± 0.11
11	0.55 ± 0.02	0.84 ± 0.06
12	0.52 ± 0.02	0.68 ± 0.04
13	2.11 ± 0.76	0.98 ± 0.37
14	1.11 ± 0.24	0.49 ± 0.12
15	1.15 ± 0.29	0.45 ± 0.12

Table S9. Summary of low-NO_x SOSiA experiments as reported in the literature. The Y_{SOSiA} and C_{OA} from the literature are multiplied during the analysis by 1.07/(ρ_{SOSiA} used in the reference) to compare with the values from this study. Wu and Johnston (2017) did not provide a ρ_{SOSiA} nor an OH_{exp}, and so we assume their ρ_{SOSiA} to be the same used here (ρ_{SOSiA} = 1.07 g cm^{-3}) and calculated OH_{exp} using their estimated ΔD5 and residence time. Moreover, we convert the ΔD_5 they report from ppb to µg m^{-3} with 370.8 g mol^{-1}, 298 K, and 1 atm to calculate their Y_{SOSiA}. Janechek et al. (2019) conducted experiments with and without ammonium sulfate (AS) seed and found that the SOSiA mass concentration would increase with the addition of seed aerosol. We re-calculate their OH_{exp} using the ΔD_5 they provide. Charan et al. (2022) does not provide a summary of C_{OA}, so we calculate them using the values in their Table 1 at 1 atm, and we use the Y_{SOSiA} from their oxidation flow tube with the particle wall loss corrections. Also, we update their OH_{exp} with their reported ΔD_5 and residence times. Han et al. (2022) provided a range of ρ_{SOSiA} of 1.6 – 1.8 g cm^{-3} for a variety of cyclosiloxane precursors, and we use a value of 1.7 g cm^{-3} for the ρ_{SOSiA} adjustment. We also adjust their OH_{exp} using their reported [OH] and ΔD_5.

Reference	**Experiment Set Up**	**Y_{SOSiA} (%)**	**OH_{exp} (s cm^{-3})**	**C_{OA} (µg m^{-3})**	**Seed**	**ρ_{SOSiA} (g cm^{-3})**
Wu and Johnston (2017)	PFA photo-oxidation chamber (50 L, τ_{res} = 15 min)	7.9	1.0×10^{11}	1.2	None	N/A, assumed to be the same used here.
		9.9	1.5×10^{11}	3.3	None	
		12.7	1.5×10^{11}	5.6	None	
		14.3	1.8×10^{11}	8.0	None	
		15.8	2.4×10^{11}	12.0	None	
		13.8	1.1×10^{11}	2.3	AS	
		15.1	9.5×10^{10}	3.2	AS	
		17.5	1.1×10^{11}	4.5	AS	
		21.8	1.5×10^{11}	9.6	AS	
		23.1	1.7×10^{11}	12.6	AS	
Janechek et al. (2019)	PAM-OFR (13.3 L, τ_{res} = 2.7 or 3.8 min)	33	2.0×10^{12}	245	N/A	0.959
		27	1.5×10^{12}	94	N/A	
		25	1.6×10^{12}	119	N/A	
		56	1.6×10^{12}	202	N/A	
		27	1.7×10^{12}	76	N/A	
Charan et al. (2022)	FEP chamber (19 m^3)	1.1	9.9×10^{10}	14.	AS	1.52
		4.0	9.3×10^{10}	31.	AS	
		0	4.7×10^{10}	0	AS	
		1.8	4.2×10^{10}	13.	AS	
Charan et al. (2022)	Caltech photo-oxidation flow tube (τ_{res} = 671 s)	1.3	1.5×10^{10}	1.6	None	1.52
		2.0	1.5×10^{11}	21	None	
		6.5	1.6×10^{11}	72	None	
		4.7	2.4×10^{11}	72	None	
		13	4.6×10^{11}	321	None	

		23	5.5×10^{11}	603	None	
		34	6.2×10^{11}	978	None	
		111	1.8×10^{12}	4024	None	
		111	2.0×10^{12}	4091	None	
		97	3.2×10^{12}	1215	None	
		90	3.3×10^{12}	1127	None	
Han et al. (2022)	Environment and Climate Change Canada OFR (16 L, τ_{res} = 2 min)	1.3	5.5×10^{10}	0.3	None	1.6-1.8
		1.3	1.4×10^{11}	1.1	None	
		6.9	3.5×10^{11}	11	None	
		17	5.0×10^{11}	31	None	
		22	6.0×10^{11}	43	None	
		29	6.8×10^{11}	61	None	
		38	9.0×10^{11}	107	None	
		44	1.2×10^{12}	144	None	
		47	1.3×10^{12}	160	None	
		50	1.7×10^{12}	178	None	
		50	1.8×10^{12}	172	None	
		1.3	5.5×10^{10}	0.5	AS	
		0.6	1.4×10^{11}	1.3	AS	
Avery et al. (2023)	PAM-OFR (13.3 L, τ_{res} = 130 s)	1.2	1.15×10^{12}	2.3	None	1.78
		10	2.42×10^{12}	18	None	1.67
		24	3.77×10^{12}	44	None	1.64
		28	4.55×10^{12}	51	None	1.61
		55	5.23×10^{12}	100	None	1.60
		70	6.21×10^{12}	126	None	1.60
		98	8.23×10^{12}	180	None	1.59

Table S10. Odum two-product model fit values. These two-product parameterizations do not account for OH_{exp}. Janechek et al. (2019) and Charan et al. (2022) state the values below, and Charan et al. (2022) provided 2 fits: with/without particle wall-loss corrections. Han et al. (2022) and Avery et al. (2023) did not provide two-product parameterizations, so we fit their data that was adjusted to ρ_{SOSiA} = 1.07 g cm^{-3}; the original ρ_{SOSiA} are in Table S9. We also perform a fit with all values, including those in the literature.

Reference	α_1	α_2	K_1	K_2
Janechek et al. (2019) (ρ_{SOSiA} = 0.959 g cm^{-3})	0.14	0.82	1.05	0.00207
Charan et al. (2022) (ρ_{SOSiA} = 1.52 g cm^{-3})	0.056/0.044	7.7/5.5	0.022/0.027	4.3×10^{-5}/6.0×10^{-5}
Han et al. (2022) (ρ_{SOSiA} = 1.07 g cm^{-3})	0.4598	1.284	1.432×10^{-2}	8.546×10^{-4}
Avery et al. (2023) (ρ_{SOSiA} = 1.07 g cm^{-3})	5.301	9.756	3.161×10^{-4}	4.209×10^{-4}
This paper (ρ_{SOSiA} = 1.07 g cm^{-3})	0.2266	0.6864	0.01478	9.611×10^{-4}
All Values (ρ_{SOSiA} = 1.07 g cm^{-3})	0.3814	1.631	0.02551	1.965×10^{-4}

Table S11. Fit VBS product mass yields (α_i) and chemical aging rate coefficients ($k_{age,gas}$). The $k_{age,gas}$ is for the aging-VBS model where OH_{exp} is explicitly parameterized with the and "bin-hopping" as described in Sect. 3.2. We perform fits using the data from our experiments and all values, which includes those in the literature. For α_i smaller than 10^{-5}, we mark them as 0.

C^*	0.1	1	10	100	1000	10000	$k_{age,gas}$	$k_{age,particle}$
This study α_i (no aging)	8.47 $\times 10^{-4}$	0	0.119	0	0.704	0.176	N/A	N/A
This study α_i	4.20 $\times 10^{-3}$	3.22 $\times 10^{-4}$	7.33 $\times 10^{-3}$	9.05 $\times 10^{-2}$	1.02 $\times 10^{-4}$	0.898	2.18 $\times 10^{-12}$	1.99 $\times 10^{-12}$
This study α_i ($k_{age,particle} = 0$)	1.11 $\times 10^{-3}$	2.82 $\times 10^{-4}$	1.41 $\times 10^{-2}$	6.84 $\times 10^{-2}$	2.48 $\times 10^{-4}$	0.916	2.64 $\times 10^{-12}$	0
All values α_i (no aging)	4.69 $\times 10^{-2}$	2.31 $\times 10^{-5}$	0	0	0.953	0	N/A	N/A
All values α_i	1.27 $\times 10^{-3}$	7.81 $\times 10^{-3}$	2.10 $\times 10^{-3}$	7.77 $\times 10^{-2}$	1.93 $\times 10^{-4}$	0.911	2.10 $\times 10^{-12}$	1.98 $\times 10^{-12}$

Table S12. Experiment particle surface area densities and OH to particle collision flow, which we denote as the maximum observable $k_{age,particle}$. These maximum values are calculated assuming an effective OH uptake coefficient of 1, and the surface area densities are calculated using the particle size distributions measured with the SMPS. The corresponding effective uptake coefficients are calculated from the ratios of the maximum observable $k_{age,particle}$ and the fit $k_{age,particle}$.

Experiment	Surface Area Density (cm^2 cm^{-3})	Max $k_{age,particle}$ (cm^3 s^{-1})	Estimated Uptake Coefficient
1	6.23×10^{-6}	5.50×10^{-12}	0.362
2	9.84×10^{-6}	4.78×10^{-12}	0.416
3	9.56×10^{-6}	4.98×10^{-12}	0.400
4	3.48×10^{-5}	4.25×10^{-12}	0.468
5	6.41×10^{-5}	3.30×10^{-12}	0.603
6	8.64×10^{-5}	2.79×10^{-12}	0.714
7	1.69×10^{-5}	4.23×10^{-12}	0.470
8	3.71×10^{-5}	2.89×10^{-12}	0.688
9	7.22×10^{-5}	2.19×10^{-12}	0.907
10	7.63×10^{-5}	3.31×10^{-12}	0.601
11	1.24×10^{-4}	2.73×10^{-12}	0.730
12	2.28×10^{-4}	2.19×10^{-12}	0.910
13	2.97×10^{-6}	7.00×10^{-12}	0.284
14	2.95×10^{-6}	6.57×10^{-12}	0.303
15	2.42×10^{-6}	6.02×10^{-12}	0.331

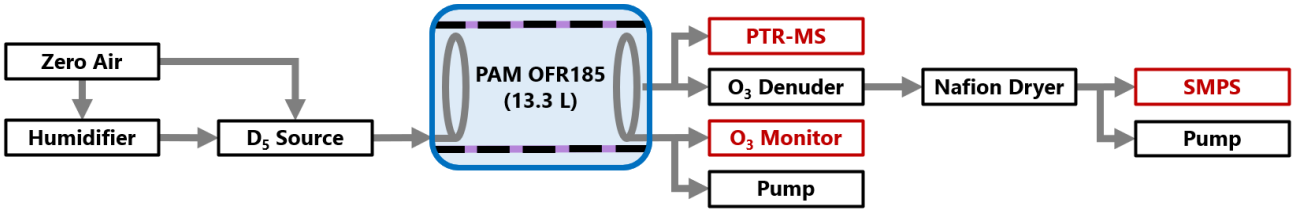


Figure S1. PAM-OFR experiment set up. The D_5 source was a syringe pump injecting into a passivated glass bulb. The side ports were equipped with conductive Teflon flow rings on both ends of the PAM-OFR. We covered 90 % of the 185 nm UV lamps to achieve lower irradiances and OH_{exp}. We conducted experiments at τ_{res} = 120 s with 6.65 L min^{-1} or 180 s with 4.43 L min^{-1} respectively.

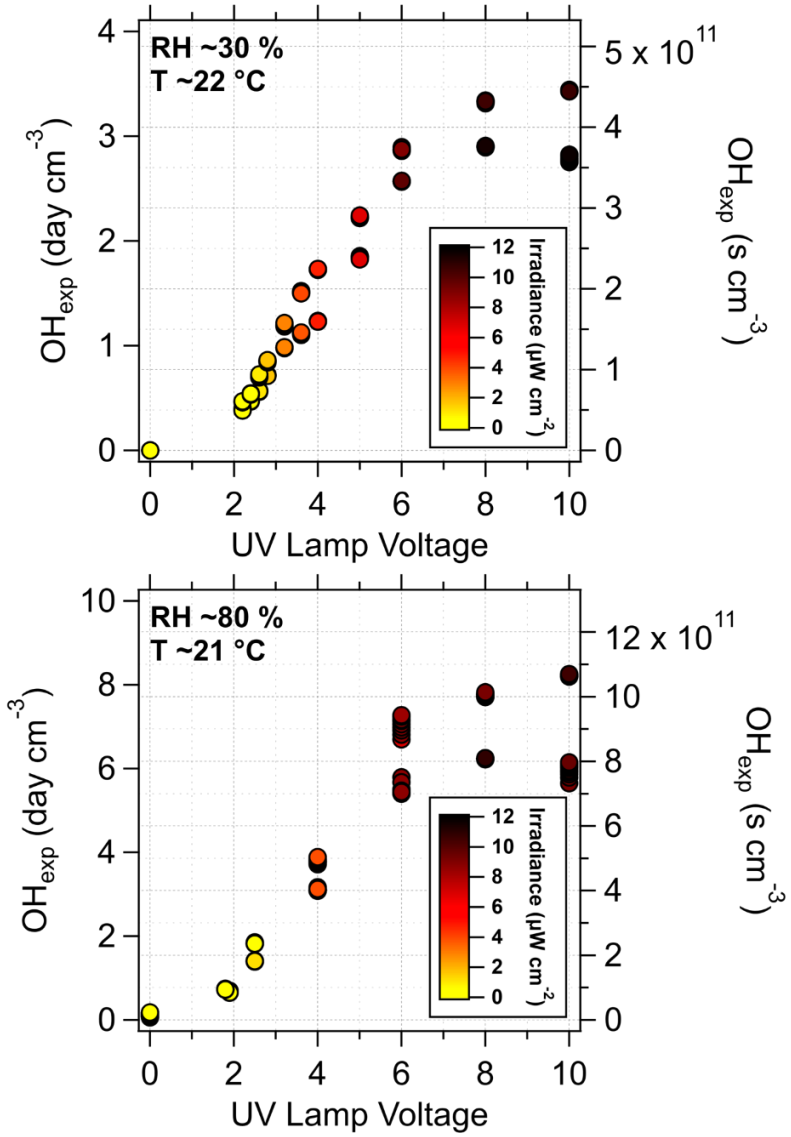


Figure S2. Offline OH_{exp} calibrations with CO at low and high humidity conditions. The OH_{exp} measured during experiments with D_5 were consistent with the offline calibration values.

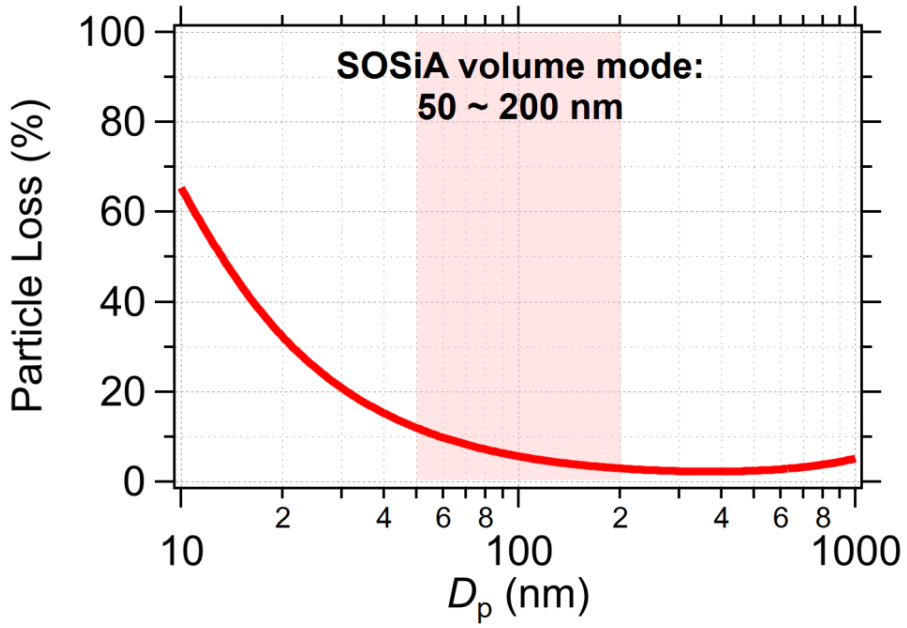


Figure S3. Calculated particle losses with diameters (von der Weiden et al., 2009) using the dimensions of the aerosol sampling line. The shaded area refers to the aerosol volume modes found during experiments.

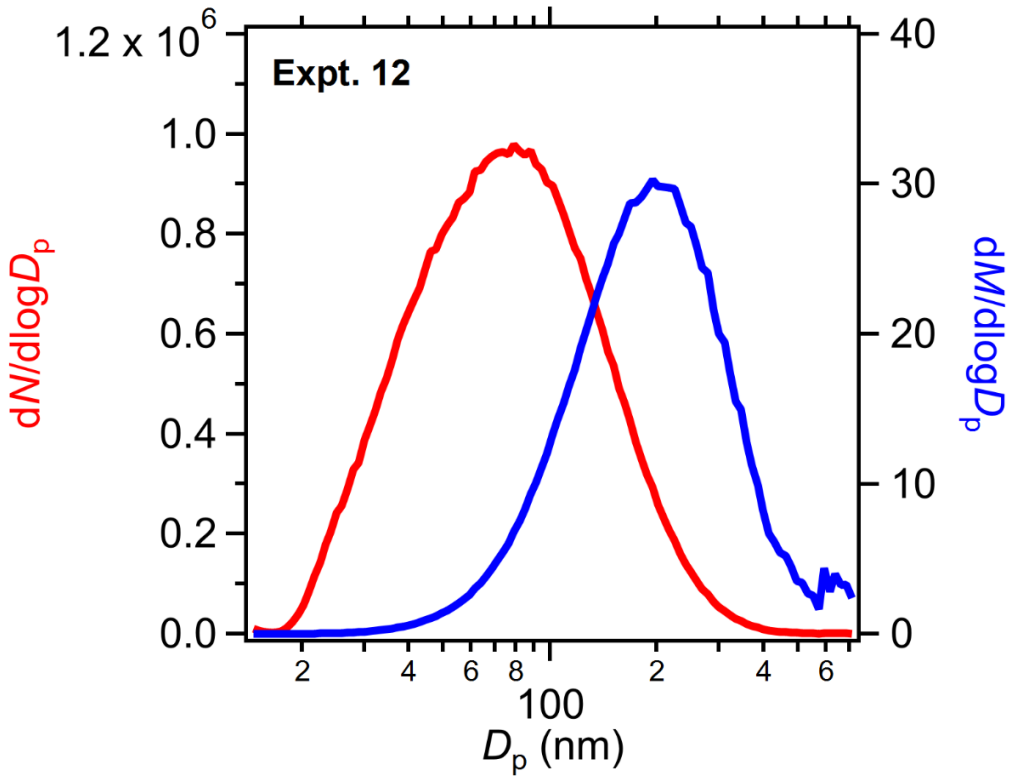


Figure S4. SOSiA particle size distribution for experiment 12, where $[D_5]_0$ and OH_{exp} were high.

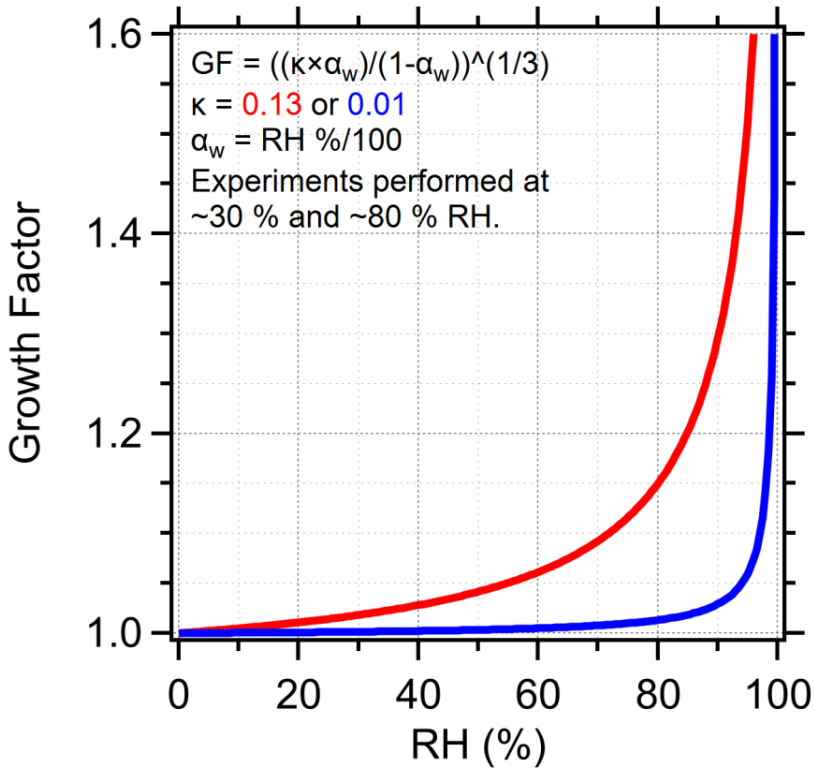


Figure S5. Particle growth factor vs. RH (%) for κ = 0.13 and 0.01. Palm et al. (2016) used the SOA hygroscopicity factor (κ = 0.13), while Janechek et al. (2019) found SOSiA to be non-hygroscopic (κ = 0.01).

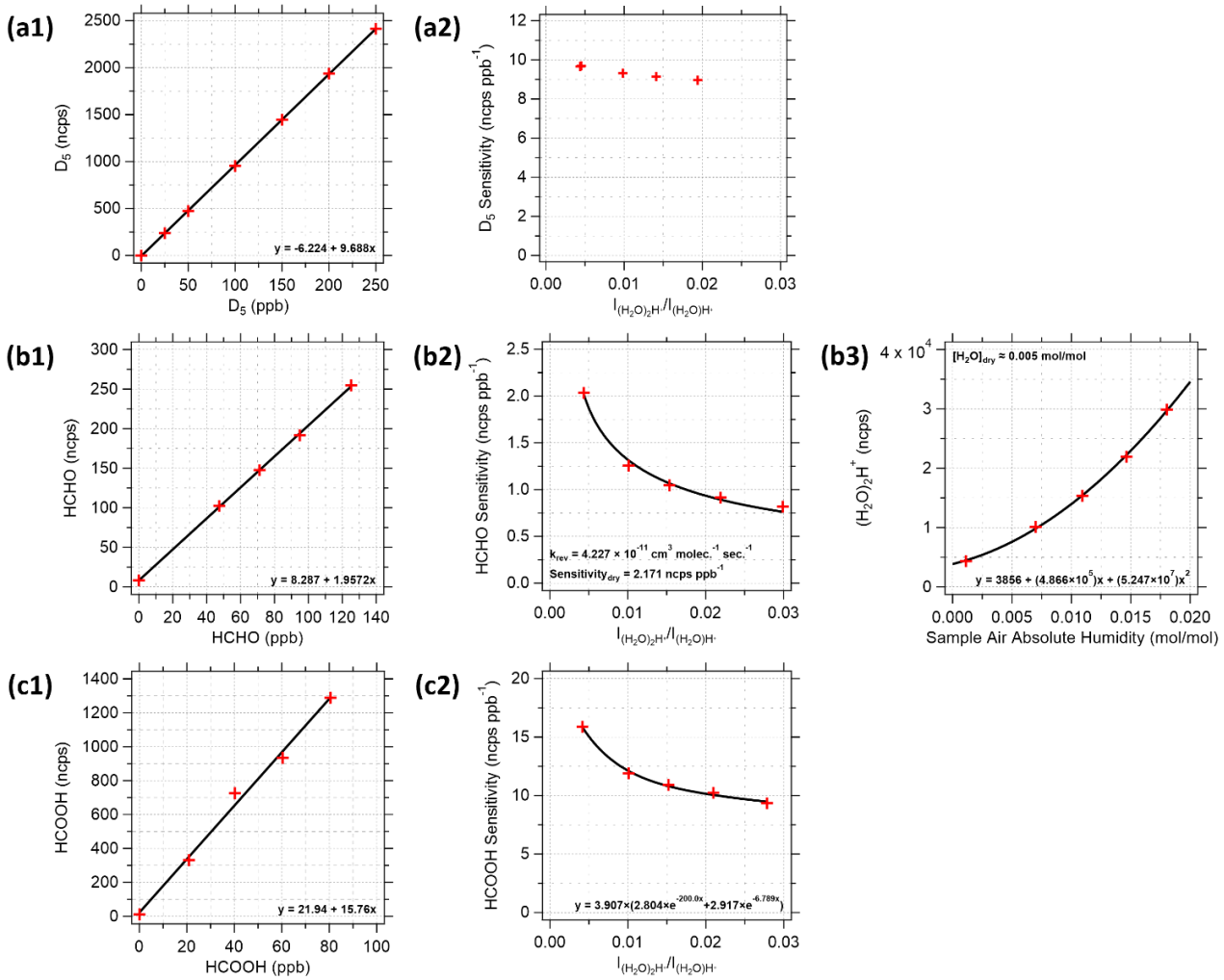


Figure S6. (a1, b1, c1) Calibration curves of D_5, HCHO, and HCOOH. The PTR-MS response was linear under these concentration ranges. (a2, b2, c2) Sensitivity variation with humidity. We found the D_5 sensitivity at *m/z* 371 under 137 Td to be consistent with changing humidity and did not apply a correction for the quantification. (b3) Polynomial fit to determine the H_2O mixing ratio contribution from the PTR-MS ion source.

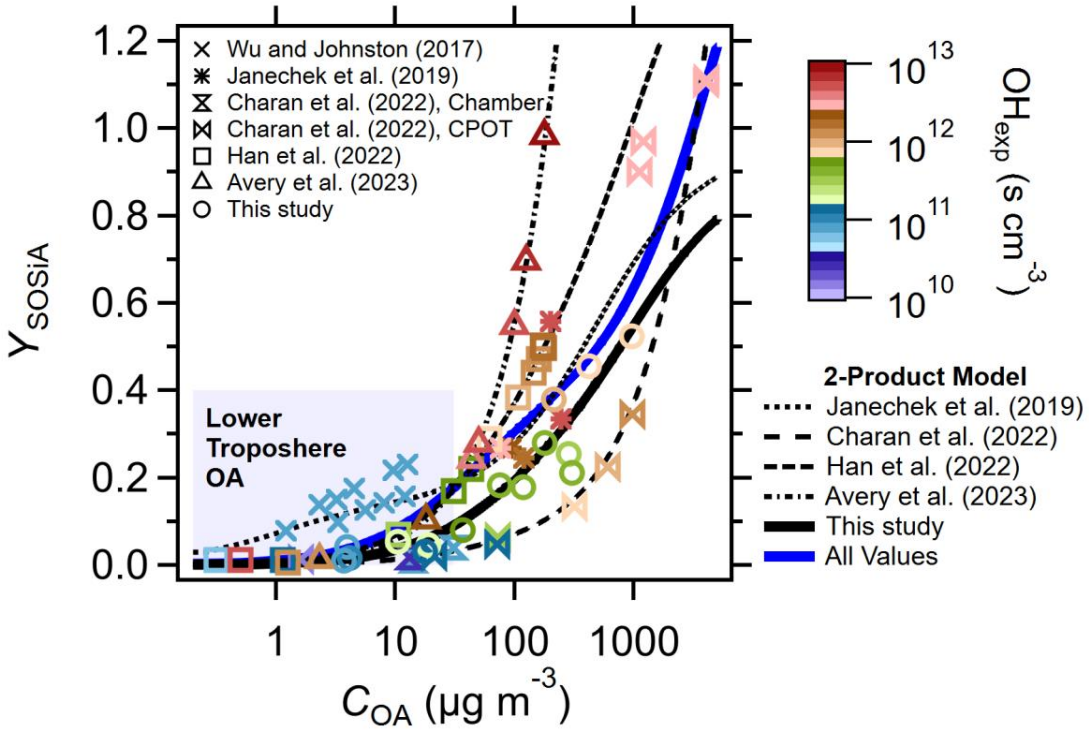


Figure S7 Comparison of Odum two-product model parameterizations between this study and the literature. The blue line is from the fit with all data, including those we report. The shaded area indicates the range of ambient OA concentrations commonly observed in the lower troposphere (Porter et al., 2021). The figure shows the particle wall loss-corrected values from Charan et al. (2022). Han et al. (2022) and Avery et al. (2023) did not provide two-product parameterizations, so we fit the values using their ρ_{SOSiA}-adjusted data (Table S10). Wu and Johnston (2017) did not have measurements of OH_{exp} or D_5 and instead provided estimates. The OH_{exp} (color scale) are those reported by the literature.

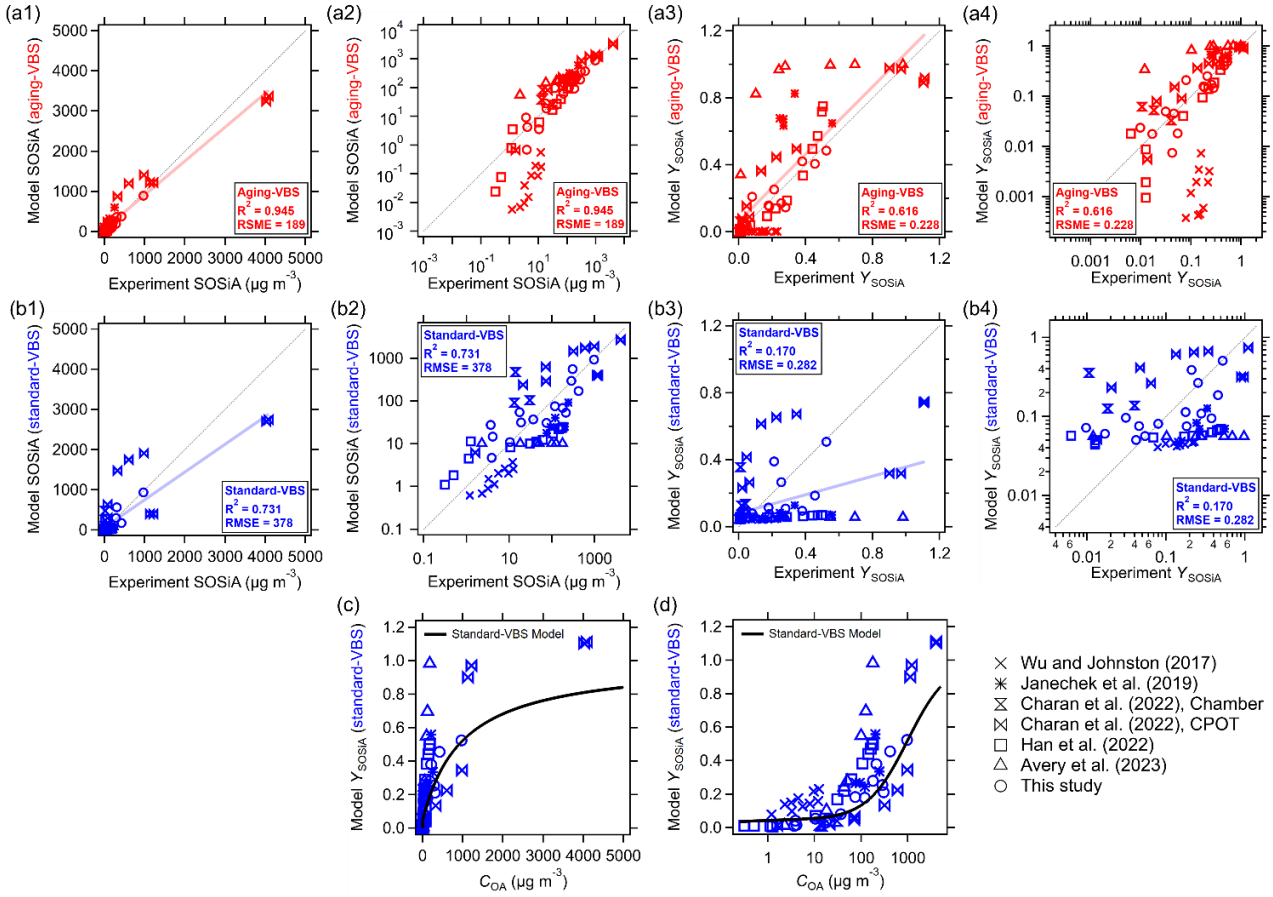


Figure S8. Comparison of the (1, 2) SOSiA mass and (3, 4) Y_{SOSiA} from the (a) aging-VBS and (b) standard-VBS parameterizations fit with values we report and those in the literature (Table S11). Panels (2) show the same data in Panels (1) but in log scale. Panels (c) and (d) show the same Y_{SOSiA} from the standard-VBS model plotted against C_{OA}, but the x-axes are in linear and log scales respectively. The R^2 and root mean square error (RMSE) of the aging-VBS model SOSiA is better than that of the standard VBS.

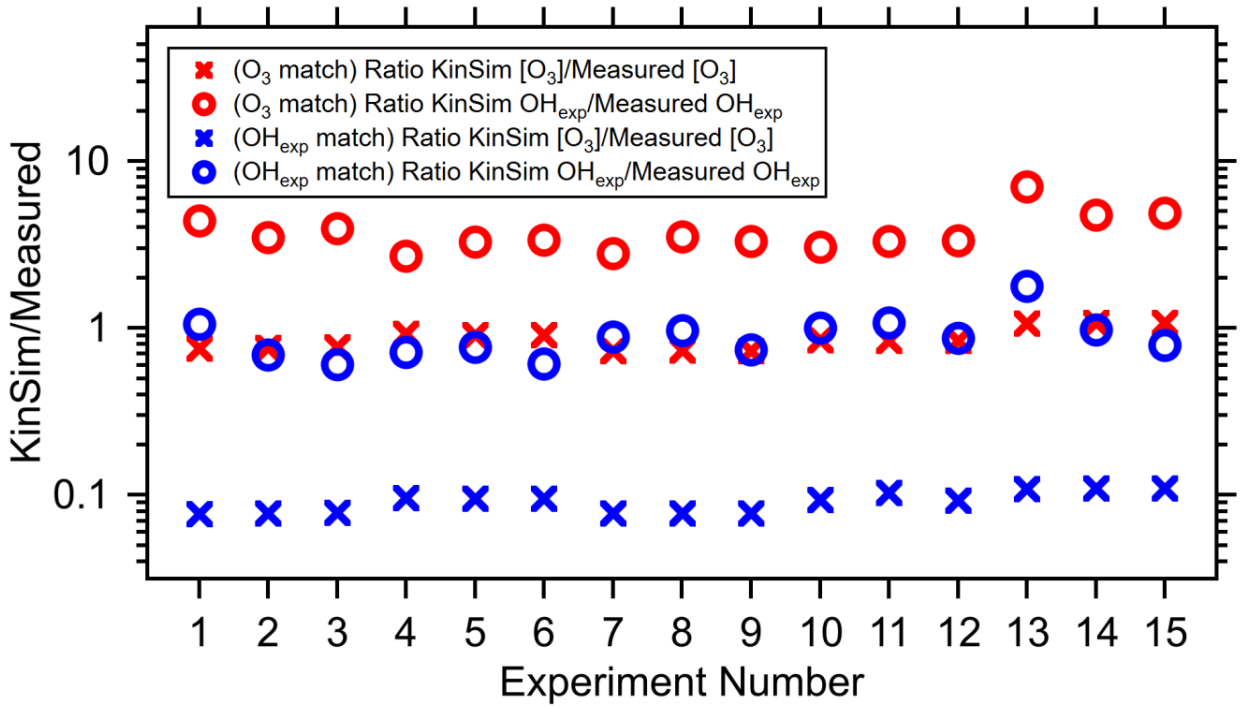


Figure S9. Ratio of the KinSim model outputs vs. measurements for each experiment. The "OH_{exp} match" and "O_3 match" refers to the cases where the UV flux is and is not adjusted so that the KinSim outputs of OH_{exp} and O_3 are in line with measurements respectively.

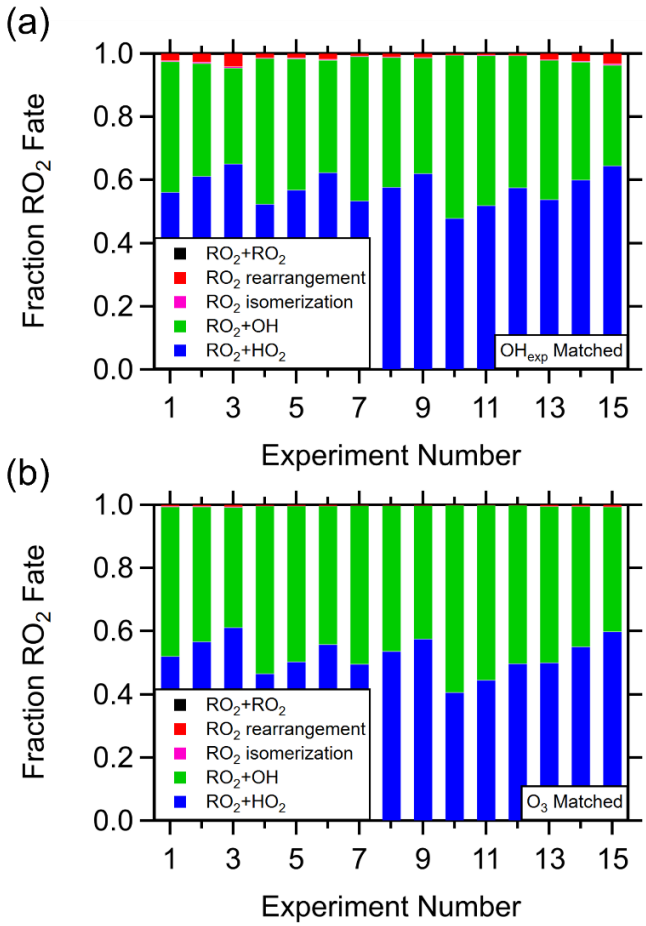


Figure S10. KinSim estimations of RO_2 fates across experiments. The top panel (a) has I_{254} and I_{185} multiplied by 0.1 (OH_{exp} matched), while the bottom (b) does not (O_3 matched). In both cases, KinSim calculated the RO_2 fates in all experiments to be dominated by the RO_2 + HO_2 and RO_2 + OH pathways.

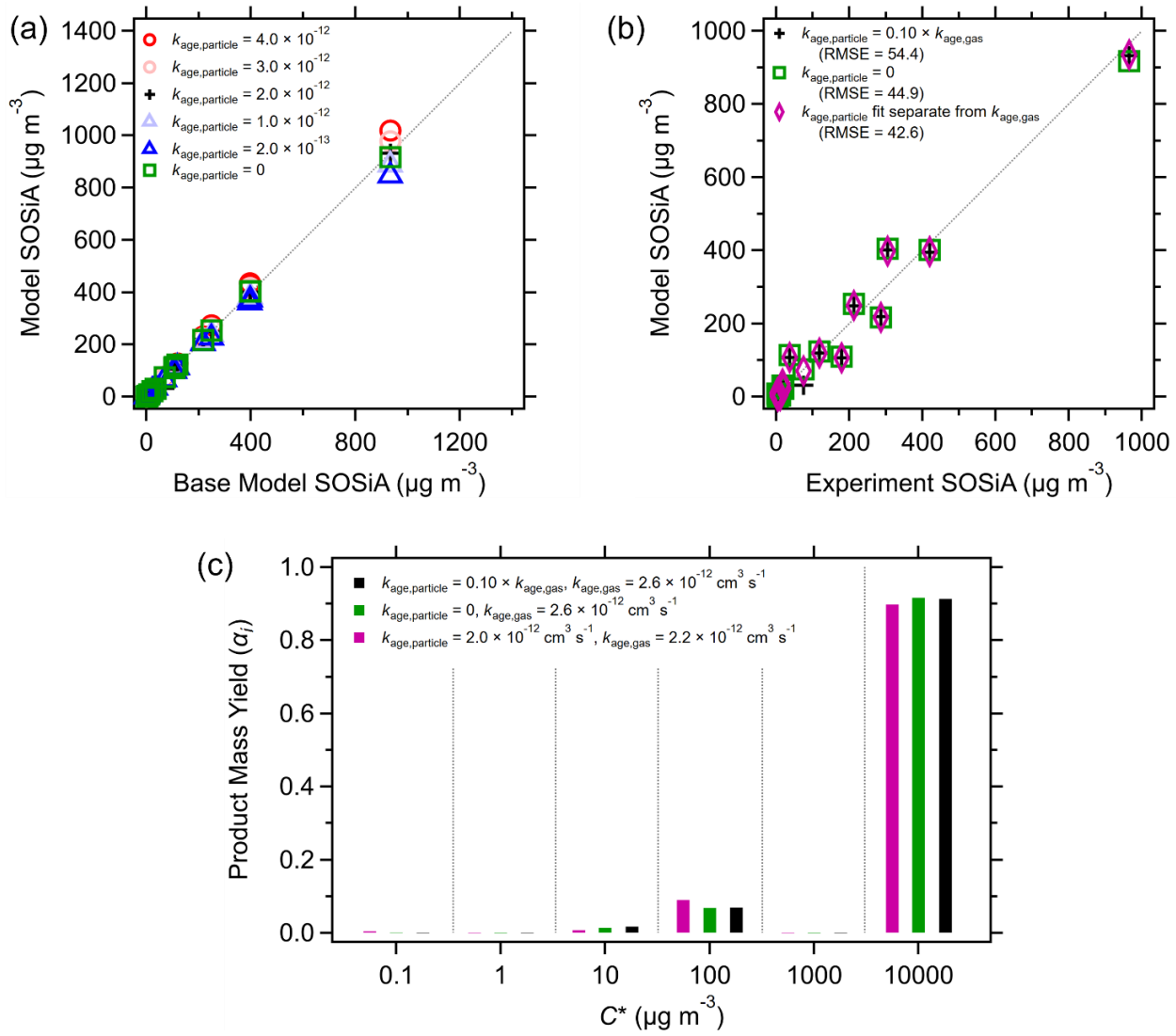


Figure S11. Sensitivity of the aging-VBS model to $k_{age,particle}$: (a) SOSiA formation at varying $k_{age,particle}$ assumptions compared using the optimized parameters found with the "base" model. The base model refers to the version where $k_{age,gas}$ and $k_{age,particle}$ are fit separately. (b) SOSiA formation using optimized parameters found under each $k_{age,particle}$ assumption. The optimized parameters produce comparable RMSE for each corresponding $k_{age,particle}$ assumption. (c) VBS found under each $k_{age,particle}$ assumption. The product mass yields vary only slightly. The purple markers and bars in panels (b) and (c) are from the aging-VBS model used in this paper where $k_{age,gas}$ and $k_{age,particle}$ are fit separately.

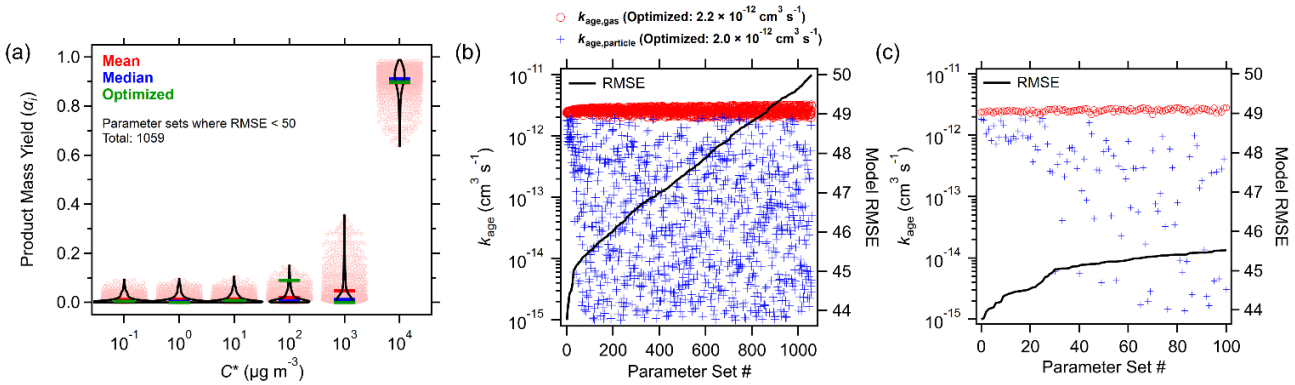


Figure S12. Range of the optimized parameter sets of (a) α_i and (b) the chemical aging rate coefficients in the fit ensemble. Panel (c) shows the same data as panel (b) but only for the 100 best-fitting parameter sets in the fit ensemble. We find a shallow minimum in RMSE for $k_{age,particle}$ around a value of 1 × 10^{-12} cm^3 s^{-1}. "Optimized" values refer to the best-fit parameter set found with MCGA global optimization. During the global optimization, we generate 768 000 Monte Carlo samples with randomly assigned parameter values. Then, we find the parameter sets where the aging-VBS model outputs RMSE < 50 against SOSiA measurements. We find small variation in the $k_{age,gas}$ while there is large variation in $k_{age,particle}$, suggesting the model is less sensitive to $k_{age,particle}$.

B.2 Supplement of "Multiphase chemistry and phase state explain nonlinear effects in the formation and evaporation of SOA from mixed monoterpene precursors"

Supplementary of "Multiphase chemistry and phase state explain non-linear effects in the formation and evaporation of SOA from mixed monoterpene precursors"

Hyun Gu Kang,[†] Masayuki Takeuchi,[‡,∥] Nga L. Ng,[¶,‡,§,⊥] Ulrich Pöschl,[†] and Thomas Berkemeier[*,†]

†*Multiphase Chemistry Department, Max Planck Institute for Chemistry, 55218 Mainz, Germany*

‡*School of Civil and Environmental Engineering, Georgia Institute of Technology, Atlanta, Georgia 30332, United States of America*

¶*School of Chemical and Bimolecular Engineering, Georgia Institute of Technology, Atlanta, Georgia 30332, United States of America*

§*School of Earth and Atmospheric Sciences, Georgia Institute of Technology, Atlanta, Georgia 30332, United States of America*

∥*Current address: Department of Mechanical Engineering, 613 University of Colorado Boulder, Boulder, Colorado 80309, United States of America*

⊥*Current address: Division of Engineering and Applied Science, California Institute of Technology, Pasadena, California 91125, United States of America*

E-mail: t.berkemeier@mpic.de

1 Moving-boundary algorithm

With the moving-boundary algorithm, the desorption flux at the surface is counteracted by a down-motion of all layer boundaries in the model, which will cause the inner-most bulk layer to merge into the adjacent layer. Effectively, the algorithm increases diffusion from the inner-most to the outer-most bulk layer when there is net desorption to keep the volume of the near-surface bulk layer constant. While this practice still results in numerical diffusion, no sudden spikes in evaporation occur (Fig. S1). We ensure that numerical diffusion has a minor influence on the calculation results by performing calculations with increased layer resolution to check for numerical convergence. This algorithm is similar to the mass redistribution algorithm adopted by Couvidat and Sartelet [1] in the Secondary Organic Aerosol Processor (SOAP) model, where the masses of the individual bulk layers are kept equal through mass transport adjustments. However, Couvidat and Sartelet [1] did not use an adaptive layer resizing algorithm like here, and the number of bulk layers was fixed. Furthermore, the moving-boundary algorithm works to keep the volume of the near-surface bulk layer constant, not those of all bulk layers.

A schematic of the moving-boundary algorithm is in Fig. S2. When there is net desorption from the particle, we calculate the molecular volume flow out of the near-surface bulk layer ($F_{\mathrm{V,out}}$, cm^3 s^{-1}) and increase the diffusion from the layer underneath to match $F_{\mathrm{V,out}}$ (Eq. S1). Here, y_{low} and V_{m} are vectors of the component molecules and their molecular volumes (cm^3) in a given layer. V_{low} is the volume of that given layer (cm^3), and $A_{\text{up-low}}$ is the interface area (cm^2) between the given layer and the one above it.

$$F_{\mathrm{V,out}} = k_{\mathrm{b,mvbd}} \times \sum (y_{\mathrm{low}} \cdot V_{\mathrm{m}}) \frac{A_{\text{up-low}}}{V_{\mathrm{low}}} \tag{S1}$$

We find the moving-boundary bulk diffusion rate coefficient ($k_{\mathrm{b,mvbd}}$, cm s^{-1}) for each bulk layer interface with Eq. S1. Then, we calculate the moving-boundary diffusion rate (Eq. S2, s^{-1}), which is applied to every underlying layer and is added to the existing bulk

diffusion rates in the ordinary differential equations.

$$\text{Rate} = k_{\text{b,mvbd}} \times y_{\text{low}} \frac{A_{\text{up-low}}}{V_{\text{low}}} \tag{S2}$$

2 Adsorption and desorption rate coefficients

We explicitly model the mass transport between the near-surface gas and particle phases. For the adsorption rate coefficient ($k_{\text{a},i}$, cm s^{-1}) of a partitioning species i, we use the molecular collision rate (Eq. S3) like in Berkemeier et al.[2]. We assume a unity mass accommodation coefficient[3,4] for all partitioning species, where ω_i is the mean thermal velocity (cm s^{-1}) of i.

$$k_{\text{a},i} = \alpha \frac{\omega_i}{4} \tag{S3}$$

We use the equation for the desorption rate coefficient from particles in the chamber ($k_{\text{d,chamber},i}$, cm s^{-1}) from Berkemeier et al.[2] (Eq. S4), where $p_{\text{vap},i}$ is the vapor pressure (atm) of i at temperature T (K), N_{A} is Avogadro's number (6.022×10^{23} mol^{-1}), R is the gas constant (82.057 cm^3 atm K^{-1} mol^{-1}), and $[Y]_{\text{b}}$ is the molecular number density of the near-surface bulk layer (cm^{-3}).

$$k_{\text{d,chamber},i} = \alpha \frac{\omega_i}{4} \times \frac{p_{\text{vap},i} N_{\text{A}}}{RT[Y]_{\text{b}}} \tag{S4}$$

Desorbing gases are suspected to interact with the Teflon filter and surfaces in the FIGAERO.[5] We model this effect by including a resistance term to the denominator in the equation for $k_{\text{d,chamber},i}$. The resistance term ($[Y]_{\text{FIGAERO}}$) goes into the denominator (Eq. S5), where $[Y]_{\text{FIGAERO}}$ represents the desorption delay caused by interactions between the desorbing species and FIGAERO surfaces.

$$k_{\text{d,FIGAERO},i} = \alpha \frac{\omega_i}{4} \times \frac{p_{\text{vap},i} N_{\text{A}}}{RT([Y]_{\text{b}} + [Y]_{\text{FIGAERO}})} \tag{S5}$$

3 Chemical mechanism

A schematic of the chemical mechanism is in Fig. S3. For simplicity, the RO_2 terminate to partitioning species or go down the RO pathway partitioning species that form the VBS and dimers. For both α-pinene and limonene, the gas-phase reaction of RO_2 + RO_2 forms either an alkoxy radical (RO) or dimers (ROOR), where the ROOR branches into three logarithmically-spaced volatility bins. The RO_2 + RO_2 $\rightarrow$ ROOR branching is shown as b_{dimer} in Table. S1).

The initial RO either terminates into VBS monomers or isomerizes and reacts with O_2 to form secondary RO_2, whose termination products have C^*_{298} that are two orders of magnitude lower. This reduction in C^*_{298} is consistent with the addition of an –OH group onto a carbon backbone.[6] The fit RO termination branching is $b_{\text{term.}}$ in Table. S1. The RO termination reaction produces a VBS monomer and either NO_2 or HO_2, following the fate of NAPINBO in the MCM, and this branching is fit ($b_{\text{NO2 loss}}$ in Table. S1).

As limonene possesses two double bonds, we assume the initial oxidation product retains a double bond and is highly volatile. This intermediate is consistent with limonaldehyde in the MCM, and limonone + NO_3 experiments report high yields of limonaldehyde.[7–10] The C^*_{298} of this double-bond intermediate is optimized for, and the intermediate reacts with NO_3 to form RO_2 and subsequent products.

4 Optimized parameters and MCGA

We use the Monte Carlo Genetic Algorithm (MCGA)[11] to optimize the model parameters on the RAVEN supercomputer, which we then locally optimize the result with the SIMPLEX method.[12] For MCGA, we would randomly generate parameter sets on 288 CPUs, sampling 80 from each CPU. Then, each CPU would take 6 of the parameter sets and 1 randomly generated one to form a subpopulation. The genetic algorithm would pull 5 parameter sets from this subpopulation and optimize over 5 generations to find 1 best fit. The best fits

across all CPUs would be pooled, and the genetic algorithm repeats until 30 generations is reached.

As the multilayer model is quite slow, we optimize the LIM and APN scenarios separately and combine the parameter sets to optimize the parameters for the heterogeneous precursor reactions. Table. S1. summarizes the optimized values in the limonene and α-pinene mechanisms, and Table. S2 has the values for the heterogeneous species reactions and diffusivity parameters.

5 Model sensitivity to parameters

To address the sensitivity of the model to optimized parameters, we provide model results after changing model input parameters individually by ± 25 %. For the monomer volatility distribution, we divide the monomer volatility bins into three groups ($C^*_{298} < 10^{-1}$, $10^{-1} \leq C^*_{298} \leq 10^1$, $C^*_{298} > 10^1$ µg m^{-3}) and make the adjustment to each group for simplicity.

We find that the model is sensitive to the monomer volatility distributions (Fig. S10), the composition-dependent bulk diffusivity parameters (Fig. S11), the NO_3-aging rate coefficient (k_{aging}, Fig. S12), oligomerization reaction parameters (Fig. S13), and $RO_{2,\text{apn}}$ + $RO_{2,\text{lim}}$ reaction parameters (Fig. S14). In the case of the pure α-pinene experiment (APN), the model is sensitive to k_{aging}, while the model did not exhibit a high sensitivity for the pure limonene experiment (LIM). Given the lower bulk oligomer content from the best fit, the bulk mass is not sensitive to adjustments in $k_{\text{fwd,olig}}$ or $k_{\text{rev,olig}}$, but the thermogram models are sensitive to the energies of activation ($E_{\text{a,fwd}}$ and $E_{\text{a,rev}}$) as oligomer decomposition is sensitive to these parameters at higher temperatures. For the MIX experiment, the model outcomes are sensitive to the $RO_{2,\text{apn}}$ + $RO_{2,\text{lim}}$ cross-reaction parameters, while for the SEQ experiment it is not due to the temporal separation of $RO_{2,\text{apn}}$ and $RO_{2,\text{lim}}$ formation.

6 Comparison of $D_\mathrm{b} - C^*$ relationship with data

To compare the D_b–C^* relationship in this model with data, we use the data summarized by Li et al.[13]. The authors used the MPBPWIN model in the Estimation Programs Interface (EPI Suite) and the Boyer–Kauzmann rule to calculate the melting point, glass transition temperature (T_g, K), and C^* (µg m^{-3}) of organic compounds. We convert the T_g to viscosity (η, Pa s) via the Vogel–Tammann–Fulcher equation (Eqs. S6 and S7) at 298 K[13]. Here, T_0 is the Vogel temperature (K), and D is the unitless fragility parameter, assumed to be 10.

$$T_0 = \frac{39.17 \times T_0}{D + 39.17} \tag{S6}$$

$$log_{10}(\eta) = -5 + 0.434 \times \frac{T_0 \times D}{T - T_0} \tag{S7}$$

We convert the $D_{\mathrm{b},298}$ values used by KM3C to viscosities η with the Stokes Einstein equation (Eq. S8), where k_b is the Boltzmann constant, T is the temperature, and r_m is the molecular radius.

$$D_\mathrm{b} = \frac{k_\mathrm{b} T}{6\pi r_\mathrm{m} \eta} \tag{S8}$$

Results of this calculation are shown in Fig. S15, showing that the D_b–C^* relationship employed in this study overestimates the viscosity estimates from MPBPWIN at high C^* values. However, these high C^* values are outside the range of the volatility distribution in this study and irrelevant for condensation of SOA. At lower C^* values, values from the D_b–C^{**} relationship fall generally within the range of the data. Unfortunately, the MPBPWIN dataset is sparse and scatters immensely for these lower C^* values.

Table S1: Optimized values for each scenario. The values assigned to the VBS bins are braching ratios for each bin. α-pinene does not have a double bond intermediate in the mechanism. LB and UB refer to the lower and upper bounds set during the optimization. Branching ratios across the VBS bins for the monomers and the dimers are normalized to 1 respectively.

	Limonene	α-pinene	LB	UB
$C^*_{298} = 10^{-4}$ (µg m^{-3})	0.280	0.002	Norm.	Norm.
$C^*_{298} = 10^{-3}$ (µg m^{-3})	0.003	0.004		
$C^*_{298} = 10^{-2}$ (µg m^{-3})	0.016	0.006		
$C^*_{298} = 10^{-1}$ (µg m^{-3})	0.219	0.010		
$C^*_{298} = 10^{0}$ (µg m^{-3})	0.100	0.025		
$C^*_{298} = 10^{1}$ (µg m^{-3})	0.001	0.040		
$C^*_{298} = 10^{2}$ (µg m^{-3})	0.002	0.039		
$C^*_{298} = 10^{3}$ (µg m^{-3})	0.379	0.013		
$C^*_{298} = \infty$ (µg m^{-3})	0.000	0.860		
Dimer bin 1	0.327	0.562	Norm.	Norm.
Dimer bin 2	0.392	0.100		
Dimer bin 3	0.281	0.338		
Intermed. C^*_{298} (µg m^{-3})	4640	N/A	10^3	10^5
Dimer C^*_{298} (µg m^{-3})	5.16×10^{-5}	1.00×10^{-5}	10^{-6}	10^{-3}
b_{dimer}	0.0972	0.0144	0.01	0.1
$b_{\text{NO2 loss}}$	0.4472	0.474	0.2	1
$b_{\text{term.}}$	0.6797	0.937	0.2	1
$k_{\text{fwd,olig}}$ (s^{-1})	3.00×10^{-6}	1.11×10^{-5}	1×10^{-6}	10^{-2}
$k_{\text{rev,olig}}$ (s^{-1})	3.53×10^{-5}	3.03×10^{-6}	1×10^{-6}	10^{-2}
$E_{\text{a,fwd}}$ (kJ mol^{-1})	98.6	55.0	30	150
$E_{\text{a,rev}}$ (kJ mol^{-1})	44.2	42.1	30	150
k_{aging} (cm^3 s^{-1})	6.51×10^{-15}	2.53×10^{-15}	10^{-17}	10^{-14}

Table S2: Optimized values for heterogeneous reactions and D_{b}. The slope (m) and intercept (b) are used in Eq. 4 to correlate $D_{\mathrm{b,298}}$ with C^{*}_{298}. Since particle-phase oligomers do not partition in the model, we assume that they have a self-D_{b} that is a multiple of that of the $C^{*}_{298} = 10^{-4}$ µg m^{-3} monomer. The $b_{\mathrm{dimer,het}}$, C^{*}_{298} of $\mathrm{ROOR_{het}}$, $E_{\mathrm{a,fwd,het}}$ and $E_{\mathrm{a,rev,het}}$ are scaled between the values for α-pinene and limonene, and so the LB and UB are set to those values.

		LB	UB
$b_{\mathrm{dimer,het}}$	0.0970	0.0144	0.0972
$k_{\mathrm{RO2+RO2,het}}$	7.18×10^{-13}	9.2×10^{-15}	9.2×10^{-13}
$\mathrm{ROOR_{het}}$ C^{*}_{298} (µg m^{-3})	1.19×10^{-5}	1.00×10^{-5}	5.16×10^{-5}
$k_{\mathrm{fwd,olig,het}}$ (s^{-1})	9.52×10^{-6}	6.00×10^{-7}	5.55×10^{-5}
$k_{\mathrm{rev,olig,het}}$ (s^{-1})	8.08×10^{-7}	6.06×10^{-7}	1.77×10^{-4}
$E_{\mathrm{a,fwd,het}}$ (kJ mol^{-1})	98.4	55.0	98.6
$E_{\mathrm{a,rev,het}}$ (kJ mol^{-1})	43.1	42.1	44.2
Slope (m)	0.761	0.4	1
Intercept (b)	14.9	13	16
D_{b} multiple for olig.	3.91×10^{-3}	10^{-4}	1
ΔH^{dif} (kJ mol^{-1})	150	50	200
$[Y]_{\mathrm{FIGAERO}}$ (cm^{-3})	9.54×10^{24}	10^{21}	10^{26}

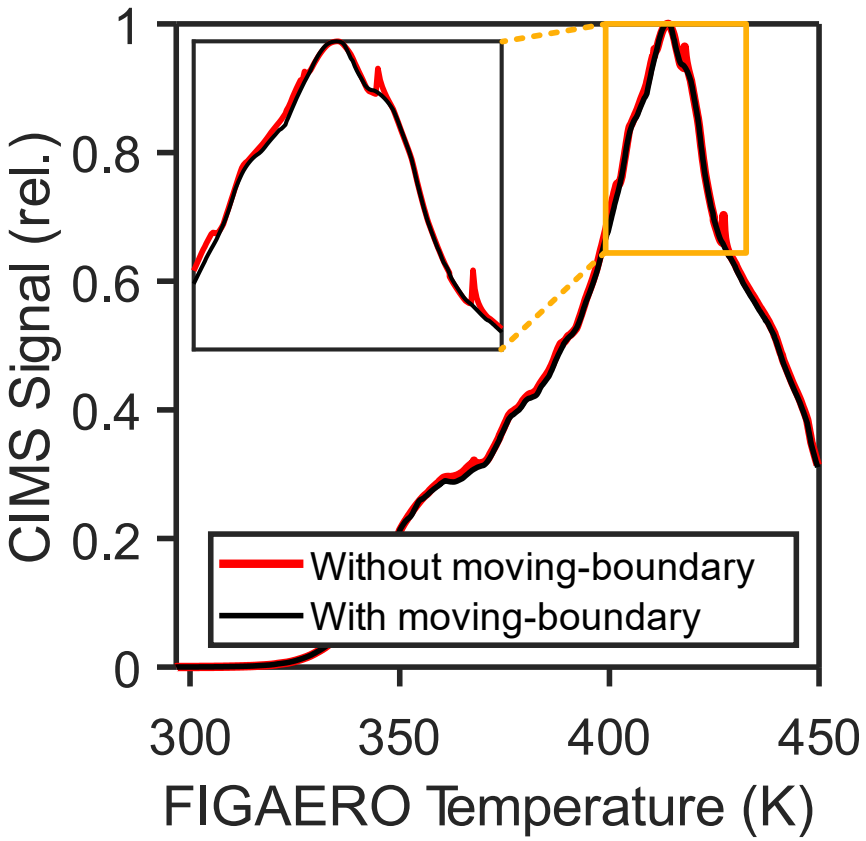


Figure S1: Smoothing of model outputs with the moving-boundary algorithm on an example FIGAERO thermogram. The black and red lines show the model results with and without the moving-boundary algorithm, and the "spikes" that appear in the red line are caused by numerical diffusion as layers merge.

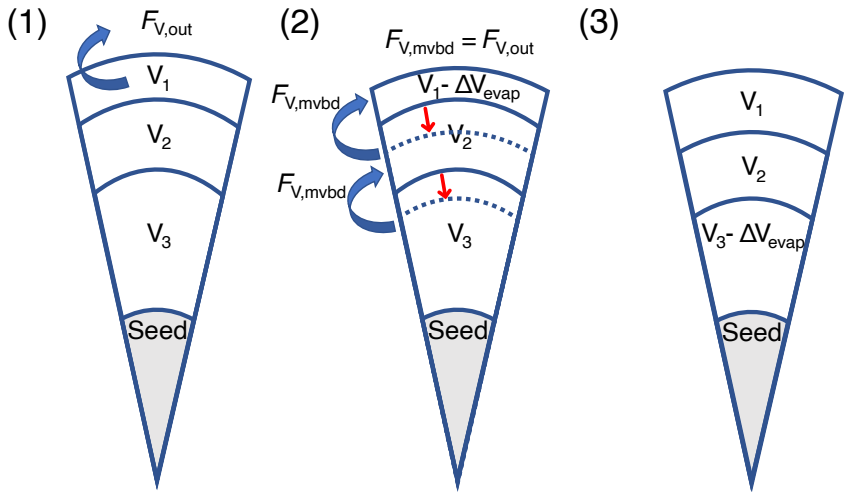


Figure S2: Illustration of the moving-boundary algorithm. When there is a positive net volume leaving the near-surface bulk layer (ΔV_{evap}), diffusion from the lower layers towards the surface is increased to keep the volume of the near-surface bulk layer constant. The red arrows show the resulting shift in the bulk layer boundaries.

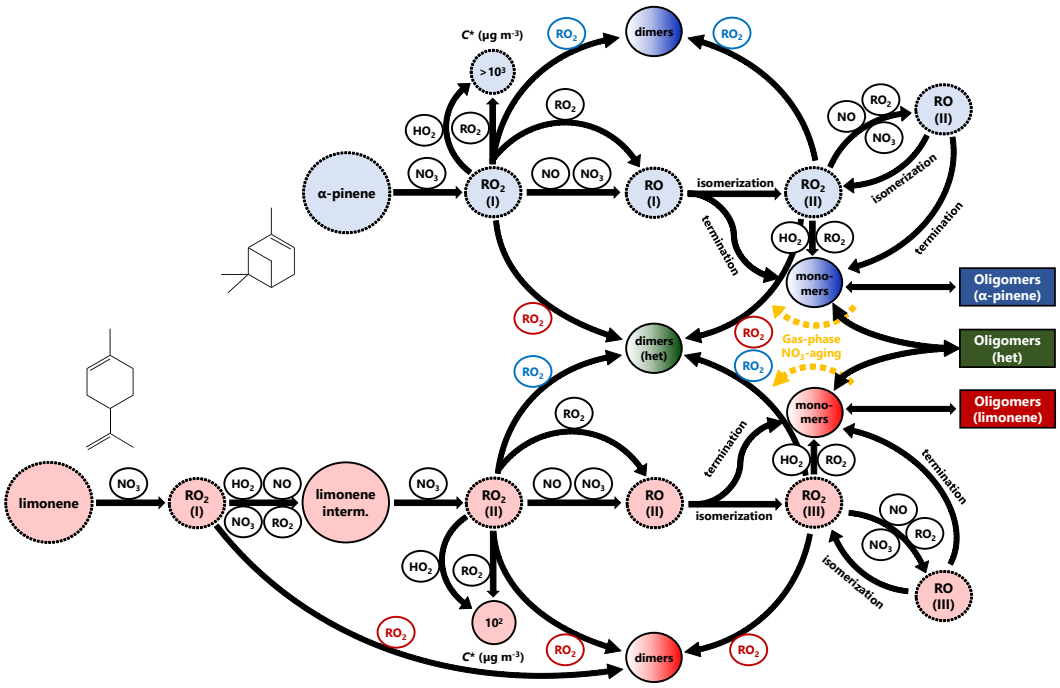


Figure S3: Mechanism schematic. Limonene follows a two-step RO_2 process as the molecule has two double bonds. The mechanism includes reactions where α-pinene and limonene products react to form heterogeneous species.

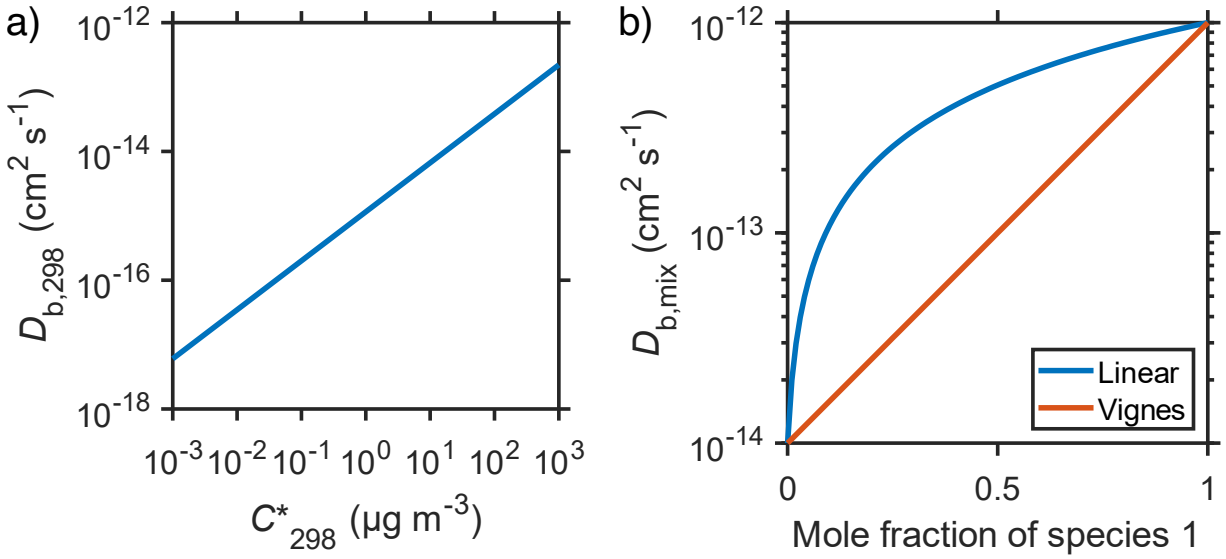


Figure S4: (a) Relationship between C^*_{298} and $D_{b,298}$. (b) Illustration of Vignes and linear mixing rules with an example two species mixture. Species 1 and 2 have self D_b of 1×10^{-12} and 10^{-14} cm^2 s^{-1} respectively.

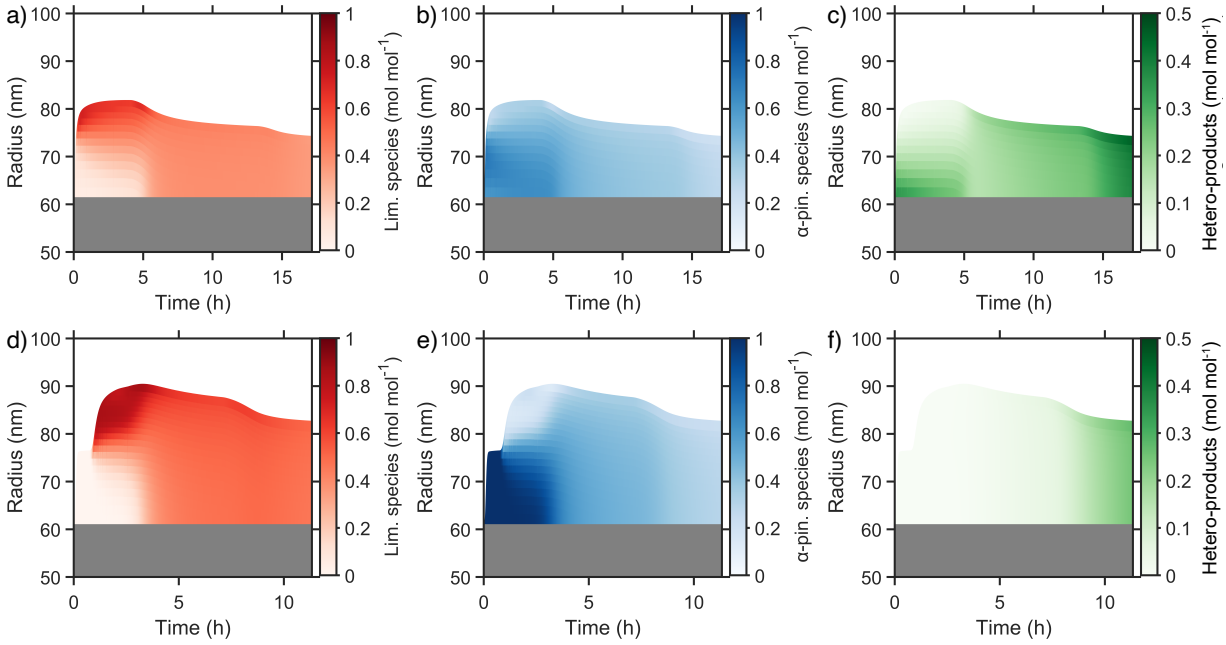


Figure S5: Limonene, α-pinene, and heterogeneous species molar fractions in each layer for (a,b,c) MIX and (d,e,f) SEQ.

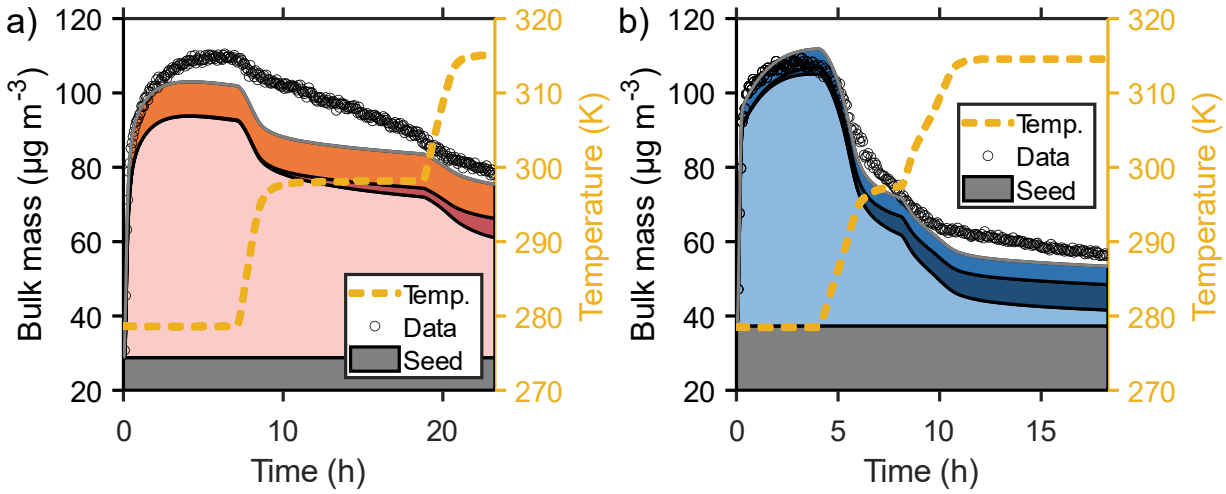


Figure S6: (a) LIM and (b) APN results from a monolayer bulk model while using fit parameters from the multilayer bulk model.

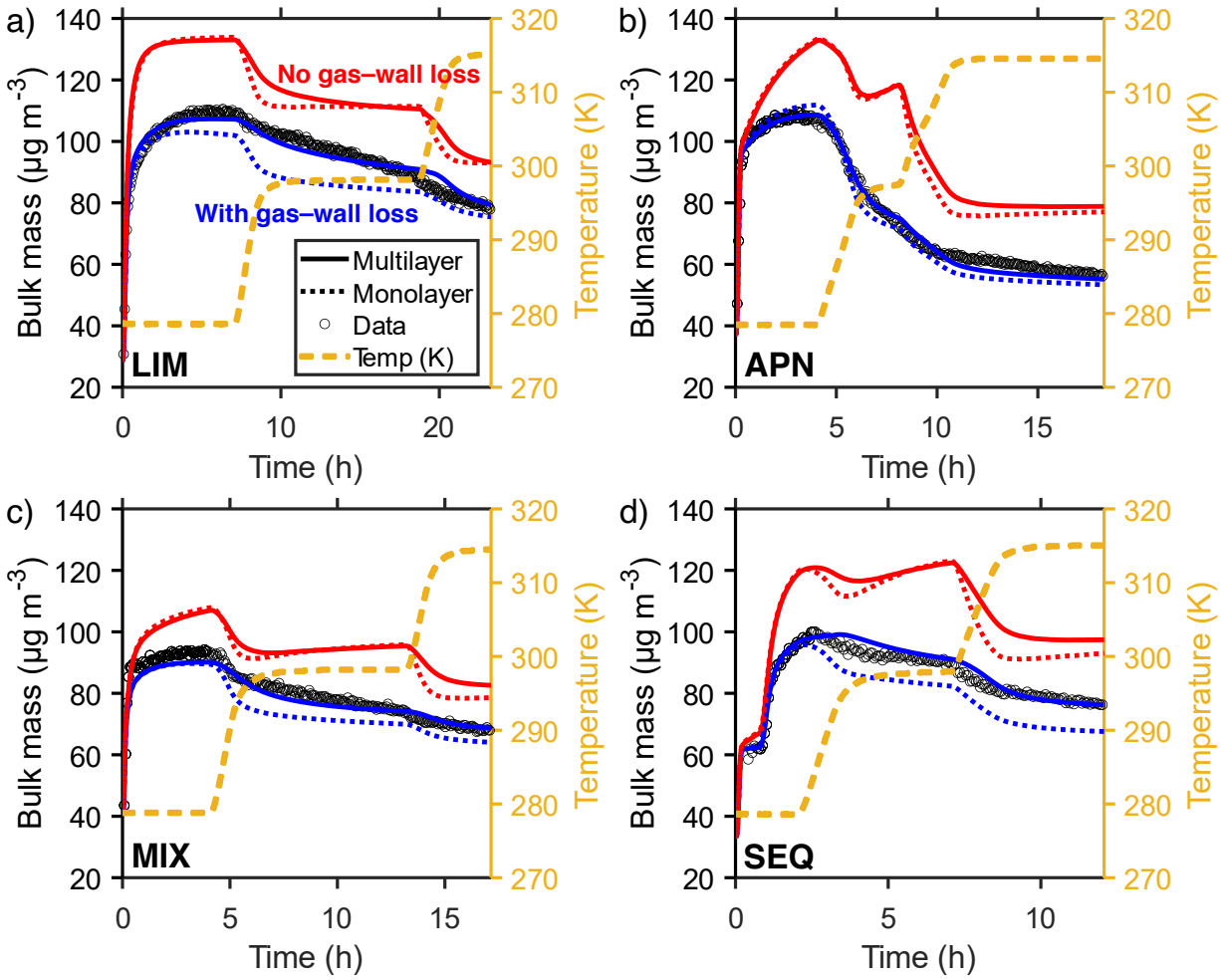


Figure S7: Multilayer (solid line) and monolayer (dotted line) model results for (a) LIM, (b) APN, (c) MIX, and (d) SEQ. Blue and red lines are results with and without gas-wall loss. The increase in SOA formation in APN and SEQ with the monolayer model come from the NO_3-aging of semi-volatiles evaporating with the increase in chamber temperature.

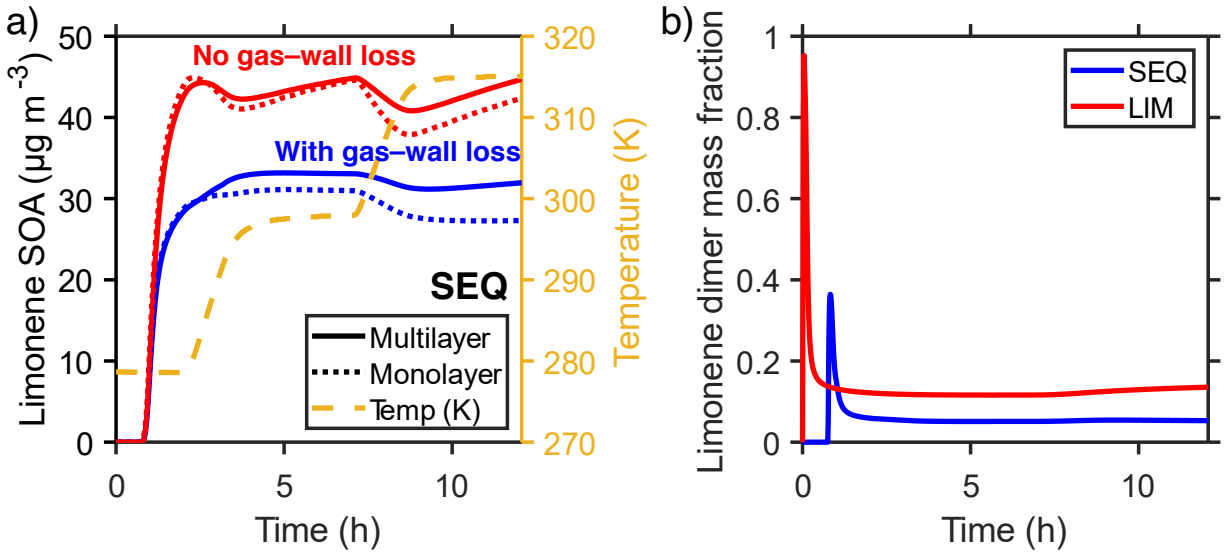


Figure S8: (a) Multilayer (solid line) and monolayer (dotted line) model results of limonene SOA in SEQ, and (b) limonene dimer fraction of limonene SOA by mass in SEQ (blue) and LIM (red). Here, the model limonene SOA and dimer masses include the limonene portion of heterogeneous species.

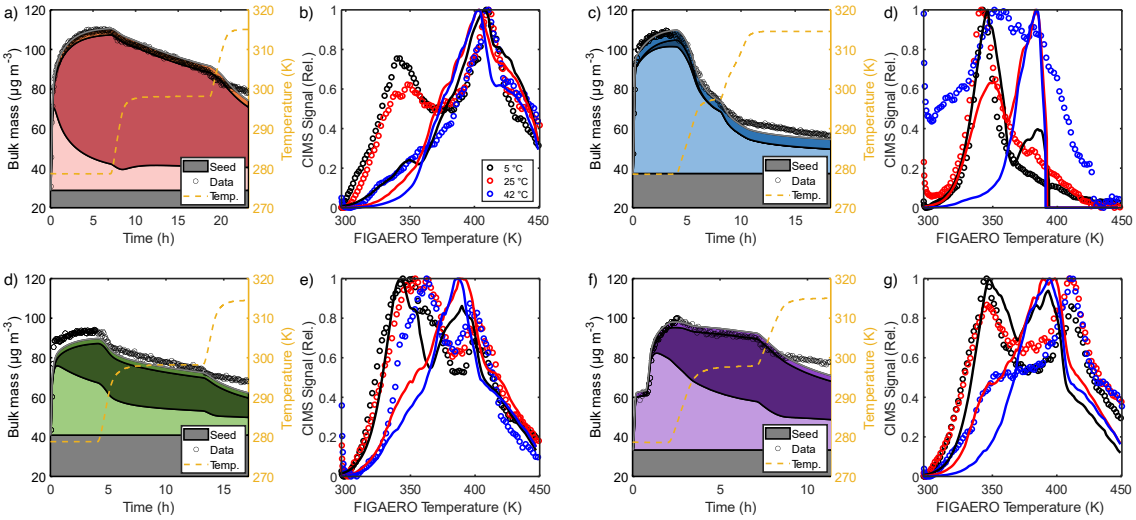


Figure S9: Optimized monolayer bulk model results of the chamber and FIGAERO scenarios for (a,b) LIM, (c,d) APN, (d,e) MIX, and (f,g) SEQ. While the model fits well with the SOA formation and evaporation in the chamber, the first peak that appears around 340 K in the LIM thermograms are not captured by the model. The first peak in the MIX and SEQ are attributed to the α-pinene species.

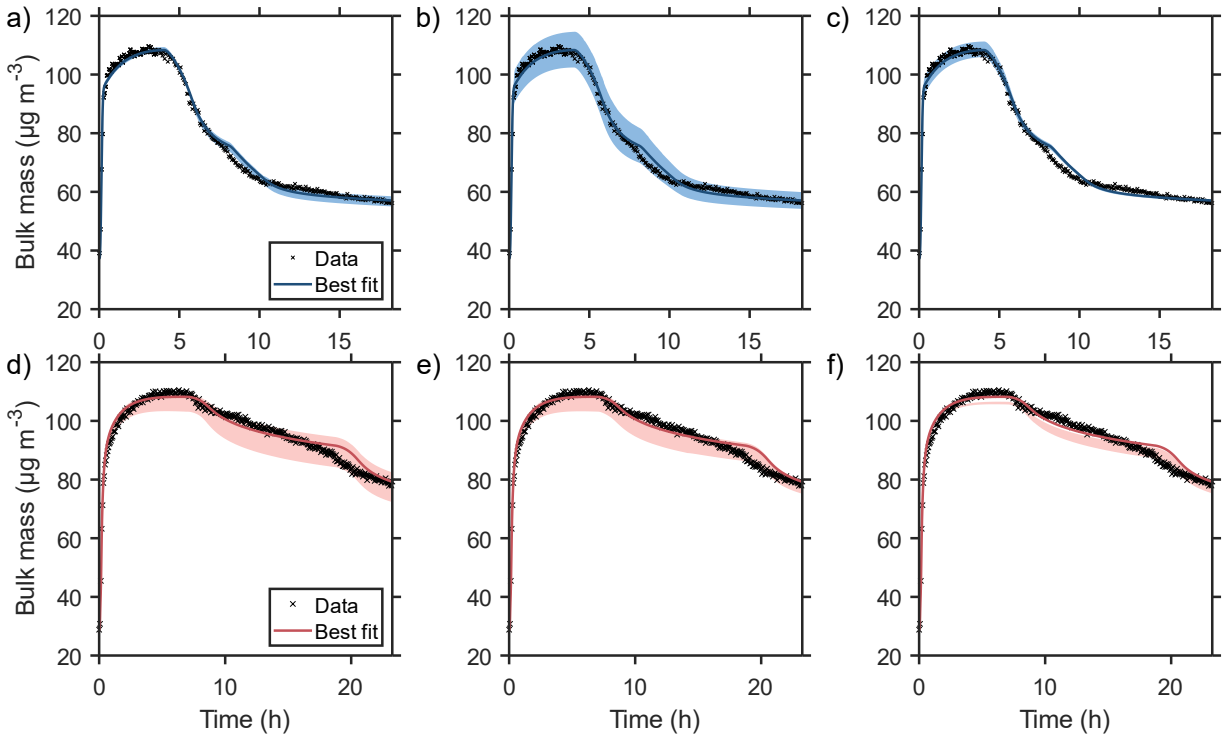


Figure S10: Model sensitivity to the monomer VBS distribution for the APN (a, b, c) and LIM chamber experiments (d, e, f). Each column shows a ±25 % adjustment to the volatility distribution $C^*_{298} < 10^{-1}$ (a, d), $10^{-1} \leq C^*_{298} \leq 10^{1}$ (b, e), and $C^*_{298} > 10^{1}$ µg m^{-3} (c, f). The dark line shows the best fit result, and the shaded area shows the range of model outcomes when the parameters are adjusted within ±25 %.

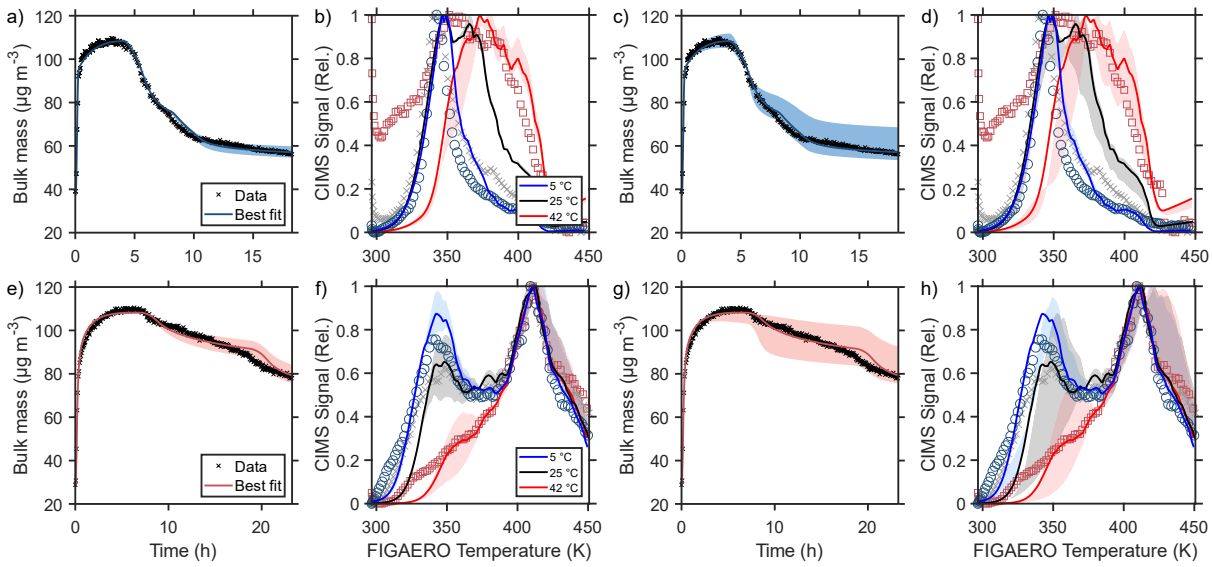


Figure S11: Chamber bulk mass and FIGAERO-CIMS thermogram model sensitivity to (a,b,e,f) the slope (m) and (c,d,g,h) intercept (b) in Eq. 4 for (a,b,c,d) APN and (e,f,g,h) LIM. The dark line shows the best fit result, and the shaded area shows the range of model outcomes when the parameter is adjusted within ±25 %.

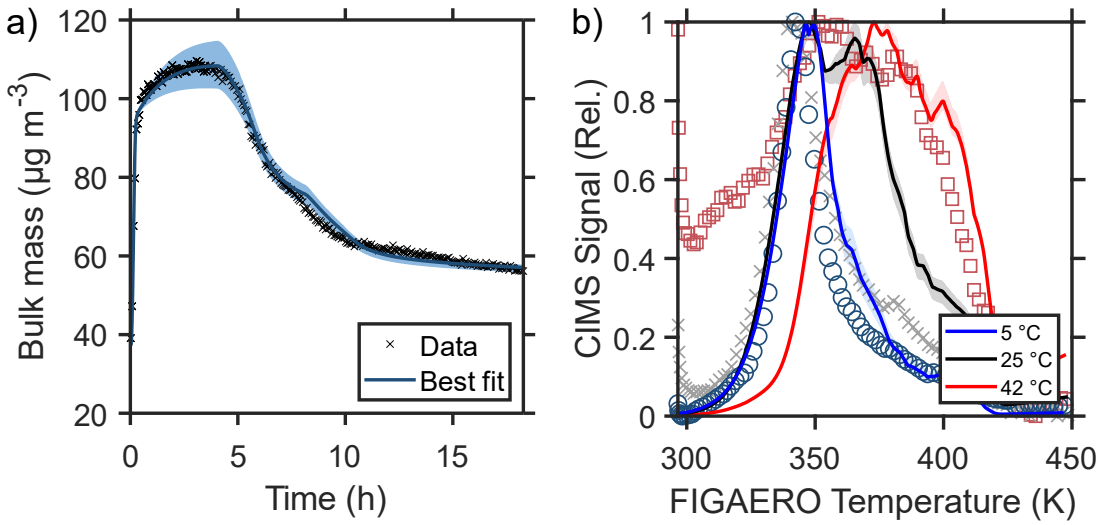


Figure S12: Model sensitivity to the NO_3-aging rate coefficient (k_{aging}) in the APN experiment. The model suggests that a higher kaging results in higher initial SOA growth. The dark line shows the best fit result, and the shaded area shows the range of model outcomes when the parameter is adjusted within ±25 %.

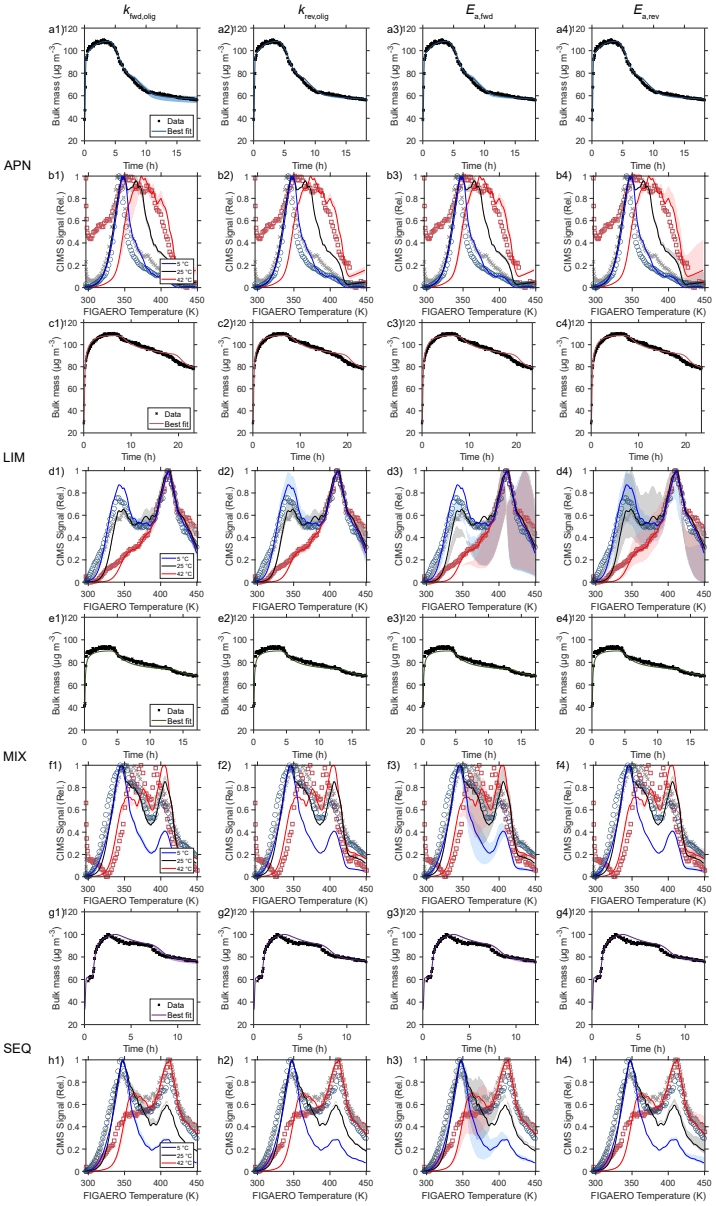


Figure S13: Model sensitivity to (1) $k_{\mathrm{fwd,olig}}$, (2) $k_{\mathrm{rev,olig}}$, (3) $E_{\mathrm{a,fwd}}$, and (4) $E_{\mathrm{a,rev}}$ in the APN (a, b), LIM (c, d), MIX (e,f), and SEQ (g, h) experiments. While the simulated SOA masses in the chamber are not very sensitive due to the slow $k_{\mathrm{fwd,olig}}$ resulting from the optimization, the FIGAERO-CIMS thermogram results are sensitive to the energies of activation of the forward and reverse oligomerization reactions.

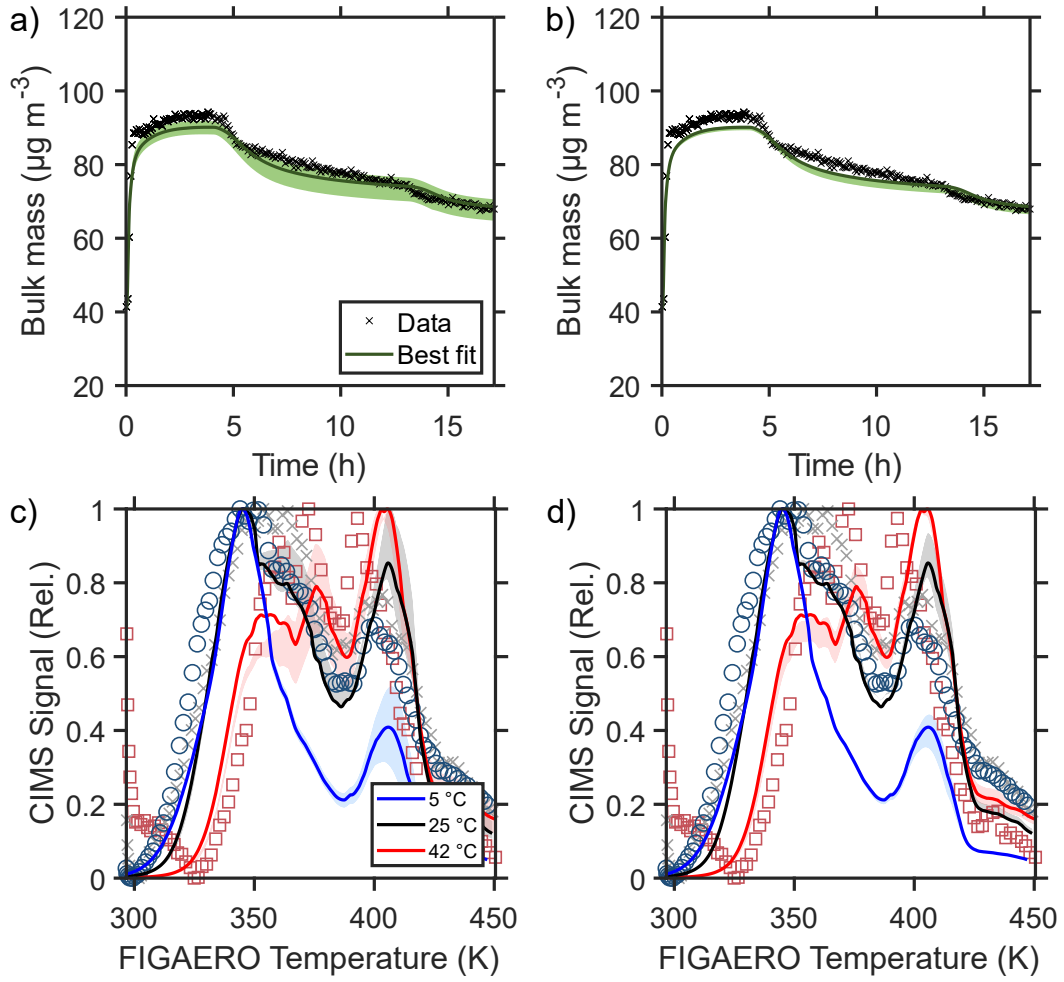


Figure S14: Model sensitivity to the branching ratio ($b_{\mathrm{dimer,het}}$; a, c) and reaction rate coefficient (b, d) of the $RO_{2,apn} + RO_{2,lim} \rightarrow ROOR_{het}$ reaction in the MIX experiment. Higher $b_{\mathrm{dimer,het}}$ leads to higher initial SOA growth due to rapid heterodimer formation.

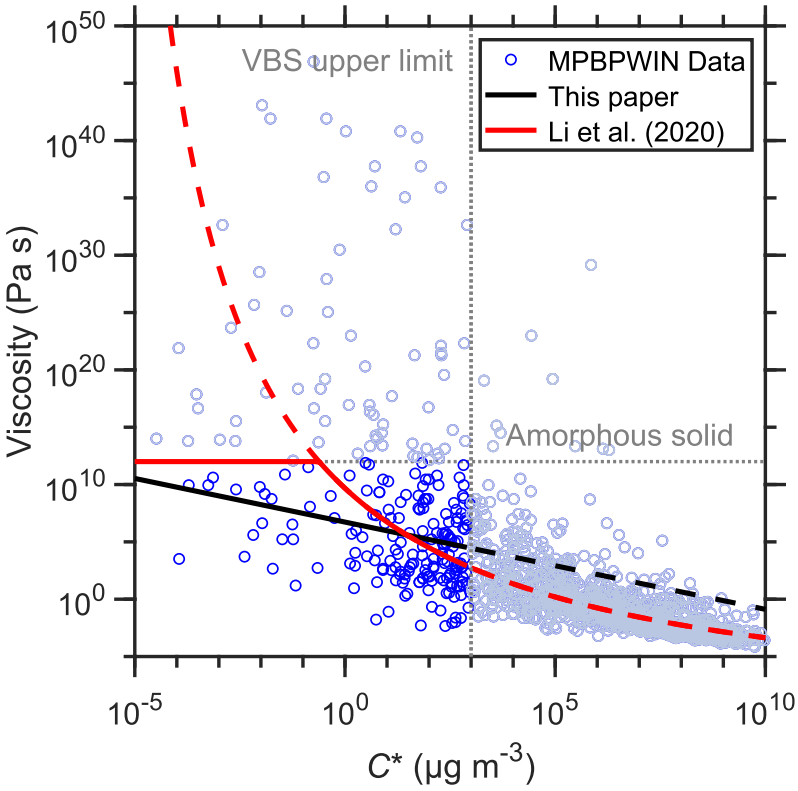


Figure S15: Comparison of D_b–C^* relationship in KM3C when translated to viscosity values (solid black line) with MPBPWIN model data (markers) and the viscosity–C^* relationship (solid red line) proposed by Li et al.[13]. Li et al.[13] also propose an SOA viscosity upper limit corresponding to viscosities of amorphous solids. The dotted black and red lines show the translated D_b–C^* relationship and the viscosity–C^* relationship beyond the VBS range in this study and viscosity limits. Within the VBS and viscosity limits in this study, the viscosities from the D_b–C^* relationship is within the range of values predicted by MPBPWIN.

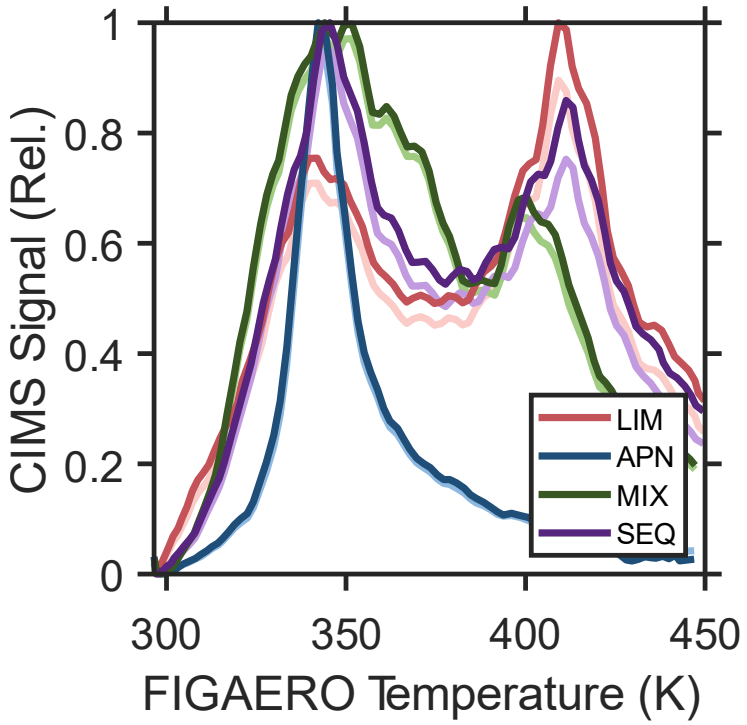


Figure S16: SOA thermograms measured with the FIGAERO-CIMS for each experiment, where dark and light lines represent all ions and the CHON ions, respectively. Across experiments, a large fraction ($>$ 80 %) of detected ions contain nitrogen, suggesting that most are organonitrates.

References

(1) Couvidat, F.; Sartelet, K. The Secondary Organic Aerosol Processor (SOAP v1.0) model: a unified model with different ranges of complexity based on the molecular surrogate approach. *Geosci. Model Dev.* **2015**, *8*, 1111–1138.

(2) Berkemeier, T.; Takeuchi, M.; Eris, G.; Ng, N. L. Kinetic modeling of formation and evaporation of secondary organic aerosol from NO_3 oxidation of pure and mixed monoterpenes. *Atmos. Chem. Phys.* **2020**, *20*, 15513–15535.

(3) Julin, J.; Winkler, P. M.; Donahue, N. M.; Wagner, P. E.; Riipinen, I. Near-Unity Mass Accommodation Coefficient of Organic Molecules of Varying Structure. *Environ. Sci. Technol.* **2014**, *48*, 12083–12089.

(4) Liu, X.; Day, D. A.; Krechmer, J. E.; Brown, W.; Peng, Z.; Ziemann, P. J.; Jimenez, J. L. Direct measurements of semi-volatile organic compound dynamics show near-unity mass accommodation coefficients for diverse aerosols. *Commun. Chem.* **2019**, *2*, 98.

(5) Schobesberger, S.; D'Ambro, E. L.; Lopez-Hilfiker, F. D.; Mohr, C.; Thornton, J. A. A model framework to retrieve thermodynamic and kinetic properties of organic aerosol from composition-resolved thermal desorption measurements. *Atmos. Chem. Phys.* **2018**, *18*, 14757–14785.

(6) Pankow, J. F.; Asher, W. E. SIMPOL.1: a simple group contribution method for predicting vapor pressures and enthalpies of vaporization of multifunctional organic compounds. *Atmos. Chem. Phys.* **2008**, *8*, 2773–2796.

(7) Hallquist, M.; Wängberg, I.; Ljungström, E.; Barnes, I.; Becker, K.-H. Aerosol and Product Yields from NO_3 Radical-Initiated Oxidation of Selected Monoterpenes. *Environ. Sci. Technol.* **1999**, *33*, 553–559.

(8) Spittler, M.; Barnes, I.; Bejan, I.; Brockmann, K.; Benter, T.; Wirtz, K. Reactions of NO_3 radicals with limonene and α-pinene: Product and SOA formation. *Atmos. Environ.* **2006**, *40*, 116–127.

(9) Fry, J. L.; Kiendler-Scharr, A.; Rollins, A. W.; Brauers, T.; Brown, S. S.; Dorn, H.-P.; Dubé, W. P.; Fuchs, H.; Mensah, A.; Rohrer, F.; Tillmann, R.; Wahner, A.; Wooldridge, P. J.; Cohen, R. C. SOA from limonene: role of NO_3 in its generation and degradation. *Atmos. Chem. Phys.* **2011**, *11*, 3879–3894.

(10) Mayorga, R.; Xia, Y.; Zhao, Z.; Long, B.; Zhang, H. Peroxy Radical Autoxidation and Sequential Oxidation in Organic Nitrate Formation during Limonene Nighttime Oxidation. *Environ. Sci. Technol.* **2022**, *56*, 15337–15346.

(11) Berkemeier, T.; Ammann, M.; Krieger, U. K.; Peter, T.; Spichtinger, P.; Pöschl, U.; Shiraiwa, M.; Huisman, A. J. Technical note: Monte Carlo genetic algorithm (MCGA) for model analysis of multiphase chemical kinetics to determine transport and reaction rate coefficients using multiple experimental data sets. *Atmos. Chem. Phys.* **2017**, *17*, 8021–8029.

(12) Press, W. H., Ed. *Numerical recipes in C: the art of scientific computing*, 2nd ed.; Cambridge University Press: Cambridge ; New York, 1992.

(13) Li, Y.; Day, D. A.; Stark, H.; Jimenez, J. L.; Shiraiwa, M. Predictions of the glass transition temperature and viscosity of organic aerosols from volatility distributions. *Atmos. Chem. Phys.* **2020**, *20*, 8103–8122.

B.3 Supplement of "Surface crust formation controls evaporation kinetics of secondary organic aerosols"

Supporting Information for

Surface crust formation controls evaporation kinetics of secondary organic aerosols

Meredith Schervish[1,†], Hyun Gu Kang[2], Lisa M. Wingen[1], Kieudiem Nguyen[1], Cheyenne Begay[1], Jacqueline Wilson[3,§], Manish Shrivastava[3], Yuzhi Chen[3], John E. Shilling[3], Nga L. Ng[4], Ulrich Pöschl[2], Thomas Berkemeier[2,], Alla Zelenyuk[3,], Manabu Shiraiwa[1,*]*

Contents:
Pages S1-S29
Additional description of methods
Isoprene SOA evaporation and condensation
Figs. S1-S17
Tables S1-S4
References

Additional description of methods

Calculation of diffusivity based on T_g. In this work, we base the calculated the viscosity of the mixture on optimized individual species' glass transition temperatures (T_g). This approach has been validated and widely utilized for calculating viscosities and diffusivities of complex SOA mixtures [1–3]. T_g represents an intrinsic property of the species and therefore is the appropriate optimization parameter. The glass transition temperature, $T_{g,m}$, of the mixture of components in layer m is given by the mass fraction weighted average of the individual component glass transition temperatures

$$T_{g,m} = \sum_i f_{i,m} T_{g,i} \quad (1)$$

Where $f_{i,m}$ is the mass fraction of species i in layer m and $T_{g,i}$ is the glass transition temperature of species i. The viscosity of each layer (η_m) can then be computed from the average glass transition temperature of that layer using the modified Vogel-Fulcher-Tammann (VFT) equation.

$$T_{0,m} = \frac{39.17 \cdot T_{g,m}}{D + 39.17} \quad (2)$$

$$\log(\eta_m) = -5 + 0.434 \cdot \frac{T_{0,m} D}{T - T_{0,m}} \quad (3)$$

Here $T_{0,m}$ is the Vogel temperature, D is the fragility, here assumed to equal 10 [4], and T is the temperature.

The model parameter controlling mass transport is the bulk diffusivity in each layer ($D_{b,m}$) and so we compute the diffusivity in each layer from the viscosity in each layer using the Stokes Einstein equation.

$$D_{b,m} = \frac{kT}{6\pi a \eta_m} \quad (4)$$

Here k is the Boltzmann constant and $\boldsymbol{\alpha}$ is the radius of the diffusing species, here assumed to be 1nm. The Stokes-Einstein equation is known to break down in ultra-viscous solutions, predicting too low diffusivities. In this work, while some pure-component diffusivities would be calculated to be this viscous, the mixture viscosity leads to a minimum diffusivity of 10^{-18} cm^2 s^{-1}, which is still physically relevant. The Stokes-Einstein equation also show deficiencies when the diffusing molecules are much smaller than the molecules

making up the solution matrix. In this work, the size difference between the smallest and largest species in a system is no more than a factor of 3 and thus, we expect the Stokes-Einstein relationship to hold.

This method implicitly assumes that the pure-component bulk-phase diffusivity of species *i* represents the diffusivity of every species in the mixture. As all the individual species have similar sizes, this simplifying assumption is likely reasonable, however in systems with molecules that vary by over an order of magnitude in size, the diffusivity would likely need to be computed for each individual species. A strength of this approach over other multicomponent parameterizations (discussed in the following section), is that treatment of species with different diffusivities within a matrix of a given viscosity can be readily implemented by simply using a different radius for the diffusing species in the Stokes-Einstein equation. Additionally, it is assumed that the organics form a non-interacting ideal mixture.

Other multicomponent diffusivity parameterizations. Previous work employing a composition-dependent diffusivity methodology has employed a mole fraction-based geometric mean diffusivity approach based on Vignes et al [5–8]. This assumption will impact the specific parameters as the mass fraction T_g approach increases the importance of high molecular weight, highly viscous species in the viscosity calculation, thus not requiring their actual mass and/or viscosity to be as high to form a surface crust as in the mole fraction-based approach. A surface crust can be achieved using either approach and the overall results are consistent across both approaches as shown in Fig. S5 for the PEG 400 evaporation case.

Evaporation rates of HEG and PEG particles. Figure S1 shows measured and modeled volume fraction remaining (VFR) for the evaporation of size-selected PEG 1000, PEG 400, PEG 300, and PEG 200 for different particle sizes. While simulations of most PEG systems lead to good agreement, the modeled PEG 200 evaporation plateaus early at a higher VFR than the observations. This is due to the relatively large amount of low to non-volatile species needed to reproduce the initial slow evaporation as the highest volatility species in PEG 200 will evaporate nearly instantaneously. While the model does not perfectly

align with the observed evaporation behavior, it effectively captures the remarkable differences between the evaporation of HEG and PEG mixtures.

Figure S2a-f show the time evolution of the diameter over the initial diameter ($d_p/d_{p,0}$) and the absolute diameter (d_p) of HEG, PEG 300, and PEG 400 particles from measurements (points) and model simulations (lines). The KM-GAP model reproduces the change in diameter over time well for all systems. The change in particle diameter with time (dd_p/dt) versus time (t) is shown in Fig. S2g-i. The change in particle volume with time (dV_p/dt) is shown in Fig. S2j-k. For a spherical particle dV_p/dt will be dependent on the net flux at the surface (J_{net}) as

$$\frac{dV_p}{dt} = -J_{\mathrm{net}} \cdot S_{\mathrm{p}} \cdot v_{molec} \tag{5}$$

where S_p is the surface area of the particle at a given time and v_{molec} is the volume of a single molecule. J_{net} is the difference of adsorption flux and desorption flux ($J_{net} = J_{ads} - J_{des}$). From this the change in particle diameter over time can be calculated as follows given that the surface area of a sphere is $SA = \pi {d_p}^2$.

$$\frac{\pi}{6}\frac{d{d_p}^3}{dt} = -J_{\mathrm{net}} \cdot \pi {d_p}^2 \cdot v_{molec} \tag{6}$$

$$\frac{\pi}{6} \cdot (3{d_p}^2) \cdot \frac{dd_p}{dt} = -J_{\mathrm{net}} \cdot \pi {d_p}^2 \cdot v_{molec} \tag{7}$$

$$\frac{dd_p}{dt} = -2\,J_{\mathrm{net}} \cdot v_{molec} \tag{8}$$

The single-component HEG particles show a time- and size-dependent rate of diameter change (Fig S2d) due to recondensation of evaporated gases, which are removed rapidly, but not instantaneously, leading to a time-dependent net flux (Fig S3a). This time-dependence of the re-condensation flux, J_{ads}, is driven by the decrease of gas-phase concentration over time (Fig. S3d). As further evidence, Fig. S4 shows dd_p/dt versus t when the gas-phase concentration and near-surface gas-phase concentration are assumed to be constant, specifically $Z_g = Z_{gs} = 0$ cm^{-3}, simulating instantaneous vapor loss. In this case, the rate of diameter change for the single component HEG system is time- and size-independent as the net flux in Eq (8) is constant in time.

Smaller particles have faster net flux loss rates and thus larger diameter loss rates. Larger particles lose more absolute mass due to their higher surface areas, leading to a larger gas-phase concentration as shown in Fig. S3d. The gas phase concentration for each particle size decreases over time due to rapid wall loss reducing recondensation and thus increasing the rate of diameter loss over time in Fig S3d. Initially the multi-component PEG mixtures show the same behavior of smaller particles having higher diameter loss rates, but as the composition of the smaller particles changes more rapidly due to rapid loss of volatile species, the rate of diameter loss slows down and approaches 0 nm min^{-1} earlier than the larger particles. Once all the particles have lost the semi-volatile species initially present, their evaporation rates converge and continue to approach 0 nm min^{-1} at long timescales. The volume loss rate relative to the initial volume or change in volume fraction remaining (VFR) over time ($-dVFR/dt$) is shown in Fig S3m-o. For HEG particles, $dVFR/dt$ is clearly size-dependent. For PEG 300 and PEG 400 particles, small particles initially lose their relative volume faster as in the single-component HEG particles, but within 2 mins of evaporation, the relative volume loss rate becomes size independent.

The change in particle volume with time (dV_p/dt) versus particle diameter (d_p) for HEG, PEG 300, and PEG 400 particles is shown in Fig S7. For the single-component HEG particles, larger particles lose volume faster due to their larger surface areas (Fig S7a). Critically because these particles are made up of one species, their evaporation behavior is independent of the initial particle size, so when the initially 508 nm particles evaporate to 438 nm, their volume loss rate is identical to that of the initially 438 nm particles because their composition is identical to that of the initially 438 nm particles. Larger multi-component PEG 300 and PEG 400 particles also lose volume faster due to their larger surface areas, however as the particles shrink and lose the most volatile species, the rate of volume loss slows significantly (Fig S7b,c). Due to this composition change, the volume loss rate at a specific particle size becomes dependent on the initial particle size.

α-pinene SOA Oligomer decomposition. α-pinene SOA oligomer decomposition is implemented through reaction of one low volatility species in the α-pinene SOA fit (species 4) to form two semi-volatile species

(species 1 and 2). As both species 1 and 2 are highly saturated in the particle phase at the low SOA mass concentrations in this work, both evaporate rapidly once at the surface and there is little change in the result when two molecules of species 1 or two molecules of species 2 are formed from decomposition of one molecules of species 4. The representation of oligomer decomposition is meant to depict the average behavior as we only represent one oligomer species that is able to decompose. It should also be noted that species 4 is the only low volatility species and should evaporate to some extent without decomposing on the timescale of this experiment and thus its high initial mass fraction may be due to this species serving these dual purposes in the evaporative process.

Monte Carlo Genetic Algorithm optimization. Experimental data was fit by varying specific model parameters in KM-GAP using the Monte Carlo Genetic Algorithm (MCGA) [9]. In each evaporation simulation, 5 species were present. The parameters chosen to vary in each data set were the pure-component glass transition temperatures of each of the 5 species, the initial particle-phase mass fraction of each species, and the volatility of 4 of the species, the fifth of which was assumed to be non-volatile. In the simulations of α-pinene SOA evaporation, the oligomer decomposition rate constant was also fit. In all simulations, the wall loss rate constant was fit, but as they were all fit within the range of 0.2-0.4 s^{-1} and as this should be consistent across all experiments, a constant value of 0.3 s^{-1} is used. These parameters were randomly varied within user defined ranges and the fitness of each parameter set was evaluated using a least-square regression. Previous work has suggested that oligomers in SOA decompose with rate constants in the range of 10^{-5}-1 s^{-1} [10–12]. As this is a wide range for parameter sampling and this is meant to represent an average decomposition rate constant, we fit the decomposition rate constant in the range of 10^{-4}-10^{-2} s^{-1}. For the PEG 300 and PEG 400 evaporation fits, volatilities were fit within a range of a factor of 5 of measured volatilities of individual PEG species present in PEG 400 [13,14]. One higher volatility, lower viscosity species was included in the PEG 300 fit and one lower volatility, higher viscosity species was included in the PEG 400 fit, consistent with a higher volatility of short chain-length, lower molecular weight of PEG polymer molecules. The other three species were fit within the same volatility and glass transition temperature

ranges. For the α-pinene SOA evaporation fit, volatility ranges were set an order of magnitude around the semi-volatile range of the VBS (0.1-100 μg m^{-3}) [15]. The best-fit for each set of experiments was chosen after 10000 parameters sets were generated and over 50 optimization rounds were completed. It should be noted that multiple indistinguishable fits with different optimized parameters can be found for both PEG 400 and α-pinene SOA evaporation and without more constraints on any individual parameters it is impossible to determine the "better" solution. The broad conclusions about surface crust formation remain consistent through these different fits, but the individual parameter values are not unique and thus should not be overinterpreted.

Limonene + NO_3 mechanism. We adopt a mechanism from Berkemeier et al. (2020), where modifications are made to allow for the decrease in the volatility of gaseous monomers through NO_3-oxidation (Fig. S11) [16]. In the model, low-volatile vapors condense onto ammonium sulfate seed, and bulk-phase monomers react to reversibly form oligomers. The reverse oligomerization rate coefficient takes an Arrhenius form, consistent with that proposed in previous studies [16,17]. We assume that oligomers formed in the bulk-phase do not partition into the gas phase, which is consistent with the oligomers thermally decomposing before evaporation. Monomer species are distributed across logarithmically-spaced volatility bins with C^* ranging from 10^{-4} to 10^{3} μg m^{-3} and a gas-only bin. With the MCGA, we optimize the branching ratios to the VBS bins, dimers, and RO_2 and RO pathways. We also fit the oligomerization kinetic parameters, and the fit parameters are summarized in Table S2. The dimers from RO_2 + RO_2 branch across three logarithmically spaced volatility bins. The C^* of the intermediate oxidative product (IOP), which is a species representing monomers retaining a double bond, is fit.

Layer resizing and diffusivity. The model uses an adaptive layer resizing algorithm that merges adjacent layers when one becomes too thin, while splitting a layer should it become too thick. This modification prevents bulk layers near the surface from becoming too thin and inducing stiffness while allowing for

diffusivity gradients to form dynamically. To calculate the diffusion between two model bulk layers, we use the combined mass composition of the adjacent layers.

T_g versus C* relationship. To calculate the diffusivity of each layer for the limonene SOA simulations, we use the relationship proposed by Li et al. [18]:

$$T_g = 288.70 - 15.33 \times log_{10}(C^*) - 0.33 \times log_{10}(C^*) \quad (9)$$

The layer T_g and diffusivity is then calculated using the mass fraction weighted composition for each layer. However, we note that decreasing the intercept in the equation (230 K) would also result in a suitable fit to the data (Fig. S13a,c), but a crust may not form (Fig. S13b,d). This method was not used for the α-pinene SOA simulations as the best fit solution gave results within the spread of data for the T_g parameterization based on the fit volatility. Additionally, this method was not used for the PEG 400 simulations as this parameterization was not derived using large polymer species and thus its efficacy cannot be validated.

In Fig. 3c, which shows the model output when a uniform D_b across layers is applied, we assume that D_b increases with increasing temperatures following the Arrhenius equation. We use an enthalpy of diffusion of ΔH_{dif} = 80 kJ mol^{-1}.

$$D_b = D_{b,298} \times exp\left(\frac{\Delta H_{dif}}{R} \times \left(\frac{1}{298} - \frac{1}{T}\right)\right) \quad (10)$$

Matrix assisted ionization in vacuum – mass spectrometry (MAIV-MS). MAIV-MS requires the use of matrix particles, which act as both an ionization agent and a condensation surface [19]. Matrix particles are generated by atomization, which leads to particles acquiring multiple charges through spray electrification [20–22]. Briefly, matrix particles entering an MS with no external ionization source undergo evaporation as they enter the low pressures and gentle heating (~40°C) in the mass spectrometer inlet within a probe depth of ~15 nm. As the particles evaporate in the inlet, matrix molecules and co-adsorbed species are emitted from the surface layers of the particles. This method leads to soft ionization, in which species are detected as ammonium ion adducts, due to ammonia in the lab air, with some protonated adducts[23]. Glutaric acid

has been observed to be an efficient matrix, likely aided by its low melting point which leads to increased surface mobility and diffusion in the surface layers[24].

A triple quadrupole mass spectrometer (Waters, Xevo TQ-S) with the ion source removed was used to carry out MAIV-MS. Matrix particles were generated from the atomization (TSI, model 3076) of a solution of 30 mM glutaric acid (GA) in nanopure water (18.2 MΩ cm) and dried with two silica gel diffusion dryers (TSI, model 3062). The inlet of the MS was operated at a cone voltage 30 V and a source offset 50 V. The source temperature was operated at 70°C, which in practice exposes particles to a somewhat lower temperature of ~40°C for ~0.1 seconds. Mass spectra were collected in positive ion mode using 30 min. multichannel analysis (MCA) mode scans from *m/z* 20 - 700.

Generation and measurements of SOA-coated matrix particles. Ozonolysis of α-pinene occurred in the presence of matrix particles, allowing condensation of oxidation products. The SOA-coated matrix particles then entered the MS inlet either directly or after passing through several carbon denuders to provide evaporation on second timescales.

As shown in Fig. S15a, uncoated GA particles exhibit typical peaks at m/z 87 $[GA+H-H_2O-CO]^+$, 115 $[GA+H-H_2O]^+$, 133 $[GA+H]^+$, 150 $[GA+NH_4]^+$, 265 $[2\ GA+H]^+$, 282 $[2\ GA+NH_4]^+$, 414 $[3\ GA+NH_4]^+$, 546 $[4\ GA+NH_4]^+$ and 678 $[5\ GA+NH_4]^+$. These peaks remain in the SOA-coated GA particle spectra but are omitted from the product distribution analysis.

Particle size distributions were measured using a Scanning Mobility Particle Sizer (SMPS, TSI model 3938, which included a model 3082 electrostatic classifier with long DMA, model 3081A, and a model 3756 ultrafine condensation particle sizer). Particle charge equilibration for these measurements was provided by a Po-210 neutralizer (NRD, model P-2021) added at the SMPS inlet.

Further attempts to lengthen the evaporation time were attempted by the addition of another denuder (Parallel plate carbon filter denuder, Sunset Laboratory Inc.) that added an additional 7 seconds of evaporation time. This resulted in large decreases in the total ion count by a factor of ~10 and similar decreases in the GA matrix peaks (Fig. S16). There are several reasons to explain such a decrease: (1)

Large losses in the particle number concentration after passing through the additional denuder would decrease overall ion signal; (2) coating thicknesses exceeding 15-20 nm tend to inhibit GA signal, as observed in a previous study; and (3) low volatility coatings would also inhibit the surface melting of the GA particles and/or slow the evaporation of the particles, leading to low ion signal [19]. Size distribution measurements showed that passing the particle sample through an additional denuder led to only an additional 10% loss of particles. The ion signal, however, decreased by approximately a factor of 10, as shown in Fig. S16c. Size distributions also showed that the SOA coating thickness on GA was initially ~1 nm and did not change significantly after evaporation (Fig. S14). These data suggest that evaporation leaves behind an increased oligomeric coating of SOA that inhibits GA ionization and leads to the decreased ion signal.

Isoprene SOA evaporation and condensation

Chen et al (2023) observed that after allowing isoprene SOA to evaporate in the dark, subsequent condensation of isoprene SOA was suppressed [25]. In their work, they hypothesize that the isoprene SOA becomes more viscous upon evaporation and achieve good agreement with observations by simulating condensation on a more viscous homogenous particle bulk. Here, we simulate the evaporation and subsequent condensation allowing for a heterogeneous particle bulk. As in the previous evaporation simulations, we use 5 species in isoprene SOA and vary the volatility, glass transition temperature, and initial mass fraction of each to achieve good agreement with observations of evaporation (Table S4). To simulate condensation, 100 ppb of isoprene is introduced after 410 min and the OH concentration is fixed at 2×10^6 cm^{-3} as described in Chen et al [25]. Formation of semi-volatile and low volatility species is assumed to proceed via successive OH oxidation steps with rate coefficient 10^{-10} cm^3 s^{-1} for each step [26].

We achieve good agreement for both the evaporation and condensation between the observed and simulated organic aerosol concentration when a surface crust forms during evaporation and hinders the following condensation process as shown in Fig. S17. If instead, the particle is assumed to be a homogeneous liquid ($D_b = 10^{-8}$ cm^2 s^{-1}) during condensation, the organic aerosol concentration is

overestimated. If the particle bulk is assumed to be a homogeneous semi-solid (D_b = 10^{-17} cm^2 s^{-1}), the organic aerosol concentration is underestimated.

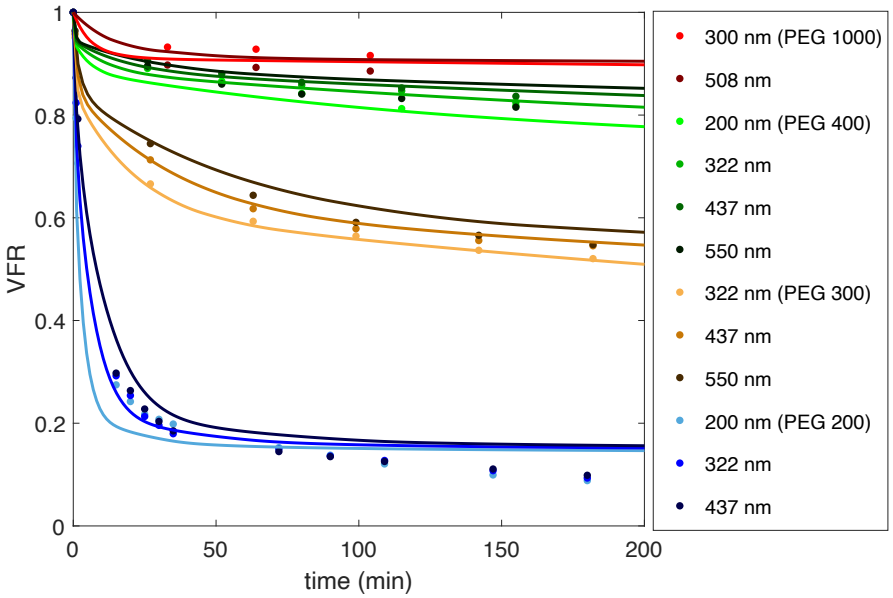


Figure S1. Measured (data points) and modeled (lines) volume fraction remaining (VFR) for the evaporation of size-selected PEG 1000 (red), PEG 400 (green), PEG 300 (orange), and PEG 200 (blue) for different particle sizes.

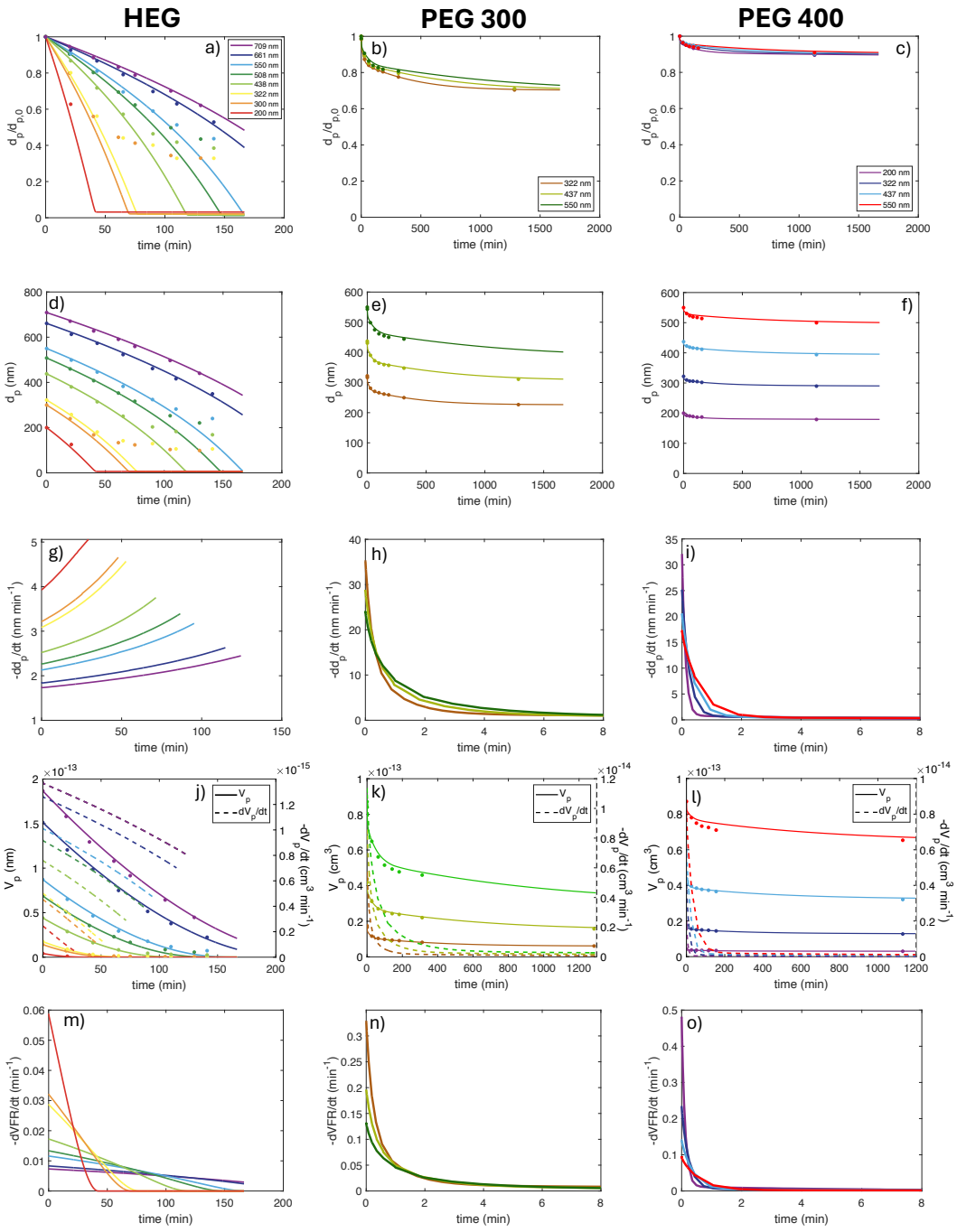


Figure S2. The top row shows diameter over initial diameter plots ($d_p/d_{p,0}$) for a) HEG, b) PEG 300, and c) PEG 400 and the second row show absolute diameter (d_p) for d) HEG, e) PEG 300, and f) PEG 400 for the data (points) and model simulation (lines). The third row shows diameter loss rates ($-dd_p/dt$) for g) HEG, h) PEG 300, and i) PEG 400 over time. The fourth row shows absolute volume (solid lines) and volume loss rate ($-dV_p/dt$, dashed lines) over time for j) HEG, k) PEG 300, and l) PEG 400. The bottom row shows the volume loss rate relative to the initial volume ($dVFR/dt$) for m) HEG, n) PEG 300, and o) PEG 400.

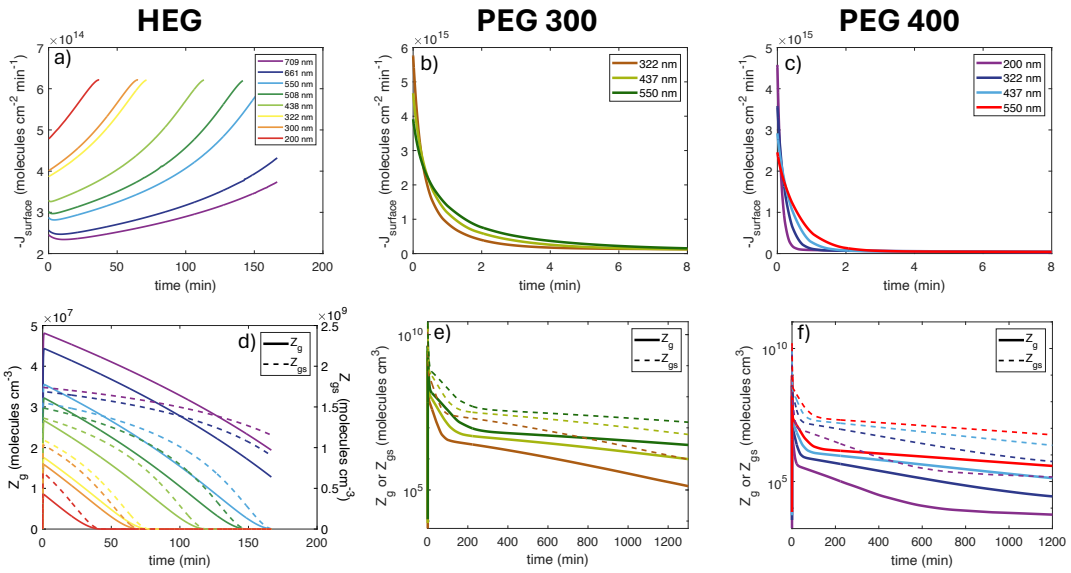


Figure S3. The top row shows the surface flux ($J_{surface}$) during evaporation for a) HEG, b) PEG 300, and c) PEG 400 particles. The bottom row shows gas-phase (Z_g, solid lines) and near-surface gas-phase (Z_{gs}, dashed lines) concentrations over time during evaporation of d) HEG, e) PEG 300, and f) PEG 400 particles of different initial sizes. Gas phase concentrations initially increase as the particles evaporate, but subsequently decrease due to rapid (but not instantaneous) wall loss.

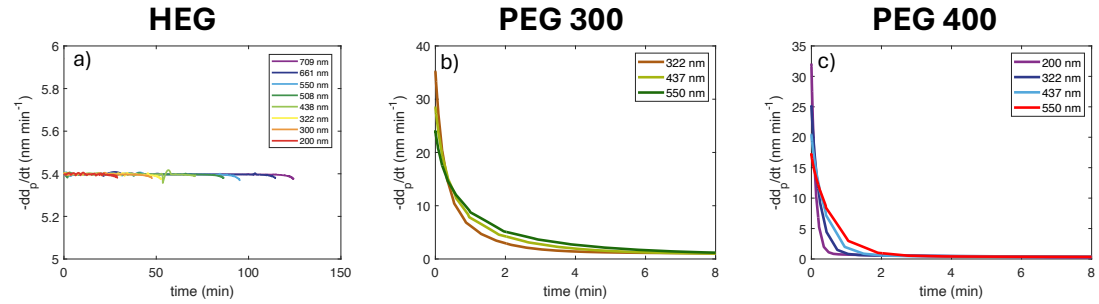


Figure S4. Loss rate of diameter per time (dd_p/dt) versus time for a) HEG, b) PEG 300, and c) PEG 400 when assuming instantaneous vapor removal ($Z_g = Z_{gs} = 0$).

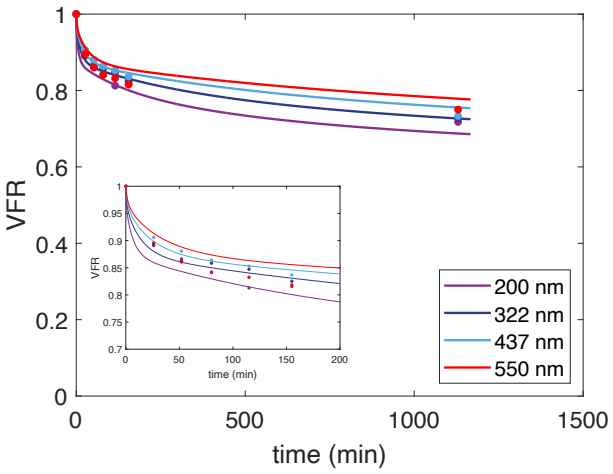


Figure S5. Best fit for PEG 400 volume fraction remaining (VFR) during evaporation using number fraction weighted average diffusivities in each layer as per Vignes et al. Insert shows a zoom in of the first 200 mins of evaporation for comparison for Fig. S1.

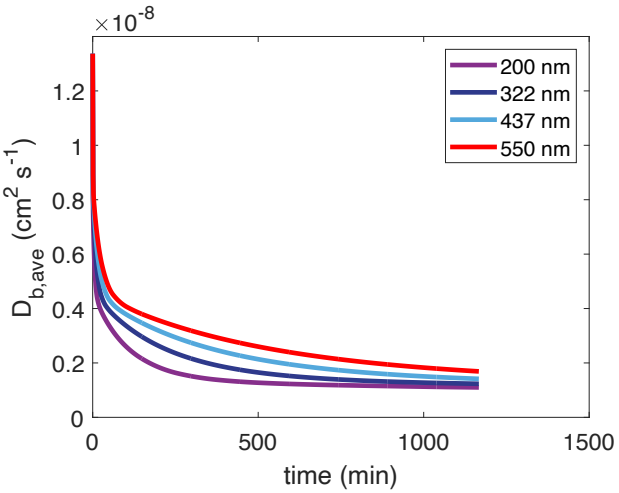


Figure S6. Evolution of the average diffusivity of the PEG 400 particles during evaporation for the best fit case. The average diffusivity is calculated as the volume-weighted averaged diffusivity within the inhomogeneous particle bulk.

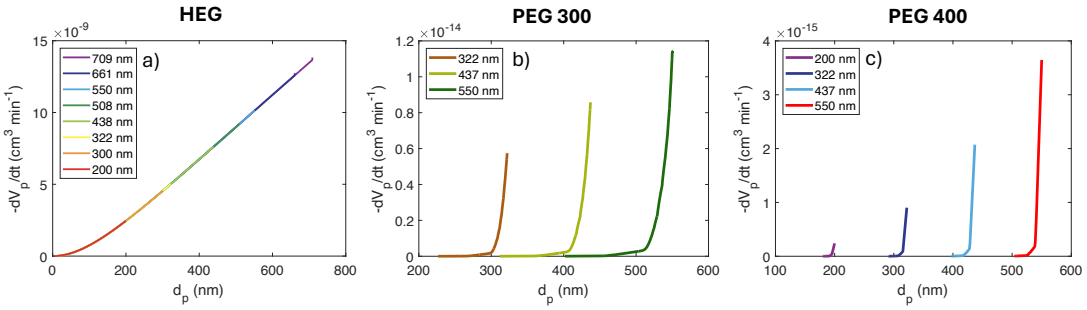


Figure S7. Rate of change of particle volume (-dV_p/dt) with time versus diameter for a) HEG, b) PEG 300, and c) PEG 400.

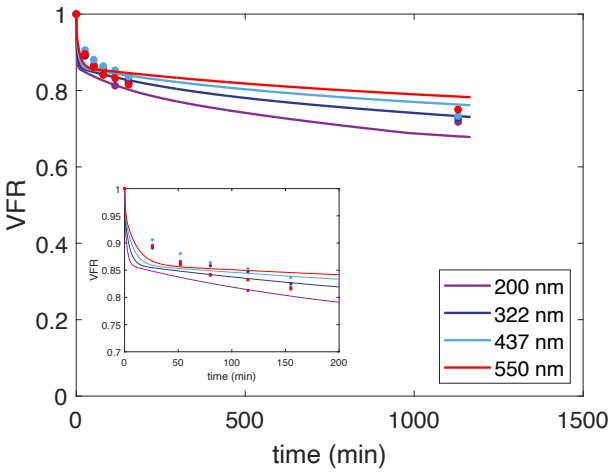


Figure S8. The best fit for the volume fraction remaining (VFR) during PEG 400 particles evaporation assuming a fixed diffusivity throughout the particle bulk. Insert shows a zoom in of the first 200 mins of evaporation for comparison for Fig. S1.

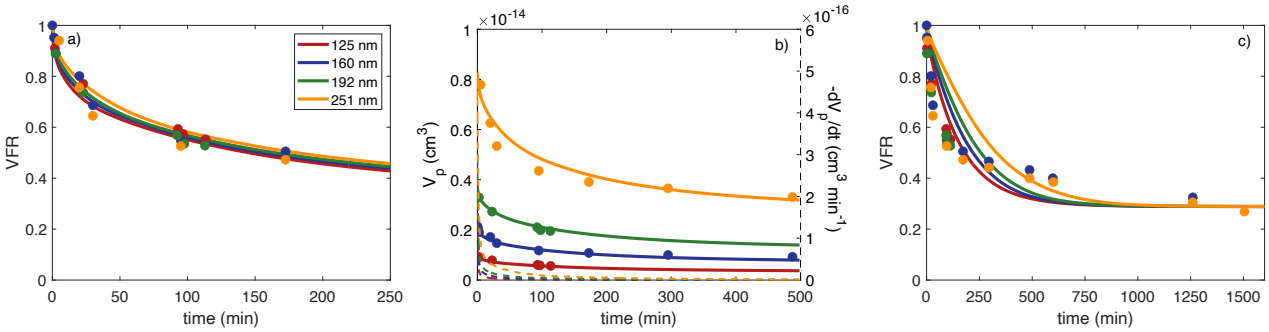


Figure S9. a) Same as Fig 2b, volume fraction remaining (VFR) for ev**a**por**a**tion of α-pinene SOA particles zoomed in to see simulation and measurement agreement at early times. b) Temporal evolution of volume of single particle (left axis, solid lines) and evaporation rate (right axis, dashed lines) for evaporation of α-pinene SOA particles. c) VFR during evaporation of α-pinene SOA particles with a fixed diffusivity of $D_b = 10^{-15}$ cm^2 s^{-1}.

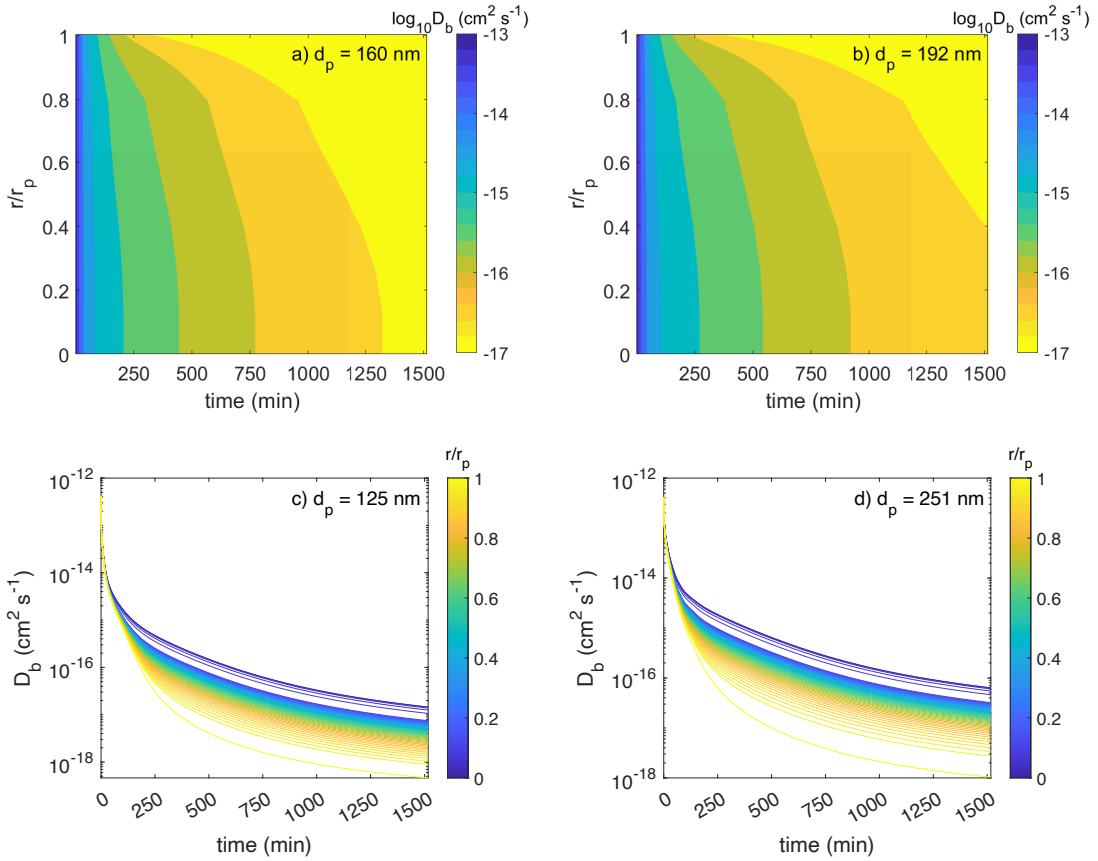


Figure S10. a) and b) Surface crust formation during α-pinene SOA evaporation for the middle two particle sizes for the best fit case. The y-axis (r/r_p) is the distance from the particle center normalized by the particle radius (r/r_p = 1 at the surface). The plots are colored by the diffusivity calculated from the composition at each distance. c) and d) Diffusivity in each particle layer over time for the smallest and largest size particles shown in Fig. 2d,e.

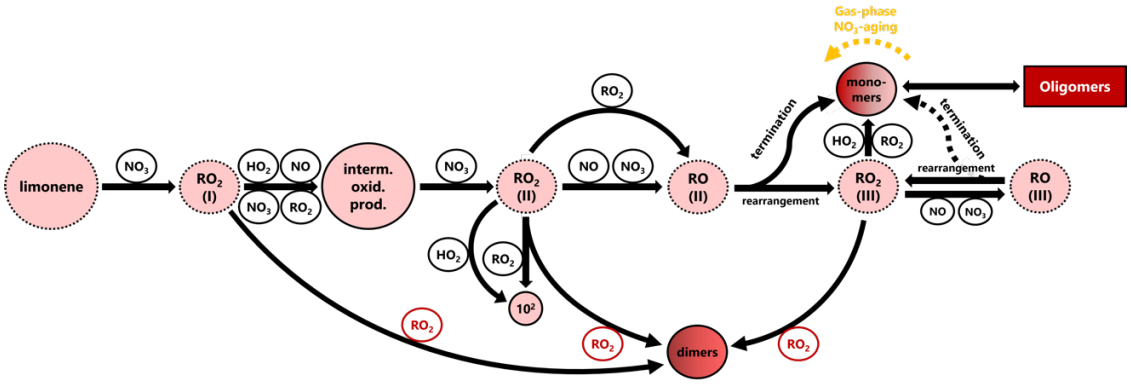


Figure S11. Model mechanism of limonene + NO_3 to SOA formation. The intermediate oxidation product is a semi-volatile product representing monomers retaining a double bond. Monomers, dimers, and the intermediate are partitioning species, while oligomers are formed in the bulk and do not evaporate.

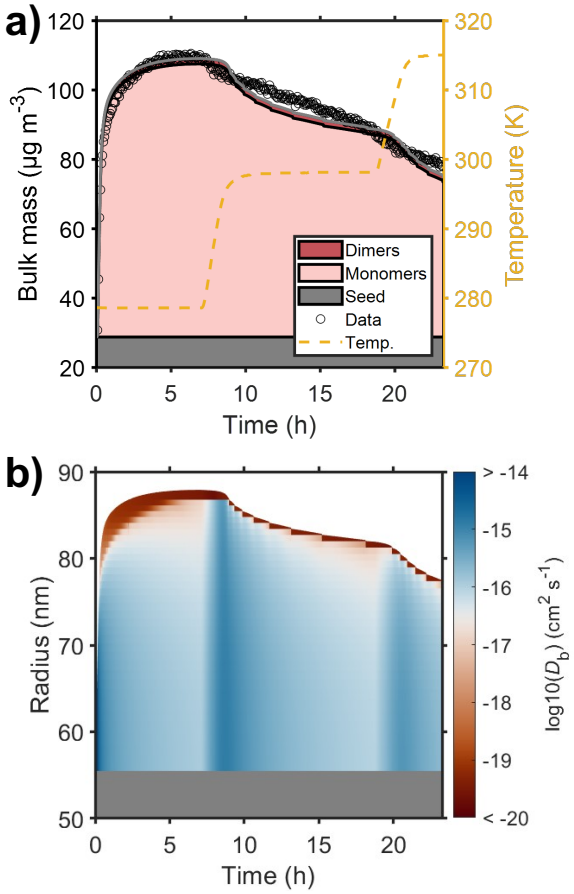


Figure S12. Formation and evaporation of limonene SOA in an environmental chamber experiment with varying temperature without bulk-phase oligomer formation. Panel a shows SOA mass concentrations, while b shows the particle radius. Colors in panel a) distinguish monomers and dimers/oligomers and in panel b) indicate the composition-dependent bulk diffusion coefficient, $\log_{10}(D_b)$. Even without oligomerization, the model is able to find a fit where a surface crust is formed.

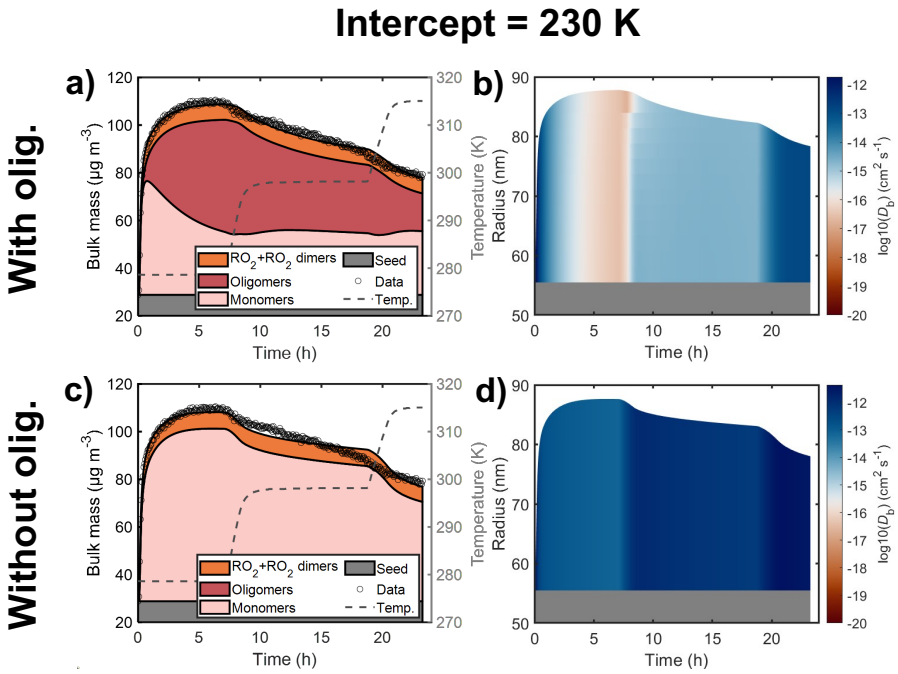


Figure S13. Model bulk masses and layer diffusivities as the intercept in the T_g versus C^* relationship is adjusted. Panels a and b show results from the model that includes bulk-phase oligomerization, while panels c and d exclude oligomerization. This model with a low T_g finds a reasonable fit (a, c), but results in a well-mixed particle without crust formation (b, d).

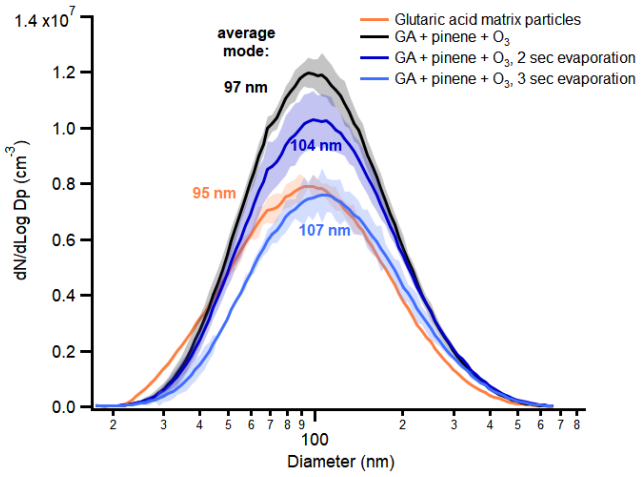


Figure S14. Particle size distribution measurements of bare glutaric acid matrix particles (orange), SOA-coated matrix particles (black), and SOA-coated matrix particles after 2-3 seconds of evaporation (dark blue, light blue, respectively). The SOA coating is ~1 nm.

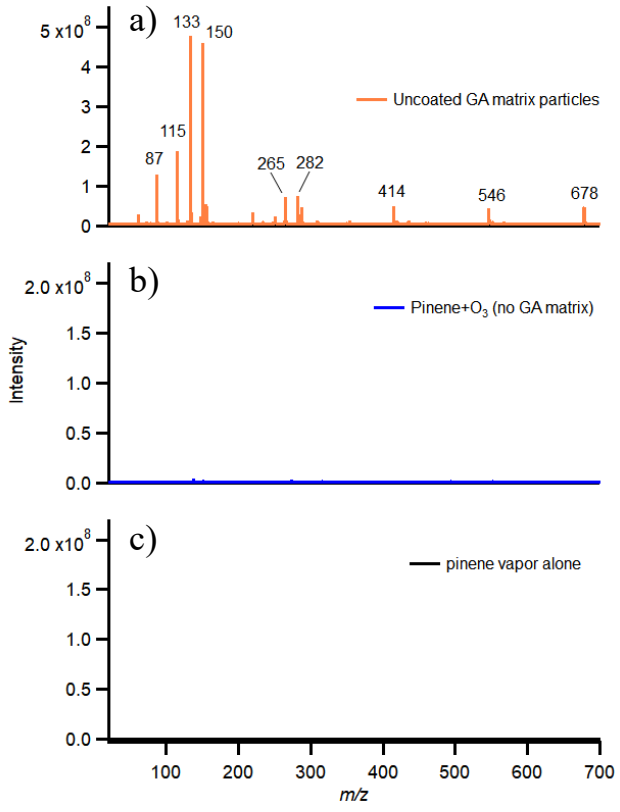


Figure S15. MAIV spectra of a) uncoated glutaric acid matrix particles, b) SOA particles in the absence of matrix particles, and c) pinene vapor alone.

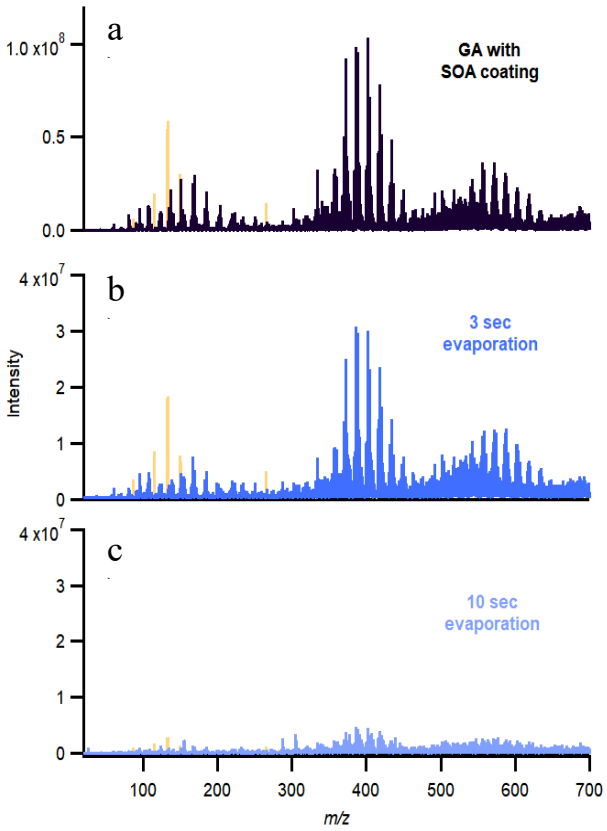


Figure S16. MAIV spectra of a) SOA-coated glutaric acid particles with no evaporation, b) after 3 s of evaporation, and c) after 10 s evaporation with additional denuder.

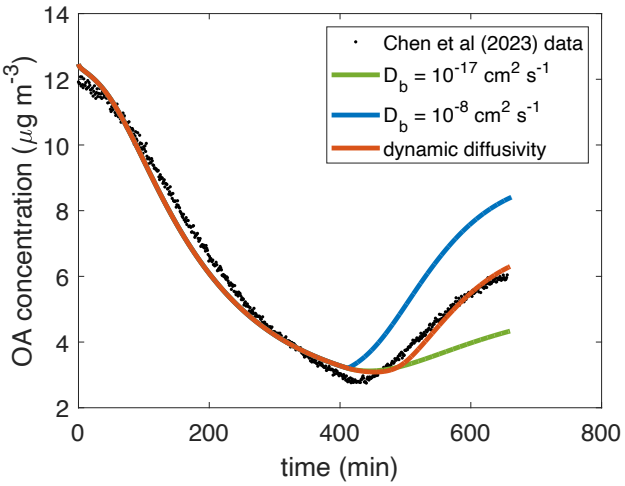


Figure S17. Simulation of isoprene SOA evaporation and subsequent condensation. Points are from Chen et al (2023). Evaporation proceeds identically in every case, but at the onset of condensation, the particle bulk diffusivity is immediately changed to 10^{-8} cm^2 s^{-1} (blue), 10^{-17} cm^2 s^{-1} (green), or allowed to proceed with a dynamic diffusivity throughout condensation (orange). Exposure to fresh isoprene SVOCs occurs at ~400 min.

Table S1. MCGA fit parameters for all PEG 300, PEG 400, and α-pinene SOA fit simulations shown in this work. C^* is the volatility, T_g is the glass transition temperature, D_b is the bulk diffusivity, and f is the initial mass fraction in the particle phase for each species with subscripts 1-5 indicating species 1-5. Species 5 is assumed to be non-volatile. k_{wall} is the first-order vapor wall loss rate coefficient and k_{decomp} is the first-order oligomer decomposition rate coefficient.

Parameters	**α-pinene SOA T_g (Fig. 2b)**	**PEG 400 T_g (Fig. 1b)**	**PEG 300 (Fig. 1b)**	**PEG 400 number fraction (Fig. S5)**	**PEG 400 no dynamic diffusivity (Fig. S8)**
C^*_1 **(ug m^{-3})**	16.9	96.224.02	104.56	67.02.015	92.76
C^*_2	4.29	2.58	33.16	2.16	6.87
C^*_3	0.605	0.11	1.78	0.105	0.12
C^*_4	0.012	0.007	0.094	0.021	0.0097
$D_{b,1}/T_{g,1}$ **(cm^2 s^{-1}/K)**	187.2	124.37	116.98	2.99×10^{-7}	1.08×10^{-7}
$D_{b,2}/T_{g,2}$	226.3	127.67	134.09	5.93×10^{-10}	-
$D_{b,3}/T_{g,3}$	235.9	154.92	152.14	8.75×10^{-12}	-
$D_{b,4}/T_{g,4}$	254.01	166.72	166.7	7.78×10^{-13}	-
$D_{b,5}/T_{g,5}$	300.1	219.71	220.44	1×10^{-17}	-
f_1	0.05	0.054	0.05	0.074	0.078
f_2	0.06	0.06	0.11	0.16	0.14
f_3	0.15	0.14	0.23	0.12	0.073
f_4	0.44	0.06	0.27	0.2	0.35
f_5	0.29	0.69	0.35	0.45	0.36
k_{wall} **(s^{-1})***	0.3	0.3	0.3	0.3	0.3
k_{decomp} **(s^{-1})**	8.34×10^{-5}	-	-	-	-

*k_{wall} was fit to between 0.2-0.4 s^{-1} in all runs and was fixed at 0.3 s^{-1} in all simulations

Table S2. MCGA fit parameters for PEG 200 and PEG 1000 fits. C^* is the volatility, T_g is the glass transition temperature and f is the initial mass fraction in the particle phase for each species with subscripts 1-5 indicating species 1-5. Species 5 is assumed to be non-volatile. k_{wall} is the first-order gas-phase wall loss rate coefficient.

Parameters	**PEG 200 (Fig S1)**	**PEG 1000 (Fig S1)**
C^*_1 **(ug m^{-3})**	1656.54	2.98
C^*_2	33.17	0.0084
C^*_3	4.76	0.0014
C^*_4	0.34	5.74e-5
$T_{g,1}$ **(K)**	208.6	150.3
$T_{g,2}$	239.0	201.2
$T_{g,3}$	258.8	248.1
$T_{g,4}$	275.9	283.1
$T_{g,5}$	301.4	302.7
f_1	0.26	0.20
f_2	0.30	0.28
f_3	0.31	0.28
f_4	0.073	0.065
f_5	0.064	0.18
k_{wall} **(s^{-1})**	0.3	0.3

Table S3 MCGA fit parameters for the limonene + NO_3 model.

Parameter	With oligomerization	Without oligomerization
Monomer bin branching (1) ($C^* = 10^{-4}$ μg m^{-3})	2.22×10^{-1}	2.00×10^{-1}
Monomer bin branching (2) ($C^* = 10^{-3}$ μg m^{-3})	3.57×10^{-3}	2.05×10^{-2}
Monomer bin branching (3) ($C^* = 10^{-2}$ μg m^{-3})	1.94×10^{-3}	1.02×10^{-1}
Monomer bin branching (4) ($C^* = 10^{-1}$ μg m^{-3})	1.48×10^{-1}	1.53×10^{-1}
Monomer bin branching (5) ($C^* = 10^{0}$ μg m^{-3})	2.41×10^{-1}	2.32×10^{-1}
Monomer bin branching (6) ($C^* = 10^{1}$ μg m^{-3})	1.86×10^{-1}	1.96×10^{-1}
Monomer bin branching (7) ($C^* = 10^{2}$ μg m^{-3})	1.73×10^{-1}	1.38×10^{-2}
Monomer bin branching (8) ($C^* = 10^{3}$ μg m^{-3})	2.40×10^{-2}	7.87×10^{-2}
Monomer bin branching (9) (gas only)	4.90×10^{-4}	4.00×10^{-3}
Dimer bin branching (1)	0.83	0.02
Dimer bin branching (2)	0.16	0.80
Dimer bin branching (3)	0.01	0.18
C^* of IOP (μg m^{-3})	1623	1914
C^* of dimer (μg m^{-3})	2.83×10^{-4}	2.77×10^{-5}
$RO_2 + RO_2 \rightarrow$ dimer branching	0.086	0.093
$RO \rightarrow$ product + NO_2 branching	0.95	0.90
$RO \rightarrow$ product branching	0.65	0.92
$k_{fwd,olig}$ (s^{-1})	1.63×10^{-5}	N/A
$k_{rev,olig}$ (s^{-1})	2.55×10^{-4}	N/A
Oligomer dissociation energy of activation (kJ mol^{-1})	141	N/A
$k_{aging,NO3}$ (cm^3 s^{-1})	1.07×10^{-14}	2.28×10^{-14}

Table S4. Parameters for isoprene SOA evaporation. C^* is the volatility, T_g is the glass transition temperature and f is the initial mass fraction in the particle phase for each species with subscripts 1-5 indicating species 1-5. k_{wall} is the first-order gas-phase wall loss rate coefficient and k_{decomp} is the first-order oligomer decomposition rate coefficient.

Parameters	**Isoprene SOA (Fig S17)**
C^*_1 **(ug m^{-3})**	100
C^*_2	10
C^*_3	1
C^*_4	0.05
$T_{g,1}$ **(K)**	255
$T_{g,2}$	275
$T_{g,3}$	280
$T_{g,4}$	295
$T_{g,5}$	310
f_1	0.27
f_2	0.2
f_3	0.09
f_4	0.38
f_5	0.07
k_{wall} **(s^{-1})***	10^{-3}
k_{decomp} **(s^{-1})**	1.2×10^{-4}

SI References

(1) Shiraiwa, M.; Li, Y.; Tsimpidi, A. P.; Karydis, V. A.; Berkemeier, T.; Pandis, S. N.; Lelieveld, J.; Koop, T.; Pöschl, U. Global Distribution of Particle Phase State in Atmospheric Secondary Organic Aerosols. *Nat. Commun.* **2017**, *8* (1), 15002. https://doi.org/10.1038/ncomms15002.

(2) Zhang, Z.; Li, Y.; Ran, H.; An, J.; Qu, Y.; Zhou, W.; Xu, W.; Hu, W.; Xie, H.; Wang, Z.; Sun, Y.; Shiraiwa, M. Simulated Phase State and Viscosity of Secondary Organic Aerosols over China. *Atmospheric Chem. Phys.* **2024**, *24* (8), 4809–4826. https://doi.org/10.5194/acp-24-4809-2024.

(3) Luu, R.; Schervish, M.; June, N. A.; O'Donnell, S. E.; Jathar, S. H.; Pierce, J. R.; Shiraiwa, M. Global Simulations of Phase State and Equilibration Time Scales of Secondary Organic Aerosols with GEOS-Chem. *ACS Earth Space Chem.* **2025**, *9* (2), 288–302. https://doi.org/10.1021/acsearthspacechem.4c00281.

(4) DeRieux, W.-S. W.; Li, Y.; Lin, P.; Laskin, J.; Laskin, A.; Bertram, A. K.; Nizkorodov, S. A.; Shiraiwa, M. Predicting the Glass Transition Temperature and Viscosity of Secondary Organic Material Using Molecular Composition. *Atmospheric Chem. Phys.* **2018**, *18* (9), 6331–6351. https://doi.org/10.5194/acp-18-6331-2018.

(5) Vignes, A. Diffusion in Binary Solutions. Variation of Diffusion Coefficient with Composition. *Ind. Eng. Chem. Fundam.* **1966**, *5* (2), 189–199. https://doi.org/10.1021/i160018a007.

(6) O'Meara, S.; Topping, D. O.; Zaveri, R. A.; McFiggans, G. An Efficient Approach for Treating Composition-Dependent Diffusion within Organic Particles. *Atmospheric Chem. Phys.* **2017**, *17* (17), 10477–10494. https://doi.org/10.5194/acp-17-10477-2017.

(7) Marshall, F. H.; Berkemeier, T.; Shiraiwa, M.; Nandy, L.; Ohm, P. B.; Dutcher, C. S.; Reid, J. P. Influence of Particle Viscosity on Mass Transfer and Heterogeneous Ozonolysis Kinetics in Aqueous–Sucrose–Maleic Acid Aerosol. *Phys. Chem. Chem. Phys.* **2018**, *20* (22), 15560–15573. https://doi.org/10.1039/C8CP01666F.

(8) Milsom, A.; Squires, A. M.; Ward, A. D.; Pfrang, C. Molecular Self-Organization in Surfactant Atmospheric Aerosol Proxies. *Acc. Chem. Res.* **2023**, *56* (19), 2555–2568. https://doi.org/10.1021/acs.accounts.3c00194.

(9) Berkemeier, T.; Ammann, M.; Krieger, U. K.; Peter, T.; Spichtinger, P.; Pöschl, U.; Shiraiwa, M.; Huisman, A. J. Technical Note: Monte Carlo Genetic Algorithm (MCGA) for Model Analysis of Multiphase Chemical Kinetics to Determine Transport and Reaction Rate Coefficients Using Multiple Experimental Data Sets. *Atmospheric Chem. Phys.* **2017**, *17* (12), 8021–8029. https://doi.org/10.5194/acp-17-8021-2017.

(10) Hall IV, W. A.; Johnston, M. V. Oligomer Content of α-Pinene Secondary Organic Aerosol. *Aerosol Sci. Technol.* **2011**, *45* (1), 37–45. https://doi.org/10.1080/02786826.2010.517580.

(11) D'Ambro, E. L.; Schobesberger, S.; Zaveri, R. A.; Shilling, J. E.; Lee, B. H.; Lopez-Hilfiker, F. D.; Mohr, C.; Thornton, J. A. Isothermal Evaporation of α-Pinene Ozonolysis SOA: Volatility, Phase State, and Oligomeric Composition. *ACS Earth Space Chem.* **2018**, *2* (10), 1058–1067. https://doi.org/10.1021/acsearthspacechem.8b00084.

(12) Heitto, A.; Lehtinen, K.; Petäjä, T.; Lopez-Hilfiker, F.; Thornton, J. A.; Kulmala, M.; Yli-Juuti, T. Effects of Oligomerization and Decomposition on the Nanoparticle Growth: A Model Study. *Atmospheric Chem. Phys.* **2022**, *22* (1), 155–171. https://doi.org/10.5194/acp-22-155-2022.

(13) Krieger, U. K.; Siegrist, F.; Marcolli, C.; Emanuelsson, E. U.; Gøbel, F. M.; Bilde, M.; Marsh, A.; Reid, J. P.; Huisman, A. J.; Riipinen, I.; Hyttinen, N.; Myllys, N.; Kurtén, T.; Bannan, T.; Percival, C. J.; Topping, D. A Reference Data Set for Validating Vapor Pressure Measurement Techniques: Homologous Series of Polyethylene Glycols. *Atmospheric Meas. Tech.* **2018**, *11* (1), 49–63. https://doi.org/10.5194/amt-11-49-2018.

(14) Bannan, T. J.; Le Breton, M.; Priestley, M.; Worrall, S. D.; Bacak, A.; Marsden, N. A.; Mehra, A.; Hammes, J.; Hallquist, M.; Alfarra, M. R.; Krieger, U. K.; Reid, J. P.; Jayne, J.; Robinson, W.; McFiggans, G.; Coe, H.; Percival, C. J.; Topping, D. A Method for Extracting Calibrated Volatility

Information from the FIGAERO-HR-ToF-CIMS and Its Experimental Application. *Atmospheric Meas. Tech.* **2019**, *12* (3), 1429–1439. https://doi.org/10.5194/amt-12-1429-2019.
(15) Donahue, N. M.; Epstein, S. A.; Pandis, S. N.; Robinson, A. L. A Two-Dimensional Volatility Basis Set: 1. Organic-Aerosol Mixing Thermodynamics. *Atmospheric Chem. Phys.* **2011**, *11* (7), 3303–3318. https://doi.org/10.5194/acp-11-3303-2011.
(16) Berkemeier, T.; Takeuchi, M.; Eris, G.; Ng, N. L. Kinetic Modeling of Formation and Evaporation of Secondary Organic Aerosol from NO_3 Oxidation of Pure and Mixed Monoterpenes. *Atmospheric Chem. Phys.* **2020**, *20* (24), 15513–15535. https://doi.org/10.5194/acp-20-15513-2020.
(17) Trump, E. R.; Donahue, N. M. Oligomer Formation within Secondary Organic Aerosols: Equilibrium and Dynamic Considerations. *Atmospheric Chem. Phys.* **2014**, *14* (7), 3691–3701. https://doi.org/10.5194/acp-14-3691-2014.
(18) Li, Y.; Day, D. A.; Stark, H.; Jimenez, J. L.; Shiraiwa, M. Predictions of the Glass Transition Temperature and Viscosity of Organic Aerosols from Volatility Distributions. *Atmospheric Chem. Phys.* **2020**, *20* (13), 8103–8122. https://doi.org/10.5194/acp-20-8103-2020.
(19) Qin, Y.; Wingen, L. M.; Finlayson-Pitts, B. J. Toward a Molecular Understanding of the Surface Composition of Atmospherically Relevant Organic Particles. *Proc. Natl. Acad. Sci.* **2022**, *119* (35), e2209134119. https://doi.org/10.1073/pnas.2209134119.
(20) Forsyth, B.; Liu, B. Y. H.; Romay, F. J. Particle Charge Distribution Measurement for Commonly Generated Laboratory Aerosols. *Aerosol Sci. Technol.* **1998**, *28* (6), 489–501. https://doi.org/10.1080/02786829808965540.
(21) Tsai, C.-J.; Lin, J.-S.; Deshpande, C. G.; Liu, L.-C. Electrostatic Charge Measurement and Charge Neutralization of Fine Aerosol Particles during the Generation Process. *Part. Part. Syst. Charact.* **2005**, *22* (5), 293–298. https://doi.org/10.1002/ppsc.200500961.
(22) Pervukhin, V. V.; Sheven', D. G.; Kolomiets, Yu. N. Collison Nebulizer as a New Soft Ionization Source for Mass Spectrometry. *Tech. Phys.* **2016**, *61* (8), 1262–1268. https://doi.org/10.1134/S1063784216080211.
(23) Qin, Y.; Perraud, V.; Finlayson-Pitts, B. J.; Wingen, L. M. Peroxides on the Surface of Organic Aerosol Particles Using Matrix-Assisted Ionization in Vacuum (MAIV) Mass Spectrometry. *Environ. Sci. Technol.* **2023**, *57* (38), 14260–14268. https://doi.org/10.1021/acs.est.3c02895.
(24) Consta, S.; Wingen, L. M.; Qin, Y.; Perraud, V.; Finlayson-Pitts, B. J. Modeling the Ionization Mechanism of Amorphous Solid Particles without an External Energy Source Coupled to Mass Spectrometry. *Phys. Chem. Chem. Phys.* **2024**, *26* (44), 28220–28233. https://doi.org/10.1039/D4CP03597F.
(25) Chen, Y.; Zaveri, R. A.; Vandergrift, G. W.; Cheng, Z.; China, S.; Zelenyuk, A.; Shilling, J. E. Nonequilibrium Behavior in Isoprene Secondary Organic Aerosol. *Environ. Sci. Technol.* **2023**, *57* (38), 14182–14193. https://doi.org/10.1021/acs.est.3c03532.
(26) Karl, M.; Brauers, Th.; Dorn, H.-P.; Holland, F.; Komenda, M.; Poppe, D.; Rohrer, F.; Rupp, L.; Schaub, A.; Wahner, A. Kinetic Study of the OH-Isoprene and O3-Isoprene Reaction in the Atmosphere Simulation Chamber, SAPHIR. *Geophys. Res. Lett.* **2004**, *31* (5). https://doi.org/10.1029/2003GL019189.

B.4 Supplement of "Temperature-dependent multiphase chemical kinetics explain uniform atmospheric nanoparticle growth rates"

Supplementary Materials for

Zhiqiang Zhang[1], Hyun Gu Kang[1], Ulrich Pöschl[1], Thomas Berkemeier[1,*]
[1]Multiphase Chemistry Department, Max Planck Institute for Chemistry, Mainz 55128, Germany. *Corresponding author. Email: t.berkemeier@mpic.de

This PDF file includes:

Materials and Methods
Supplementary Text
Figures S1 to S3
Table S1

Materials and Methods

Kinetic model

We apply a kinetic multilayer model of multiphase chemistry (KM3C) to estimate the diffusion limitations affecting the initial steps of condensational growth of SOA right after nucleation in the atmosphere. The detailed descriptions of the model could be found in previous studies (Shiraiwa et al., 2012; Berkemeier et al., 2020). The model compartments consist of gas, near-surface gas, sorption layer, quasi-static surface (first outer bulk layer) and several bulk layers (Figure S3). Generally, the model explicitly treats gas phase diffusion, vapor-pressure based partitioning (adsorption and desorption) and bulk diffusion. The model applies an adaptive layer-resizing algorithm that dynamically splits layers when a layer grows too large and merges adjacent layers when they are too thin. Desorption lifetime is calculated from the relationship between vapor pressure and desorption energy (Knopf et al., 2024) as shown in Figure S4. The model also considers Kelvin effect (D_{k10}), temperature dependence of volatility (ΔHvap) and bulk diffusivity (ΔHdif). We applied the kinetic model to a field observation in Hyytiälä on 17th August 2020, and laboratory experiments of dark α-pinene ozonolysis conducted at Cosmics Leaving Outdoor Droplets (CLOUD) chamber at European Organization for Nuclear Research (CERN) (Stolzenburg et al., 2018). Measurements were fitted by optimizing uncharacterized parameters with Monte Carlo Genetic Algorithm (MCGA, Berkemeier et al., 2017).

Adaptive layer resizing and moving-boundary algorithm

KM3C implements an adaptive layer resizing algorithm that splits a layer when it becomes too thick and reaches the upper threshold, and merges two adjacent layers when the depths are too thin and drops below the lower threshold (Kang et al., 2026; Schervish et al., 2026). This algorithm is able to account for diffusivity gradients dynamically when nanoparticles grow (or shrink) and can prevent numerical stiffness when layers becoming too thin. To calculate the diffusivity between two bulk layers in the model, for the bulk layer near the surface, we consider the mass composition of that layer, while for the other inner layers, we combine mass composition of the two adjacent layers.

We found nanoparticle growth is dominated by surface-to-bulk transposition. Based on partitioning theory, the surface-to-bulk transfer rate coefficient (k_{sb}) can be calculated expressed as Eq. S1:

$$k_{sb} = k_{bs}\frac{k_d}{k_a} \times \frac{\sum[Y]_b \times RT}{p_{vap}N_A} \tag{S1}$$

in which, k_d and k_a are the desorption and adsorption rate coefficients. $\sum[Y]_b$ is the sum of the molecular concentrations of bulk-phase species (cm^{-3}). p_{vap} is the vapor pressure (Pa) of the partitioning species, R is the gas constant (8.314×10^6 cm^3 Pa K^{-1}

mol^{-1}), T is the temperature (K), and N_A is Avogadro's number (6.022×10^{23} mol^{-1}). k_{bs} is the bulk-to-surface transfer rate coefficient, and can be calculated with Eq. S2:

$$k_{bs} = \frac{2 \times D_b}{D(1) + D(2)} \tag{S2}$$

where D_b is the bulk diffusivity, $D(1)$ is the depth of sorption layer, and $D(2)$ is the depth of the near-surface bulk layer. When nanoparticles grow to the threshold of adaptive layer resizing algorithm, the near-surface bulk layer will split into two layers, leading to a sudden increase in growth rate. To solve this problem, we implement a moving-boundary algorithm (Couvidat and Sartelet, 2015; Kang et al., 2026). With this algorithm, KM3C can keep the depth of the near-surface bulk layer constant by increasing diffusion from the first bulk layer to the second bulk layer when particle grow The diffusion rates calculated based on the molecular volume flow into the near-surface bulk layer are applied when solving ordinary differential equations.

Temperature dependence of volatility

Temperature dependence of saturation mass concentration is according to Clausius-Clapeyron equation.

$$C_T^* = C_{298K}^* \times exp(-\frac{\Delta H_{vap}}{R}(\frac{1}{T} - \frac{1}{300})) \tag{S3}$$

ΔH_{vap} is the enthalpy of vaporization, and it can be linked with C_{298K}^* by an empirical linear fit (Epstein et al., 2010). We optimize this relationship within reasonable range according to literature (Stolzenburg et al., 2022), where m_{Hvap} and b_{Hvap} are the slope and intercept respectively. The optimized parameters are shown in Table S1.

$$\Delta H_{vap} = m_{\mathrm{Hvap}} \times \log_{10} C_{298K}^* + b_{\mathrm{Hvap}} \tag{S4}$$

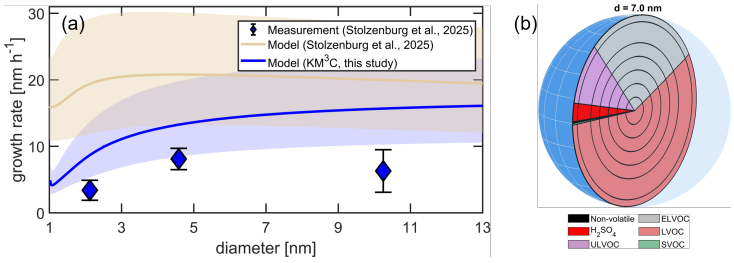


Figure S1: *Model overestimates nanoparticle growth rates in field measurement by assuming high particle phase diffusivity. Same as Figure 1, but with high diffusivity ($D_{b,\,298\,K} = 10^{-15} cm^2 s^{-1}$).*

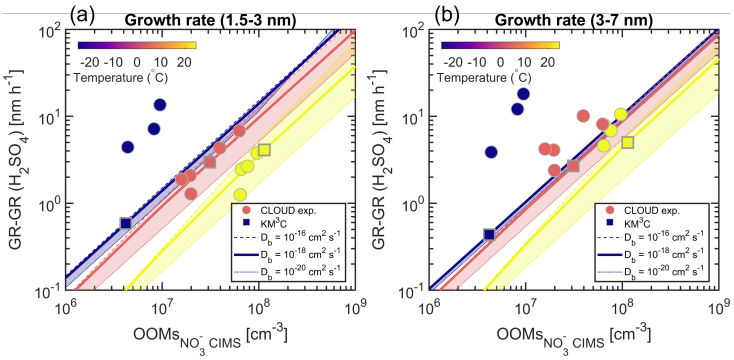


Figure S2: *Model underestimates nanoparticle growth in CERN CLOUD chamber with with OOMs only measured by nitrate-CI. Same as Figure 3, but growth rates were modelled with OOMs only measured by nitrate-CI.*

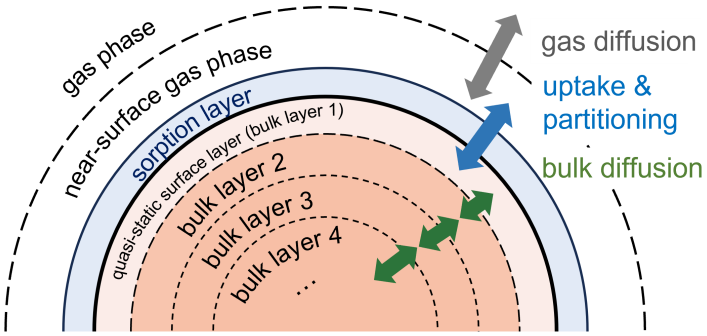


Figure S3: *Description of KM3C kinetic model. Overview of the compartments and explicit processes incorporated in the kinetic model implemented in this study.*

Table S1: *Optimized parameters in* $\Delta H_{vap} - C^*_{298K}$ *relationship.*

Scenarios	Parameters	optimized values
$D_b - C^*$ method	m_{Hvap}	-6.71
	b_{Hvap}	135.78

References

Berkemeier, T., Ammann, M., Krieger, U. K., Peter, T., Spichtinger, P., Pöschl, U., Shiraiwa, M., and Huisman, A. J.: Technical note: Monte Carlo genetic algorithm (MCGA) for model analysis of multiphase chemical kinetics to determine transport and reaction rate coefficients using multiple experimental data sets, Atmos. Chem. Phys., 17, 8021–8029, 2017.

Berkemeier, T., Takeuchi, M., Eris, G., and Ng, N. L.: Kinetic modeling of formation and evaporation of secondary organic aerosol from NO_3 oxidation of pure and mixed monoterpenes, Atmos. Chem. Phys., 20, 15 513–15 535, 2020.

Couvidat, F. and Sartelet, K.: The Secondary Organic Aerosol Processor (SOAP v1.0) model: a unified model with different ranges of complexity based on the molecular surrogate approach, Geoscientific Model Development, 8, 1111–1138, 2015.

Epstein, S. A., Riipinen, I., and Donahue, N. M.: A Semiempirical Correlation between Enthalpy of Vaporization and Saturation Concentration for Organic Aerosol, Environmental Science & Technology, 44, 743–748, pMID: 20025284, 2010.

Kang, H. G., Takeuchi, M., Ng, N. L., Pöschl, U., and Berkemeier, T.: Multiphase Chemistry and Phase State Explain Nonlinear Effects in the Formation and Evaporation of SOA from Mixed Monoterpene Precursors, ACS ESamp;T Air, 2026.

Knopf, D. A., Ammann, M., Berkemeier, T., Pöschl, U., and Shiraiwa, M.: Desorption lifetimes and activation energies influencing gas–surface interactions and multiphase chemical kinetics, Atmospheric Chemistry and Physics, 24, 3445–3528, 2024.

Schervish, M., Kang, H. G., Wingen, L. M., Nguyen, K., Begay, C., Wilson, J., Shrivastava, M., Chen, Y., Shilling, J. E., Ng, N. L., Pöschl, U., Berkemeier, T., Zelenyuk, A., and Shiraiwa, M.: Surface Crust Formation Controls Evaporation Kinetics of Secondary Organic Aerosols, Environmental Science amp; Technology, 60, 7995–8006, 2026.

Shiraiwa, M., Pfrang, C., Koop, T., and Pöschl, U.: Kinetic multi-layer model of gas-particle interactions in aerosols and clouds (KM-GAP): linking condensation, evaporation and chemical reactions of organics, oxidants and water, Atmos. Chem. Phys., 12, 2777–2794, 2012.

Stolzenburg, D., Fischer, L., Vogel, A. L., Heinritzi, M., Schervish, M., Simon, M., Wagner, A. C., Dada, L., Ahonen, L. R., Amorim, A., Baccarini, A., Bauer, P. S., Baumgartner, B., Bergen, A., Bianchi, F., Breitenlechner, M., Brilke, S., Buenrostro Mazon, S., Chen, D., Dias, A., Draper, D. C., Duplissy, J., El Haddad, I., Finkenzeller, H., Frege, C., Fuchs, C., Garmash, O., Gordon, H., He, X., Helm, J., Hofbauer, V., Hoyle, C. R., Kim, C., Kirkby, J., Kontkanen, J., Kürten, A., Lampilahti, J., Lawler, M., Lehtipalo, K., Leiminger, M., Mai, H., Mathot, S., Mentler, B., Molteni, U., Nie, W., Nieminen, T., Nowak, J. B., Ojdanic, A., Onnela, A., Passananti, M., Petäjä, T., Quéléver, L. L. J.,

Rissanen, M. P., Sarnela, N., Schallhart, S., Tauber, C., Tomé, A., Wagner, R., Wang, M., Weitz, L., Wimmer, D., Xiao, M., Yan, C., Ye, P., Zha, Q., Baltensperger, U., Curtius, J., Dommen, J., Flagan, R. C., Kulmala, M., Smith, J. N., Worsnop, D. R., Hansel, A., Donahue, N. M., and Winkler, P. M.: Rapid growth of organic aerosol nanoparticles over a wide tropospheric temperature range, Proceedings of the National Academy of Sciences, 115, 9122–9127, 2018.

Stolzenburg, D., Wang, M., Schervish, M., and Donahue, N. M.: Tutorial: Dynamic organic growth modeling with a volatility basis set, Journal of Aerosol Science, 166, 106 063, 2022.